NNT : 2018SACLS230

Etude et modélisation des phénomènes thermohydrauliques résultant du quench d'un aimant supraconducteur refroidi en hélium supercritique

Thèse de doctorat de l'Université Paris-Saclay
préparée à l'Université Paris-Sud
CEA / IRFU / DACM

École doctorale n°576 : particules hadrons énergie et noyau : instrumentation, image, cosmos et simulation (PHENIICS)
Spécialité de doctorat : énergie nucléaire

Thèse présentée et soutenue à Saclay, le 19 octobre 2018, par

M. Yawei HUANG

Composition du Jury :

M. Frédéric Bouillault Professeur, Université Paris-Saclay (GEEPS)	Président
M. Marco Breschi Professeur, University of Bologna (UNIBO)	Rapporteur
Mme Monika Lewandowska Professeur, West Pomeranian University of Technology Szczecin (Institute of Physics)	Rapporteur
M. Luca Bottura Ingénieur de recherche, CERN (Magnet Group)	Examinateur
M. Daniel Ciazynski Ingénieur de recherche, CEA Cadarache (IRFM/STEP)	Examinateur
M. Bertrand Baudouy Ingénieur de recherche, CEA Saclay (IRFU/DACM)	Directeur de thèse
M. Walid Abdel Maksoud Ingénieur de recherche, CEA Saclay (IRFU/DACM)	Co-Directeur de thèse

Thèse de doctorat

——谨以此献给我的父母

感谢他们多年的教诲与养育

Remerciements

Cet ouvrage est le fruit de trois ans de travail de thèse que j'ai effectué au Commissariat à l'Energie Atomique et aux Energies Alternatives (CEA) de Saclay, au sein du Laboratoire de Cryogénie et des Stations d'Essais (LCSE) du Département des Accélérateurs, de Cryogénie et de Magnétisme (DACM) de l'Institut de Recherche sur les Lois Fondamentales de l'Univers (IRFU).

Dans ce cadre, je veux commencer par remercier la direction du DACM et du LCSE, Mess. Pierre Védrine, Philippe Brédy, Christophe Mayri et Mme. Roser Vallcorba Carbonell, de m'avoir chaleureusement accueilli dans leur équipe et d'avoir mis à ma disposition les moyens nécessaires à la réalisation de mes travaux. Je remercie aussi l'ancien chef du projet JT-60SA, M. Laurent Génini, de m'avoir intégré rapidement dans son équipe de projet et d'avoir mis à ma disposition toutes les ressources humaines, matérielles et financières importantes pour la réalisation de ma thèse.

Je me suis très honoré d'avoir Mme. Monika Lewandowska, Mess. Marco Breschi, Luca Bottura, Frédéric Bouillault, et Daniel Ciazynski dans mon jury de thèse. Je les remercie pour l'intérêt qu'ils ont prêté à mon travail et la contribution qu'ils ont donné à l'amélioration de ce manuscrit, et tout particulièrement Mme. Monika Lewandowska et M. Marco Breschi pour le minutieux travail de rapporteur qu'ils ont fourni.

Je remercie M. Bertrand Baudouy, mon directeur de thèse, de m'avoir encadré tout au long de mon travail de thèse. Je veux le remercier pour ses conseils pédagogiques, pour sa disponibilité constante pour son étudiant, pour sa rigueur en détail scientifique pour la recherche et la publication, qui étaient des supports indispensables pour le progrès de mon travail de thèse, et aussi pour son humour et sa qualité humaine pour rendre son étudiant dans une bonne ambiance de recherche.

S'il s'agit d'une thèse juteuse, je dois exprimer ma reconnaissance à M. Walid Abdel Maksoud, mon encadrant de thèse et aussi l'actuel chef du projet JT-60SA. Je le remercie d'avoir cru en mes compétences et de m'avoir embauché pour cette thèse très intéressante. En tant que son premier thésard, je le remercie pour son dynamisme d'encadrement, pour sa présence constante et pour ses échanges toujours très utiles pour l'avancement de ma recherche. La réalisation de mes travaux de recherche pendant ces trois ans est en grande mesure grâce à sa vaste connaissance du domaine, ses compétences en projet de recherche, son attitude positive et sa qualité humaine. J'ai donc l'honneur d'avoir réalisé mon projet de thèse avec lui.

Je tiens à remercier les membres de l'équipe du projet JT-60SA, grâce à qui les expériences des aimants ont toutes eu une grande réussite et qui ont tous apporté une contribution importante à mon travail, en particulier, Mess. Damien Médioni, Charles Mailleret, Pascal Godon, Romain Godon et Nicolas Commaux.

Je remercie M. Benoît Lacroix, ingénieur de recherche au CEA Cadarache, grâce à qui mon apprentissage et usage du code numérique m'ont permis d'obtenir des résultats satisfaisants. Je remercie aussi Mme. Laurence Vieillard pour son occupation de toutes mes formations pendant ces trois ans de thèse. Je remercie toutes les personnes avec qui j'ai passé de bons moments pendant le repas et la pause-café, et avec qui j'ai côtoyé pendant ces trois dernières années.

Pour finir, je remercie du fond de mon cœur mes parents qui m'ont toujours soutenu spirituellement et matériellement dans tous mes projets professionnels ou personnels. Je remercie aussi ma femme qui est venue en France pour m'accompagner pendant ma thèse et qui m'a aussi donné beaucoup de supports dans la vie quotidienne. Sans eux, je n'en serais pas là aujourd'hui.

Merci beaucoup !

Contents

List of Figures

[63] Steven Van Sciver. *International Cryogenics Monograph Series*. 2012.

List of Tables

General introduction

Inspired by the Sun's natural fusion process, a considerable work has been contributed to attempt to use controlled fusion energy to produce the electricity on Earth. The principal advantages[1] of fusion power have been identified to be safe (non-radioactive fusion fuels), environmentally friendly (inert substance helium as fusion product) and to some extent, provide limitless source of energy (fuel production based on lithium and water). Since the mid of the last century, several approaches of man-made fusion have been attempted, including the muonic fusion[2], the inertial-confinement fusion[3] and the magnetic confinement fusion[1]. Among them, the magnetic confinement fusion has been demonstrated to be the most feasible way of realizing a power plant, leading to two alternative toroidal confinements, the Stellarator machine invented by Lyman Spitzer at Princeton in the early 1950s[3] and the Tokamak machine firstly realized in Russia in the early 1970s[4]. The idea is to apply the strong magnetic fields on the hot charged plasma particles (of around 1.5×10^8 °C) to keep them sufficiently away from the container wall so that the surface of the wall will not melt or evaporate to cool down the fusion material. The Tokamak configuration is typically selected as the essential process of realizing fusion power plant thanks to its optimized stability of the hot plasma confinement and also due to the construction complexity in the early Stellarator realizations[1].

In order to check the scientific feasibility in a Tokamak and to address the potential issues related to the manufacturing techniques, several Tokamak machines have been constructed during the last decades. From the first small size machine T-3[4] to the large Tokamaks, Joint European Torus (JET)[5] in Culham (UK), Tokamak Fusion Test Reactor (TFTR)[6] in Princeton (US) and JT-60U Tokamak[7] in Naka (Japan), the fusion scientists have succeeded to achieve the large-scale fusion power from 2 MW to 16 MW, with the highest power amplification up to $Q = 0.65$ (=produced fusion power/total input heating power) in JET[8]. All these Tokamak experiments are together demonstrating the scientific feasibility for magnetic confinement fusion. Nevertheless, these Tokamaks are all manufactured with normal resistive copper magnets cooled by water. The large amounts of electrical energy consumed by these copper magnets are actually the biggest limits (as well as some other limits, e.g. the capability of the machine to withstand large fluencies of 14 MeV neutrons without failure, etc) of achieving a net output power from the Tokamak ($Q > 1$). So that, the best solution is to use superconducting magnets. They are manufactured with superconducting materials that, when temperature decreases to a critical value (T_c), will have no resistance against an electrical current, such as NbTi and Nb_3Sn. In addition, these superconducting magnets are based on a very robust (mechanical and electrical) conductor configuration with high and controlled heat transfer, called the Cable-In-Conduit Conductor (CICC)[9], in which the supercritical helium circulates by forced flow (except for the case of superfluid helium bath, such as the Tore Supra[10]).

[1] J. Ongena et al. *Nature Physics* **12**. 398–410. 2016.
[2] L. W. Alvarez et al. *Physical Review* **105**. 1127–1128. 1957.
[3] G. McCracken and P. Stott. *Academic Press*. 2012.
[4] L. A. Artsimovich. *Nuclear Fusion* **12**. 215–252. 1972.
[5] P. H. Rebut. *Plasma Physics and Controlled Fusion* **34**. 1749–1758. 1992.
[6] K. M. McGuire et al. *Physics of Plasmas* **2**. 2176–2188. 1995.
[7] T. Fujita et al. *Nuclear Fusion* **39**. 1627–1636. 1999.
[8] M. Keilhacker et al. *Nuclear Fusion* **39**. 209–234. 1999.
[9] M. O. Hoenig and D. B. Montgomery. *IEEE Transactions on Magnetics* **11**. 569–572. 1975.
[10] D. Ciazynski et al. *IEEE Transactions on Magnetics* **24**. 1567–1570. 1988.

Both the superconducting property and the CICC configuration have led the fusion magnets more powerful in the magnetic energy and also more stable at cryogenic conditions.

However, the complexity of such superconducting magnet also brings a multitude of design issues that need to be addressed during the whole R&D program. One of these issues is called ***quench***. Indeed, the word "quench" is for describing a fast transition from the conductors superconducting state to its normal resistive state. When it happens in a superconducting magnet, large amounts of heating energy will be produced due to Joule effect in the conductors *normal zone* and will rapidly increase the conductors temperature. If this temperature reaches a sufficiently high value, an irreversible damage will then be brought to the superconducting magnet due to the over thermal dilation in the materials. In addition, the large Joule heat will also be transferred by forced convection to the supercritical helium coolant. The helium is then rapidly heated and pressurized until reaching a threshold value that could probably provoke a deterioration of the entire cryogenic system. From the point of view of magnet security, such transient thermohydraulic phenomena taking place during a quench have thus attracted a lot of attention in the Tokamak research domain during the last decades.

In order to address the above physics issues and the potential technical features needed for a superconducting fusion power plant, the worldwide biggest fusion project, International Thermonuclear Experimental Reactor (ITER), has thus been launched in 2006 next to CEA Cadarache in France. The main objective of ITER is to achieve a fusion power output of 500 MW corresponding to a power amplification of $Q = 10$[11]. In parallel, some smaller sized superconducting Tokamaks have also been constructed and operated to provide direct experiences for ITER, such as the EAST in China[12], the KSTAR in Korea[13], the SST-1 in India[14], the WEST (upgraded from Tore Supra) in France[15,16] and the JT-60SA (upgraded from JT-60U) in Japan[17]. These superconducting Tokamaks are recent equipments and are always very difficult to be manufactured from the economic and technical points of view, thus rare to be found in the world. In particular, the JT-60SA, as the largest superconducting Tokamak to be built before ITER, is fully constructed with superconducting magnets, with the 18 Toroidal Field (TF) coils allowing to provide a strong toroidal field to stabilize the plasma. Therefore, this Tokamak will have the highest plasma energy (plasma current around 5.5 MA) and the highest magnetic stored energy (peak field in the TF system around 5.65 T) ever before. A multitude of novelties concerning both scientific research and technical features will definitely be provided by this project to the international fusion community.

The quench phenomenon in a CICC has been extensively studied with the realization of classical quench experiments in a small size CICC[18–20] and in a magnet-grade CICC[21] by imposing a local heating power or a critical current to quench the superconductors. Several analytical models[22–24] have been precisely proposed to analyze the thermohydraulic phenomena taking place during a quench of the CICC, combining quench propagation, helium pressure rise and helium flow expulsion. Nevertheless, very few studies have been precisely carried out to analyze the quench experiments of a real Tokamak magnet. The Tore Supra, with the similar configuration to JT-60SA, has actually

[11] IAEA Vienna. *ITER Engineering Design Activities Documentation.* 2001.
[12] B. Wan. *Nuclear Fusion* **49**. 2009.
[13] G. S. Lee et al. *Nuclear Fusion* **40**. 575–582. 2000.
[14] S. Pradhan et al. *Nuclear Fusion* **55**. 2015.
[15] C. Bourdelle et al. *Nuclear Fusion* **55**. 2015.
[16] Editor. *World nuclear news.* 2016.
[17] K. Yoshida et al. *The Journal of Japan Society of Plasma Science and Nuclear Fusion Research* **9**. 214–219. 2010.
[18] C. A. Luongo et al. *Cryogenics* **34**. 611 –614. 1994.
[19] A. Martinez et al. *Cryogenics* **34**. 591 –594. 1994.
[20] P. Bruzzone et al. *IEEE Transactions on Applied Superconductivity* **12**. 516–519. 2002.
[21] A. Anghel. *Cryogenics* **38**. 459–466. 1998.
[22] L. Dresner. *IEEE Transactions on Magnetics* **25**. 1710–1712. 1989.
[23] L. Bottura and O. C. Zienkiewicz. *Cryogenics* **32**. 659–667. 1992.
[24] A. Shajii and J. P. Freidberg. *Journal of Applied Physics* **76**. 3149–3158. 1994.

undergone several quench experiments and analyses on two of the 18 superconducting TF coils[10]. However, the Tore Supra TF coils are cooled with superfluid helium bath at 1.8 K, which is different from the JT-60SA TF coils cooled with forced flow of supercritical helium in a CICC. In addition, the ITER Toiroidal Field Model Coil (TFMC)[25] as well as the Central Solenoid Model Coil (CSMC)[26] have been tested by increasing the inlet helium temperature up to quench without bringing any layout modifications inside the coil, as the experimental protocol for the quench test of JT-60SA TF coils. However, they are manufactured with Nb_3Sn, which is different from the material used in the JT-60SA, the NbTi. As a result, it will be very interesting to carry out such a precise study of the quench experiments realized on the entire 18 NbTi TF coils in the JT-60SA.

In order to obtain a better understanding on the transient thermohydraulic phenomena taking place during a quench of the CICC-based superconducting magnet, several numerical codes have also been developed during the last decades, from the conductor-level code, Gandalf[27], Mithrandir[28] or THEA[29], to the magnet-grade code, Vincenta[30] or 4C[31]. They are based on similar analytical features and have been extensively validated with quench experiments performed on CICC cables[32–35] or on one layer inserts[36,37]. Nevertheless, it is very rare to find numerical study of the quench experiments realized on a real Tokamak magnet which is much more complex to model. Thereby, this PhD report will apply the approach of modelling and identifying one single phenomenon at a time during the numerical analysis of the JT-60SA TF coils quench tests without building a complete magnet predictive model. In order to achieve this goal, the state-of-the-art 1D code THEA will be chosen thanks to its capability of modelling the quench state in a fully transient way and to its possibility of being easily modified in the open source files for physical studies.

The three above statements together justify the great interest of studying and modelling the thermohydraulic phenomena taking place during the quench of a superconducting magnet cooled with supercritical helium.

For carrying out this study, in Chapter 1 we firstly present the notions and parameters that are related to the quench problem in a CICC-based superconducting magnet cooled with supercritical helium. Basically, the longitudinal quench propagation along the conductor or the transversal heat transfer between the conductors have been addressed as well as some key parameters, such as the superconducting properties of the NbTi, the electrical resistivity of Cu, and the thermal conductivity or the specific heat of the materials, etc. The forced flow of supercritical helium in the CICC have also be precisely studied, including the pressure drop issue due to friction factor, and the CICC cooling efficiency by forced convection.

In order to check the magnets performance and hence mitigate their fabrication risks, the 18 superconducting TF coils have all been tested at their nominal operating conditions of current and temperature (25.7 kA and 5 K). A progressive temperature increase has been applied to the helium inlet up to the quench temperature, followed by a current fast discharge as soon as the quench is detected to protect the magnet. Chapter 2 presents in details the configuration of the CICC-based

[10] D. Ciazynski et al. *IEEE Transactions on Magnetics* **24**. 1567–1570. 1988.
[25] A. Ulbricht et al. *Fusion Engineering and Design* **73**. 189–327. 2005.
[26] T. Kato et al. *Fusion Engineering and Design* **56-57**. 59 –70. 2001.
[27] L. Bottura. *Journal of Computational Physics* **125**. 26–41. 1996.
[28] R. Zanino, S. DePalo, and L. Bottura. *Journal of Fusion Energy* **14**. 25–40. 1995.
[29] L. Bottura, C. Rosso, and M. Breschi. *Cyogenics* **40**. 617–626. 2000.
[30] V. Amoskov et al. *Plasma Devices and Operations* **14**. 47–59. 2006.
[31] R. Zanino et al. *Fusion Engineering and Design* **85**. 752–760. 2010.
[32] S. DePalo, L. Bottura, and R. Zanino. *Journal of Fusion Energy* **14**. 49–58. 1995.
[33] R. Zanino, L. Bottura, and C. Marinucci. *Advances in Cyogenics Engineering* **43**. 181–188. 1998.
[34] L. Bottura, C. Marinucci, and P. Bruzzone. *IEEE Transactions on Applied Superconductivity* **12**. 1528–1532. 2002.
[35] K. Sedlak and P. Bruzzone. *Cryogenics* **72**. 9 –13. 2015.
[36] R. Zanino, R. Bonifetto, and L. S. Richard. *IEEE Transactions on Applied Superconductivity* **20**. 491–494. 2010.
[37] R. Bonifetto et al. *IEEE Transactions on Applied Superconductivity* **27**. 1–8. 2017.

JT-60SA TF coils as well as the entire electric and cryogenic systems installed in the Cold Test Facility (CTF) at CEA Saclay allowing to protect the magnet in case of quench and to achieve the necessary quench experimental data for further analyses. In particular, the experimental protocol of setting up the whole quench test has been explained in this chapter for preparing the following studies.

With the purpose of verifying the whole instrumentation system in the CTF, two quench experiments have been carried out on the first tested TF coil. In total, 19 quench tests were finally accomplished on the 18 superconducting TF coils. Relying on these achieved experimental measurements, the first study has been contributed to find the most appropriate data processing method allowing to deduce the quench resistance evolutions for the further studies. Different quench dynamic phases can then be identified during the entire quench propagation phenomenon in the superconducting TF coil. Then, the physical phenomena driving each one of these phases have been precisely studied with the experimental approaches[38]. For instance, a simplified physical model has been built to analyze the normal zone length evolution. Finally, a categorisation of all kinds of quench dynamics has been attempted for the 19 quench tests relying on all the previous experimental analyses. This part of study will be presented in Chapter 3.

Nevertheless, there are always some driving physical phenomena as well as some hypotheses that could not be verified or studied in the experimental analysis. A single pancake numerical model[39] taking into account the longitudinal and transversal heat transfers in the pancake has been developed in the THEA code in order to analyze one physical phenomenon at a time without building a too complex global predictive model of the entire magnet. This single pancake model has been validated on the quench experiments data and has been successfully applied to make further more detailed analyses of the transient thermohydraulic phenomena identified during the different quench dynamic phases. All the work related to the numerical study constitutes Chapter 4.

[38] Y. Huang et al. *Fusion Engineering and Design* **124**. 147 –152. 2017.
[39] Y. Huang et al. *IEEE Transactions on Applied Superconductivity* **28**. 1–5. 2018.

CHAPTER 1

Quench in a superconducting magnet cooled with supercritical helium

Objectives

- **To provide the context and the problem of this study**
- **To give a detailed description about the thermal and electric properties of a superconducting Cable-In-Conduit Conductor that will be applied to study the thermohydraulic phenomena during a quench**
- **To introduce the main issues related to the quench propagation in a superconducting magnet in order to carry out a detailed study of the quench tests of JT-60SA TF coils**

1.1 Context and Problem

1.1.1 Project of superconducting Tokamak JT-60SA

JT-60SA is an advanced superconducting Tokamak upgraded from the original JT-60U which is made up of resistive copper coils. As the largest superconducting Tokamak to be built before ITER, JT-60SA takes the main mission of developing the steady-state operating scenarios and addresses key physics issues for an efficient start up of ITER experimentation and for the preliminary research towards the DEMO reactor. Within the Broader Approach agreement, JT-60SA is jointly constructed by Japan and Europe. In particular, the 18 superconducting Toroidal Field (TF) coils are provided half by General Electric (GE) in France[40,41] and half by ASG in Italy[42]. Fig. 1.1 shows the D-shaped TF coils (encircled in red) which are vertically installed in the 15.5 m high Tokamak machine. The 18 superconducting TF coils are cooled with supercritical helium at nominal temperature of around 5 K and carry an operating current of 25.7 kA. The whole TF system in Tokamak can produce a nominal peak field of 5.65 T which leads to an electromagnetic stored energy of about 1.06 GJ.

In order to check the coils performance and hence mitigate their fabrication risks, all the 18 superconducting TF coils, before shipping to QST in Japan, are tested in a single coil configuration

[40] P. Decool et al. *Fusion Engineering and Design* **124**. 24 –28. 2017.
[41] P. Decool et al. *IEEE Transactions on Applied Superconductivity* **28**. 4200604. 2018.
[42] Gian Mario Polli et al. *Fusion Engineering and Design* **124**. 123 –126. 2017.

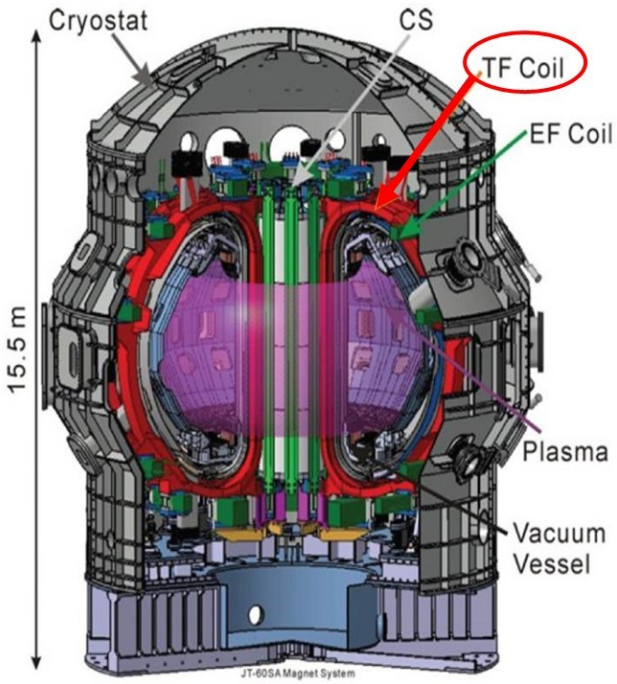

Figure 1.1 – Cut view of the JT-60SA basic device with TF coils encircled in red from K. Yoshida et al.

in the Cold Test Facility (CTF) at CEA Saclay[43,44]. Thereby, this PhD study of the thermohydraulic phenomena taking place of the quench in a superconducting magnet cooled with supercritical helium has been launched and carried out in the Division of Accelerators, Cryogenics and Magnetism (DACM) at CEA Saclay.

1.1.2 Technological characteristics of JT-60SA TF coils

a) Toroidal Field coil

Each D-shaped TF coil is 7.5 m long and 4.5 m wide with a mass around 16.5 t. It is wound with Cable-In-Conduit Conductors (CICCs) in two directions, clockwise (CK) or anticlockwise (ACK), as presented in Fig. 1.2a. When taking a look at the cross-section of the TF coil, as presented in Fig. 1.2b, we can see that each TF coil contains a stainless steel casing and a 6-Double-Pancake (DP) winding pack, separated by an 9 mm thick G10 epoxy fibreglass insulation. Each DP consists of two adjacent pancakes that are wound with the same CICC but in two opposite directions (as mentioned above, CK and ACK). Thereby, 12 pancakes stacked from the bottom to the top can be recognized in the winding pack cross-section. Fig. 1.2b also shows that each pancake is wound around the D-shape in 6 turns (represented by the 6 rectangles in a row) making a total length of 113.277 m. Each rectangle thus represents the cross-section of one CICC which can carry the 25.7 kA nominal current for the coil. The peak field in the single coil configuration when tested in the CTF cryostat can reach 3.04 T. This is an equivalent uniform value estimated on the entire cable cross-section by giving the same electric field of 10 mV/m[45]. Concerning the superconducting CICC applied in the JT-60SA TF coils, more details will be presented below.

[43] W. Abdel Maksoud et al. *Fusion Engineering and Design* **124**. 14–17. 2017.
[44] W. Abdel Maksoud et al. *IEEE Transactions on Applied Superconductivity* **28**. 1–4. 2018.
[45] A. Torre. *Internal report*. 2015.

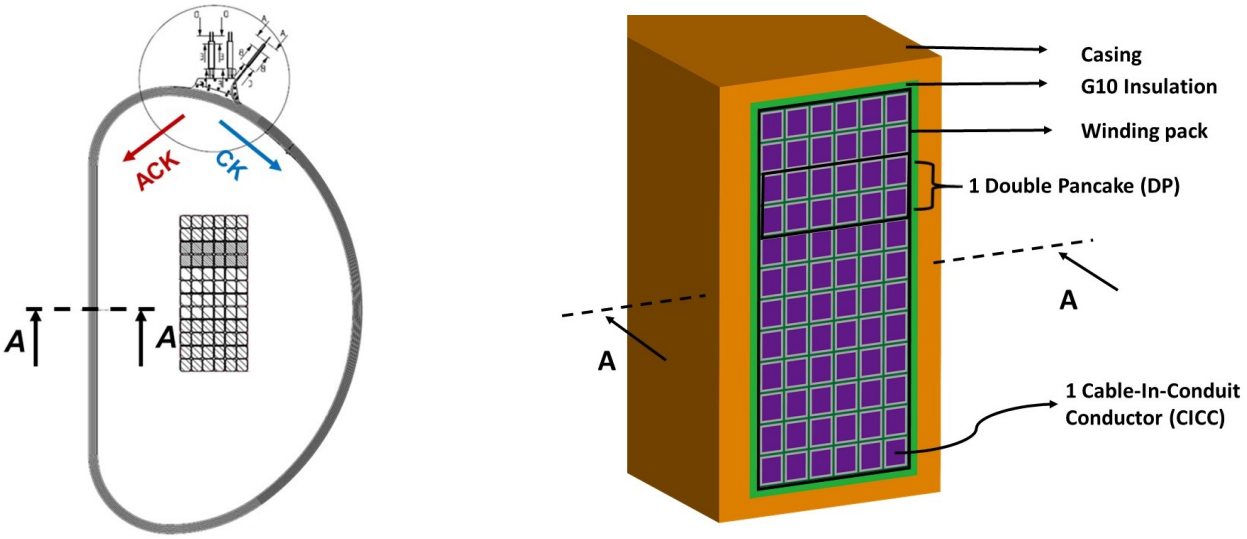

(a) Top view of D-shaped TF coil

(b) Cross-section of the TF coil

Figure 1.2 – Detailed views of the TF coil

b) Properties of CICC

The concept of the Cable-In-Conduit Conductor (CICC) has been proposed for the demand of large high field ($5 \backsim 9\,\mathrm{T}$ range) stabilized magnets applied in a fusion Tokamak. The idea is to have superconducting and copper wires cabled together and inserted inside a structurally strong material that form a void fraction for the forced circulation of the supercritical helium coolant. The CICC configuration has been demonstrated to obtain a higher cooling efficiency with a helium flow than that in a conventional hollow conductor because of a larger contact surface between the superconducting wires and the helium flow[9]. During the last decades, different CICC layouts have been designed to build high field large-size superconducting magnets, such as the first large realization with Nb_3Sn CICC in Westinghouse-Large Coil Task (LCT)[46] and the large NbTi CICC firstly used in the poloidal coils of Large Helical Device (LHD)[47]. Nowadays, as the actual CICC configurations are able to achieve the performance demand of realizing high field large-size superconducting magnets, very limited layout variations remain to be considered for a CICC, e.g. twist pattern, void fraction and jacket alloy[48]. In addition, both NbTi and Nb_3Sn CICC generally became the unquestioned choice for the superconducting fusion conductors, especially for the ITER conductor design[11]. Indeed, the ability of scaling over a broad range of physical size thanks to its mechanically robust structure, the ability of undergoing strong current (10-100 kA) thus high magnetic stored energy for the fusion conductors as well as the low heating effect under varied field and the good heat transfer thanks to its strands subdivision are together bringing a popularity to the CICC.

Concerning the present update project of JT-60SA, the TF coils are also manufactured with the NbTi CICC, as presented in Fig. 1.3. This CICC is multi-twisted cable composed of NbTi and Cu strands embedded in a 2 mm thick rectangular Stainless Steel (SS) jacket. This forms a cross-section of $22\,\mathrm{mm} \times 26\,\mathrm{mm}$ with a 32 % of void fraction[49] (see the left diagram of Fig. 1.3). Each CICC will then be wrapped by a 1 mm thick G10 insulation against the electrical short circuit between the conductors. The pressurized helium will be circulated in the CICC and cool the conductor

[9] M. O. Hoenig and D. B. Montgomery. *IEEE Transactions on Magnetics* **11**. 569–572. 1975.
[46] L. Dresner et al. *Cryogenics* **29**. 875–882. 1989.
[47] K. Takahata et al. *Fusion Engineering and Design* **20**. 161–166. 1993.
[48] P. Bruzzone. *Physica C - Superconductivity and Its Applications* **470**. 1734–1739. 2010.
[11] IAEA Vienna. *ITER Engineering Design Activities Documentation*. 2001.
[49] P. Decool et al. *IEEE Transactions on Applied Superconductivity* **26**. 2016.

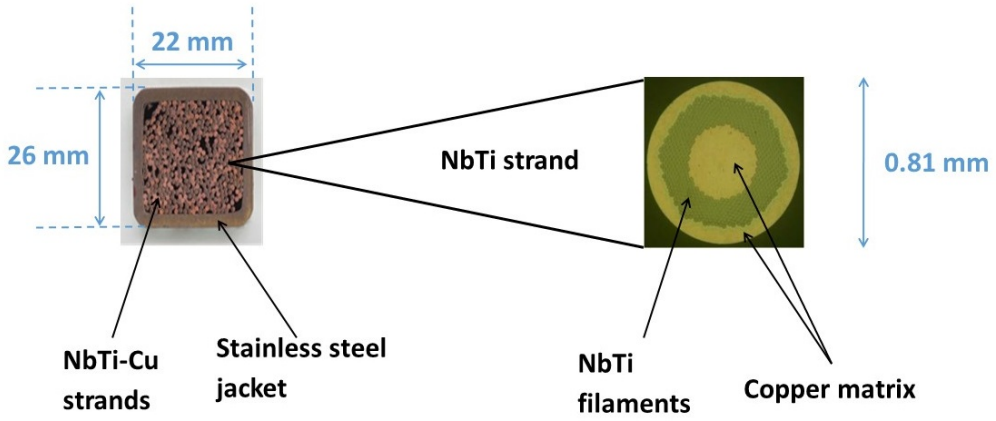

Figure 1.3 – Cross-section of the CICC for JT-60SA TF Coils

by forced flow convection. This CICC contains 324 NbTi strands and 162 copper strands, with a nonSC:SC ratio of 1.66 in the NbTi strands allowing to satisfy the design criterion of the strands critical performances[50] (see the right diagram of Fig. 1.3). One can refer to Table 1.1 for more information about the cross-sectional area of the major materials in the CICC. These parameters will also be applied in the following computations in Section 1.4.

Table 1.1 – Cross-sectional area of the different materials in the CICC

Material	**Symbol**	**Cross-sectional area (mm^2)**
NbTi section	S_{NbTi}	**56.8**
Cu section	S_{Cu}	**180**
He section	S_{He}	**123**
SS Jacket section	S_{Jacket}	**176**
G10 insulator section	S_{Ins}	**100**

1.1.3 Quench in a CICC-based superconducting magnet

The initiation of a quench depends directly on the critical current of the superconducting strands. A high performance superconducting strand can support a higher critical current which then makes the quench more difficult to be initiated, thus can keep the superconducting magnet thermally more stable and technically more secure. Thereby, the first property to be presented is the critical surface of the superconducting material NbTi, which is the one applied in the JT-60SA TF coils manufacture.

As already explained in the general introduction, when a quench is triggered in the CICC, large amounts of Joule effect energy will be produced and will provoke a rapid temperature increase as well as a quench propagation in the conductor. Meanwhile, the helium flow will also be heated and pressurized which can lead to a helium expulsion towards the outside conductor. Such multiphysical phenomenon during a quench has been previsouly studied by developping both analytical model[22,23,51] and numerical model[24,27–30]. These studies mainly rely on a heat equation

[50] L. Zani, P. Barabaschi, and E. Di Pietro. *Fusion Engineering and Design* **88**. 555–558. 2013.
[22] L. Dresner. *IEEE Transactions on Magnetics* **25**. 1710–1712. 1989.
[23] L. Bottura and O. C. Zienkiewicz. *Cryogenics* **32**. 659–667. 1992.
[51] A. Shajii and J. P. Freidberg. *Journal of Applied Physics* **76**. 3159–3171. 1994.
[24] A. Shajii and J. P. Freidberg. *Journal of Applied Physics* **76**. 3149–3158. 1994.
[27] L. Bottura. *Journal of Computational Physics* **125**. 26–41. 1996.
[28] R. Zanino, S. DePalo, and L. Bottura. *Journal of Fusion Energy* **14**. 25–40. 1995.
[29] L. Bottura, C. Rosso, and M. Breschi. *Cyogenics* **40**. 617–626. 2000.
[30] V. Amoskov et al. *Plasma Devices and Operations* **14**. 47–59. 2006.

applied in the CICC, including the heat enthalpy terms, the heat flux terms such as thermal conduction or heat exchange between conductor and helium, and the Joule heat produced in the copper. Thereby, the electric and thermal properties of the CICC materials and the helium coolant will need to be precisely described below.

One has to note that one of the biggest challenges to study the quench in a CICC is actually based on the CICC configuration itself. Indeed, the mutual thermal coupling can be identified among all the three components of a CICC, which means the thermal couplings between conduit (SS jacket) and strands (NbTi + Cu), between conduit and helium as well as between strands and helium. Nevertheless, the thermal resistance between conduit and strands is not a parameter that can be explicitly determined, which strongly depends on their thermal contact area when manufacturing the CICC. One of the following studies in this chapter will then focus on the thermohydraulic coupling between the forced helium flow and the conductor (conduit + strands), with a high heat transfer thanks to the good ratio between cross-secion and wet perimeter of the thin strand (diameter $<$ 1 mm). In addition, another characteristic also need to be addressed in a CICC, the high pressure drop issue[52]. Since the mass flow rate affected by the pressure drop will in turn have an effect on the cooling efficiency in the CICC. So that these two characteristics will be discussed in more details when addressing the thermohydraulic coupling between helium and conductor.

Finally, the quench propagation problem in a superconducting magnet will be addressed with some simplified analytical models and based on the above described parameters. Different aspects will be taken into account: hot spot temperature that can be reached during the quench of a CICC, longitudinal quench propagation along the conductor as well as the transversal quench propagation due to the thermal conduction in the inter-conductor insulation.

1.2 Properties of materials and coolant in the CICC

1.2.1 Performance of superconductor

a) Superconductivity

When the temperature of a superconducting materials is cooled below a so-called "critical" temperature (usually designated as T_c), the electrical resistance for the passage of a direct current becomes completely zero ($\rho_e = 0\,\Omega \cdot \mathrm{m}$). This phenomenon is called *Superconductivity*. It was firstly discovered by Heike Kamerlingh Onnes when studying the resistance of solid mercury at cryogenic temperature around 4.2 K[53]. Later then, W. Meissner and R. Ochsenfeld discovered another important property of the superconductor: when ahcieving the superconducting state ($T < T_c$), the internal magnetic field will be ejected from the superconducting bulk ($B = 0\,\mathrm{T}$)[54]. This is then known as the most fundamental property of a superconductor, called the Meissner effect (or Meissner–Ochsenfeld effect).

Nevertheless, the Meissner effect does not cause a complete expulsion of the magnetic field but instead creates a surface current. A superconductor with little or no magnetic field within it is said to be in the Meissner state. When the applied magnetic field is too large, the Meissner state breaks down so that the superconductivity is destroyed. Superconductors can then be divided into two classes according to how this breakdown occurs. In Type I superconductors, Meissner state is present up to the bulk critical magnetic field (B_c), above which the magnetic field is completely expelled from the superconductor, as presented in the left diagram of Fig. 1.4[55]. Whereas in Type

[52] L. Muzzi et al. *Superconductor Science and Technology* **28**. 1–2. 2015.
[53] H. Kamerlingh Onnes. *Proceedings of Huygens Institute* **14 I**. 113–115. 1911.
[54] W. Meissner and R. Ochsenfeld. *Naturwissenschaften* **21**. 787–788. 1933.
[55] N. Haleeda, M. Awang Kechik, and R. Abd-Shukor. *Pertanika Journal of Science and Technology* **2**. 2016.

II superconductors, the Meissner state is only present up to a lower critical value (B_{c1}), above which the magnetic flux penetrates into the superconducting bulk through some isolated points (or vortices) leading to a mixed state called the vortex state[56] (see the right diagram of Fig. 1.4). When increasing to the second critical field (B_{c2}), the magnetic field penetration is complete leading to a fully normal state in the superconductor, as presented in the right diagram of Fig. 1.4.

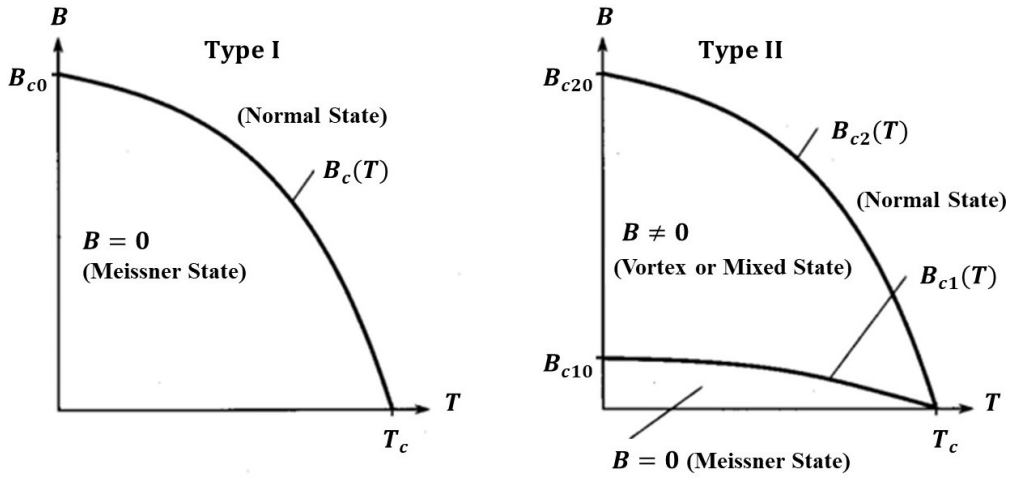

Figure 1.4 – Comparison between superconductors type I and type II

In addition to mercury in which the first superconductivity was discovered, the Type I superconductivity is generally exhibited by pure metals, e.g. aluminium, lead and indium. Nevertheless, these materials are unsuitable as superconducting magnet materials due to their low B_c values around 0.1 T[57]. Whereas the Type II superconductors have a much broader application in the magnet-grade domain thanks to the capability of retaining the superconductivity under a higher critical field value. For instance, the alloy superconductor NbTi that will be discussed below has a high value of $B_{c2}(\text{NbTi}) = 10.5\,\text{T}$ measured at 4.2 K[57]. This becomes one of the most basic reasons for which the JT-60SA TF coils are manufactured with the NbTi superconductor.

b) Critical surface of NbTi

In addition to the critical temperature (T_c), the critical magnetic field (B_c or B_{c2} for Type II superconductor) and the critical current density (j_c) also allow to define a superconducting state, as presented in Fig. 1.5. For any given superconducting materials, the operating domain of superconductors should always comply with the intertwined relations among the three parameters, limited with the so-called *critical surface*. T_c and B_c are thermodynamic properties that for a given superconducting material are invariant to metallurgical processing. Whereas j_c is still possible to be enhanced dramatically by means of metallurgy alone[57]. The manufacturing impact on the strands performance in j_c will be studied in Chapter 3. The critical surface separates two principal states, the non-dissipative superconducting state below the surface and the dissipative normal state above the surface. Indeed, the superconducting state will be changed into the normal state if any of the three parameters reach their critical value. A large amount of Joule heat will then be produced in the normal state and will provoke a further transition propagating from near to far in the conductor. This phenomenon is called *quench*. The quench dynamics in the superconducting magnet will be the key issue to be addressed in this PhD report. One should also note that other factors, e.g. mechanical stress or strain level, that may have an influence on the critical surface (T_c; B_c; j_c) will not be studied in this document.

[56] A. Abrikosov. *Reviews of Modern Physics* **76**. 975 –979. 2004.
[57] Y. Iwasa. *Springer*. 2009.

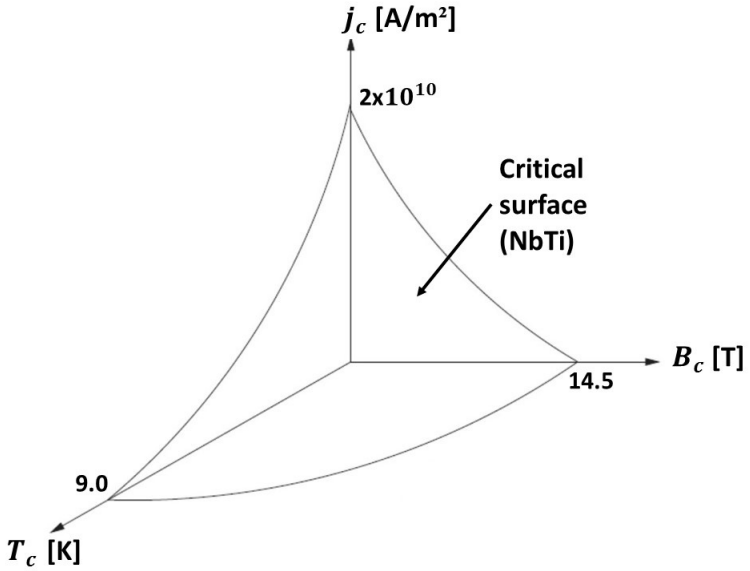

Figure 1.5 – Schematic critical surface of a typical Type II superconductor (with properties of NbTi)

As the manufacturing material used in the JT-60SA TF coils, the critical surface properties has also been presented for the alloy NbTi in Fig. 1.5. We can know that T_c is around 9 K at zero field and B_c (or B_{c2} for NbTi) is around 14.5 T when approaching the absolute zero ($\backsim$ 0 K). The critical current density can theorectically reach $2 \times 10^{10}\,\mathrm{A/m^2}$ at $T_c = 0\,\mathrm{K}$ and $B_c = 0\,\mathrm{T}$. These values are determined with the average performance strands that are used in the JT-60SA TF coils[58].

In 1983, M. Lubell has given a suitable fit for the NbTi upper critical field B_{c2} as a function of temperature[59] relying on a pinning force model[60,61], as presented in Eq. (1.1):

$$B_{c2} = B_{c20}\,[1 - (\frac{T}{T_{c0}})^n] \tag{1.1}$$

where the parameters can be found in Table 1.2.

Table 1.2 – Critical parameters of the NbTi CICC in JT-60SA TF coils

Parameter	**Value**[1]	**Unit**	**Comment**
$\mathbf{j_c(B,T)}$		[A/m^2]	Critical current density
$\mathbf{j_{op}(B,T)}$	$\mathbf{4.525 \times 10^8}$	[A/m^2]	Operating current density
$\mathbf{T_c(B)}$		[K]	Critical temperature
$\mathbf{B_{c2}(T)}$		[T]	Upper critical field
$\mathbf{T_{c0}}$	**8.9913**	[K]	Maximum critical temperature ($B = 0\,\mathrm{T}$)
$\mathbf{B_{c20}}$	**14.4559**	[T]	Maximum upper critical field ($T = 0\,\mathrm{K}$)
$\mathbf{T_{cs}(B, j_{op})}$		[K]	Current sharing temperature
$\mathbf{j_{cref} * C_0(T)}$	$\mathbf{1.24 \times 10^{11}}$	[A · T/m^2]	Reference critical current density & Field coefficient
($\boldsymbol{\alpha}$, $\boldsymbol{\beta}$, $\boldsymbol{\gamma}$, **n**)	$\boldsymbol{\alpha = 0.8885}$, $\boldsymbol{\beta = 1.1947}$ $\boldsymbol{\gamma = 2}$, $\mathbf{n = 1.7}$	[–]	Parameters

[1] JT-60SA TF coils parameters determined with average performance strands[58]

[58] L. Zani, D. Ciazynski, and A. Torre. *Internal report.* 2016.
[59] M. S. Lubell. *IEEE Transactions on Magnetics* **19**. 754–757. 1983.
[60] Charles Bean. *Reviews of Modern Physics* **36**. 31 –39. 1964.
[61] D. G. Hawksworth and D. C. Larbalestier. *Proceedings of the 8th Symposium on Engineering Problems of Fusion Research* **1**. 249–254. 1979.

This fit determined for the first time an empirical exponent value of $n = 1.7$ for the commercial NbTi, which seems to be more satisfactory than using the original theoretical value of $n = 2$. Rearranging Eq. (1.1) to solve for temperature yields a useful formula for critical temperature as a function of field, as presented in Eq. (1.2):

$$T_c = T_{c0}\,(1 - \frac{B}{B_{c20}})^{1/n} \tag{1.2}$$

where the parameters can be found in Table 1.2.

Eq. (1.2) is an explicitly inverse relation between the critical temperature (T_c) and the magnetic field. This means that the higher the magnetic field, the lower the critical temperature, thus the easier a quench can be triggered. We recall that T_c has been firstly mentioned for describing the transition from a normal state to a superconducting state. Indeed, T_c is defined as the temperature at which the current passes entirely in the normal resistive part ($T \geqslant T_c$), e.g. in the copper strands of the JT-60SA CICC. Nevertheless, before the current entirely passes through the copper strands, an intermediate phase must exist: the current is shared between NbTi and Cu strands. We then define a so-called current sharing temperature, denoted as T_{cs}. When $T = T_{cs}$, the current starts to switch from the NbTi strands to the copper strands. Like T_c, such current sharing temperature also has a direct relation with the magnetic field and current density, as explained below.

For the pratical use in the real machine design, L. Bottura has proposed a fit of the NbTi critical surface where the critical current density is defined as a function of the temperature and magnetic field, as presented in Eq. (1.3)[62]:

$$j_c(T,B) = \frac{j_{cref} * C_0}{B}\,(\frac{B}{B_{c2}(T)})^{\alpha}\,(1 - \frac{B}{B_{c2}(T)})^{\beta}\,(1 - (\frac{T}{T_{c0}})^{1.7})^{\gamma} \tag{1.3}$$

with $B_{c2}(T)$ expressed in Eq. (1.1) and the parameters presented in Table 1.2.

This general fit for NbTi has been verified with published measurement data and has shown a typical overall accuracy of the order of 5 % covering a range of field from 0 T to 9 T and temperature from 1.9 K to 9 K. Indeed, the T_{cs} can be defined implicitly as the temperature at which the operating current density in the NbTi part (j_{op}) is equal to the critical current density, presented as $j_c(T_{cs}, B_{op}) = j_{op}$[62]. Thereby, the interest of introducing Eq. (1.3) results from the way of determining the current sharing temperature with an iterative computation converging j_c to j_{op}. The obtained temperature is then an adequate engineering value for characterizing the T_{cs} in a real machine design.

For instance, Table 1.2 gives $j_{op} = 4.525 \times 10^8\,\mathrm{A/m^2}$ of the JT-60SA TF coils as well as the other necessary values of the parameters applied in Eq. (1.3). These allow to determine the T_{cs} spacial profile along the CICC (of central pancake, see Fig. 2.6) based on its magnetic field map[58], as presented in Fig. 1.6.

Fig. 1.6 shows that a "V-shaped" magnetic field map (blue line) has been distributed along the entire 113.277 m long TF coils CICC. Here is the case of the central location pancake in the coil. A peak field value of 3.04 T can be observed near the inlet of the CICC at $x = 2.7$ m, as already mentioned before. In addition, such magnetic field map is also an equivalent average estimation over the entire CICC cross-section in order to cover the major performance of the coil (i.e. operating T_{cs}). The computation with Bottura's fit obtains the lowest T_{cs} of 7.42 K. When it is near the middle of the conductor at around $x = 60$ m, the highest T_{cs} has been reached at 8.42 K. Such 1 K difference of T_{cs} will then have some effects on the quench dynamics, for which more detailed studies will be carried out in Chapters 3 and 4.

[62] L. Bottura. *IEEE Transactions on Applied Superconductivity* **10**. 1054–1057. 2000.
[58] L. Zani, D. Ciazynski, and A. Torre. *Internal report.* 2016.

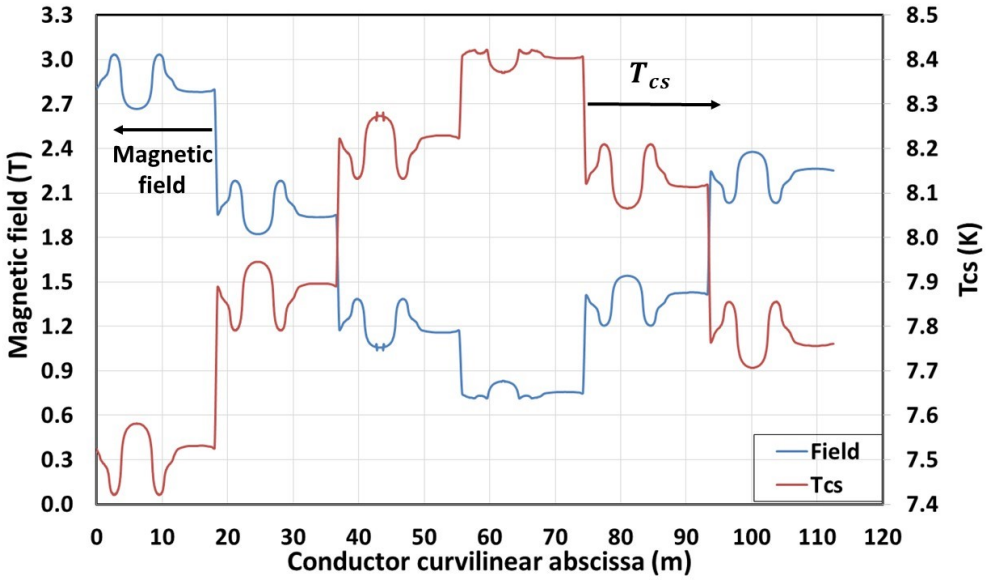

Figure 1.6 – Spacial profile of the current sharing temperature and the effective magnetic field in the JT-60SA TF coils CICC where the peak field region locates (central pancake)

1.2.2 Materials in the CICC

a) Electrical resistivity

When a quench is triggered at T_c, the copper part will undertake most of the currents since the NbTi electrical resistivity (ρ_{NbTi}), in case of quench, can rapidly increase to about 3 orders of magnitude more than the copper one (ρ_{Cu}). Nevertheless, the copper matrix can still produce a large amount of Joule heat under the strong operating current. In this section, we will give a bibliographical study of the correlations (or databases) applied for the copper electrical resistivity in order to prepare for our following studies.

First of all, we have to know that the most basic parameter to be considered for ρ_{Cu} is the residual resistivity ratio (RRR). This is a parameter that allows to characterize the impurity and the overall quality of the sample. Originally, it is defined as the ratio of the resistivity of a material at room temperature around 300 K and at 0 K, $RRR = \rho(300\,\mathrm{K})/\rho(0\,\mathrm{K})$. However, as the superconducting materials always have a resistivity close to zero below T_c, the RRR is then calculated in a different way in the case of superconducting cables, such as the NbTi CICC in JT-60SA TF coils. It will be using the residual resistivity just before the superconducting transition at around 9 K at zero field, as defined in Eq. (1.4):

$$RRR = \frac{\rho(290\,\mathrm{K})}{\rho(9\,\mathrm{K})} \tag{1.4}$$

with the room temperature during the coils test of around 290 K.

Thereby, a RRR value for the ρ_{Cu} has been experimentally estimated to be around 130. For the following analyses of the JT-60SA TF coils quench tests, the copper with $RRR = 130$ will be applied as the input material.

In addition, the copper electrical resistivity also depends on the temperature and the magnetic field. When the metal temperature decreases to a certain level, the resistivity tends to a constant value, referred to as the residual resistivity ρ_0. This residual resistivity is strongly dependent on the purity and on the amount and distribution of lattice imperfections in the metal[63]. The total resistivity

[63] Steven Van Sciver. *International Cryogenics Monograph Series*. 2012.

can thus be expressed in Eq. (1.5) according to the Matthiessen's rule[64]:

$$\rho = \rho_0 + \rho(T, B) \tag{1.5}$$

Fig. 1.7 shows ρ_{Cu} as a function of magnetic field computed at the nominal operating temperature of TF coils ($T = 5\,\mathrm{K}$). We can see that ρ_{Cu} is positively linked to the field variation. Moreover, different databases have also been applied and made into comparisons in the same figure. We can see that the four databases are having a common value of around $0.12\,\mathrm{n\Omega \cdot m}$ at zero field except the one with "LHC" database[65] (red solid line). Indeed, The ρ_{Cu} evolution with "LHC" database is almost parallel to the one with "ITER" database but with a nearly constant difference of about $0.01\,\mathrm{n\Omega \cdot m}$. This could be due to the correction factor applied for the different cases but based on the same database (remain to be verified). Whereas the ρ_{Cu} computed with "MetalPak"[66] and "CRYOCOMP"[67] databases has shown a nearly identical evolution between them. This could also be explained by the fact that an early collaboration between the "MetalPak" author, V. Arp and the "CRYOCOMP" author, P. Eckels, may have led the two program correlations to be based on a same database[67]. An average difference around 10 % between "MetalPak" (or "CRYOCOMP") and "ITER" (or "LHC") databases can be revealed within the 10 T field scope. Up to now, the "ITER" database has been proved to be coherent with both the "LHC" database (maybe the same) and the "MetalPak" database (about 10 % discrepancy). Moreover, the "ITER" database is also the one that has been largely used in the fusion magnets domain, as in our study case. Thereby, we will apply the "ITER" database to provide the ρ_{Cu} correlations for the following studies.

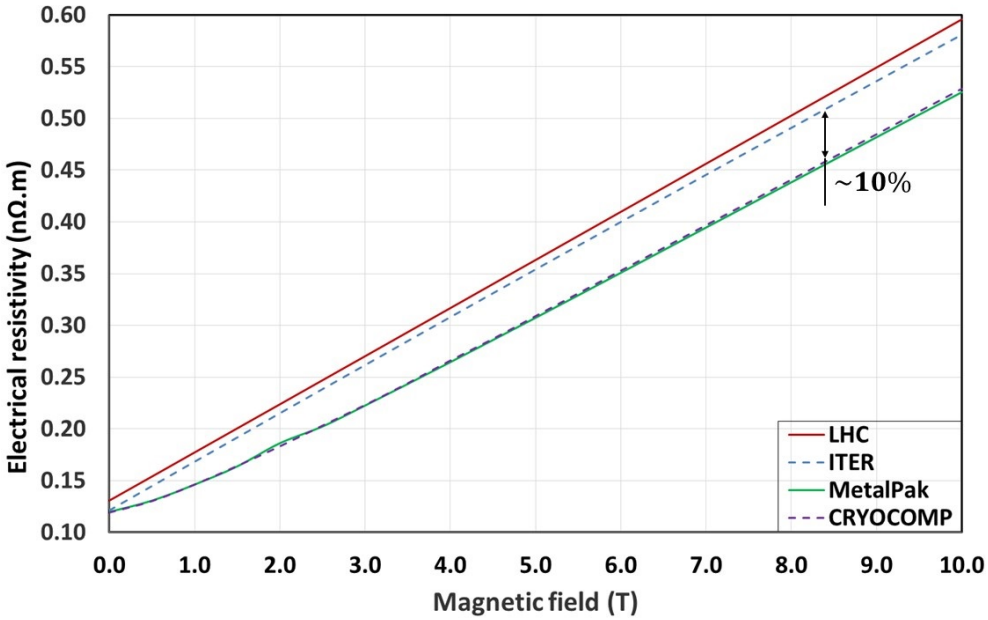

Figure 1.7 – Copper electrical resistivity as a function of magnetic field, with copper in $RRR = 130$ at $T = 5\,\mathrm{K}$

Relying on the "ITER" database, the copper electrical resistivity as a function of temperature has also been plotted at $B = 3\,\mathrm{T}$ (near the peak field) in Fig. 1.8. We can see that ρ_{Cu} is also in a positive relation with the temperature, as with the magnetic field. At cryogenic temperature range (from 5 K to 20 K), the constant resistivity residual in the case of JT-60SA TF coil is around $0.265\,\mathrm{n\Omega \cdot m}$. Whereas the linear variation phase between 60 K and 100 K corresponds to a slope of $0.066\,\mathrm{n\Omega \cdot m/K}$.

[64] F. C. Schwerer, J. W. Conroy, and Sigurds Arajs. *Journal of Physics and Chemistry of Solids* **30**. 1513 –1525. 1969.
[65] E. Floch. *Cern.* 2003.
[66] V. Arp. *Nist.* 2003.
[67] P. Eckels, R. Stewart, and V. Arp. *Eckels Engineering Inc.* 1993.

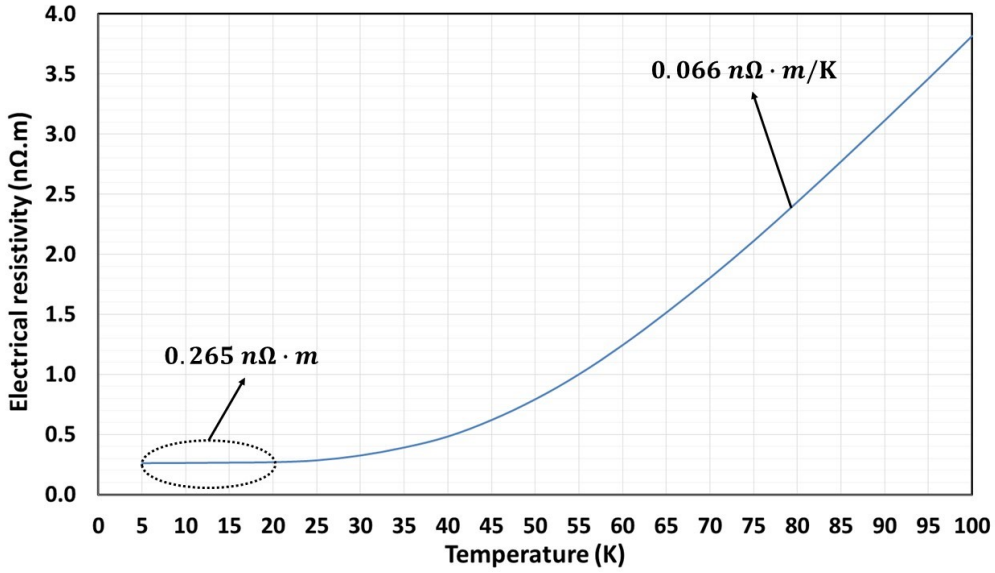

Figure 1.8 – Copper electrical resistivity as a function of temperature, with copper in $RRR = 130$ at $B = 3\,\mathrm{T}$

According to the above study of the copper electrical resistivity, a brief conclusion can be made that during the quench propagation in a CICC, two effects will need to be considered for the Joule heat production (by ρ_{Cu}): the thermo-resistivity due to temperature variation and the magneto-resistivity due to current discharge (for magnet protection). These properties of ρ_{Cu} will be applied for the quench behaviour study in Chapter 3.

b) Thermal conductivity

Regarding the thermal conductivity of the CICC components, normal materials like copper (Cu), Stainless Steel (SS) and G10 insulation will apply the correlations from "NIST" database[68], whereas the superconducting material NbTi will be based on the "CRYOCOMP" database[67] valid in a temperature range from 1 K to 300 K. Indeed, the superconducting material NbTi is not available in "NIST" database. In Fig. 1.9, we can see that at cryogenic temperatures, the copper thermal conductivity (blue dashed line) is $2 \backsim 3$ orders of magnitude higher than the other materials (NbTi, SS and G10). At about $T = 26\,\mathrm{K}$, λ_{Cu} increases to a maximal value of around $1500\,\mathrm{W/m \cdot K}$ and then decreases with the temperature. However, λ_{NbTi}, λ_{SS} and λ_{G10} are all having a monotone increase with the temperature. In particular, the insulator G10 has the worst thermal conductivity and almost stays at a constant low level of around $0.1\,\mathrm{W/m \cdot K}$. The NbTi and SS materials are almost having the same order of thermal conduction capability around several watts per meter kelvin. As a result, the high-thermal-conductivity copper matrix plays an important role in the thermal homogenisation in a CICC during the quench.

[68] R. Radebaugh et al. *Material Measurement Laboratory / Applied Chemicals and Materials Division.* 2018.

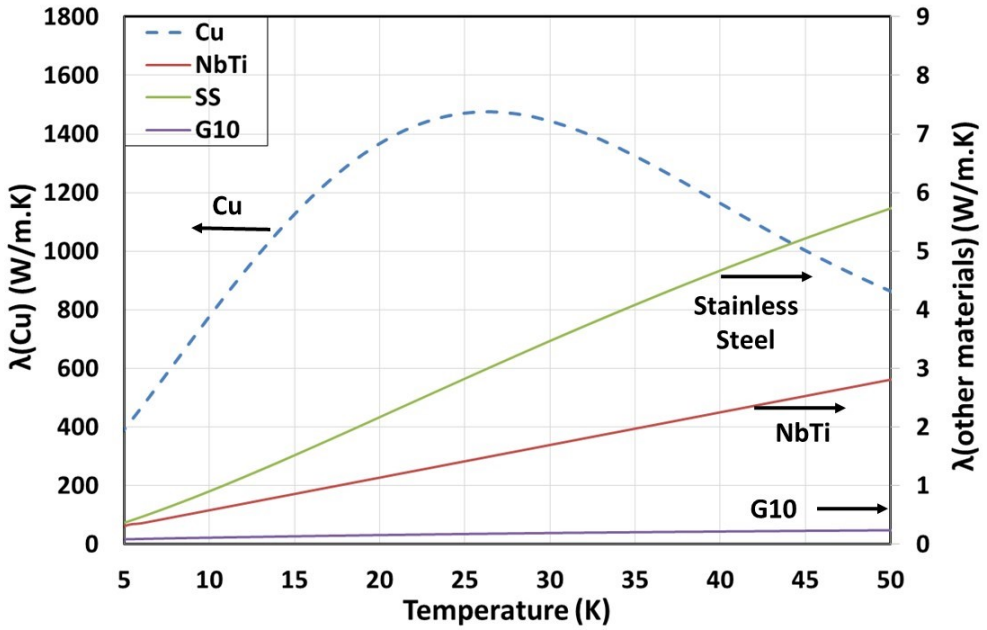

Figure 1.9 – Thermal conductivity of the different materials in the CICC as a function of the temperature, with copper in $RRR = 130$

c) Specific heat

Concerning the volumetric specific heat (Cp_v), it is an important parameter for computing the hot spot temperature in the CICC during a quench. The volumetric specific heat is obtained by the product of mass specific heat and mass density for each material. The information of the mass density can be found in Table 1.3. The normal materials (Cu, SS and G10) are always based on the "NIST" database with the correlations of mass specific heat, whereas the superconducting material NbTi will directly apply the volumetric specific heat correlations based on a bibliographical study of E. Floch[65]. A large range of temperature is valid with these correlations, from 1.8 K to 1000 K. Fig. 1.10 shows the volumetric specific heat as a function of the temperature under 0 T, with all the materials in a CICC. They all increase with the temperature. At the TF coils nominal temperature of $T = 5\,\mathrm{K}$, the volumetric specific heat for copper (an order of $10^3\,\mathrm{J/m^3 \cdot K}$) is lower than the NbTi and both of them are also lower than the Cp_v of SS and G10 (an order of $10^4\,\mathrm{J/m^3 \cdot K}$). As having the most rapid increase and the highest value in Cp_v, NbTi strands will be the most predominant component to store the Joule effect energy during a quench. This NbTi effect will also be discussed and compared with other materials during the computations of the hot spot temperature in a CICC (see Section 1.4.1). It is also to note that the jump in the specific heat of NbTi at around 9 K indicates the phase transition between normal and superconducting state at zero field.

Table 1.3 – Mass density of the different materials in the CICC

Material	**Mass density ($\mathbf{kg/m^3}$)**
NbTi	6550
Cu	8960
Stainless Steel	7900
G10	1948

[65] E. Floch. *Cern.* 2003.

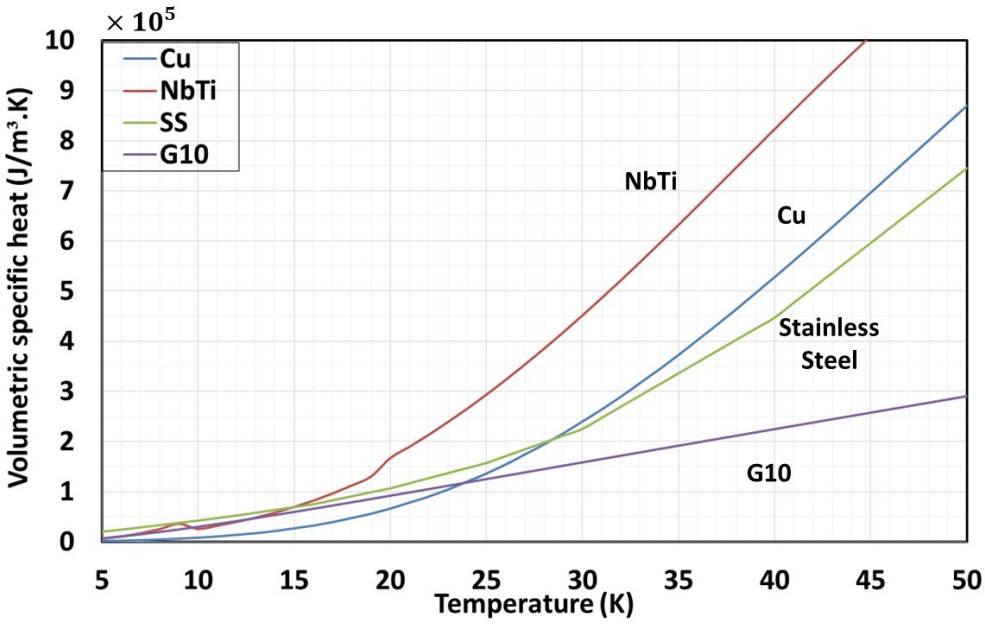

Figure 1.10 – Volumetric specific heat of the different materials in the CICC as a function of the temperature, with the magnetic field at 0 T and the copper in $RRR = 130$

1.2.3 Supercritical helium coolant

The JT-60SA TF coils are cooled by forced flow with supercritical helium. Relying on the helium phase diagram in Fig. 1.11[63], we can see that the helium saturation line separating the gas and liquid region ends in the critical point at $T_c = 5.20\,\mathrm{K}$ and $P_c = 2.27\,\mathrm{bar}$, where the liquid and gas phases disappear to become a single supercritical helium phase. The physical properties of a supercritical fluid, such as mass density, viscosity and thermal diffusivity, etc, are intermediate between those of the liquid and gas. The motivation of circulating the supercritical helium in the TF coils is based on its high pressure application domain, so that the high pressure drop issue in a CICC can be overcome. This high pressure drop issue will be studied in more details in the next subsection.

Moreover, Fig. 1.11 also shows that at atmospheric pressure, the boiling temperature (or saturated temperature) of the normal liquid helium (He I) is $T_c = 4.22\,\mathrm{K}$. This is why most commercial NbTi samples started their critical surface tests at 4.2 K. Finally, a triple point can be revealed in Fig. 1.11, at $T_\lambda = 2.17\,\mathrm{K}$ and $P_\lambda = 0.05\,\mathrm{bar}$. This is called "lambda point" where the three phases of helium coexist, including the normal liquid helium (He I), the superfluid helium (He II) and the gas helium. As the cooling helium in the TF coils is in the supercritical state, the following discussions will only focus on the helium physical properties covering an operating range of temperature from 5 K to 50 K and pressure from 7.5 bar to 15 bar. These properties will all be based on the common database "HePak"[69], for its wide valid range of the state equations from 0.8 K to 1500 K and up to 1000 bar.

a) Mass density

Fig. 1.12 shows the evolution of the helium mass density as a function of temperature and pressure. For a given temperature, the higher the pressure, the larger the mass density is. When under a certain pressure, the helium mass density is decreasing with the temperature. These are all coherent with the classic fluids characteristics. If we take the nominal conditions for quench test, at $T = 5\,\mathrm{K}$

[63] Steven Van Sciver. *International Cryogenics Monograph Series*. 2012.
[69] V. Arp, B. McCarty, and J. Fox. *Nist*. 1993.

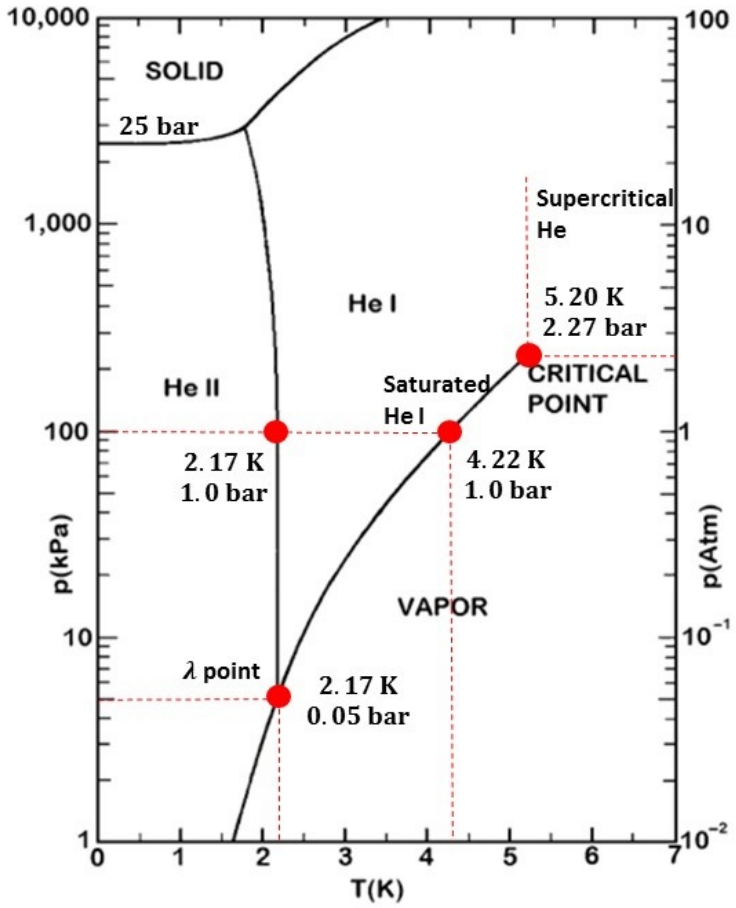

Figure 1.11 – Phase diagram of the helium in Pressure-Temperature[63]

and $P = 10\,\text{bar}$, a mass density of $143\,\text{kg/m}^3$ can be obtained. This value will be used for the following simplified computations of the CICC pressure drop.

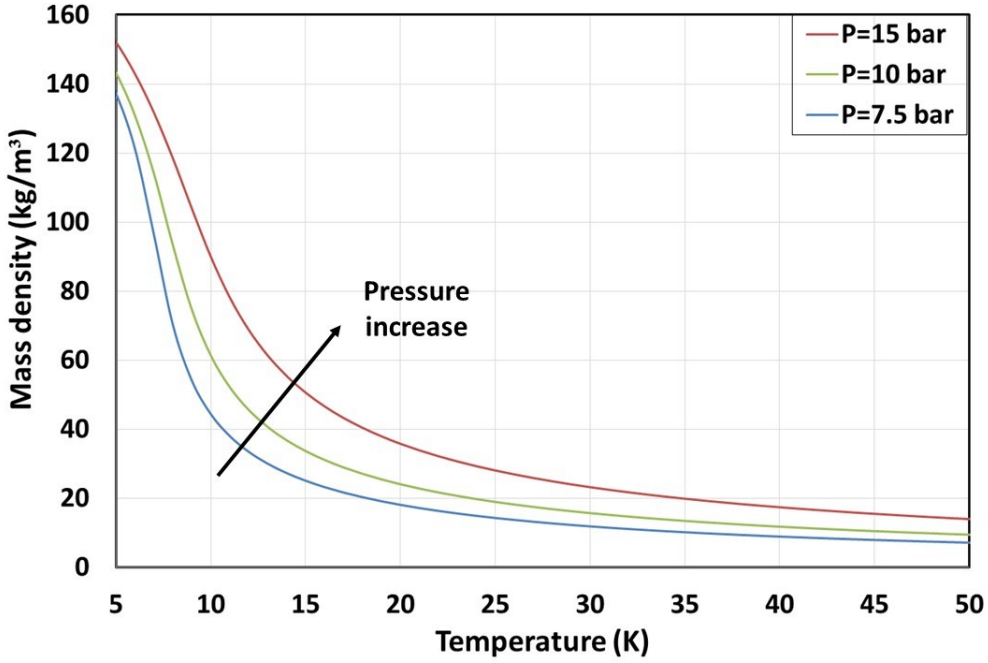

Figure 1.12 – Mass density of the helium as a function of the temperature and pressure

b) Thermal conductivity

Concerning the thermal conductivity of the supercritical helium, Fig. 1.13 tells that, for a given pressure, the helium thermal conductivity is firstly undergoing a slight decrease near 10 K then increases linearly with the temperature. For a given temperature, the pressure increase also leads to a slight increase in the helium thermal conductivity. Nevertheless, the order of magnitude of the supercritical helium is around $10^{-2}\,\mathrm{W/m \cdot K}$, which is nearly neglected in front of the CICC materials thermal conductivity (about $2 \backsim 4$ orders of magnitude of difference). This indicates that during a quench propagation in the CICC, the thermal conduction in the supercritical helium flow by Fourier's law will not be a predominant effect when comparing with the thermal conduction in the cables. Such helium property will also be discussed in the CICC hot spot temperature computations.

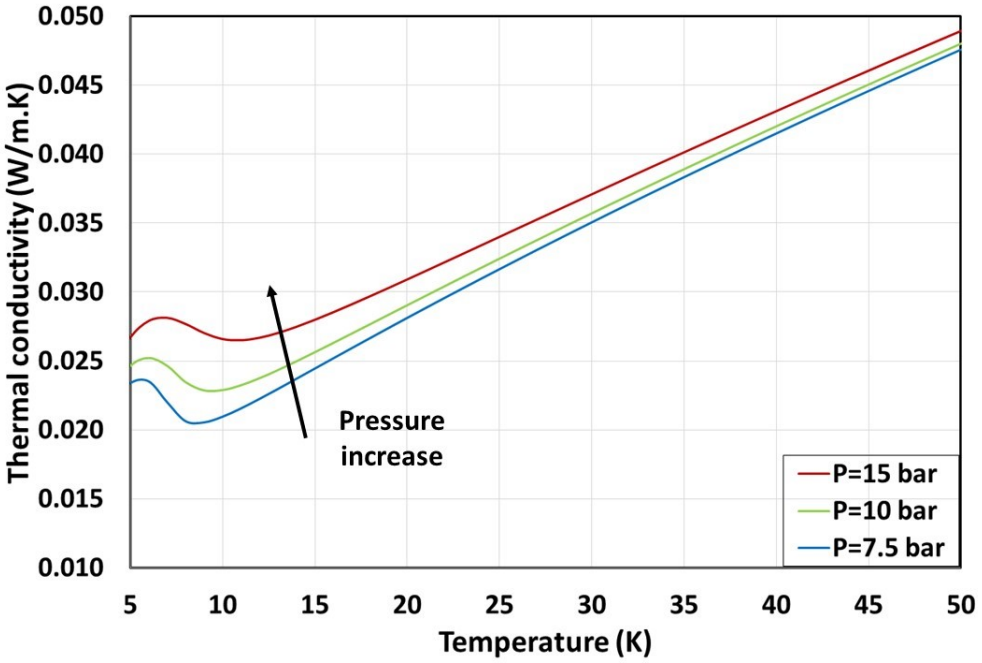

Figure 1.13 – Thermal conductivity of the helium as a function of the temperature and pressure

c) Specific heat

The last property to be presented for the supercritical helium is the volumetric specific heat at constant pressure. Fig. 1.14 shows that for a given pressure, the volumetric specific heat firstly increases with the temperature to around 8 K followed by a fast decrease. We can see that before the maximal point at $T = 8\,\mathrm{K}$, the volumetric specific heat decreases with the pressure. Since then, a positive dependence appears. At the nominal conditions of the quench test (5 K, 10 bar), the helium volumetric specific heat is around $5 \times 10^5 \mathrm{J/m^3 \cdot K}$, which is about 100 times larger than that of the CICC materials. This indicates that during the nominal testing conditions, the supercritical helium has the largest capacity to store the external heat load and to maintain the cryostability of the coils.

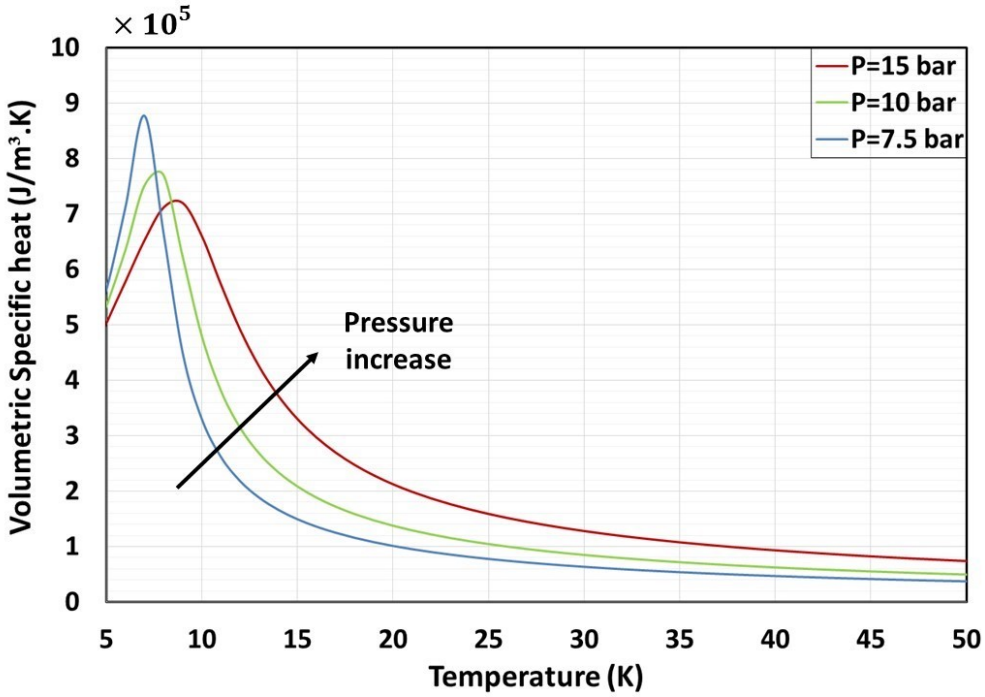

Figure 1.14 – Volumetric specific heat of the helium at constant pressure as a function of temperature and pressure

1.3 Thermohydraulic coupling between helium and conductor

Thermohydraulic coupling between helium and conductor plays an important role in the cryostability of the CICC and in the heat exchange during a quench. This section will then address two major issues that can affect the thermohydraulic coupling between helium and conductor: the helium mass flow rate related to the CICC friction factor and the heat exchange by helium flow forced convection.

1.3.1 Mass flow rate in the CICC

As already mentioned before, the high pressure drop is the biggest issue to be addressed for a CICC. In order to obtain an order of magnitude of the pressure drop in the JT-60SA TF coils, the classical equation of Darcy-Weisbach law will be applied[49], as written in Eq. (1.6). This equation was given by combining the prediction of the pressure loss as a function of the fluid, velocity, pipe diameter and the type of pipe material[70], and the measurements of the turbulent flows in pipes and in open channels[71]. It is valid for fully developed incompressible flow with a Mach number in the conductor far below 1, thus will be a theoretically approximate estimation for the helium mass flow rate in the CICC.

$$\Delta P = \frac{f\,L}{D_h}\frac{\rho\,V^2}{2} \tag{1.6}$$

where ΔP is the pressure drop due to helium friction, f the friction factor, D_h the hydraulic diameter, ρ the helium mass density, V the helium flow velocity, L the pipe length.

Replacing the helium flow velocity with the mass flow rate in Eq. (1.7), we can obtain a more practical equation of the pressure drop as a direct function of the mass flow rate, as written in

[49] P. Decool et al. *IEEE Transactions on Applied Superconductivity* **26**. 2016.
[70] J. Weisbach. *Theoretische Mechanik, Vieweg und Sohn, Braunschweig* **1**. 535. 1845.
[71] H. Darcy. *Mallet-Bachelier, Paris*. 268. 1857.

Eq. (1.8).

$$\dot{m} = \rho\, A_w\, V \tag{1.7}$$

$$\Delta P = \frac{f\, L}{2\, D_h\, A_w^2} \frac{\dot{m}^2}{\rho} \tag{1.8}$$

where A_w is the wetted cross-section and $\dot{m}$ the helium mass flow rate.

However, the friction factor f is a complex function of the pipe roughness, pipe diameter, fluid kinematic viscosity, flow velocity and the effect of fluid properties. Therefore, an empirical fit has been determined at the OTHELLO test facility (CEA Cadarache, France) for all the CICCs that are used for the TF coils manufacture[49]. Eq. (1.9) shows the relation between the friction factor and the Reynolds number involving the triple parameters (α, β, γ). Different CICCs are measured to have different values for the triple parameters. Here we take the group of the 6 CICCs used in the manufacture of the 6 Double-Pancakes (DPs) in a certain TF coil (the most studied coil TFC12) as an example to give the next computations (see Table 1.4).

$$f = \alpha + \beta \cdot Re^{\gamma} \tag{1.9}$$

Table 1.4 – Coefficients of the friction factor of the Double-Pancakes (TFC12)

CICC	$\boldsymbol{\alpha}$	$\boldsymbol{\beta}$	$\boldsymbol{\gamma}$
DP1	0.108324	46.816013	-0.76919
DP2	0.093188	14.285054	-0.60613
DP3	0.10006	38.654367	-0.752987
DP4	0.09402	32.58314	-0.722027
DP5	0.116246	49.730547	-0.786395
DP6	0.096512	32.33305	-0.734751

In order to introduce the mass flow rate term for the following pressure drop computations, the Reynolds number can be expressed as Eq. (1.10) with the mass flow equation in Eq. (1.7) and the hydraulic diameter definition in Eq. (1.11):

$$Re = \frac{\rho V D_h}{\mu} = \frac{4 \cdot \dot{m}}{\mu \cdot p_w} \tag{1.10}$$

$$D_h = \frac{4 A_w}{p_w} \tag{1.11}$$

where μ is the helium dynamic viscosity and p_w the wetted perimeter.

Combining Eq. (1.8), Eq. (1.9) and Eq. (1.10), we can obtain for the 6 manufactured CICCs their pressure drop as a function of (α, β, γ) and $\dot{m}$, as presented in Eq. (1.12).

$$\Delta P_i = f(\alpha_i,\, \beta_i,\, \gamma_i,\, \dot{m}_i)\ (i = 1, ..., 6) \tag{1.12}$$

Knowing that the helium cooling circuits are in parallel in the 6 CICCs, an equation system can then be written with the identical pressure drop in the 6 CICCs. Moreover, each CICC has been used to manufacture one double-pancake, i.e. two adjacent pancakes wound in clockwise and anticlockwise. Thereby, the mass flow rate in these two adjacent pancakes can be taken as identical (with the same friction factor). We can then take the only half of the total mass flow rate of the real testing conditions for our computations, with $\dot{m}_{tot} = 12\,\mathrm{g/s}$. Finally, we obtain a system of 7 equations with 7 unknowns (ΔP and $\dot{m}_i$), as presented in Eq. (1.13):

$$\begin{cases} \dot{m}_{tot} = \sum_{i=1}^{6} \dot{m}_i \\ \Delta P = \Delta P_i\ (i = 1, ..., 6) \end{cases} \tag{1.13}$$

Table 1.5 – Hydraulic parameters and testing conditions for the TF coils CICC

Parameter	**Value**	**Unit**
Strand outer diameter ($\mathbf{d_{so}}$)	0.81	[mm]
Number of strands ($\mathbf{n}$)	486	[–]
Void fraction ($\boldsymbol{\eta}$)	32	[%]
Helium area ($\mathbf{A_w}$)	125.8	[mm^2]
Wetted perimeter ($\mathbf{p_w}$)	1.108	[m]
Hydraulic diameter ($\mathbf{D_h}$)	0.454	[mm]
Pancake length ($\mathbf{L}$)	113.277	[m]
Average pressure[1] ($\mathbf{P_{av}}$)	10	[bar]
Average temperature[1] ($\mathbf{T_{av}}$)	5	[K]

[1] The average nominal conditions during the quench tests of JT-60SA TF coils

The necessary hydraulic parameters and testing conditions can be found in Table 1.5.
The above computations allow to give the mass flow rate distribution among the 6 CICCs (or 6 DPs), as presented in Fig. 1.15. We can see that in this TF coil, the DP1 has the smallest mass flow rate of 1.93 g/s whereas the DP6 has the largest one of 2.08 g/s. A difference of 0.15 g/s has appeared due to the different friction factors. One has to know that a same pressure drop has been produced around 550 mbar in the parallel helium circuits. This is coherent with the experimental pressure drop measured to around 600 mbar at nominal conditions (5 K, 10 bar). In addition, the Reynolds number during the nominal conditions has been computed to around 1650, which indicates a laminar regime of the helium flow in the TF coil. The friction factor impact on the helium mass flow rate thus on the helium cooling effect will be studied in more details in Chapter 3.

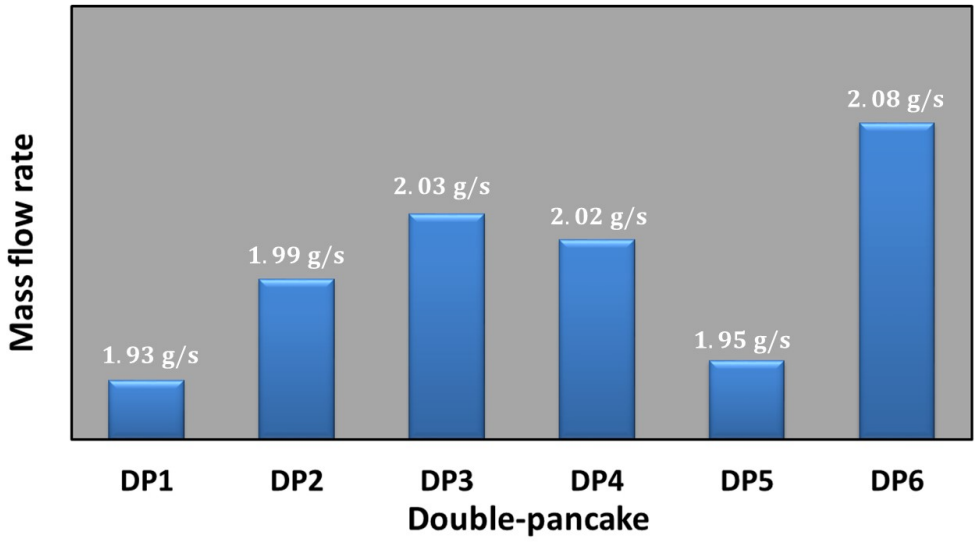

Figure 1.15 – Distribution of the helium mass flow rate in the 6 DPs of TFC12

1.3.2 Heat exchange between helium and conductor

Despite of the high pressure drop issue, CICC is largely applied for its high cooling efficiency, or the so-called forced convection coefficient h_{fc}. Fig. 1.16 gives a schematic diagram for the heat exchange between the forced helium flow and the conductor, including the superconducting and copper strands and the stainless steel jacket inner wall. According to the Newton's law of cooling, we can give a basic expression for this heat exchange written as:

$$q_{fc} = h_{fc}\,(T_{cond} - T_{He}) \tag{1.14}$$

where q_{fc} is the thermal flux density [W/m^2] deposited on the conductor, T_{cond} and T_{He} are respectively the conductor and helium temperatures.

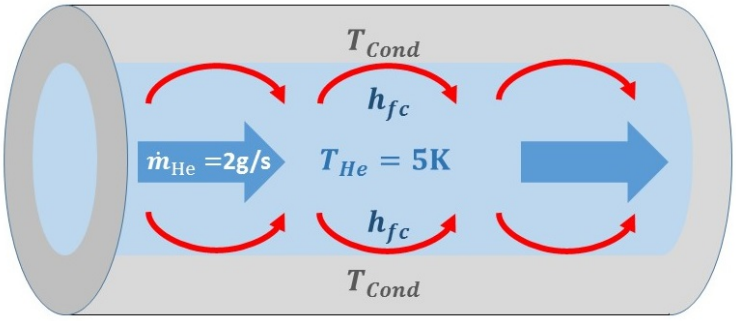

Figure 1.16 – Schematic diagram of the forced helium convection in the CICC

The forced convection coefficient h_{fc} depends on the velocity and the thermophysical properties of the fluid such as the mass density, the viscosity, the specific heat, the thermal conductivity and the geometry and the state of the solid surface[72]. These make the h_{fc} estimation very complex to allow rigorous mathematics analytical solutions. Therefore, the empirical correlations involving the dimensionless numbers (Reynolds, Nusselt, Prandtl, etc.) based on the conservation equations were developed.

During the last century, many correlations based on the Reynolds analogy[73] have been proposed to model the heat transfer in pipes, from the empirical fit modifications, such as Colburn-Reynolds analogy[74] and Dittus-Boelter correlation[75], to the recent adaptations to the fusion CICC configurations, such as the Wendelstein 7-X magnet system[76]. According to the quench test conditions of the JT-60SA TF coils, two empirical correlations will be discussed in the next for the two different regimes: temperature-increasing phase before quench with laminar flow regime and fast transient quench phase with turbulent flow regime.

During the temperature-increasing phase of the JT-60SA TF coils, the Reynolds number of the supercritical helium flow circulated in the CICC has been computed to around 1650, thus in a laminar regime ($Re < 2300$). An appropriate correlation has been proposed for the CICC case in 1995 by Y. Wachi, M. Ono and T. Hamajima[77] based on the laminar regime correlation in Eq. (1.15):

$$Nu = \frac{h\,D_h}{\lambda} = 4.36 \tag{1.15}$$

where h is the convection coefficient, D_h the hydraulic diameter, λ the fluid thermal conductivity.

[72] B. Baudouy et al. *Techniques de l'Ingénieur*. 12–16. 2015.
[73] O. Reynolds. *Proc. Manchester Lit. Philos. Soc.* **14**. 7–12. 1874.
[74] A. P. Colburn. *Trans. Am. Inst. Chem. Eng.* **29**. 174–210. 1933.
[75] F. Dittus and L. Boelter. *University of California Publications in Engineering* **2**. 443–461. 1930.
[76] X. Cheng. *Cryogenics* **34**. 659–666. 1994.
[77] Y. Wachi, M. Ono, and T. Hamajima. *IEEE Transactions on Applied Superconductivity* **5**. 568–571. 1995.

According to the measurements of the heat transfer characteristics of the supercritical helium in a CICC, Wachi et al. have found that at the laminar regime, the forced convection coefficient is $\mathbf{1.5-1.8}$ times larger than calculated values from the relation of $Nu = 4.36$. According to the nominal conditions at 5 K and 10 bar, we can obtain for the forced convection coefficient a value around $378\,\mathrm{W/m^2 \cdot K}$. In addition, a temperature difference between the helium and the conductor can also be obtained to around 7.9 mK relying on an average thermal flux density deposited on the TF coils CICC (around $q_{fc} = 3\,\mathrm{W/m^2}$)[78]. Such temperature difference is nearly neglected when comparing to the 300 mK difference between helium inlet and outlet or to the T_{cs} difference among the different positions in the CICC (more than 100 mK). This then shows the high cooling efficiency characteristic of the CICC configuration.

In case of quench, the mass flow rate as well as the Reynolds number will immediately increase to a value of more than 10 times higher than the one in laminar regime in the TF coils CICC (see Chapter 4). Thereby, a turbulent regime correlation will be applied. We choose the Dittus-Boelter-Giarratano (DBG) correlation[79] thanks to its adaptation to the forced convection of supercritical helium in a CICC, as in our case. This empirical fit is based on the experimental data measured with Reynolds number ranged from 10^4 to 3.8×10^5, pressures from 3 bar to 20 bar and fluid temperatures from 4.4 K to 30 K, as presented in Eq. (1.16):

$$Nu = \frac{h\,D_h}{\lambda} = 0.0259\,Re^{0.8}Pr^{0.4}(\frac{T_{wall}}{T_{He}})^{-0.716} \tag{1.16}$$

where T_{wall} is the solid wall temperature of the CICC.

One may have noted that this correlation is somewhat implicit in the temperature since T_{wall} is often an unknown parameter during the quench test. Nevertheless, we can combine Eq. (1.14) to the correlation Eq. (1.16) to rewrite an equation as a function of the only unknown, temperature difference ($\Delta T = T_{wall} - T_{He}$), as presented below:

$$h_{fc} = \frac{q_{fc}}{\Delta T} = 0.0259\,Re^{0.8}Pr^{0.4}(\frac{\Delta T + T_{He}}{T_{He}})^{-0.716}\frac{\lambda}{D_h} \tag{1.17}$$

The forced convection coefficient (h_{fc}) can thus be determined by resolving ΔT in Eq. (1.17). This correlation will be used to acquire h_{fc} during the following quench studies (see Chapters 3 and 4).

To summarize, the above studies have proved a quasi-neglected temperature difference between conductor and helium (less than 10 mK). This indicates a good cooling efficiency in the CICC even at the laminar regime. The forced convection coefficient has been determined to around $378\,\mathrm{W/m^2 \cdot K}$ in the TF coils CICC at their nominal testing conditions. For the following studies, we will choose the Dittus-Boelter-Giarratano correlation in Eq. (1.16) for the turbulent regime and the corrected laminar correlation in Eq. (1.15) for the laminar regime to compute the forced convection coefficient h_{fc} of supercritical helium.

[78] F. Juster. *Internal report.* 2011.

[79] P. Giarratano, V. Arp, and R. Smith. *Cryogenics.* 385–393. 1971.

1.4 First simple quench computations

1.4.1 Hot spot temperature in the CICC

As already mentioned, when the temperature increases to T_{cs}, the current starts to switch from the NbTi strands to the copper part. Large amounts of Joule effect energy will then be produced due to the resistive copper part and will provoke a further quench propagation in the conductor which in turn leads to a higher Joule heat thus a higher temperature in the CICC. Such a chain process then brings one of the dimensioning problems for a superconducting magnet: the irreversible degradation of the magnet due to the over thermal dilation by the large Joule heat. In order to address this issue, a study of the hot spot temperature T_{hs} will be firstly carried out in this section.

The heat equation for computing hot spot temperature on one single heating point (thus independent of the space variable) in the CICC without other heat exchange can be written as Eq. (1.18):

$$\frac{d(C_{cond}(T)\cdot T(t))}{dt} = \frac{\rho_{Cu}(T,B)}{S_{Cu}S_{cond}} I^2(t) \tag{1.18}$$

where ρ_{Cu} is the the electrical resistivity of copper which depends on the temperature and magnetic field (see Section 1.2.2), S_{Cu} the cross-sectional area of copper and C_{cond} the temperature dependent volumetric specific heat of the entire CICC, as expressed in Eq. (1.19):

$$C_{cond}(T) = \frac{S_{NbTi}}{S_{cond}} C_{NbTi}(T) + \frac{S_{Cu}}{S_{cond}} C_{Cu}(T) + \frac{S_{SS}}{S_{cond}} C_{SS}(T) + \frac{S_{Ins}}{S_{cond}} C_{Ins}(T) + \frac{S_{He}}{S_{cond}} C_{He}(T) \tag{1.19}$$

where the volumetric specific heat of each component can be found in Fig. 1.10 and Fig. 1.14, and S_{cond} is the cross-sectional area of the entire CICC including NbTi, copper, stainless steel, G10 insulation and helium, as expressed in Eq. (1.20):

$$S_{cond} = S_{NbTi} + S_{Cu} + S_{SS} + S_{Ins} + S_{He} \tag{1.20}$$

where the different materials cross-sectional area can be found in Table 1.1.

Eq. (1.18) has been written with the assumption of having a perfect temperature homogenisation in the entire CICC cross-section. This is based on the fact that the temperature difference between conductor and helium is neglected thanks to the high forced convection coefficient and that the thermal conductivity of copper matrix is high enough to lead an efficient heat conduction in the conductor. So that an average approach has been applied in Eq. (1.19) for the volumetric specific heat of the entire CICC.

Regarding the coil current $I(t)$ in Eq. (1.18), we recall that a nominal condition of $I_0 = 25.7\,\text{kA}$ will be maintained before quench. However, when a quench is initiated, the resistive voltage developed due to the normal state will be detected and compared with a threshold voltage of 100 mV. If this voltage increase lasts for more than 100 ms corresponding to the quench detection and action time (τ_{da}), a fast discharge of the current will then be triggered to release the stored magnetic energy on the dump resistor of $R_d = 6.2\,\text{m}\Omega$. This current variation process before and after a quench can be expressed in Eq. (1.21):

$$\begin{cases} I(t) = I_0 & \textbf{when } t < \tau_{da} \\ I(t) = I_0 \cdot exp(\dfrac{-(t-\tau_{da})}{\tau}) & \textbf{when } t \geqslant \tau_{da} \\ \text{with } \tau = \dfrac{L}{R} \end{cases} \tag{1.21}$$

where τ is the time constant of the current discharge in the TF coil. It can be approximately computed with the ratio between the coil self-inductance of $L = 62\,\text{mH}$ and the electrical resistance

of the dumping circuit (R) taken to be the same as $R_d = 6.2\,\mathrm{m\Omega}$. We obtain $\tau \approx 10\,\mathrm{s}$. The maximal temperature (T_{max}) reached at the end of the current discharge then corresponds to the hot spot temperature. It can be computed by discretizing the Eq. (1.18), as written in Eq. (1.22):

$$T_{max} = T_0 + \int_{t=0}^{t=\tau_{da}} \frac{\rho_{Cu}(T,B)\cdot I_0^2}{C_{cond}(T)\cdot S_{Cu}S_{cond}}dt + \int_{t=\tau_{da}}^{t=+\infty} \frac{\rho_{Cu}(T,B)\cdot I(t)^2}{C_{cond}(T)\cdot S_{Cu}S_{cond}}dt \tag{1.22}$$

where T_0 is the initial temperature of the copper part at the moment of detecting a quench ($V \geqslant 100\,\mathrm{mV}$). It is measured to be around 7.5 K for the JT-60SA TF coils. The initial magnetic field will be taken at the peak field value of 3.04 T for a pessimistic computation.

In order to carry out a study of the different materials thermal effect on the hot spot temperature, the above components of the CICC (NbTi alloy, copper matrix, SS jacket, G10 insulator and helium flow) will be globally or partially taken into account in the following computations. Fig. 1.17 then presents the time evolution of the conductor temperature computed with different components of the CICC. The quench detection and action time has been fixed at the testing condition of $\tau_{da} = 100\,\mathrm{ms}$. The time at $t = 0\,\mathrm{s}$ represents the beginning of the current Fast Discharge (FD).

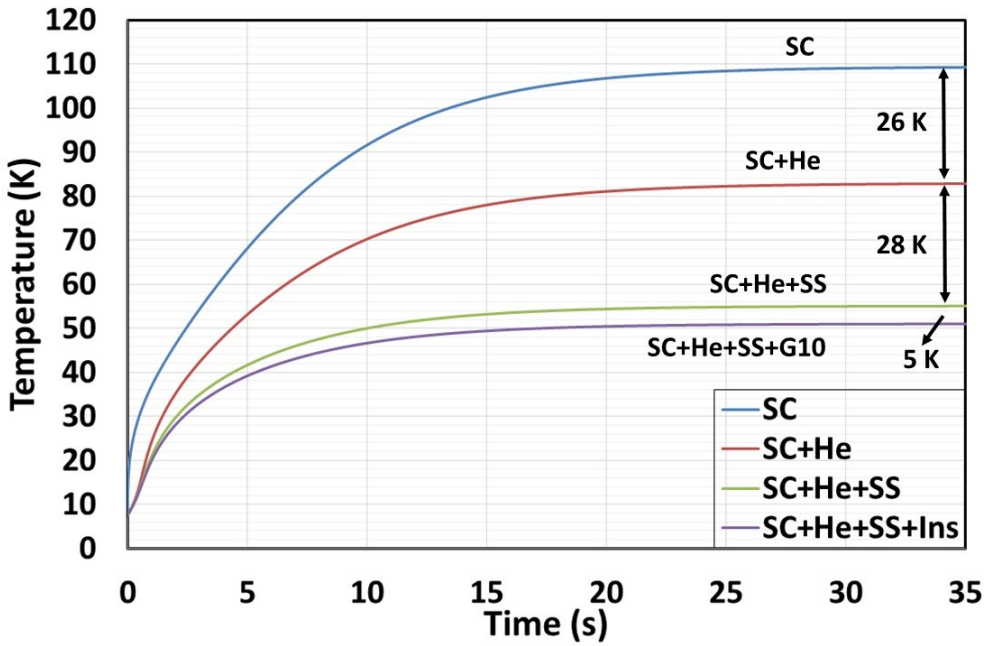

Figure 1.17 – Computation of the hot spot temperature taking into account the different thermal components of the CICC, $\tau_{da} = 100\,\mathrm{ms}$

We can see that when it is in the adiabatic case, i.e. without helium flow (blue line), the pure superconducting cable (NbTi+Cu) can reach a hot spot temperature of around 110 K. When cooling with helium (red line), T_{hs} has been reduced of 24 % with respect to the adiabatic case. This corresponds to the large capability of storing energy thanks to the large value of helium Cp_v. When adding the component of stainless steel jacket in the computation, a T_{hs} of around 34 % reduction with respect to the "SC+He" case can be achieved (see green line). This indicates that the SS jacket of the JT-60SA TF coils CICC has almost the same thermal effect on the Joule heat diffusion than the helium flow when having a quench. Thereby, such an efficient cooling effect on the T_{hs} has been revealed. Finally, when taking into account all the CICC components in the computation (see violet line), a T_{hs} around 50 K can be obtained at the maximal temperature plateau. This corresponds to only 9 % of reduction in T_{hs} when comparing with the last "SC+He+SS" case. This is actually coherent with the low Cp_v value of G10 insulator which has only very limited thermal effect on the Joule heat diffusion.

In addition to the above components thermal effects, the quench detection and action time (τ_{da}) has also a non-negligible impact on the CICC hot spot temperature. Fig. 1.18 shows that, from

0 ms (red line) to 500 ms (orange line), the longer the τ_{da} lasts, the higher the T_{hs} will be achieved. A difference of 5 K has been produced due to the 500 ms difference in the current discharge moment. This can be simply explained by the fact that a longer τ_{da} allows the nominal current to heat for a longer period thus leading to a higher Joule effect energy to provoke a higher temperature rise in the CICC. In the following study, the parameter T_{hs} will be precisely applied when building a simplified physical model of computing the normal zone length evolution in Chapter 3.

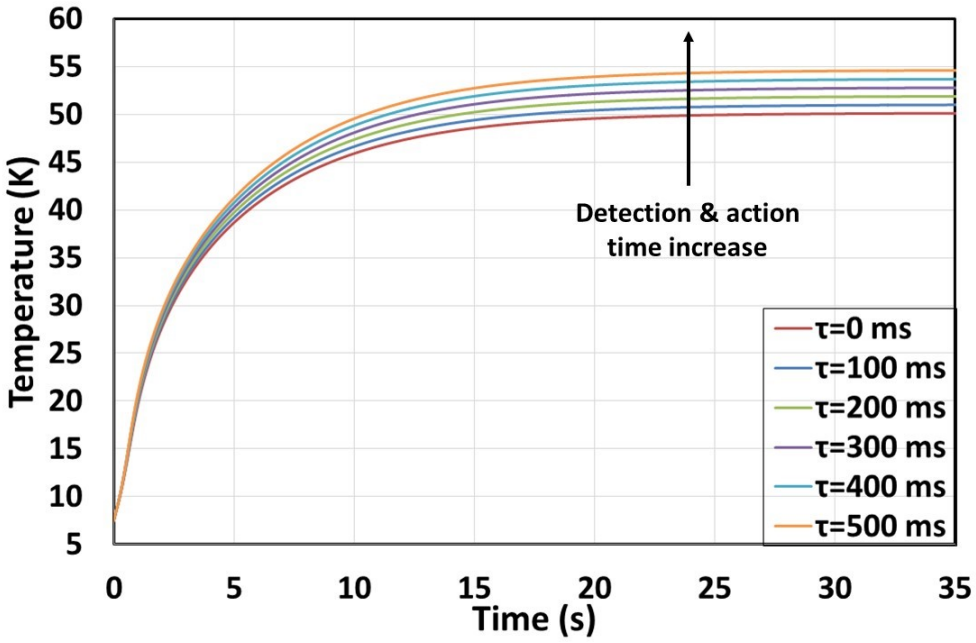

Figure 1.18 – Computation of the hot spot temperature with all the thermal components of the TF coils CICC and with different quench detection and action time τ_{da} from 0 ms to 500 ms

1.4.2 Longitudinal quench propagation in the CICC

As the key issue to be addressed in this PhD report, the quench propagation in a CICC is a multiphysical phenomenon coupling electromagnetism and thermohdyraulics. When the quench is triggered, a heat front can be formed to separate the superconducting magnet into two regions. In addition, this model neglects the heating induced flow in the helium (see Fig. 1.19):

- Normal zone where the Joule heat is produced when reaching or above the quench temperature, with $T \geqslant T_q$
- Superconducting zone where no Joule heat is produced staying below the quench temperature, with $T < T_q$.

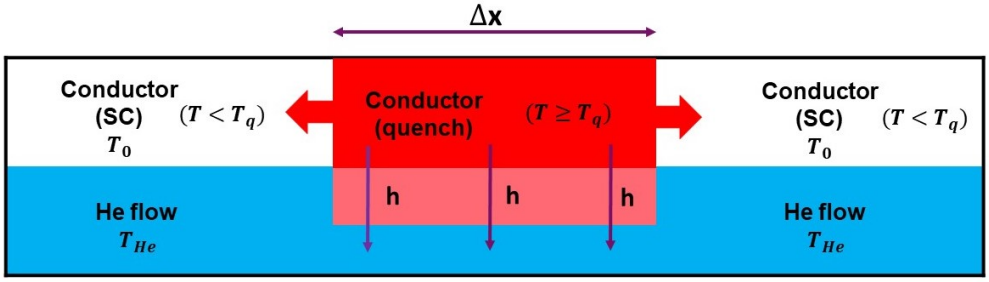

Figure 1.19 – Schema of the quench propagation in a CICC

Here we take a superconducting transition temperature, called *quench temperature* (T_q), defined as the average of T_c and T_{cs}. Indeed, during the quench test of the TF coils, it is complex to measure the real T_{cs} or difficult to say if the measured temperature corresponds to T_c in the magnet-grade system. Thereby, a T_q has been defined for talking about the TF coils quench temperature, experimentally or analytically. For the following computations in this section, we make an assumption that the current passes completely in the NbTi below T_q and completely in the copper matrix when reaching T_q in order to simplify the quench computation equations. According to the experimental data, T_q is taken to be 7.5 K.

a) Adiabatic case

We start from a first simple case of heat equations describing the quench propagation in an adiabatic CICC, written as Eq. (1.23):

$$\begin{cases} C_{cond}\dfrac{\partial T}{\partial t}(x,t) = \lambda_{cond}\dfrac{\partial^2 T}{\partial x^2}(x,t) + \dfrac{\rho_{Cu} I^2}{S_{Cu} S_{cond}} & (T \geqslant T_q) \\ C_{cond}\dfrac{\partial T}{\partial t}(x,t) = \lambda_{cond}\dfrac{\partial^2 T}{\partial x^2}(x,t) & (T < T_q) \end{cases} \tag{1.23}$$

where λ_{cond} is the average thermal conductivity estimated with the entire cross-section of the CICC (see the components thermal conductivity in Fig. 1.9 and Fig. 1.13).

Eq. (1.23) is written with the hypothesis that the properties of the CICC (C_{cond}, λ_{cond} and ρ_{Cu}) are all constant and can be estimated at the local quench temperature (T_q). This is based on the fact that the quench propagation phenomenon generally depends on the quench front dynamics with a local temperature always around T_q[80]. In 1960, W. Cherry and J. Gittleman have proved that the equation system Eq. (1.23) allows to obtain a solution under the type of progressive wave[81]. This is actually based on the propagative phenomenon of the quench front in a CICC, as described by Eq. (1.23). Therefore, Eq. (1.23) can be rewritten in form of the wave equations by carrying out a variable change of $T(x,t) = T(\xi)$ (with $\xi = x - v_l\, t$), as presented in Eq. (1.24):

$$\begin{cases} -v_l\, C_{cond}\dfrac{dT(\xi)}{d\xi} = \lambda_{cond}\dfrac{d^2 T(\xi)}{d\xi^2} + \dfrac{\rho_{Cu} I^2}{S_{Cu} S_{cond}} & (T \geqslant T_q) \\ -v_l\, C_{cond}\dfrac{dT(\xi)}{d\xi} = \lambda_{cond}\dfrac{d^2 T(\xi)}{d\xi^2} & (T < T_q) \end{cases} \tag{1.24}$$

where v_l represents the longitudinal quench propagation velocity.

The integration constants when resolving the partial differential equations should be adjusted to the boundary conditions presented in Eq. (1.25):

$$\begin{cases} T(\xi) = T_0 & \textbf{when } \xi \to +\infty \\ T(\xi) = T_q & \textbf{when } \xi = 0 \\ \dfrac{d^2 T(\xi)}{d\xi^2} = 0 & \textbf{when } \xi \to -\infty \end{cases} \tag{1.25}$$

where $\xi \to +\infty$ corresponds to the far right in the superconducting zone where the conductor temperature is considered to be the boundary temperature T_0. $\xi = 0$ corresponds to the interface between the normal zone and superconducting zone where the conductor temperature is at the quench temperature T_q. Whereas the $\xi \to -\infty$ corresponds to the far left in the normal zone where the conductor temperature will tend to a hot spot temperature leading to $\frac{d^2 T(\xi)}{d\xi^2} = 0$[81].

[80] Walid Abdel Maksoud. *Thesis.* 2010.
[81] W. H. Cherry and J. I. Gittleman. *Solid State Electronics* **1**. 287–305. 1960.

The typical second-order differential equations can then be resolved to obtain an analytical solution for the longitudinal quench propagation velocity in the CICC, as presented in Eq. (1.26).

$$v_l = \frac{I}{C_{cond}} \sqrt{\frac{\rho_{Cu}\,\lambda_{cond}}{S_{Cu} S_{cond}\,(T_q - T_0)}} \tag{1.26}$$

where the thermophysical properties of the CICC (C_{cond} and λ_{cond}) are computed at the quench temperature T_q. The cross-sectional area of the conductor S_{cond} only takes into account the cable part, i.e. NbTi and copper strands. This is based on the fact that the thermal conductivity of copper is much higher than the other materials (see Fig. 1.9) leading to a predominant thermal effect on the longitudinal quench propagation.

Eq. (1.26) indicates that the longitudinal quench propagation velocity (v_l) is positively related to the current (I) and is inversely proportional (square root) to the temperature difference between T_q and T_0. As the coil current is maintained at the nominal value of 25.7 kA, we will thus focus on the temperature difference effect on the v_l. Indeed, the boundary temperature in the superconducting zone (T_0) is time dependent in our case, since the quench test of the TF coils were carried out by increasing the global helium temperature from the coil inlet (see Chapter 2), i.e. an ongoing varied value in T_0. Thereby, the longitudinal quench propagation velocity is computed with different boundary temperature T_0, as presented in Fig. 1.20.

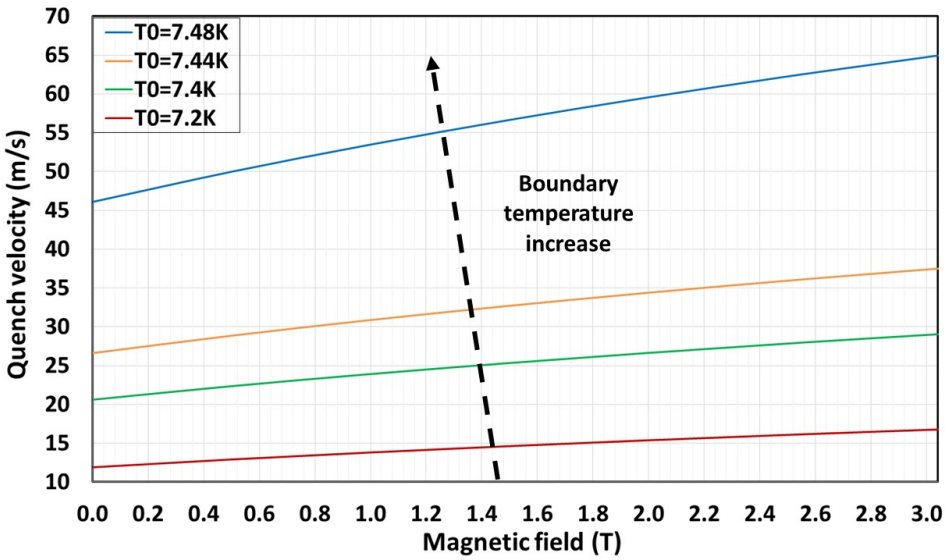

Figure 1.20 – Evolution of the adiabatic longitudinal quench propagation velocity as a function of the magnetic field at different boundary temperature (T_0)

Fig. 1.20 shows that within the nominal field conditions in the TF coils ranging from 0 T to 3.04 T, v_l is nearly in a linear dependence with the magnetic field. In addition, the inverse relation between the longitudinal quench propagation velocity and the temperature difference ($T_q - T_0$) has also been revealed in Fig. 1.20. We can see that the more the boundary temperature is close to the quench temperature fixed at 7.5 K, the higher the longitudinal quench velocity will be. For instance, the computation with $T_0 = 7.48$ K leads to a v_l 5 times higher than the one at $T_0 = 7.2$ K. This indicates the predominant effect of such temperature difference ($T_q - T_0$) on the quench propagation velocity. This effect will also be applied in Chapter 4 for further study. In addition, these boundary temperatures as well as the peak field value of $B_{max} = 3.04$ T will be applied to carry out the following computations of the quench propagation with helium cooling effect.

b) Helium cooling case

In the case of the quench propagation in a CICC cooled by helium forced flow, the heat equations will take into account the helium cooling effect by forced convection with the heat exchange coefficient noted as h (see Fig. 1.19). The equations governing the dynamics of the normal zone and the superconducting zone are written in Eq. (1.27):

$$\begin{cases} C_{cond}\dfrac{\partial T}{\partial t}(x,t) = \lambda_{cond}\dfrac{\partial^2 T}{\partial x^2}(x,t) + \dfrac{\rho_{Cu}\, I^2}{S_{Cu}S_{cond}} - \dfrac{h\, P_m}{S_{cond}} \cdot [T(x,t) - T_{He}] & (T \geqslant T_q) \\ C_{cond}\dfrac{\partial T}{\partial t}(x,t) = \lambda_{cond}\dfrac{\partial^2 T}{\partial x^2}(x,t) - \dfrac{h\, P_m}{S_{cond}} \cdot [T(x,t) - T_{He}] & (T < T_q) \end{cases} \tag{1.27}$$

where P_m is the wetted perimeter in the CICC and T_{He} the helium temperature.

We recall that this model is based on a helium bath cooling protocol with T_{He} being constant. It is actually different from the CICC problem with the T_{He} increasing along the time. Thereby, including the constant properties of the CICC, we make another assumption that the forced convection coefficient h is also constant in the equations. Indeed, the quench propagation phenomenon generally depends on the quench front dynamics, as already explained in the adiabatic case. So that a constant helium property can be applied at this local quench front position in the CICC. And the helium temperature can be taken to be the boundary temperature in the CICC (T_0) thanks to its high forced convection coefficient. With the same variable change and the boundary conditions, we can obtain an analytical solution of the longitudinal quench propagation velocity in the helium cooling case, as written in Eq. (1.28):

$$v_l = \frac{\frac{\rho_{Cu}\, I^2}{S_{Cu}S_{cond}} - 2\frac{h\, P_m}{S_{cond}}\Delta T}{C_{cond}} \sqrt{\frac{\lambda_{cond}}{(\frac{\rho_{Cu}\, I^2}{S_{Cu}S_{cond}} - \frac{h\, P_m}{S_{cond}}\Delta T)\Delta T}} \tag{1.28}$$

with $\Delta T = T_q - T_{He} = T_q - T_0$.

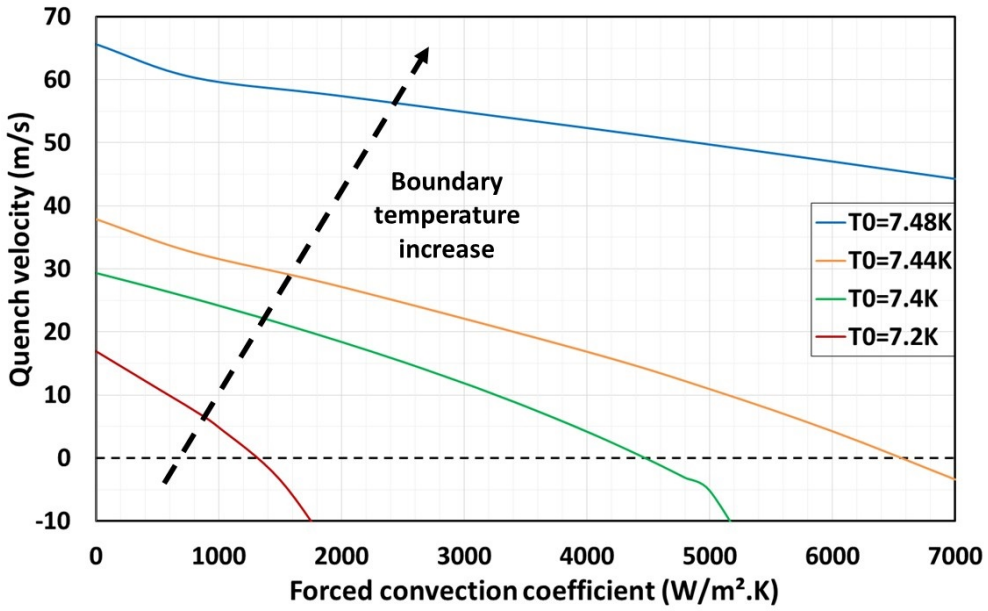

Figure 1.21 – Evolution of the longitudinal quench propagation velocity as a function of the forced helium convection coefficient, computed with different T_0 at $B = 3.04$ T

As already mentioned above, the different boundary temperatures as well as $B = 3.04$ T have been applied to compute the longitudinal quench propagation velocity v_l as a function of the forced convection coefficient h. Fig. 1.21 shows that the quench velocity decreases rapidly with h, until

reaching a negative value. For instance, at $T_0 = 7.4\,\mathrm{K}$, the critical value is around $h = 4500\,\mathrm{W/m^2 \cdot K}$ (see green line). This actually indicates that the normal zone starts to shrink when the TF coils CICC reaches such a forced convection coefficient so that the transited CICC will get back to the superconducting state. When $h = 0$, we can see that the quench velocity is equal to the one computed at adiabatic case of around 30 m/s. In general, the more the boundary temperature is close to the quench temperature, a higher h value will be needed to stop a normal zone expansion. This is coherent with the fact that mitigating a strong quench dynamics due to low ΔT will definitely need a sufficiently high cooling efficiency to evacuate the Joule heat. More details will be presented in Chapter 3 about the experimental quench velocity in the TF coils.

1.4.3 Transversal thermal conduction in the insulation

In parallel with the longitudinal quench propagation along the CICC, the transversal thermal conduction through the inter-conductor insulation is also a non-negligible phenomenon taking place in a superconducting coil like the JT-60SA TF coils. In order to get an order of magnitude of the transversal heat transfer time through the 2 mm thick G10 insulator (2 mm is the insulation thickness between two conductors in the TF coil), we write two heat equations for the two sides of the insulator, as presented in Eq. (1.29):

$$\begin{cases} \dfrac{d(C_{heat}(T) \cdot T_{heat}(t))}{dt} = -\dfrac{\lambda_{ins}(T)}{e_{cond}} \dfrac{T_{heat}(t) - T_{cold}(t)}{e_{ins}} + \dfrac{\rho_{Cu}(T,B) \cdot I(t)^2}{S_{Cu}\, S_{cond}} & \text{(heat side)} \\ \dfrac{d(C_{cold}(T) \cdot T_{cold}(t))}{dt} = -\dfrac{\lambda_{ins}(T)}{e_{cond}} \dfrac{T_{cold}(t) - T_{heat}(t)}{e_{ins}} & \text{(cold side)} \end{cases} \tag{1.29}$$

where the heat side of the insulator corresponds to the quenched CICC with obviously the Joule heat produced in the copper matrix whereas the cold side of the insulator corresponds to the superconducting CICC not yet reaching T_{cs} thus without any Joule heat. A heat transfer will then be taking place through the insulator due to a temperature gradient (see the schematic illustration in Fig. 1.22). These equations will be resolved by making two hypotheses:

- The temperatures in the heat and cold sides CICCs are assumed to be homogeneous in the entire cross-sections, as already applied in the hot spot temperature computations. Thereby, the general volumetric specific heat can be computed with the two average values, T_{heat} and T_{cold}.
- The temperature in the 2 mm thick insulator is also assumed to be homogeneous so that the thermal conductivity of the insulator can be obtained with an average temperature between T_{heat} and T_{cold}, as $T_{ins} = \frac{T_{heat}+T_{cold}}{2}$. This assumption is made for simplifying the following computations which are carried out to obtain an order of magnitude of the transversal heat transfer time through the inter-conductor insulation.

In this computations, all the CICC components are taken into account including conductor and helium. The quench detection and action time is always fixed at $\tau_{da} = 100\,\mathrm{ms}$ for the current discharge $I(t)$. The initial conditions are taken to be $T_i = 7.5\,\mathrm{K}$ and $B_i = 3.04\,\mathrm{T}$. The evolution of the heat and cold temperatures can thus be obtained by discretizing the above equations in Eq. (1.29).

Fig. 1.22 shows the time evolution of the two side temperatures of the 2 mm G10 insulator. The red line represents the temperature rise under the Joule heat effect whereas the blue line represents the cold side temperature increased by thermal conduction through the insulation. The T_{cs} at cold side (black dashed line) has also been plotted in the same figure to compare with the cold side temperature increase. An initial value around 7.9 K has been taken corresponding to the position where starts the second turn of the "D-shaped" CICC in TF coils (see T_{cs} at around $x = 19\,\mathrm{m}$ in Fig. 1.6).

We can see in Fig. 1.22 that the heat side temperature, after triggering a quench, increases rapidly along the time, whereas the cold side has been seen a much delayed increase due to the heat

transfer through the 2 mm thick insulator. In addition, T_{cs} has also a slight increase during this period, which is due to the current discharge (triggered when detecting a quench) leading to a magnetic field decrease in the conductors. We can see that the time for the heat to transfer in the 2 mm thick G10 and then to increase the cold side temperature up to its T_{cs} is around 6 s. Such order of magnitude of quench delay will be used in the following studies. Indeed, for a complex magnet configuration like JT-60SA TF coils, transversal heat transfer phenomenon through the inter-conductor insulation could have a predominant effect on the quench dynamics. The potential competition between longitudinal and transversal quench propagations will thus be studied in more details for the JT-60SA TF coils quench tests (see Chapters 3 and 4).

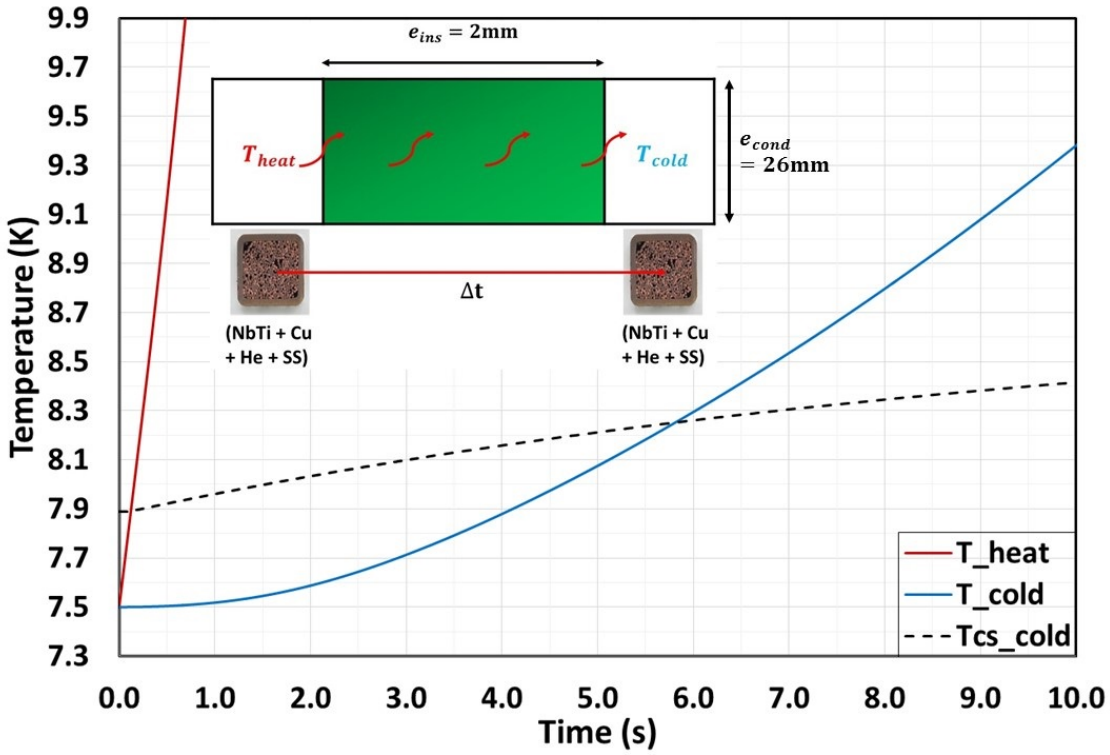

Figure 1.22 – Time evolution of the temperature at the heat and cold sides of the 2 mm insulation between the conductors

Conclusions

This first chapter allows to introduce all the related notions and parameters for describing the quench problem in a Cable-In-Conduit Conductor (CICC) based superconducting magnet cooled with supercritical helium. We have started by talking about the JT-60SA Tokamak context of this PhD study as well as the mains issues to be addressed in this PhD report. Then, the characteristics of the superconducting material NbTi as well as the thermal and electric properties of all the CICC components including conductor and helium have been presented. Such as the NbTi critical surface, the copper electrical resistivity, the thermal conductivity and the specific heat, etc. In addition, the thermohydraulic coupling between conductor and helium have been well studied with the two major characteristics of CICC, friction factor and forced helium flow convection coefficient. Finally, we have given several simplified analytical computations to describe the quench related notions for the JT-60SA TF coils CICC, including the hot spot temperature, the longitudinal quench propagation velocity and the potential heat transfer phenomenon through a G10 insulation. In the rest of this PhD report, we will rely on the above introduced parameters and notions to carry out a more detailed study on the thermohdyraulic phenomena taking place during the quench of a superconducting magnet cooled with supercritical helium.

CHAPTER 2

Description of the JT60-SA TF coils quench experiments in the Cold Test Facility

Objectives

- **To give an overview of the Cold Test Facility as well as the main characteristics for the JT-60SA TF coils**
- **To describe the instrumentation available for studying the physical phenomena during the TF coils quench experiments**
- **To explain the experimental protocol of performing a quench test**

2.1 JT-60SA Cold Test Facility and the tested TF coils

2.1.1 Description of the Cold Test Facility

In order to check the coils performance and hence mitigate the manufacturing risks, and to perform the acceptance tests for the 18 TF coils of the Tokamak JT-60SA before their delivery to Japan, the European Joint Undertaking for ITER, Fusion for Energy (F4E), and the European voluntary contributors have collaborated to design and set up the so-called Cold Test Facility (CTF) at CEA Saclay. The CTF is designed to test one coil at a time at nominal current of 25.7 kA and at cryogenic temperature cooled with supercritical helium between 5 K and 7.5 K to check the temperature margin against quench scenario.

Fig. 2.1 gives a panorama of the entire CTF with the key components indicated in white arrows. From left to right, we can see that:

- A helium refrigerator which includes compressor, oil removal system and cold box can provide a maximal refrigerating power of 500 W at 5 K. This refrigerator allows to cool the helium temperature from 300 K to 8 K then to liquefy the gas helium (GHe) to around 4.5 K. A helium mass flow rate of around 34 g/s can be provided by this refrigerator to cool the tested coil.
- A set of cryogenic transfer lines interconnect the helium refrigerator, the valve box and the cryostat.
- The valve box is equipped with liquid nitrogen (LN2) thermal shield at 80 K. All cryogenic components for helium distribution are integrated in this 2 m diameter valve box, including the valves, the two safety valves, the helium pump, the liquid helium tank, the superconducting

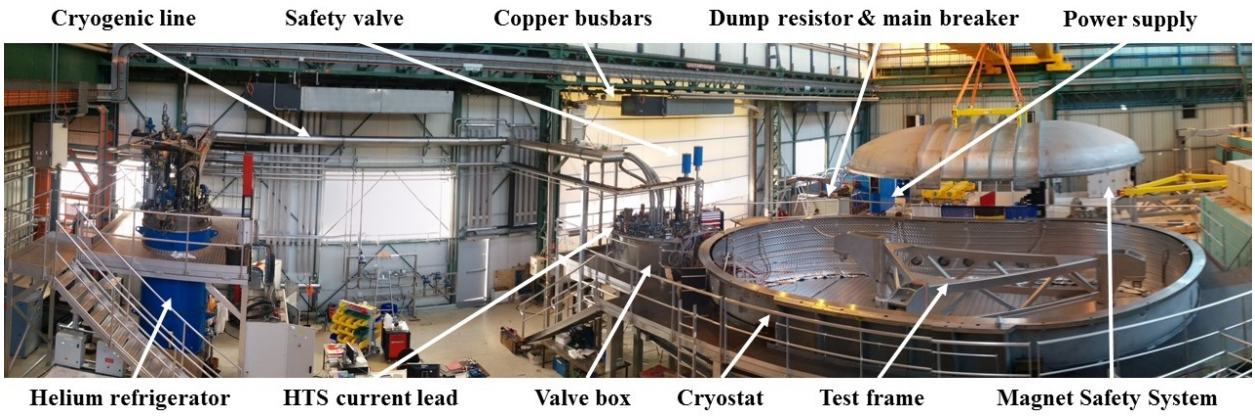

Figure 2.1 – Panorama photo of the Cold Test Facility

feeders, the heat exchangers, the two High Temperature Superconducting (HTS) current leads and the heaters.

- The two current leads of the facility are manufactured with HTS AgAuMg/Bi-2223 stacks[82] and need to be cooled with 3.6 g/s of 50 K GHe each during operation at 25.7 kA.
- The two safety valves are opened when the helium pressure overpasses 20 bar during the quench test.
- The valve box and the cryostat are connected by a bellow that compensates the ±2 mm of deformation of the cryostat under vacuum[83].
- The 11.5 m × 6.5 m large cryostat is also equipped with integrated LN2 thermal shield at 80 K. It is connected to vacuum pumps, vacuum instrumentation and leak detection equipment, making the inside TF coil thermally insulated by vacuum. The cryostat actually has a common vacuum with the valve box. The vacuum system will allow to reach around 10^{-5} mbar for the coils cryogenic tests[84].
- The cryogenic test frame in the cryostat is used for fixing the TF coil inside the cryostat and is actively cooled by LN2 at 80 K to minimize the heat conduction to the coil.
- The blue cabinet is the power supply[83] used to energize the coil at its nominal current of 25.7 kA with a stability of 10^{-4} during 8 h. A DC voltage of 10.8 V is also provided in the power supply allowing to ramp down and ramp up the current up to 200 A/s. The current passed through the water-cooled copper busbars, the HTS current leads and then goes to the tested coil through the superconducting feeders.
- The upright grey cabinet is the Magnet Safety System (MSS) allowing to protect the coil by opening the circuit and discharging the magnetic stored energy on the dump resistor during a quench. The main breaker is composed of 6 parallel poles of 5 kA allowing to open in only 100 ms if a major defect is detected by the MSS.
- The fast data acquisition system of the CTF then allows to obtain the experimental data during the quench propagation in the TF coils and to study their quench behaviour.

After obtaining an overview of the key components in CTF, we then focus on the most important part, the tested TF coils, to give a more detailed description. Fig. 2.2 shows the position of the single coil test configuration inside the CTF cryostat. The TF coil is fixed by the test frame with three hooks in G10 material. At the bottom of Fig. 2.2, we can see that the coil has been connected both hydraulically and electrically to the valve box (which locates outside the Fig. 2.2). Finally, we can also see a red circle wire which is stuck to the the coil casing. It is actually an important

[82] R. Wesche. *IEEE Transactions on Applied Superconductivity* **24**. 2014.
[83] Walid Abdel Maksoud et al. *Fusion Engineering and Design* **96-97**. 208–211. 2015.
[84] M. Chantant et al. *Fusion Engineering and Design* **86**. 561–564. 2011.

instrumentation that allows to obtain the inductive voltage measurements produced in this closed circuit during a magnetic field variation, e.g. during the current discharge in case of quench. This wire is called *pick-up coil*. We will discuss in more details for its application in the data processing method in Section 3.1.1.

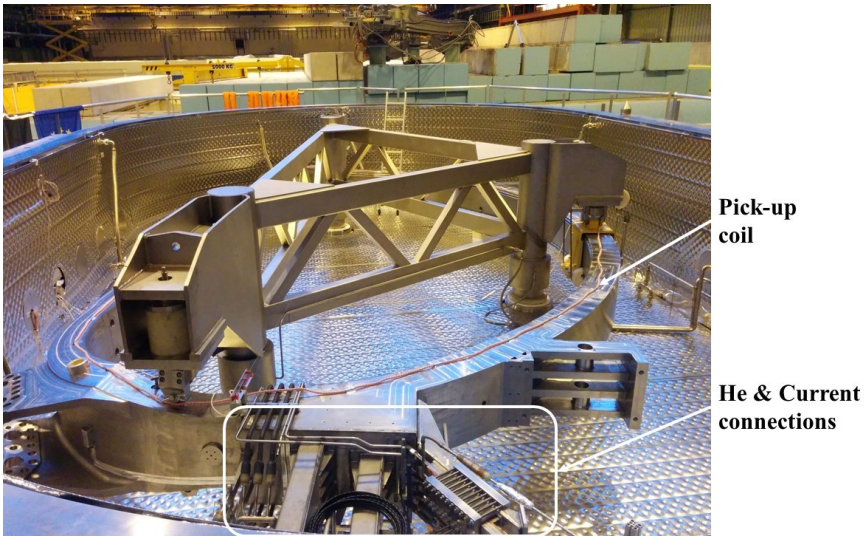

Figure 2.2 – Photo of the TF coil in the cryostat

2.1.2 Characteristics of the superconducting TF coil for JT-60SA

Based on the general presentation of the TF coils characteristics in Section 1.1.2, a more detailed description will be given in this section. Fig. 2.3a shows a 3D top view of the JT-60SA TF coil. We recall that the D-shaped TF coil is approximately 7.5 m long, 4.5 m wide and 16.5 t in weight. On one side of the coil curved leg, all the helium and electrical connecting joints are located. Fig. 2.3b shows the details about the helium outlet piping (dark blue tubes) exiting from the 5 twin boxes and the 2 feeder joints. The 7 tubes are then electrically insulated with breakers before combining into a principal outlet to go out towards the valve box. The helium inlet piping has only been partially presented in white tubes as well as their principal outlet partially presented by orange tube. The yellow tubes are the helium circulations for cooling the casing. Finally, the electrical connecting joints are actually hidden in the 5 twin boxes but have been presented in the 2 feeder joints (orange-grey branches). Regarding the TF coils hydraulic and electric connections as well as their corresponding instrumentation, more detail will be presented in the following Section 2.2.

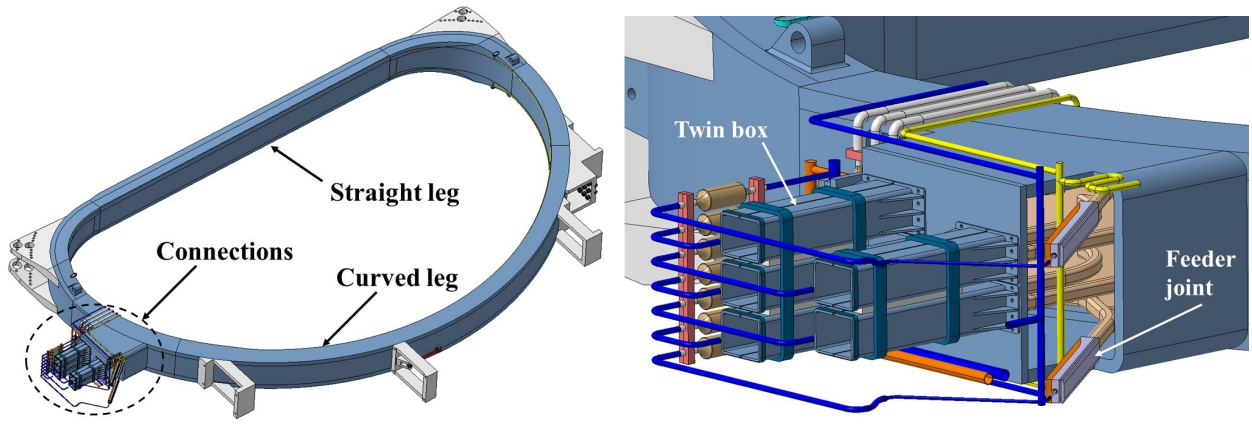

(a) General view of TF coil

(b) Detailed view of coil connection

Figure 2.3 – 3D view of the TF coil

Now, we are giving a further description of the main design characteristics of the JT-60SA TF coils. As we already know, each TF coil is composed of two major parts, Winding Pack (WP) and casing. The WP is composed of 6 Cable-In-Conduit Conductor (CICC) lengths, wound in 6 Double-Pancakes (DPs). Each DP consists of two adjacent pancakes wound in 6 turns along two opposite directions, clockwise (CK) and anticlockwise (ACK). In total, there are 12 single pancakes stacked in the WP, with each one in a total length of 113.277 m. The 12×6 CICCs cross-sections can thus be presented in Fig. 2.4a. The CICC in each pancake is impregnated with a 1 mm thick epoxy fibreglass G10 material, making the CICCs always separated by a 2 mm thick insulator. The whole WP is then wrapped in a ground insulation and impregnated with G10 material to form a thickness of around 9 mm insulated from the casing. And the casing itself is manufactured with non-magnetic stainless steel material.

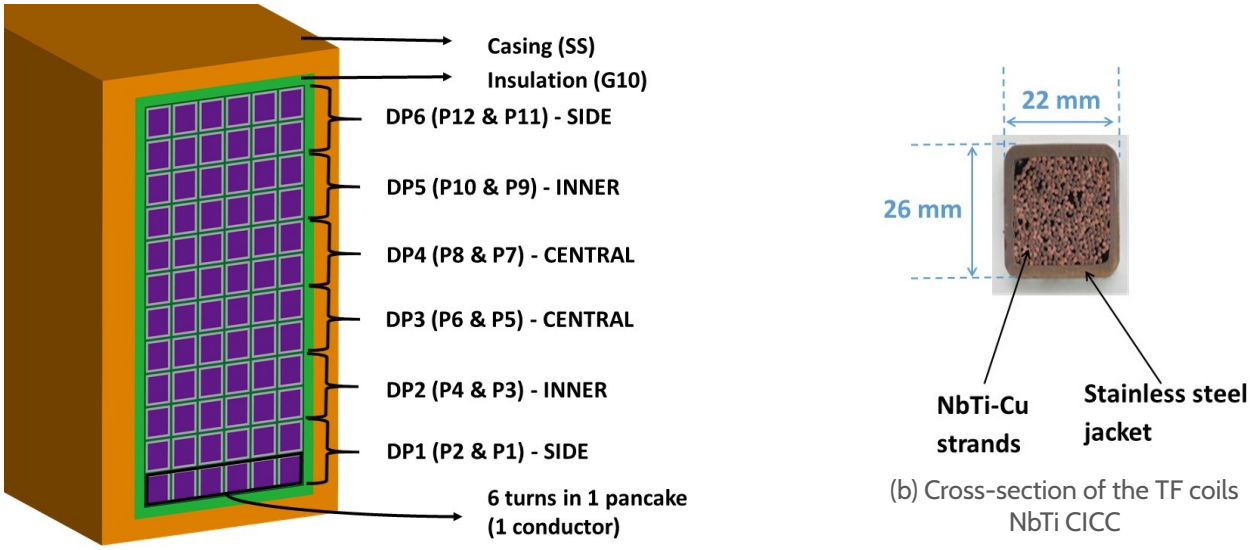

(a) Cross-section of the TF coil with the pancakes classification

(b) Cross-section of the TF coils NbTi CICC

Figure 2.4 – Design characteristics of the JT-60SA TF coils

In order to achieve all the necessary experimental measurements and hence facilitate the further study of the coil quench behaviour, we need to enumerate the 12 pancakes from the bottom one (P1) to the top one (P12), as presented in Fig. 2.4a. Knowing that each two adjacent pancakes (e.g. P1 and P2) are manufactured with a same CICC but wound in two opposite directions, we then divide the 12 pancakes into 6 DPs with their corresponding number, from the bottom one (DP1) to the top one (DP6). Moreover, one need to know that the majority of the phenomena during a quench will be strongly dependent on the coil geometric symmetry. We then classify the 6 DPs into 3 symmetrical types, with the two upper and lower DPs named SIDE pancakes, the relatively inside DPs named INNER pancakes and the two middle DPs named CENTRAL pancakes, as indicated in Fig. 2.4a. We also recall that each elementary rectangle in Fig. 2.4a represents the cross-section of a NbTi CICC, as presented by Fig. 2.4b. The JT-60SA TF coils are manufactured with these CICCs. The external dimension of the CICC is 22 mm $\times$ 26 mm including the 2 mm thick Stainless Steel jacket and the 32 % of void fraction[49]. The highly pressurized helium can then be circulated in the CICC and cool the conductor by forced flow convection. More details about the CICC dimension can be found below in Table 2.1.

The JT-60SA TF coils work at a nominal current of 25.7 kA at 5 K and reach their quench at around 7.5 K which is determined experimentally during the test. Such nominal current can actually reach a peak value of the coil self-field around 3.19 T in the central pancake (P8). This peak field has been estimated at the High Field Side (HFS) of the CICC cross-section which is the closest position

[49] P. Decool et al. *IEEE Transactions on Applied Superconductivity* **26**. 2016.

to the coil center[45,85], as presented in Fig. 2.5. In order to carry out the following quench studies in Chapters 3 and 4, we choose to apply an equivalent uniform magnetic field, as presented with the middle point (MID) in Fig. 2.5. This field value allows to give the same electric field of 10 mV/m[45] computed on the cable cross-section by taking into account the transversal magnetic field gradient. And it also allows to cover the majority of the conductor performance.

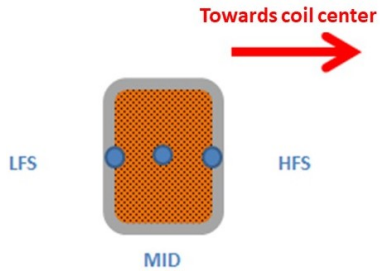

Figure 2.5 – Schematic illustration of the magnetic field computation at different points of the CICC

Fig. 2.6a shows the "average-performance" magnetic field map that will be applied in the rest of this PhD report[85]. Three representative positions of pancakes have been plotted, including the central pancake P8 (DP4) in blue line, the inner pancake P10 (DP5) in yellow line and the side pancake P12 (DP6) in red line. Indeed, the TF coil symmetric property allow to give the similar field map in DP1 and DP6, DP2 and DP5 or in DP3 and DP4. Moreover, the manufacture of adjacent pancakes with a same CICC also allows to reduce the representative double-pancake field maps to only one of the adjacent pancakes, e.g. P8 in DP4. Nevertheless, it is to note that these pancakes are all anti-clockwise ones with the peak field region closer to the coils inlet, thus easier to be quenched.

We can see in Fig. 2.6a that from the side pancake to the central one, the field map is getting less and less uniform. In particular, the central pancake P8 is showing a "V-shaped" field map where a certain length (from 55 m to 75 m) has an even lower field intensity (below 1 T) which is less than 1/3 of the peak field. When taking a zoom view on the pancakes first turn ($0 - 18.88$ m) in Fig. 2.6b, the peak field value always appears in the central pancake P8 of around 3.04 T, as already applied in Chapter 1. Moreover, there exists nearly two peak field locations at 2.7 m and 9.3 m. This will have a direct impact on the quench initiation and propagation dynamics since the current sharing temperature (T_{cs}) is decreasing as the magnetic field increases thus easier to quench the coils inlet (see Section 1.2.1).

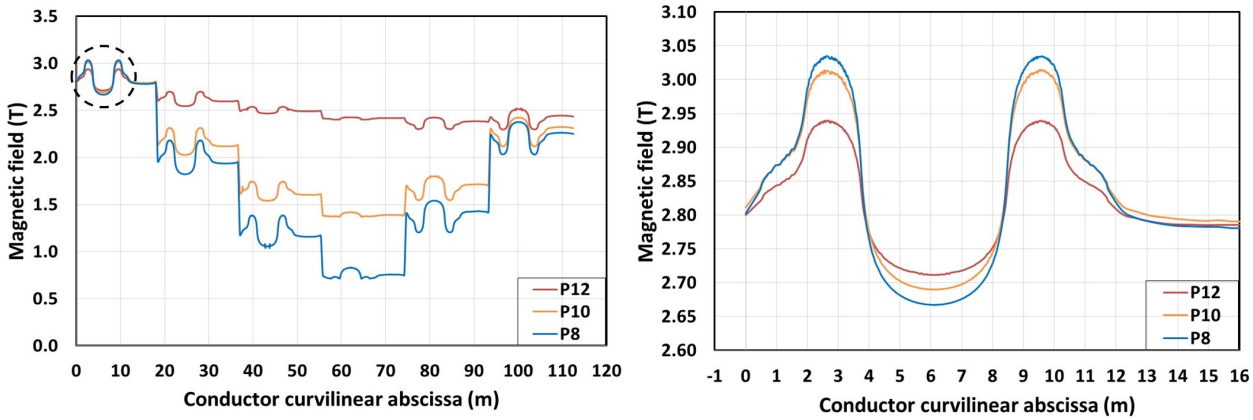

(a) General view

(b) Detailed view

Figure 2.6 – Spatial magnetic field map in the coil

For more details, the main characteristics of the JT-60SA TF coil have been resumed in Table 2.1.

[45] A. Torre. *Internal report.* 2015.

[85] D. Ciazynski et al. *Fusion Engineering and Design* **124**. 169–172. 2017.

One can refer to this table for the following study of the TF coils quench behaviours in case of need.

Table 2.1 – Principal characteristics of the JT-60SA TF coil

Characteristic	**Symbol**	**Value & Unit**
Peak field in the TF system (Tokamak)	$B_{max}(Tokamak)$	**5.65 T**
Peak field in the CTF conditions (MID)[1]	B_{max}	**3.04 T**
Nominal current	I_n	**25.7 kA**
Nominal temperature	T_n	**4.7 K**
Single coil self-inductance	L_{coil}	**62 mH**
Current sharing temperature[2]	T_{cs}	**7.42 K**
Quench temperature[3]	T_q	**7.50 K**
Hot spot temperature in CTF conditions[4]	T_{hs}	**37 K**
Critical current density[5]	j_c	**3793 A/mm²**
Operating current density	j_{op}	**452 A/mm²**
Stored magnetic energy in CTF conditions	$E_m(coil)$	**20.5 MJ**
Coil dimension	$L \times w$	**7.5 m × 4.5 m**
Coil weight	m_{coil}	**16.5 t**
CICC dimension (including jacket)	$L \times w$	**26 mm × 22 mm**
Void fraction in CICC	η	**32 %**
Stainless steel jacket thickness	e_{jacket}	**2 mm**
Stainless steel wrappings thickness	$e_{wrappings}$	**0.1 mm**
NbTi section	S_{NbTi}	**56.8 mm²**
Cu section	S_{Cu}	**180 mm²**
He section	S_{He}	**123 mm²**
SS Jacket section	S_{Jacket}	**176 mm²**
Wrappings section	$S_{wrappings}$	**15 mm²**
Strand diameter	D_{st}	**0.81 mm**
NbTi strand number	n_{NbTi}	**324**
Cu strand number	n_{Cu}	**162**
Pancake number	$n_{pancake}$	**12**
Pancake length	$L_{pancake}$	**113.277 m**

[1] To note: HFS peak field estimated to 3.19 T
[2] Computed with the peak field of $B_{max} = 3.04$ T
[3] Average value determined experimentally during the quench tests in the CTF (see Table 2.3)
[4] Numerical result computed by THEA
[5] Computed at nominal conditions

2.2 Instrumentation of the Cold Test Facility

In order to obtain the maximum information during the TF coils quench tests and to carry out the further quench behaviour studies, a set of electric and cryogenic measuring instrumentation has been installed in the CTF with their key components presented in the scheme Fig. 2.7. Generally, the red lines represent the electric system whereas the blue lines are for helium flow circulation of the TF coil.

Fig. 2.7 shows that the helium comes from an inlet helium valve then passes through the principal inlet tube before entering into the coil. When approaching the inlet of the coil, the helium flow is firstly separated into 6 branches corresponding to 6 DPs then continues to be divided into 2 sub-branches for each DP to circulate in parallel in the 12 single pancakes from the inlet to the outlet. The average mass flow rate in each pancake is around 2 g/s. Two types of pancakes outlet can be revealed. In the two side pancakes P1 and P12, their helium outlet flow will pass through the feeder joint then directly combine into the principal outlet tube. Regarding the other ones (P2 ∽ P11), the helium in the two adjacent pancakes will firstly combine into a same flow of around 4 g/s via the electric and hydraulic junction called "twin box" (see Fig. 2.3b), then flows out to the

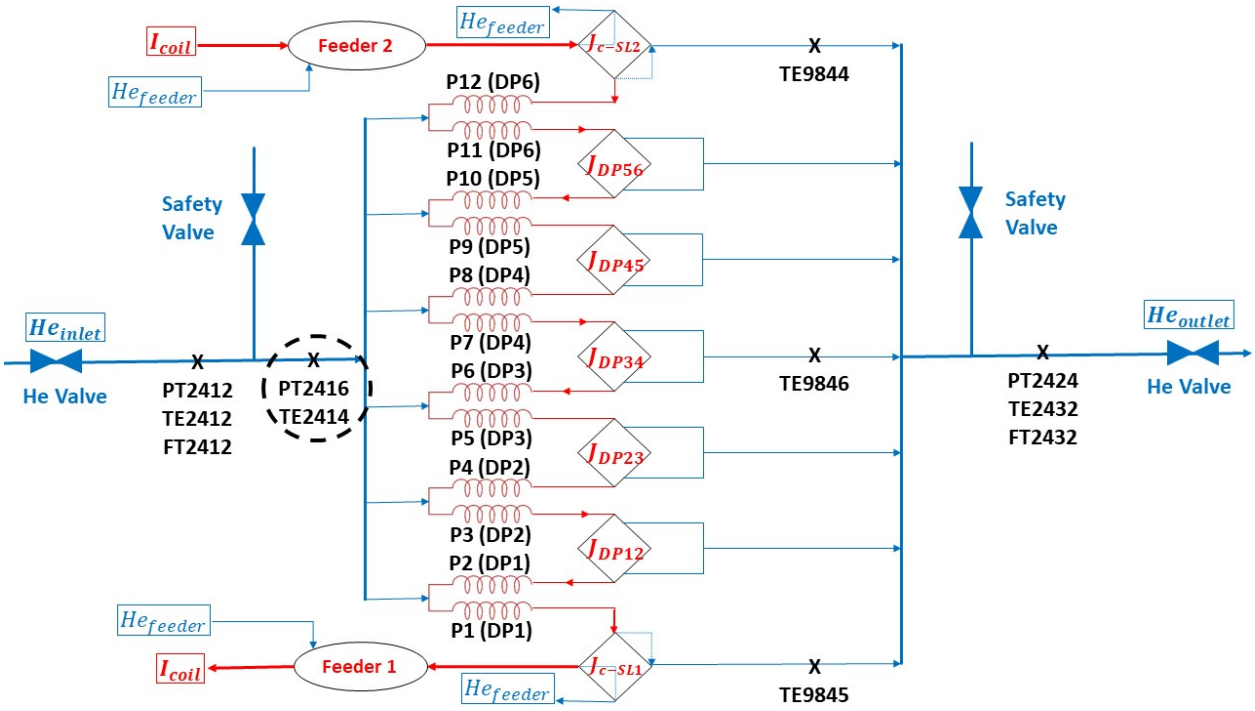

Figure 2.7 – Schematic of the electric and cryogenic instrumentation for the TF coil (PT=pressure transmitter, TE=temperature transmitter, FT=mass flow rate transmitter,J_{DP}=inter-pancake joint and J_{c-SL}=joint connecting coil and superconducting feeder)

principal outlet tube and mix with all the pancakes outflow. The total helium flow of 24 g/s then passes through the outlet helium valve to return to the helium refrigerator.

Fig. 2.7 also shows that at the inlet and outlet of the tested coil, the helium pressures, temperatures and mass flow rates can be measured with the CTF cryogenic instrumentation. In general, the measuring instrumentation is only installed in the principal tube locating in the valve box since the TF coil could not undergo any hardware modifications during the quench test. We can see that the inlet helium instrumentation, PT2412, TE2412 and FT2412, are located outside the dividing position where the safety valve branch and helium valve branch are connected (the same for outlet). Indeed, when the quench is detected in the coil, both the inlet and outlet helium valves will be closed so that no helium flow can be injected from this moment. In parallel, the helium heated near the quench location will be expelled out of the coil and then evacuated through the safety valve branch. Thereby, the general inlet instrumentation installed in the helium valve branch will no longer be able to give the correct measurements due to the stop of the helium flow in this branch. A closer measuring point, i.e. before the branch separation towards the safety valve, will be more helpful to acquire the helium temperature and pressure information during the quench. This is why we have installed the transmitters PT2416 and TE2414 that are situated around 5 m away from the coil inlet, as presented in black dashed circle in Fig. 2.7. Based on the same objective of obtaining the complete helium outlet temperatures, three more sensors have been installed at the pancakes outlet, including the transmitters TE9844 and TE9845 for the two side pancakes as well as TE9846 for the central pancakes combined outflow. These sensors (Cernox Bare Chip[86]) are simply glued on the surface of the outlet tubes, thus can only give an order of magnitude of the helium temperature which is however not accurate enough for analysis. These measurements will indicate for example the arrival of the heat front at the pancake outlet thanks to an abrupt temperature rise.

To summarize, the cryogenic transmitters with the helium measurements directly used for the following analysis are listed in Table 2.2 as well as their corresponding helium parameters. It is to note that TE2414 and PT2416 are the closest helium measurements to the coil in the whole

[86] LakeShore Cryotronics. *Website*. 2018.

instrumentation system and will thus be taken as referenced helium temperature and pressure for the further analyses.

Table 2.2 – Cryogenic measuring transmitters correspondence

Parameter	**Transmitter**	**Comment**
T_{in}	TE2414	closer to the coil than TE2412
T_{out}	TE2432	
P_{in}	PT2416	closer to the coil than PT2412
P_{out}	PT2424	
$\dot{m}_{in}$	FT2412	
$\dot{m}_{out}$	FT2432	

Concerning the electrical circuit system, the coil is energized with the nominal DC current of 25.7 kA. Fig. 2.7 shows that the current (red lines) is connected from one superconducting feeder (Feeder 2), then passes in series through the 12 pancakes (P1 $\backsim$ P12) and their inter-pancake joints ($J_{DP12} \backsim J_{DP56}$) up to exit from another superconducting feeder (Feeder 1). The joint index actually represents the electrical connection between the two corresponding double-pancakes, e.g. J_{DP12} is the joint connecting DP1 and DP2. Thanks to the CTF instrumentation, we can have access to the coil current, the voltage of the 6 DPs, the voltage of the inter-pancake joints as well as the voltage on the superconducting feeders. These measurements will allow to make the analysis on the coils quench behaviour. One last thing to note from this schematic diagram is that the two feeders, as manufactured with the same superconducting cable to the TF coils, are cooled with a separate helium circulation with almost the same helium condition of around 5 K.

In the following text, we will give a more detailed description about the CTF instrumentation for measuring voltages, helium temperatures, pressures and mass flow rates.

2.2.1 Voltage measurement

As introduced above, the CTF instrumentation allows to obtain the voltage measurements of the 6 double-pancakes (Vb1 $\backsim$ Vb6), the 5 inter-pancake joints (Jb1 $\backsim$ Jb5), the 2 superconducting feeders (LS1 & LS2) as well as the total voltage (Vbt) of the entire winding pack, as presented in Fig. 2.8. All these signals are continuously sent to the fast acquisition system called AS-Net, with a frequency generally fixed to 1 kHz as well as to 10 kHz during the 80 s quench. Nevertheless, the joints voltage is only accessible for the French coils due to the AS-Net coordination in the CTF. These accurate and precise voltage measurements will allow to carry out the detailed study of the TF coils quench behaviour.

It is to note that the measured voltage of each DP is the sum of the inductive voltage in a solenoid circuit and the resistive voltage due to a quench, as written in Eq. (2.1):

$$U(t) = L\frac{dI(t)}{dt} + I(t) \cdot R(t) \tag{2.1}$$

where U is the voltage of the DP, L the global inductance of the DP including the self-inductance and the mutual one, I the coil current, R the normal resistance of the DP in case of quench and the time t.

We take one of the double-pancakes DP1 to give an explanation of the voltage measurement. Fig. 2.9 shows the DP1 voltage evolution during a quench test (red line). A very abrupt decrease to around -28 V can be observed near the start of the current discharge ($t = 0$ s), followed by a progressive increase tending to 0 V. The first large negative voltage can be explained by the fact that the fast discharge of the current when opening the circuit leads to a large negative value in the inductive voltage (LdI/dt). As the current discharge slope is getting lower along the time, a less and less

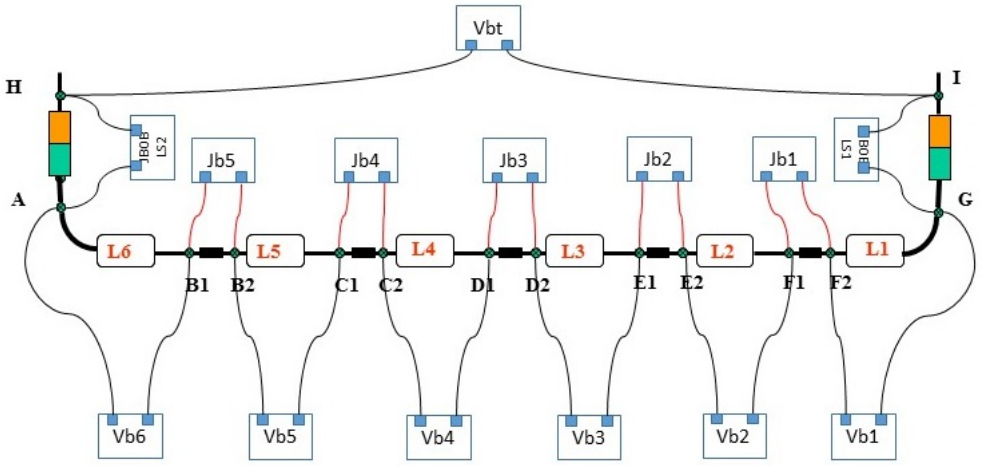

Figure 2.8 – Voltage measurements for TF coil

negative value will then appear in the inductive voltage during the current discharge. Moreover, this negative voltage also contains a positive part which corresponds to the increase of the normal zone resistive voltage as well as the heating effect by this resistance. However, as this resistive voltage is much lower than the inductive one, it does not change the voltage sign but only induces some visible change of slope like around 3 s in Fig. 2.9.

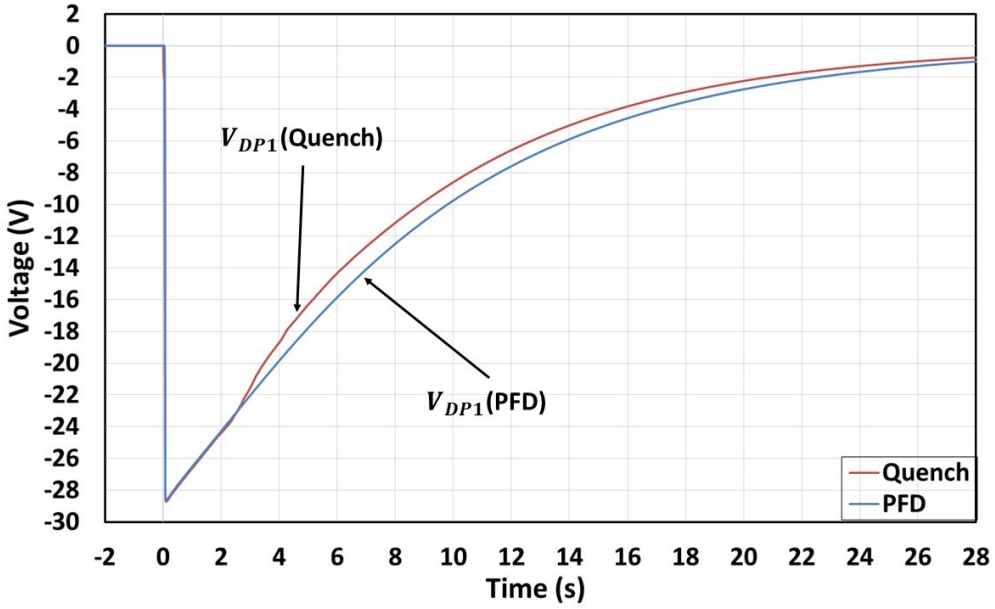

Figure 2.9 – Voltage measurements of DP1 during a quench test and a Pure Fast Discharge

One must note that another DP1 voltage evolution has also been plotted in the same Fig. 2.9, corresponding to a so-called Pure Fast Discharge (PFD) test (blue line). It is a test at nominal conditions around 25.7 kA and 5 K, during which a current fast discharge has been triggered manually without forming any quench in the coil. The objective was to verify the coils insulation characteristics and their cryomagnetic performance during a current fast discharge. Indeed, among the 18 tested TF coils, two of them have been realized with this PFD test, including TFC10 and TFC01. They are actually the two first TF coils respectively manufactured by France and Italy.

Fig. 2.9 shows a more uniform evolution of the DP1 voltage during the PFD test (blue line) than the one during a quench test (red line), since no evident slope change can be revealed in the PFD test. Indeed, as the PFD test has no quench propagation during the current discharge, the voltage measurements correspond to a purely inductive voltage only depending on the current variation. Thus a continuous evolution can be observed in the PFD voltage.

As the voltage measurements only give the sum value of the inductive and resistive part, an appropriate data processing method will then be needed to deduce the quench resistive voltage as well as the quench resistance before carrying out the quench behaviour study. In Chapter 3, several approaches will be discussed to find the most appropriate way of quench data processing based on the PFD test measurements.

2.2.2 Temperature measurement

As introduced above, the temperature sensors (TE2412, TE2414 and TE2432) installed for the principal inlet and outlet temperatures are all Cernox^{TM} 1050 sensors with the packaging option of Copper canister, noted as CX-AA. The canister here represents the small measuring package size leading to a more convenient mounting element in the experiments. Fig. 2.10 shows the diameter of the gold-plated cylindrical copper canister to around 3 mm. The calibrated CX-1050 works from 1.4 K to 325 K with the standard helium fluid. Moreover, this sensor has a good sensibility at low temperature (with an accuracy of ±5 mK at 5 K) thanks to its sensible resistance variation at low temperature as well as an appropriate thermal response time around 0.4 s[86] which is considered precise enough in front of the temperature evolution time during the TF coils quench test around several tens of minutes.

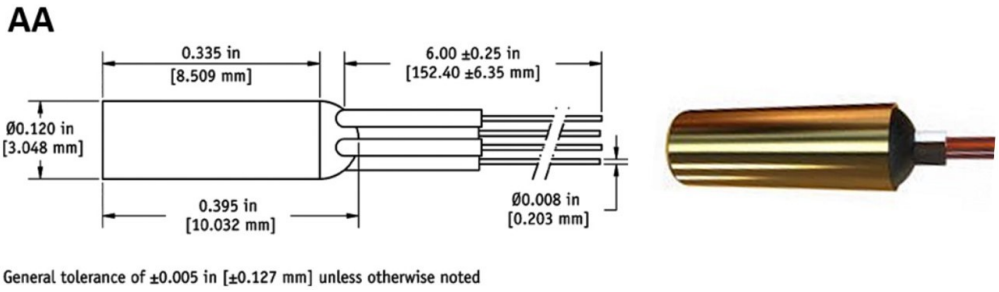

Figure 2.10 – Schematic diagram of the CX-AA sensor with a reference photo on the right

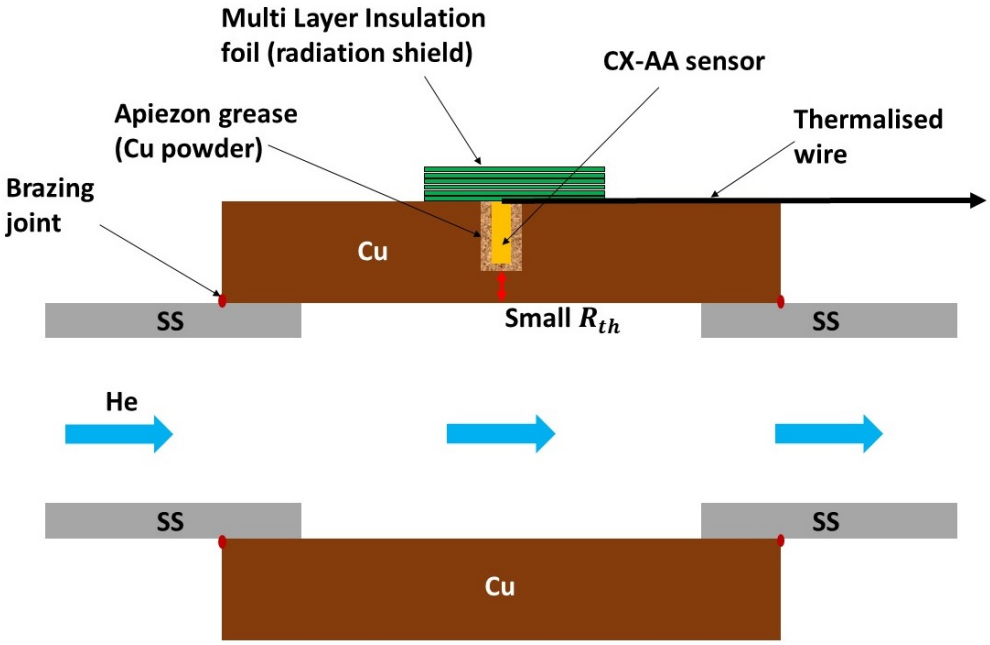

Figure 2.11 – Schematic diagram of the installed position for the CX-AA sensors when measuring the helium temperature

[86] LakeShore Cryotronics. *Website*. 2018.

These CX-AA sensors have been installed by inserting in a segment of copper block which is in direct contact with the helium, as presented in Fig. 2.11. In order to reinforce the thermal contact between sensor and copper block as much as possible, the Apiezon grease material mixed with copper powder has been filled in the hole where the sensor is installed. Like that, the high thermal conductivity in copper allows the sensor to provide accurate measurements of helium temperature for the analysis (with small thermal resistance, R_{th}, between sensor and fluid interface). In addition, the Multi Layer Insulation (MLI) foil is also covered on the sensor as the radiation shield. The wires are thermalised at the fluid temperature by being stuck directly on the helium tube through the aluminium tapes. All these preparations are done to achieve measurements at a high accuracy.

Another advantage of the CX-AA sensor is the low sensibility to the magnetic field. According to the manufacturer, this sensor can be used with magnetic fields up to 30 T for temperatures greater than 2 K. This can be verified with the magnetic field-dependent temperature deviations as a function of magnetic field in Fig. 2.12. We can see that for a temperature of 5K and magnetic field of 2.5T, the temperature deviation $\Delta T/T$ is about 0.1 %, i.e. 5mK.

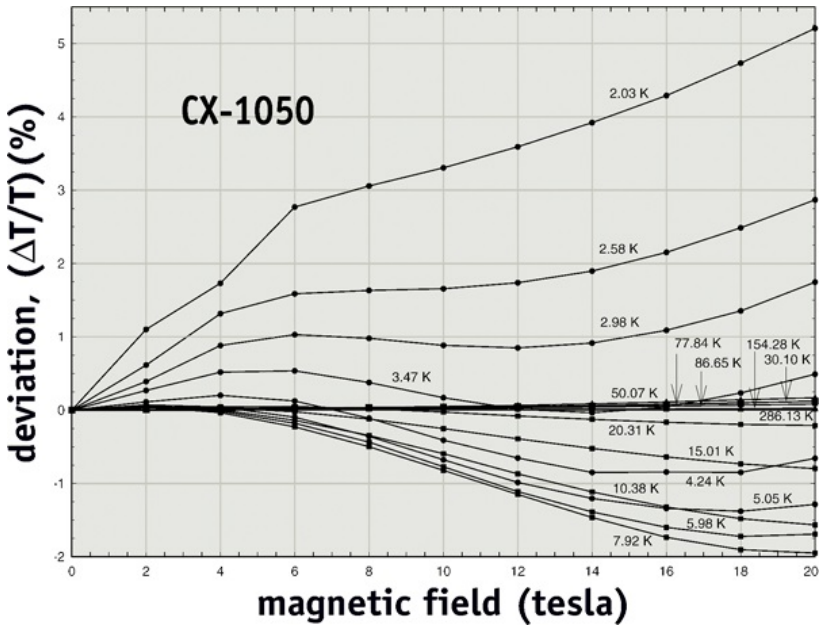

Figure 2.12 – Typical temperature errors as a function magnetic field B for the sensor Cernox 1050

If we sum up the uncertainties coming from the sensors calibration, the magnetic field deviation and the precision limit of the data acquisition system in CTF, the final accuracy of Cernox sensors used in the TF coils quench tests is determined to around 20 mK at 5 K and 0.5 K at 300 K.

2.2.3 Pressure measurement

According to Fig. 2.7, we know that there are two types of pressure measurements, absolute pressure transmitters (e.g. PT2412, PT2416 and PT2424) and differential pressure transmitters (PDT) used for measuring the pressure difference between inlet and outlet of the circulator or for venturi mass flow measurements (e.g. FT2412, FT2432). They are all from the Yokogawa brand relying on digital DPharp sensor technology to get accurate and reliable readings quickly[87], as presented in Fig. 2.13.

DPharp digital sensor uses two single crystal silicon resonators vibrating at their natural frequencies. When pressure is applied, one of the resonators goes into tension, while the other goes into compression mode. The CPU directly counts the sensor output frequencies without any additional

[87] Yokogawa Electric Corp. *Website*. 2018.

Figure 2.13 – Photo of the Yokogawa pressure transmitters

A/D conversion. Due to the excellent elastic properties of silicon material, the DPharp sensor exhibits great linearity and repeatability, with no inherent hysteresis. Resonant sensor also provides a large output signal resulting in greater sensitivity and higher turndown.

According to the manufacturer data, the Yokogawa absolute PTs carry out the relative measures to perfect vacuum pressure (absolute zero pressure) so that they are not affected by fluctuations in the local atmospheric pressure. All absolute pressure measurements are positive under a maximum working pressure of 35 bar. The advantage is that they have a high accuracy of $\pm 0.075\,\%$ as well as a short measuring response time of 90 ms allowing to acquire precise data. Moreover, a good stability of $0.2\,\%$ per 15 years also ensures the measurements accuracy.

2.2.4 Mass flow rate measurement

The two signals for measuring the inlet and outlet helium mass flow rate are FT2412 and FT2432. Here used two venturi flow meters to perform the measurements. Fig. 2.14 shows the sketch of a venturi meter, with a section change from the pipe D to the throat d, as well as the two pressure measuring points, P_1 and P_2. Here also used the Yokogawa differential pressure transmitters (PDT). They measure the difference between P_1 and P_2, with the reference point called low-side pressure and the high-side pressure to make the comparisons. The PDT reading can be either negative or positive depending on whether the low-side or high-side is the larger value. A mass flow accuracy of $3\,\%$ can be obtained for the PDT-based venturi.

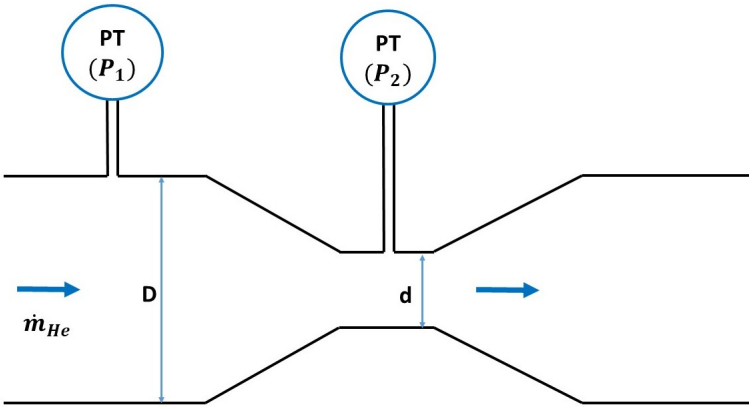

Figure 2.14 – Principle of the venturi flow meters for measuring mass flow rate

According to the Bernoulli Equation and the volumetric flow rate expression, we can obtain the mass flow rate ($\dot{m}_{He}$) as a function of the pressure drop (ΔP) between pipe and throat in the

compressible flow conditions[88], as written in Eq. (2.2):

$$\dot{m}_{He} = \frac{C}{\sqrt{1-\beta^4}}\,\epsilon\,\frac{\pi}{4}\,d^2\,\sqrt{2\rho\Delta P} \tag{2.2}$$

where C is the discharge coefficient that takes into account the slight difference between the real mass flow rate and the theoretical one for incompressible fluid due to the small pressure loss in the reality. This coefficient has been determined by warm and cold calibration tests in CTF to $C_{inlet} = 0.989$ and $C_{outlet} = 0.994$[88]. β is the diameter ratio between the pipe $D = 22.9\,\text{mm}$ and the throat $d = 7.0\,\text{mm}$, expressed as d/D. ρ is the fluid mass density. ΔP is the differential pressure expressed as $\Delta P = P_1 - P_2$ and ϵ the expansion coefficient taking into account the compressibility of the fluid[89] as expressed in Eq. (2.3):

$$\epsilon = \sqrt{\left(\frac{\gamma\tau^{\frac{2}{\gamma}}}{\gamma-1}\right)\left(\frac{1-\tau^{\frac{\gamma-1}{\gamma}}}{1-\tau}\right)\left(\frac{1-\beta^4}{1-\beta^4\,\tau^{\frac{2}{\gamma}}}\right)} \tag{2.3}$$

where τ is the pressure ratio defined as P_2/P_1, and γ the isentropic exponent. Eq. (2.3) is actually based on an isentropic expansion assumption. This is due to the fact that when the pressure changes very quickly from P_1 to P_2 on passing through the venturi contraction, no heat transfer occurs and no work is done by or on the fluid making the expansion isentropic[89]. A value of $\epsilon = 0.9987$ can be obtained for the calibration testing conditions (5 K and 4.3 bar). Finally, the total winding mass flow rate of the helium is measured to around 24 g/s with an accuracy obtained by Yokogawa PDT of around 3 %.

2.3 Experimental protocol of the quench test for the TF coils

In the following sections, three principal steps will be presented for explaining the experimental protocol of setting up a quench test in the TF coil. The first step is to energize the coil at nominal conditions with a "multi-stairs" mode, as presented in Fig. 2.15. The helium flow always maintains a steady state during this phase. The second step starts at around $t = -1650\,\text{s}$ in Fig. 2.15. A progressive increase in the inlet and outlet helium temperatures have been achieved before reaching the quench. This phase is called the temperature-increasing phase, with the helium flow staying at a slow transient state. Finally, when the quench is triggered at $t = 0\,\text{s}$, a current Fast Discharge (FD) will be carried out during about 30 s leading to a fast transient state in the helium flow. More details will be explained step by step below.

2.3.1 Steady state at nominal conditions

The first step of the experimental protocol is to reach a stable cryogenic system at nominal conditions of around 4.7 K at the inlet (red line) and around 5.4 K at the outlet (blue line), as presented in Fig. 2.16. When achieving this stability at around $t = -4900\,\text{s}$, the current will be increased to a first plateau of 10 kA with the time needed of about 100 s under an increasing ramp of 100 A/s. Then we wait for about 5 min for the helium cryogenic system to again stabilize (shown on the outlet temperature). Actually, when the current increases in the coil, a heat load increase will be produced due to eddy currents in the casing and between the superconducting strands (hysteresis) and due to resistive connecting joints. This explains the slight helium temperature rise at the outlet. After achieving this first current plateau, a second current increase is then realized with the same ramp up to 15 kA followed by a certain waiting for the cryogenic stability. The same approaches are repeated to reach the third current plateau of 20 kA and finally to reach the nominal current

[88] A. Serrand, W. Abdel Maksoud, and L. Genini. *Internal report.* 2013.
[89] Michael J. Reader-Harris. *Thermopedia.* 2011.

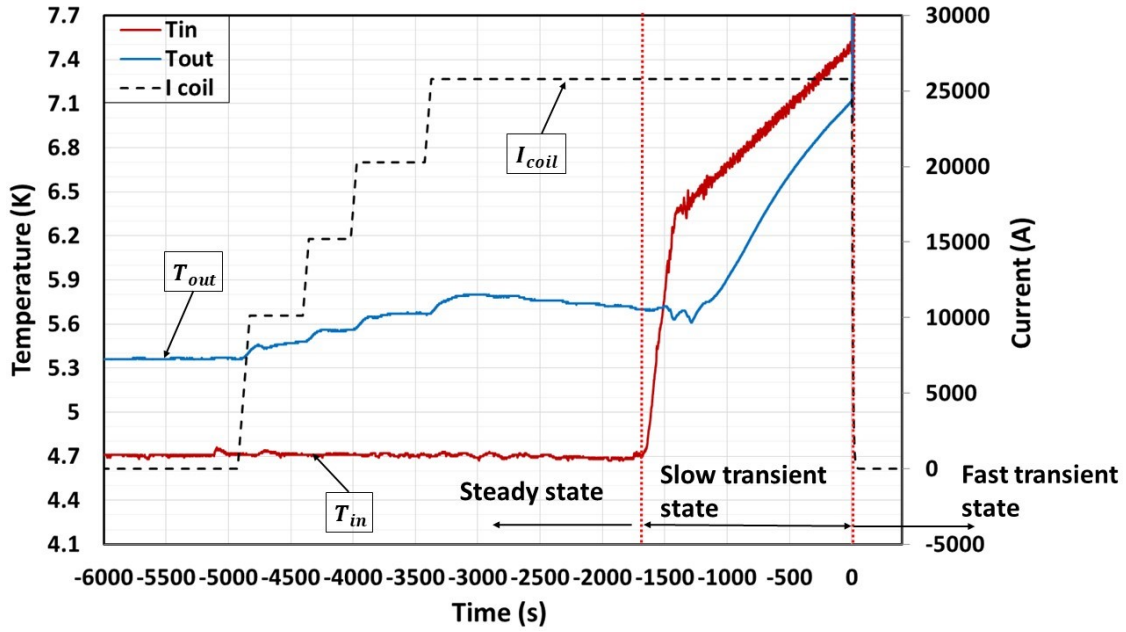

Figure 2.15 – Temperature and current evolution during the whole quench test of the TF coils

of 25.7 kA. Such current increase mode with 100 A/s ramp up and several plateaus is to avoid the overheat in the current leads that may also cause a resistive voltage rise up to critical value and triggering the MSS.

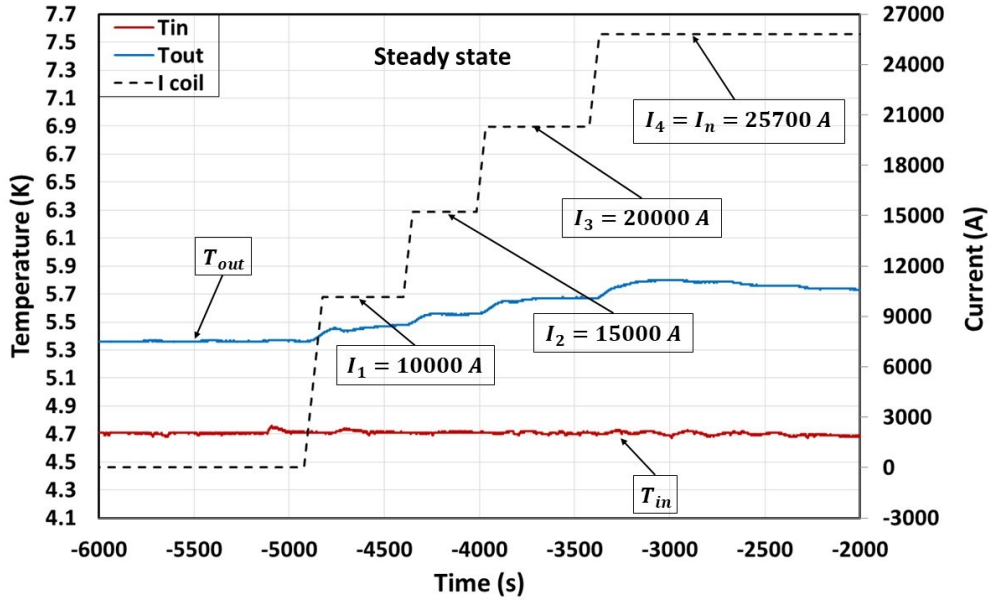

Figure 2.16 – Temperature and current evolution during the helium steady state

One can see that before energizing the coil at around $t = -4900$ s, the helium flow allows a constant temperature difference of around 0.7 K between the inlet and the outlet due to the external heat load deposited on the winding pack (e.g. from casing). The same steady state has again been achieved after reaching the nominal current at around $t = -3000$ s, with a higher temperature difference tending to 1 K due to the Joule heat in the resistive joints. As the current rise has been separated into several plateaus, the helium outlet temperature only performs a very slight increase (< 0.1 K) at a time and then reaches very rapidly a stable level. The entire coil energizing phase can thus be considered to maintain a steady state at the nominal conditions.

2.3.2 Slow transient state during the temperature-increasing phase

Once the coil is reaching again its stable conditions at nominal current and has nearly a constant difference of 1 K between inlet and outlet, the inlet helium temperature then starts to be increased by mixing the warm helium flow (from the heat bypass flow of the cold pump) and the original cold helium at around 5 K.

Fig. 2.17 shows that from $t = -1650$ s, the inlet temperature increases with a first rapid ramp of around 0.4 K/min in order to overpass the outlet temperature. Once it is done at around 6.4 K, the inlet temperature will be continuously increased but at a slower rate of around 0.05 K/min. We can see that the inlet temperature always keeps at least 0.3 K higher than the outlet until reaching the quench. For example, a difference of about 0.4 K can be observed at the quench initiation time at $t = 0$ s. Such temperature-increasing protocol is actually determined empirically by the CTF in order to trigger a quench near the coil's inlet where the peak field region locates (thus low T_{cs}) and to ensure no layout modifications inside the coil[43]. Fig. 2.17 also shows that a quench temperature has been measured to about 7.5 K at $t = 0$ s. Since then, the current is fast discharging whereas the temperature has an abrupt increase.

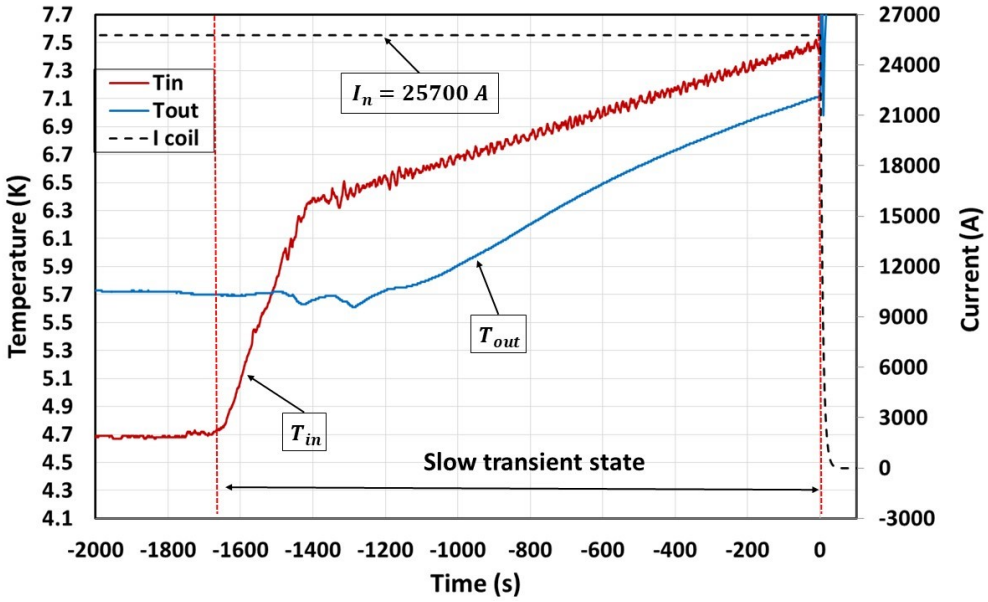

Figure 2.17 – Temperature and current evolution during the helium slow transient state

The whole temperature-increasing phase lasts for 30 min. During this phase, the helium inlet and outlet temperatures are both having an increase whereas the helium mass flow rate maintains almost stable to around 2 g/s in each pancake. This is a mass flow rate demanded for achieving a sufficient cooling effect by forced convection during the TF coils quench tests. As the coil is cooled with the supercritical helium, a higher temperature leads to a lower mass density, thus gives a higher helium flow velocity under the same mass flow rate. In this case, the coil will have a progressive increase in the helium flow velocity, as well as a progressive increase of the cooling effect by forced convection in the pancakes. This allows to consider that the temperature-increasing phase is a slow transient state for the forced helium flow in the TF coil. This part of phenomenon will be studied in more details in Chapters 3 and 4.

[43] W. Abdel Maksoud et al. *Fusion Engineering and Design* **124**. 14–17. 2017.

2.3.3 Fast transient state during the current FD

a) Quench detection and magnet protection

In order to avoid damaging the TF coils during the quench test, a security system has been designed and set up in the CTF, called the Magnet Safety System (MSS). As discussed before, when the helium inlet temperature increases to reach the lower quench temperature near the coil inlet, the conductor becomes resistive. This will be detected by the MSS. Once the normal resistance voltage reaches the threshold of $V_{th} = 100\,\text{mV}$ and lasts for over $\tau_{da} = 100\,\text{ms}$, the main breaker ("CP" in Fig. 2.18) will be opened by the MSS to cut the power supply. Once the circuit is opened, the magnetic energy stored in the coil is dumped in the $6.2\,\text{m}\Omega$ resistor (RD) in order to avoid overheating the coil. The current discharge can be approximately taken as an exponential evolution with a time constant estimated to be around 10 s. This value is determined by the ratio between the coil inductance $L = 62\,\text{mH}$ and the discharge circuit resistance taken to be equal to the dump resistor $R = 6.2\,\text{m}\Omega$. In the reality, the normal resistance can be increased with the normal zone length and the heating effect so as to the discharge circuit resistance. Thereby, a shorter time constant value will be achieved during the current discharge. In addition, Fig. 2.18 also indicates that the current discharge circuit is generally composed of water-cooled cables of $6000\,\text{mm}^2$ and copper busbars of $24\,000\,\text{mm}^2$.

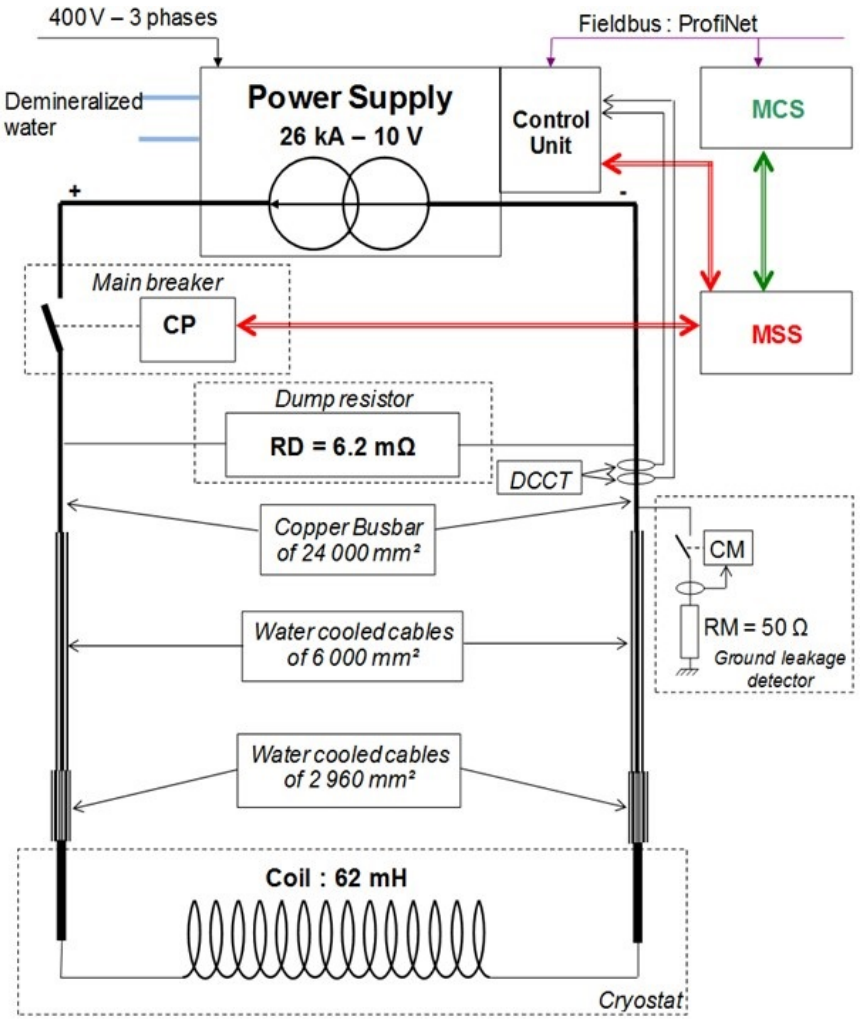

Figure 2.18 – Electrical circuit of the Cold Test Facility

Fig. 2.19 shows the magnet protection scheme integrated in the MSS against a quench. Each electrical section of the coil has been protected, including the 6 DPs of the coil, the superconducting feeders with their junctions to coil, and the current leads in copper and HTS (not shown). Moreover,

an additional *pick-up* coil has also been positioned inside the cryostat (see Fig. 2.2) to detect the possible global quench of the tested TF coil, as presented in Fig. 2.19.

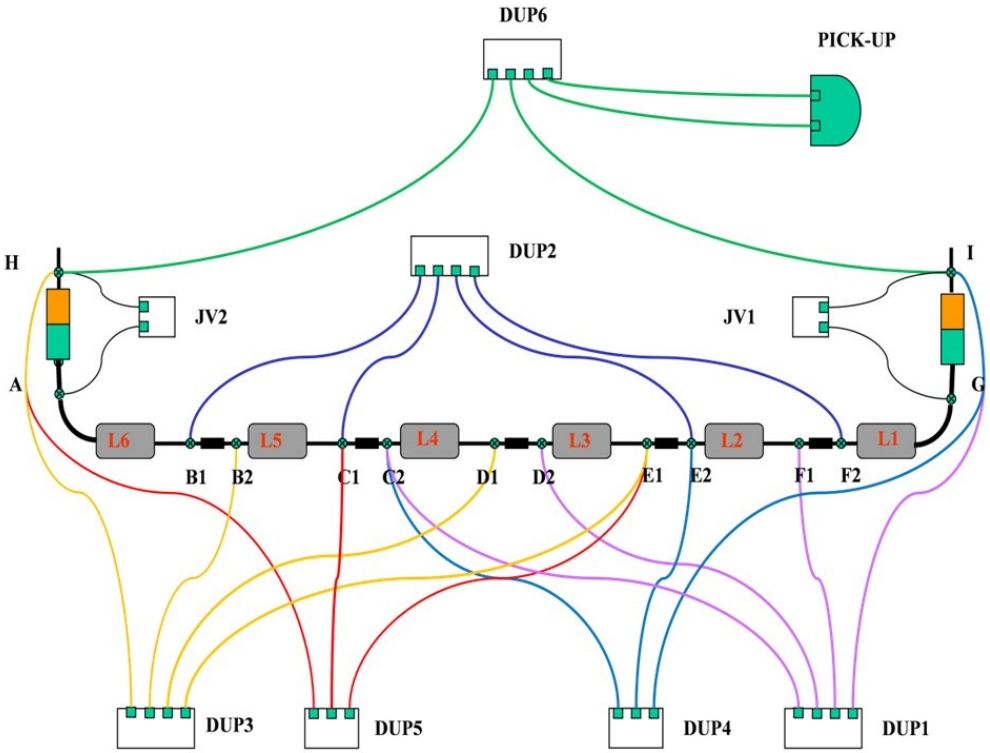

Figure 2.19 – Scheme of the magnet protection in the Cold Test Facility

Indeed, the MSS is based on a fully integrated electronic system. Detection is realized with the comparison between the measured differential voltage and the quench voltage threshold and delay (V_{th}; τ_{da}). The quench detectors use classical differential voltage measurements, as presented by the "DUP" boxes in Fig. 2.19. The principle of quench detection can be written as in Eq. (2.4) (with an example of DUP1):

$$\begin{aligned} U_1 &= L_1 \frac{dI}{dt} + R_1 I \\ U_2 &= L_2 \frac{dI}{dt} + R_2 I \\ DUP1 &= U_1 - \alpha U_2 = (R_1 - \alpha R_2) I \end{aligned} \tag{2.4}$$

where U_1 and U_2 are the voltage measurements of DP1 and DP2 with the inductive voltage part and the resistive voltage. The coefficient α is applied to compensate the two DPs inductive voltages so that only the resistive voltage part ($(R_1 - \alpha R_2)I$) can be detected by $DUP1$. For instance, when any one of the two DPs is quenched, DUP1 always allows to reveal the resistive voltage increase and to trigger a current Fast Discharge (FD) if the resistive voltage overpasses V_{th}. Moreover, each "DUP" box allows to detect multiple DPs with the same detection principle explained above. Thereby, all the DPs (the entire magnet) are "over" protected against a quench.

In addition to the coil quench, some other parameters are also taken into account for triggering a current FD, such as the temperature of the water-cooled copper connections to the power supply. There are thus two types of discharge to protect the coil[83]:

- Fast Discharge with the opening of the main breaker of the electrical circuit when detecting a quench in the coil.
- Slow Discharge when the temperature or the flow rate of the cooling water for the power supply connections exceeds a given value.

[83] Walid Abdel Maksoud et al. *Fusion Engineering and Design* **96-97**. 208–211. 2015.

Both of the analog signals from detectors and the digital isolated data coming from the MSS treatment part are sent to the fast acquisition system (AS-Net).

Finally, we can see from the Fig. 2.19 that, a redundant safety system has been integrated to protect the coil. For instance, the side DP1 (noted as L1 here) is protected by the differential voltage measurements DUP1 and DUP4, whereas the central DP4 (noted as L4 here) is simultaneously protected by all the DUPs. If one of the DUPs detects a quench, the MSS when receiving the safety commands will immediately cut the power supply and open the main breaker in order to trigger a current FD.

b) Current Fast Discharge

When a quench is detected in the TF coil, the MSS triggers a current FD to dump the stored magnetic energy on the external resistor of 6.2 mΩ. Fig. 2.20 shows the time evolution of the coil current discharge (black dashed line). The moment $t = 0$ s indicates the start of the FD. We can see that when $t = 25$ s, the current has already decreased to 5 % of the nominal current. In an electrical circuit involving solenoid and resistor (LR series circuit), the current discharge follows a negative exponential evolution along the time[90], written as Eq. (2.5):

$$I(t) = I_0\, e^{(-t/\tau)} \tag{2.5}$$

$$\text{with} \quad \tau = \frac{L_{coil}}{R_{tot}(t)} \tag{2.6}$$

where I_0 is the initial current at nominal conditions, τ the time constant of the discharge circuit, L_{coil} the self-inductance of the coil and R_{tot} the total resistance evolution of the circuit including the dump resistor and the coil quench resistance.

Fig. 2.20 allows to deduce an experimental time constant value of around 8.2 s, which is smaller than the theoretical value of 10 s. This can be explained by the development of the quench resistance in the entire coil leading to a higher R_{tot} than the pure dump resistance of 6.2 mΩ. Moreover, the dump resistor itself will also be heated increasing its resistance higher than the original value. Such experimentally determined time constant value (8.2 s) will be applied in the numerical model in Chapter 4.

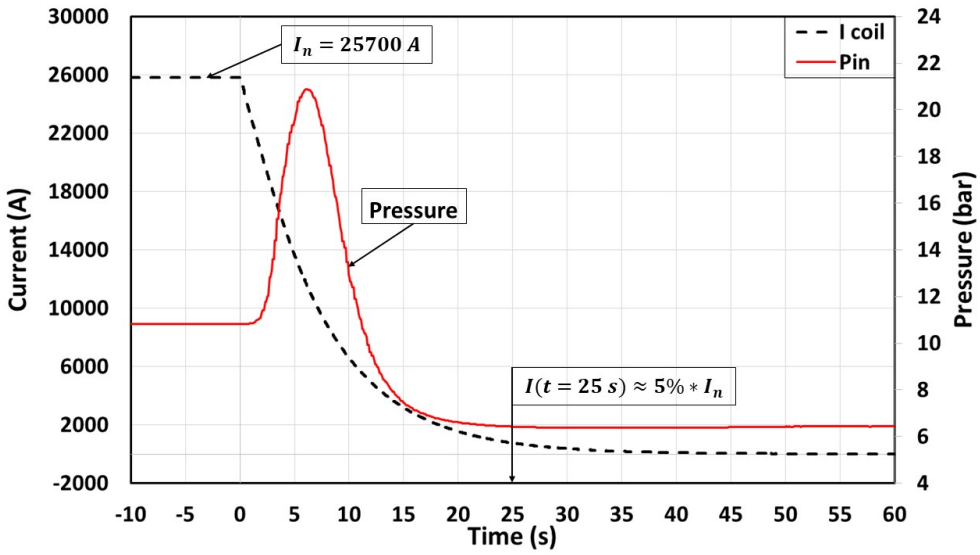

Figure 2.20 – Current fast discharge during the quench test

[90] AspenCore. *Electronics Tutorials*. 2018.

At the start of the FD, the helium inlet and outlet valves are closed immediately by the MSS whereas the safety valves are controlled to be opened with a 5 s delay. A quasi-isochoric system is then formed around the TF coil during these five first seconds. One has to know that, this 5 s delay is due to the time needed for the pneumatic safety valve to be filled in its control volume with the pressurized air ($\backsim$ 6 bar). Due to a large amount of Joule effect energy produced during the quench, a pressure rise has been induced in the helium flow, as presented in Fig. 2.20 (red solid line). When the pressure is below 20 bar, the helium flow will be repelled to a warm tank of 100 m^3 called quench buffer. Once the helium pressure exceeds 20 bar, the safety valves will be opened to release the pressurized helium into the atmosphere (see around $t = 6$ s in Fig. 2.20). The TF coil and the cryogenic circulation are then protected from the overpressure damage. One may also note a difference of pressure before and after the quench test. This is due to the fact that before quench, the helium flow is circulated in a closed refrigerating loop maintaining a pressure of around 11 bar. When the quench is triggered, the helium circulation system will be connected to the quench buffer which stays at a lower pressure level of around 6 bar.

During the current FD, the helium flow has apparently a strong variation in the cryogenic conditions which then leads to a fast transient state of the helium flow dynamics and the heat exchange in the coil. These quench-induced transient phenomena will be studied with both experimental and numerical approaches in the following chapters.

c) Data acquisition system of quench voltage

A last remark should be made here that, there are two types of voltage data record during the coils quench test: the original data signal with a unity gain of $G = 1$ and the reduced data signal with gain $G = 10$. Indeed, the capacity of the data record card in the CTF is of ± 10 V. This makes the original data only possible to be exploited before the voltage saturation to the 10 V level. Nevertheless, an important advantage with the original signal record is obviously the data integrity that can be completely kept for the detailed analysis, such as the very early normal zone propagation before triggering the FD. On the contrary, the reduced data signal can be exploited up to a range of ± 100 V, i.e. the entire voltage evolution during the whole FD. In this case, a precision of 10 times lower than that of the original data could not be avoidable. Both of them will be applied and processed for studying the coils quench behaviour in the following analyses.

2.3.4 Summary of the TF coils quench tests

After acquiring the details about the quench test experimental protocol, we will rely on a summary table to present all the 19 tests carried out on the 18 TF coils of JT-60SA in the CTF. Table 2.3 shows for the 19 quench tests their quench location, the type of the first quenched DP and the measured quench temperature at the coil inlet. We can see that, as the first received coil, TFC10 has been tested with two quench experiments in order to determine the most appropriate experimental protocol and to verify the entire instrumentation system of the CTF. These two first tests are carried out in the February of 2016 and give an experimental quench temperature for TFC10 of 7.44 K. This is close to the predicted value around $T_{cs} = 7.42$ K. According to the summary results, we can also find that the TF coils are generally having close quench temperatures around 7.5 K. Regarding the distribution of the different quench locations, it is more frequent to have a quench initiation in the side pancakes. This statistic result will be studied in more details in Chapters 3 and 4.

Table 2.3 – Summary of the quench tests carried out on the JT-60SA TF coils

	Quench location	**DP type**	$\mathbf{T_q}$**(inlet)** [**K**]
TFC10	DP6	side	7.44
TFC10bis[1]	DP1	side	7.62
TFC11	DP6	side	7.48
TFC12	DP1	side	7.48
TFC13	DP4	central	7.50
TFC14	DP3	central	7.51
TFC15	DP2	inner	7.48
TFC16	DP6	side	7.49
TFC17	DP3	central	7.50
TFC18	DP2	inner	7.54
TFC20	DP4	central	7.53
TFC01	DP5	inner	7.45
TFC03	DP6	side	7.49
TFC04	DP6	side	7.45
TFC05	DP4	central	7.48
TFC06	DP3	central	7.50
TFC07	DP6	side	7.49
TFC08	DP6	side	7.52
TFC09	DP6	side	7.48

[1] This is the second quench test carried out on the first manufactured TF coil TFC10. The quench test protocol in TFC10bis is different from the others, thus a T_q far from the average value of 7.5 K

Conclusions

This chapter allows to present an overview of the major electric and cryogenic systems in the CTF, including the 500 W helium refrigerator, the 25.7 kA power supply, the vacuum system of cryostat and valve box as well as the indispensable Magnet Safety System to protect the coil. Regarding the tested TF coils, we have also given a detailed description about the coil configuration with the classified numeration such as side, inner and central pancakes. The coil design characteristics have also been presented, such as the 113.277 m length and the 32 % void fraction in the CICC, and the average value of the peak field in the single coil test configuration in CTF of around 3.04 T. In order to obtain all the necessary parameters for studying the TF coils quench behaviour, a set of electric and cryogenic instrumentation has also been installed in the CTF. There contains the 1 kHz (up to 10 kHz) data acquisition system (AS-Net) for coil current measurement and for all necessary voltage measurements in each electrical section of the coil (DPs, joints, feeders, etc). The temperature has been measured with the Cernox sensor with an accuracy of 20 mK at nominal conditions (5 K). The helium mass flow rate has been measured with the classical venturi meters as well as the pressure measured with a membrane mode sensor. Finally, we have presented three principal steps of the experimental protocol to set up a quench test for the TF coil. The first step is to energize the coil at nominal current of 25.7 kA at 5 K. This phase is thermohydraulically a steady state phase for the coil. The second step is to increase the inlet temperature overpassing the outlet then initiating a quench close to the coil inlet. As the entire temperature-increasing phase lasts for about 30 min in a very progressive way, we then consider it as thermal slow transient state, for which a numerical study will be carried out in Chapter 4. The last step is to detect the quench and trigger a current FD. As this is the most transient phase and all the phenomena related to quench propagation are appearing during this phase, the majority of the study will then focus on this fast transient state in the following Chapters 3 and 4. Finally, we have given a summary of the 19 quench tests that will be necessary for the next analyses in Chapter 3.

CHAPTER 3

Study of the superconducting magnet quench behaviour by experimental analyses on the quench tests of the JT-60SA TF coils

Objectives

- **To highlight the different quench dynamics during the quench propagation in the JT-60SA TF coils**
- **To study the physical phenomena related to the different quench dynamics applying some experimental approaches**
- **To give an overview of the TF coils common quench behaviours with a categorisation of the quench dynamics for the 19 quench tests**

3.1 Identification of the different quench dynamics in the JT-60SA TF coils

Previous work has presented the experimental protocol of setting up a quench test for the JT-60SA Toroidal Field (TF) coils in the Cold Test Facility (CTF) as well as the electrical and cryogenic instrumentation installed for the post-quench analysis. In this chapter, we will present a study of the physical phenomena taking place during the TF coils quench tests with some necessary experimental approaches. In order to achieve this objective, the first step is to determine the most appropriate method of quench data processing for obtaining the experimental quench resistance for the 19 quench tests. The next step will be to identify the different quench dynamics during the quench propagation in the TF coils. Then some representative coils will be chosen to make the experimental analyses on the different types of quench dynamics (Sections 3.2 to 3.5). To conclude, we will realize a categorisation of the quench dynamics for all the quench tests in order to get an overview of the quench behaviours of JT-60SA TF coils.

3.1.1 Computation of the experimental quench resistance by different data processing methods

As introduced above, the first key step for studying the quench dynamics is to extract the quench resistance evolution for each Double-Pancake (DP) from the experimental data (voltage measurements). Chapter 2 shows that during the whole nominal current plateau and the current Fast Discharge (FD), we can have access to all the necessary electrical data. Fig. 3.1 shows for the first tested TF coil, TFC10, the voltage measurements on the 6 DPs (solid lines in color) and on the

pick-up coil (black solid line). The red dotted line represents the decrease of the coil current during the FD. As the measurements on all TF coils have a similar evolution, the data of TFC10 can thus be taken here as a representative example to explain the general data behaviours during the quench.

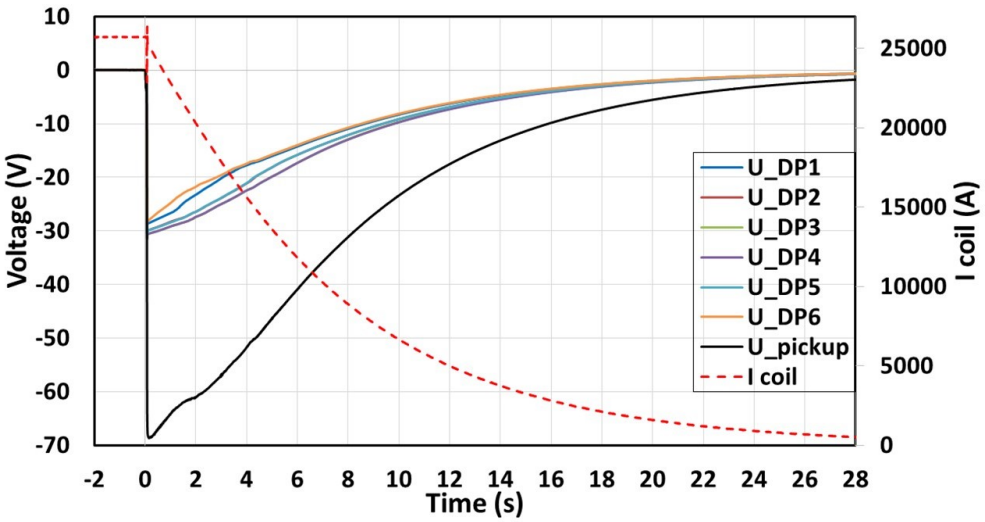

Figure 3.1 – Voltage and current measurements during TFC10 quench test

We can see that the current FD starts at $t = 0\,\text{s}$ and decreases to around 1/10 of the nominal current at $t = 20\,\text{s}$. This is coherent with the time constant of the coil current discharge of 8.2 s (see Section 2.3.3). Near the same time at $t = 0\,\text{s}$, all the 6 DPs voltages (U_DP1 ∽ U_DP6) decrease immediately to around $-30\,\text{V}$, and then increase progressively to 0 V. Such data evolution of the quench test TFC10 is actually due to a competition between two parts of the voltage measurements in the DPs, the inductive voltage $U_{DP\,ind}$ and the quench resistance voltage $U_{DP\,quench}$, as presented in Eq. (3.1):

$$\begin{aligned} U_{DP} &= U_{DP\,ind} + U_{DP\,quench} \\ &= L\frac{dI}{dt} + IR_{DP} \end{aligned} \tag{3.1}$$

where U_{DP} is the measured voltage of the DP, L the self-inductance, I the coil current (the same in all the DPs since series connection) and R_{DP} the quench resistance of the DP. As the current decreases rapidly at the beginning of the FD, the inductive voltage $L\frac{dI}{dt}$ thus contributes to a negative value compensating the positive quench resistance voltage ($U_{DP\,quench}$), together making $U_{DP} \approx -30\,\text{V}$ near the start of the FD.

The pick-up coil voltage (black solid line) presented in Fig. 3.1 is another key measurement during the test. As already mentioned in Chapter 2, it shows the inductive voltage by the time-varying magnetic field in the closed circuit of pick-up coil. Here we can observe that, at around $t = 2\,\text{s}$, the pick-up coil voltage also has a slope change. This is due to the fact that the eddy currents induced in the casing have modified the inductive coupling between the pancakes and the pick-up coil, thus led to an impact on the pick-up coil's inductive voltage. Based on these measurements, we can then deduce the experimental quench resistances for the following studies.

Fig. 3.1 shows actually the reduced signal data record (gain $G = 10$) with the integrated measurements during the entire quench test (see Section 2.3.3). Based on the data of coil TFC10, the next sections will discuss four tentative methods of quench data processing to deduce the experimental quench resistance and to determine the most appropriate approach for the following quench resistance computations.

a) Method 1: direct computation with the self-inductance L

The idea of the first method is to compute directly the self-inductance L of each DP thanks to the Pure Fast Discharge (PFD) test data (see Section 2.2.1). We then apply this self-inductance value L to compute the inductive voltage of each DP ($U_{DP\,ind}$) allowing to deduce their quench resistance voltage ($U_{DP\,quench}$). This method is thus called direct computation with the self-inductance L.

As mentioned in Chapter 2, the voltage measurement in PFD test (U_{PFD}) corresponds to the pure inductive part of each DP, which allows to compute directly the self-inductance L with the current decrease ΔI during the time step Δt, as presented in Eq. (3.2).

$$L = \frac{U_{PFD} \cdot \Delta t}{\Delta I} \tag{3.2}$$

We take the DP6 of TFC10 as an example to make the computations since DP6 is the most quenched pancake in the coil. Fig. 3.2a shows that the DP6 self-inductance when computed with $\Delta t = 0.1\,\mathrm{s}$ is too dispersed to be applied, ranging from 0.005 H to 0.020 H. In comparison, Fig. 3.2b shows a more homogeneous L value of around 0.010 H $\pm 5\,\%$ when computed with $\Delta t = 1\,\mathrm{s}$. A direct conclusion is then to choose the average value of 0.010 H as the DP6 self-inductance.

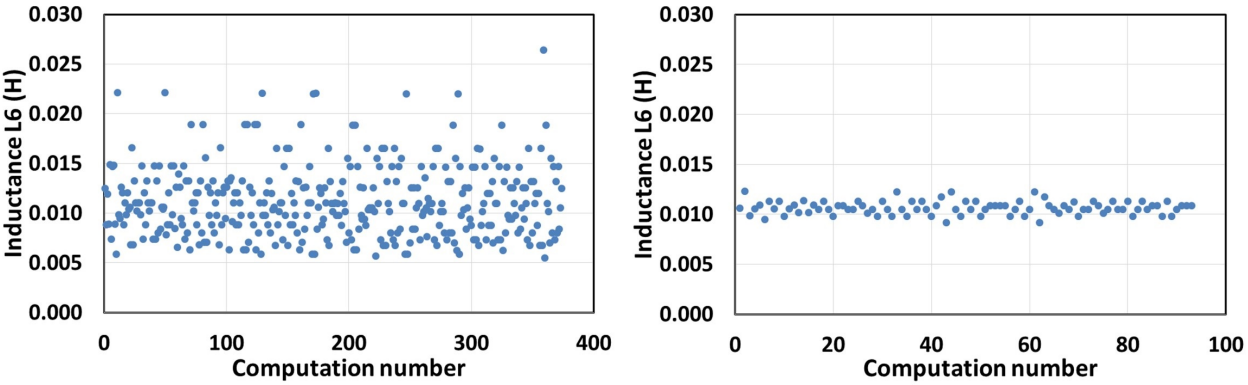

(a) $\Delta t = 0.1\,\mathrm{s}$ (b) $\Delta t = 1\,\mathrm{s}$

Figure 3.2 – TFC10 DP6 self-inductance computation with different Δt

As mentioned above, the idea is to get rid of the inductive voltage to obtain the wanted quench resistance part. We can then compute the DPs quench resistance at the certain time step Δt with the determined value $L = 0.010\,\mathrm{H}$, as written in Eq. (3.3).

$$R_{DP} = \frac{U_{DP} - L\frac{\Delta I}{\Delta t}}{I} \tag{3.3}$$

Fig. 3.3a shows that when computed with $\Delta t = 0.1\,\mathrm{s}$, quench resistance R_{DP6} behaves somewhat randomly at the beginning and then totally divergent from $t = 10\,\mathrm{s}$. This is actually due to the signal oscillations during the current measurements making the computation results alternate between negative and positive values. Meanwhile, we can see in Fig. 3.3b that the computation with $\Delta t = 1\,\mathrm{s}$, despite of the stable resistance results until $t = 20\,\mathrm{s}$, cannot have a sufficient precision to carry out an accurate analysis. Moreover, we should recall that all the computations realized with this method are based on a self-inductance value which is itself obtained with some uncertainties ($\pm 5\,\%$). This actually makes the computation results even farther to the realistic resistance values so as to the quench behaviour analysis.

Therefore, the direct computation with self-inductance of each DP cannot be chosen as the quench data processing method.

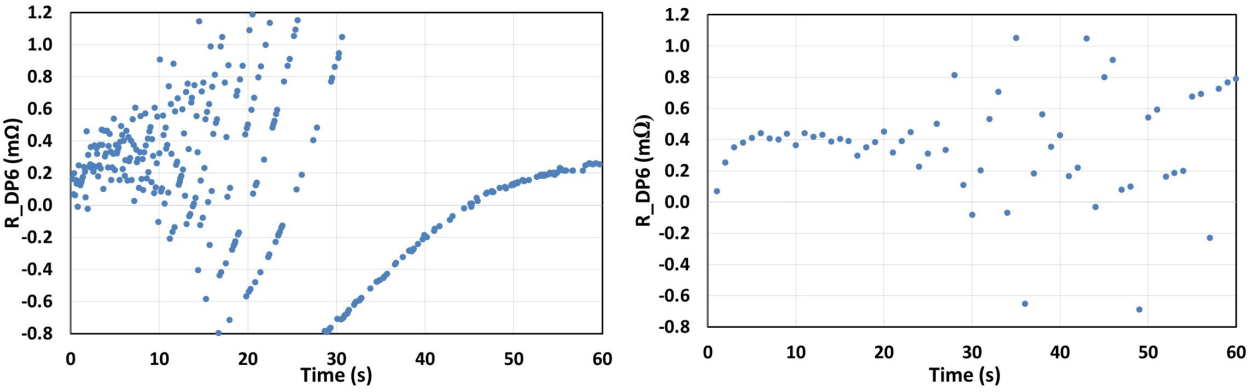

(a) $\Delta t = 0.1\,\mathrm{s}$ (b) $\Delta t = 1\,\mathrm{s}$

Figure 3.3 – TFC10 R_{DP6} computation with different Δt

b) Method 2: computation with the PFD test inductive voltage

As discussed before, the PFD voltage measurement U_{PFD} corresponds to the pure inductive voltage of each DP. The second idea is to directly take advantage of such voltage measurement during the PFD test without computing the self-inductance L. A fundamental assumption here is that the inductive voltage measured during the PFD test is identical to the one during the quench test (see Eq. (3.4)), assuming the negligibility of the coil quench resistance in front of the dump resistor of $6.2\,\mathrm{m\Omega}$ (to be verified below).

$$U_{PFD} = (L\frac{dI}{dt})_{PFD} = (L\frac{dI}{dt})_{quench} \tag{3.4}$$

Based on the above assumption, the quench resistance for each DP can thus be computed with the measured inductive voltage during PFD test as written in Eq. (3.5):

$$\begin{aligned} R_{DP} &= \frac{U_{quench} - (L\frac{dI}{dt})_{quench}}{I} \\ &= \frac{U_{quench} - (L\frac{dI}{dt})_{PFD}}{I} \\ &= \frac{U_{quench} - U_{PFD}}{I} \end{aligned} \tag{3.5}$$

where U_{quench} is the DPs voltage measurement during quench test while U_{PFD} always the DPs voltage measurement during PFD test.

Fig. 3.4 shows that, in general, this method seems to give more stable computation results of the DPs quench resistances than the first method. However, all the quench resistances still keep increasing when the current (red dotted line) decreases to nearly zero level at $t = 24\,\mathrm{s}$, which is evidently non-physical. This is incoherent with the Joule heat impact on the quench resistance evolutions. When current decreases to zero, the global temperature will reach a maximal level or even start to decrease since there is no longer Joule heat in the coil. This will definitely make the quench resistance value either stable at a certain maximal resistance plateau or decrease because of the temperature homogenisation in the entire coil. It is actually the first reason for abandoning this PFD measurement method.

The current evolution during the PFD test (black dotted line) is also plotted in Fig. 3.4. The difference between the two current evolutions (dI/dt) is almost negligible before $3\,\mathrm{s}$ and then increases with the time. In order to explain this phenomenon, we again rely on the resistor-inductor circuit of the current discharge system in the Cold Test Facility. The time constant τ can be

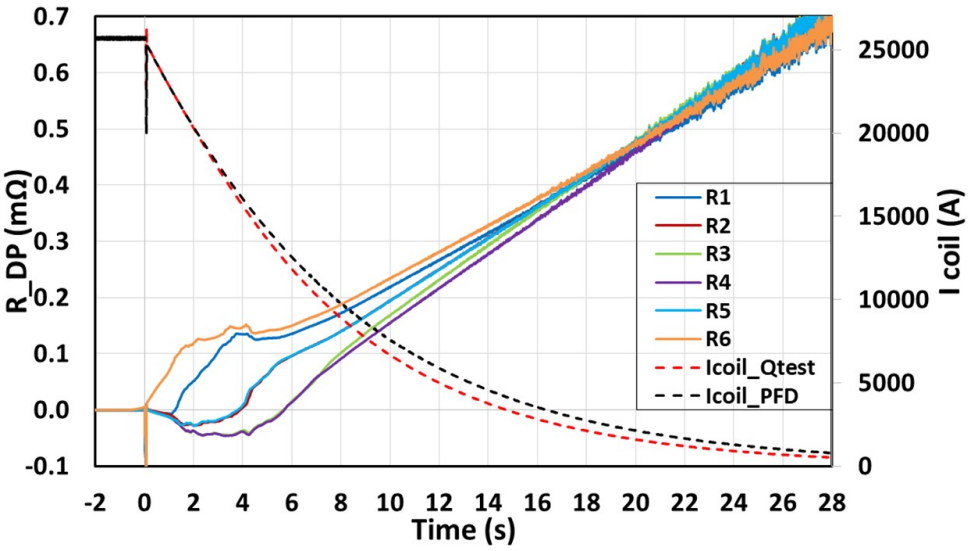

Figure 3.4 – TFC10 DPs quench resistance computed with the PFD inductive voltage method

approximately computed with Eq. (3.6):

$$\tau = \frac{L}{R(t)} \tag{3.6}$$

where L is the coil inductance and R the total resistance of the circuit including the dump resistor and the coil quench resistance varying along the time t.

As the self-inductance L is one of the intrinsic characteristics of the coil, it thus remains the same in both PFD and quench tests when carrying out in a same coil (TFC10). When there is no quench (PFD test), the circuit resistance corresponds to the pure dump resistor of 6.2 mΩ. Nevertheless, when the normal zone starts to develop in the coil, the circuit resistance will be higher due to the addition of the quench resistance. Therefore, the time constant of the quench test will be lower than the one of the PFD test making the current decrease faster during the quench propagation. This is actually coherent with the fact that in Fig. 3.4, the quench test current (red dotted line) is discharging faster than the PFD one (black dotted line). A computation shows that when $t = 5$ s, the quench test current is already 5 % less than that of the PFD test. This is also why the continuous increase of the quench resistances appears to be non-physical. Indeed, the inductive term $L\frac{dI}{dt}$ of quench test in Eq. (3.5) is being more and more underestimated by the PFD one.

According to the two last statements, we can conclude that this computation method based on the PFD voltage measurement could only be applied when the quench level remains relatively low during the first seconds of the quench propagation, i.e. when the quench resistance can be neglected in front of the dump resistor as proposed in the assumption. It will thus be difficult to carry out a full analysis with these method computations.

c) Method 3: computation with the less quenched DP inductive voltage

The third idea is to apply the DP that has the lowest quench resistance level to deduce the other DPs quench resistances. The advantage of this idea is that the computations with the DPs voltage data are all based on the same quench test allowing to reduce the uncertainty due to different quench tests. The approach is to firstly identify the less quenched DP with the voltage measurements, e.g. DP3 in TFC10, to be taken as a reference. Then we make a very pessimistic assumption that this referenced DP3 never quenches and will remain in the superconducting state during the whole FD, so that the voltage measurement of DP3 only corresponds to the pure inductive voltage. The other DPs inductive voltages can thus be computed with the DP3 voltage measurements thanks

to the proportional relation between the DPs inductive voltages. This relation is actually based on the DPs same current variation dI/dt in a series circuit making the inductive voltage relation only depend on the proportionality between the self-inductances L. So, we will firstly compute this self-inductance ratio α between the reference DP3 and the 5 other DPs based on the PFD test measurements, as presented in Eq. (3.7):

$$\alpha_i = \frac{L_i}{L_3} = \frac{(L_i \frac{dI}{dt})_{PFD}}{(L_3 \frac{dI}{dt})_{PFD}} \tag{3.7}$$

with $i = 1, ..., 6$ & $i \neq 3$.

The inductive voltage of each DP (except the DP3) during the quench test can then be computed with Eq. (3.8):

$$U_{DPi\,ind} = L_i \frac{dI}{dt} = \alpha_i L_3 \frac{dI}{dt} = \alpha_i U_{DP3\,mes} \tag{3.8}$$

where $U_{DP3\,mes}$ is the voltage measurement on DP3 during the quench test.

We can thus obtain the quench resistance for each DP applying Eq. (3.1). Fig. 3.5 shows that the computation results are generally more stable and more physical when comparing to the two first methods. Nevertheless, 4 DPs over 6 have already quenched during the first 2 seconds. Statistically, there is no reason for the two central DPs (DP3 & DP4) of the same coil still remain in the superconducting state. Moreover, we can see that from $t = 6\,\mathrm{s}$, the quench resistance of DP4 (violet line) becomes negative. It means that the reference DP3 also initiates a latter quench at this moment and has already been more quenched than the DP4. This makes the computed quench resistance of DP4 lower than zero due to the subtraction by DP3. Both of the statements indicate the big limitation of the this method assumption itself, i.e. none of the DPs can always keep the superconducting state during the whole quench test. However, we cannot ignore the fact that this method can have a good accuracy of the quench resistance computation during the very early quench phase, where the normal zone resistance of the referenced DP is still negligible.

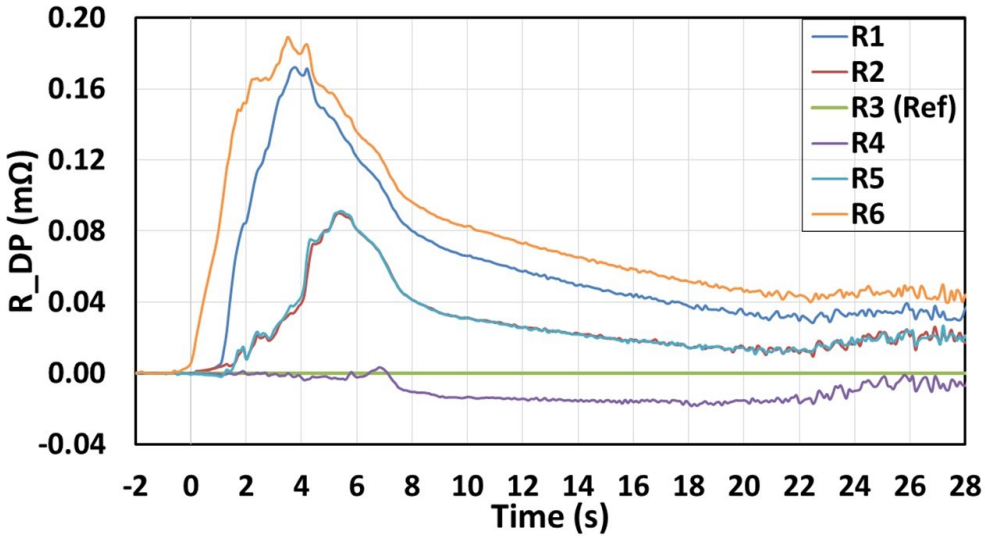

Figure 3.5 – TFC10 DPs quench resistance computed with the less quenched DP inductive voltage method

We conclude that this method cannot be available for the full scale quench resistance computation (during the entire FD), but can be applied as a referenced data processing method for studying the beginning evolution of the DPs quench resistance, e.g. from $t = -1\,\mathrm{s}$ to $t = 1\,\mathrm{s}$ for TFC10.

d) Method 4: computation with the pick-up coil inductive voltage

The last method for deducing the quench resistance is based on the Faraday's Law of electromagnetic induction, stating that any change in the magnetic field will cause an electromotive force that produces an inductive voltage. During the FD, the rapid variation of the coil current produces the magnetic field variation through the pick-up coil and induces a voltage in it. As the pick-up coil is not connected with the power supply, its voltage measurement thus corresponds to a pure inductive voltage. Knowing that the DPs inductive voltage is proportional to the one of the pick-up coil according to the relation between the self-inductances, we can then compute the DPs quench resistance with the voltage measurement on the pick-up coil. This method is thus called computation with the pick-up coil inductive voltage.

The ratio between the DPs inductive voltage and the pick-up coil voltage measurement can be obtained once again thanks to the PFD test with the pure inductive voltage measurement on each DP, as written in Eq. (3.9):

$$\gamma_i = (\frac{U_{DPi\,mes}}{U_{pickup}})_{PFD} = (\frac{L_i \frac{dI}{dt}}{U_{pickup}})_{PFD} = (\frac{L_i \frac{dI}{dt}}{U_{pickup}})_{quench} = (\frac{U_{DPi\,ind}}{U_{pickup}})_{quench} \tag{3.9}$$

where $U_{DPi\,mes}$, $U_{DPi\,ind}$ and U_{pickup} are respectively the DPs voltage measurements, inductive voltages and the pick-up coil voltage measurements during the quench test, the index $i = 1, ..., 6$.

Finally, the 6 DPs quench resistances can be computed by applying the above ratio γ_i, as presented in Eq. (3.10):

$$R_{DPi} = (\frac{U_{DPi\,mes} - \gamma_i U_{pickup}}{I})_{quench} \tag{3.10}$$

Fig. 3.6 shows the DPs quench resistance evolutions computed with the above method. We can see that it is always the side DP6 that initiates the quench of the coil. This is coherent with the voltage measurements. This time, all the DPs are having a quench propagation, especially for the central DP3 and DP4, and will reach a maximal quench resistance plateau, e.g. $R_{max\,DP6} \approx 0.26\,\text{m}\Omega$ at around $t = 4\,\text{s}$. This is in general coherent with the physical phenomena during a quench propagation. We can also see that several seconds after reaching the maximal quench resistance plateau, at around $t = 20\,\text{s}$, all of the 6 DPs are converging to a final same level of around $0.18\,\text{m}\Omega$. This is also coherent with the thermal homogenisation tendency of the entire coil temperature.

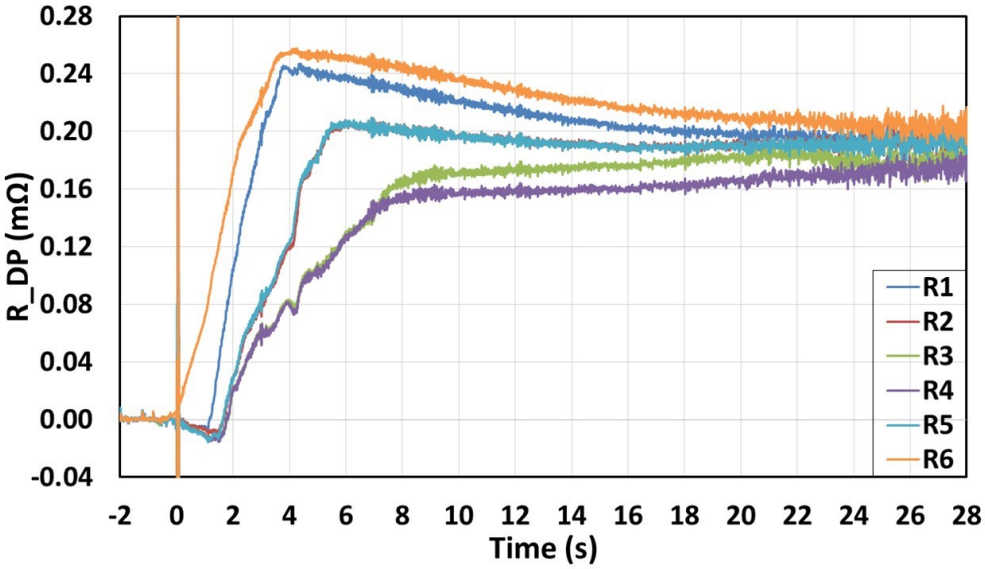

Figure 3.6 – TFC10 DPs quench resistance computed with the pick-up coil inductive voltage method

Nevertheless, one can note that during the first two seconds, the latter quenched DPs (DP1 ∽ DP5) all undergo an abnormal negative quench resistance phase. This could be due to some

electromagnetic phenomena taking place at a low quench level of the coil, for which we are still looking for the reasons. This little error leads to an average underestimation of around 7 % for the quench resistance computation. It is actually due to such underestimation at low normal zone length level that we are not sure if the resistances are still at zero or already have a certain low values. This also means that we cannot tell if the simultaneous slope change at around $t = 1.5\,\mathrm{s}$ indicates a latter new quench initiation or a delayed quench acceleration in these DPs. In this case, one may recall that the method 3 with less quenched DP computation could be an alternative approach to deduce the accurate quench resistance evolution for the very beginning of the normal zone development. But again, theses results will be completely dependent on the quench resistance development of the referenced DP, so limited from case to case. Finally, we only choose the pick-up coil method as the following data processing approach when considering the general coherence of the computed quench resistance evolutions and the sufficient accuracy (thanks to the measured data precision of 1 ms) for the coils quench behaviour study.

e) Conclusion

Regarding the 4 last attempts of quench resistance computations, we firstly get rid of the direct computation with the self-inductance L due to the uncertainty and dispersion of the results. For the second method of the PFD test inductive voltage computation, the continuous increase of the quench resistance at $I = 0\,\mathrm{A}$ is evidently a non-physical behaviour. The underestimation of the equivalent PFD measurements assumption has also been proven inaccurate for computing the DPs inductive voltage. Concerning the third method, its basic hypothesis that the less quenched DP (taken as reference) always remain in the superconducting state will be actually become more and more incoherent during the FD. We could then not rely on this approach to make the entire quench data processing during the test. The last but the most appropriate way remains actually the computation based on the pick-up coil inductive voltage measurement, despite of the negative resistance values ($R_{DP1} \backsim R_{DP5}$) appearing at the beginning of the quench propagation. Fortunately, they will not have a predominant impact on the following experimental studies of the physical phenomena (we will see in the following sections). We will thus choose this approach as our final data processing method for all the tested TF coils. It is to note that, the pick-up coil inductive voltage computation method will be named ***pick-up coil method*** in the rest of the document.

3.1.2 Identification of the different quench dynamics

Previous computation allowed us to choose the pick-up coil method as the most appropriate data processing approach for computing the experimental quench resistance of all the quench tests. With this method, we obtain the quench resistance evolutions of all the DPs in TFC12, as presented in Fig. 3.7. Here, we are taking the quench test of TFC12 as an example to give a description of the different quench dynamics since they are representative of the majority of the quench tests for other coils.

Fig. 3.7 shows a general separation of four quench dynamic phases which are based on the direct observations on the experimental quench resistance evolutions. We called ***quench initiation phase***, defining the initial quench that takes place in the side DP1 before the start of the FD ($t < 0\,\mathrm{s}$). The quench resistance during this period is undergoing a slow increase indicating the low propagation velocity of the quench. One has to know that the quench initiation can take place at all kinds of location in the coil, i.e. in the side DP, inner DP or central DP. TFC12 only shows the case of the side DP quench initiation, which however, represents more than half of the tested coils quench behaviours. This seemingly random phenomenon will be analysed with some more details in Section 3.2.

Near the start of the FD, we can see a first slope change appearing in the initial quench pancake DP1 followed by a quasi-linear increase until reaching a maximal resistance plateau of around

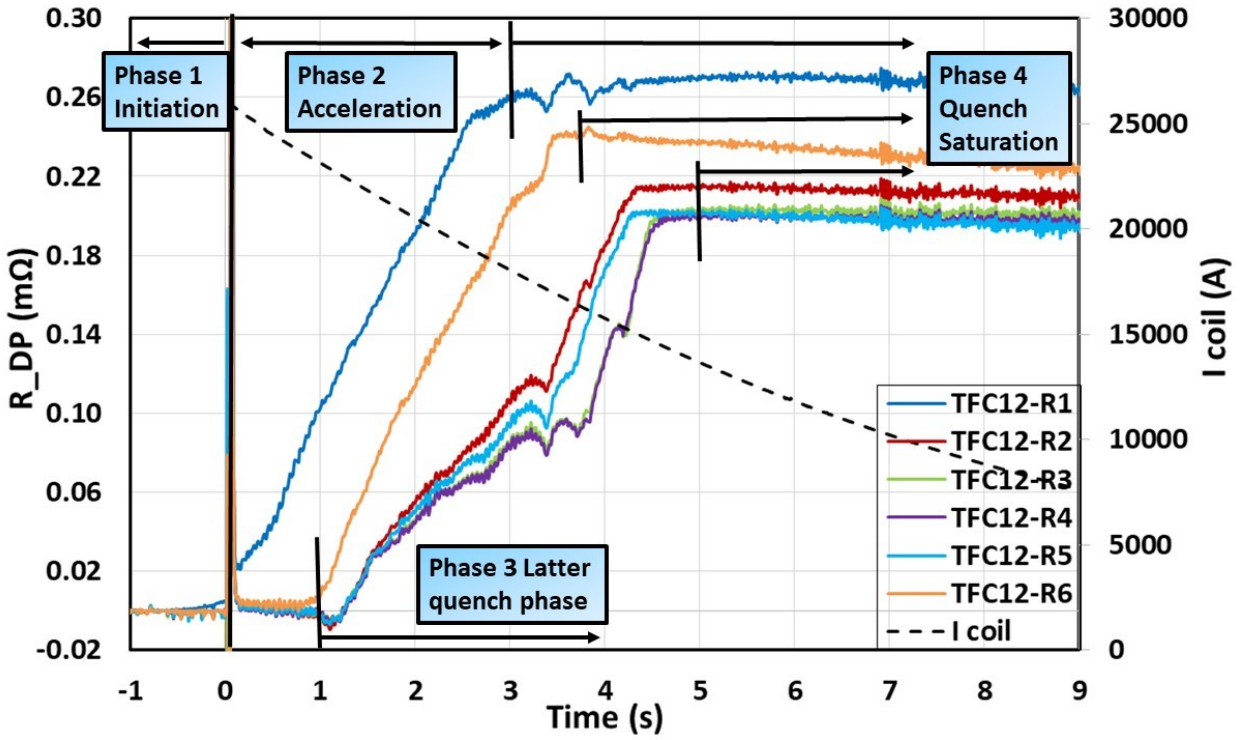

Figure 3.7 – TFC12 DPs quench resistance evolutions and quench dynamic phases

0.26 mΩ at $t = 3$ s. This period is thus called ***quench acceleration phase*** with obviously a higher propagation velocity of the quench in the DP1. Such immediate quench acceleration near the start of the FD is actually one of the different quench acceleration dynamics, which can be found in 70 % of the coils quench behaviours. A more detailed study will be made for this immediate quench acceleration phenomenon (named "early" acceleration afterwards) as well as for other types of quench acceleration dynamics in Section 3.3.

During the development of the normal zone in DP1, the other DPs (DP2 ∽ DP6) are almost having a simultaneous slope change at around $t = 1$ s. This either indicates a new quench initiation or a quench acceleration, which however remains unclear due to the slight negative resistance values appearing at the low normal zone length level (the only flaw of pick-up coil method). The side DP6, after this slope change, is having a quasi-identical quench dynamics as DP1 until reaching its maximal resistance plateau of around 0.24 mΩ at $t = 3.5$ s. Whereas the four inner and central DPs, after their simultaneous quench, are all undergoing a deceleration until a resistance plateau near the same moment at $t = 3.5$ s then a re-acceleration of the quench resistance up to the maximal plateau of around 0.20 mΩ at $t = 5$ s. This combined quench dynamics in the latter quenched DPs is thus called ***latter quench phase*** for the following studies. One will also need to know that the two sub-phases phenomena after the simultaneous quench (deceleration & re-acceleration) appear very often during the latter quench phase, representing about 3/4 of the quench tests. Also, a more detailed study will be made to highlight the simultaneous quench phenomenon, the two sub-phases phenomena as well as the other possible latter quench dynamics in Section 3.4.

Finally, when arriving at the end of the quench acceleration phase or the latter quench phase, each DP will have a maximal resistance plateau indicating the start of the last dynamic phase, called ***quench saturation phase***. This plateau could either indicate a full quench propagation over the entire DP or only a partial quench propagation stopped somewhere inside the DP, for which we will build a physical model to make some detailed analyses in Section 3.5. We can then see that the DPs resistance plateaus are all having a general decrease then converging to a nearly same level of quench resistance. This will also be discussed from the thermo- and magneto-resistance properties aspect and with the homogenisation of the entire coil temperature in Section 3.5.

3.2 Study of the physical phenomena during the quench initiation phase

3.2.1 Description of the physical phenomena during quench initiation phase

As already introduced in Section 3.1.2, the quench initiation can take place in all kinds of locations inside a coil, from the side pancake to the central one, differentiating from one quench test to another. This seemingly random behaviour allows to separate the quench initiation phase into 3 different types: quench initiation in the side DP, in the inner DP and in the central DP. We will take for each type a representative quench test to give a more detailed description. The results presented in the following figures are all computed with the original data in unitary gain $G = 1$ (see Section 2.3.3). Before presenting the different type of quench initiation dynamics, we need to explain the slight difference between the original data processing approach of obtaining the initial quench resistances and the above mentioned pick-up coil method with reduced signal data in $G = 10$.

Approach of the quench initiation resistance computation

The original data although saturated before the FD has a great interest to process thanks to the integrity of the data information. When the coil is charged at nominal current of 25.7 kA DC, there always exists the periodical oscillation due to the electrical frequency of 50 Hz in power supply. In order to get rid of this intrinsic noise, the original data has been filtered manually in averaging for each 20 ms. It is then the same method (pick-up coil method) applied to deduce the DPs quench resistances during the initiation phase. This allows to obtain a more precise resistance evolution with very low noises. We can then study the different quench initiation types with these results.

Fig. 3.8 shows for the three types of initiation dynamics the average quench resistance evolution during their initiation phase. First, we take a look at the representative tested coil TFC12. The quench initiation takes place in the side DP1 (coherent with Fig. 3.7), with the initial quench moment at around $t = -0.65$ s (blue solid line). The grey solid lines represent the resistance evolutions of the latter quenched DPs in TFC12 (DP2 $\backsim$ DP6) indicating their quasi-superconducting state before FD, i.e. the quench resistances almost negligible comparing with the quench initiation pancake DP1. Near the start of the FD (at about $t = -20$ ms), we can see that the quench resistances undergo an abrupt decrease likely due to the opening of the arc current breaker that leads to a fast transient phase for measuring.

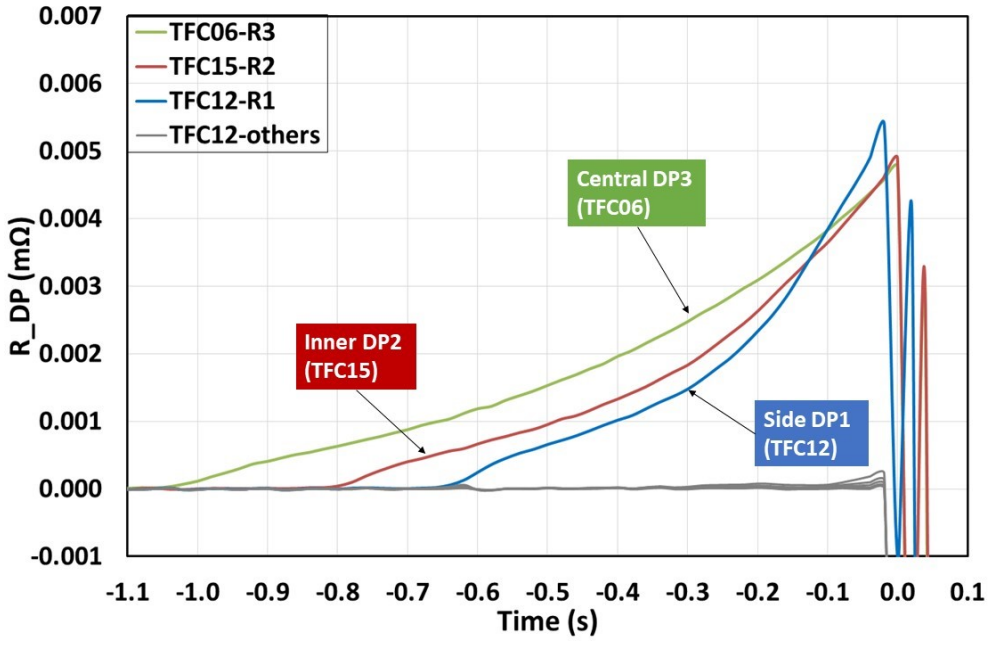

Figure 3.8 – Quench resistance evolutions during the 3 types of quench initiation phase

Fig. 3.8 gives a maximal quench resistance point in DP1 of around $5.4\,\mu\Omega$ during the initiation phase, which allows to compute the normal length with the resistance definition in Eq. (3.11):

$$L_{quench} = \frac{R_{DP} \cdot S_{Cu}}{\rho(RRR, T, B)} = 3.78\,\mathrm{m} \tag{3.11}$$

where the cross-sectional area of copper strands is $S_{Cu} = 1.8 \times 10^{-4}\,\mathrm{m}^2$, the residual resistance ratio $RRR = 130$ determined in Section 1.2.2, the cable temperature near the inlet $T = T_{inlet} = 7.5\,\mathrm{K}$ during the quench initiation, the nominal current $I = 25\,700\,\mathrm{A}$ that corresponds to the average magnetic field near the inlet $B = B_{av} = 2.88\,\mathrm{T}$ assuming a first 10 m normal zone length in DP1. The average initial quench propagation velocity can then be easily computed with Eq. (3.12):

$$v_{quench}(\mathrm{TFC12}) = \frac{L_{quench}}{\Delta t} = 5.82\,\mathrm{m/s} \tag{3.12}$$

where Δt is the time difference between the initial quench moment and the maximal point, applied with the approximate value of 0.65 s.

The quench propagation velocity 5.82 m/s is actually computed with a single pancake quench assumption. It means that we assume to have initiated the quench in one of the adjacent pancakes (e.g P1 in the DP1) so that the developed normal zone length of 3.78 m only belongs to this single pancake. This assumption is to resolve the problem of having the only access to a Double-Pancake voltage measurement during the quench test. In this case, an overestimation could be performed on the average quench propagation velocity during the initiation phase. Indeed, the two adjacent pancakes of a same DP should, from the physical aspect, have similar quench dynamics, i.e. two quench propagation together in the two adjacent pancakes. Therefore, a possible division by a factor of 2 could be applied to the determined normal zone length. Finally, the average initial quench propagation velocity can be obtained to around 3 m/s which remains within the same order of magnitude. A more detailed numerical study will be carried out to verify the number of quenched pancakes during the initiation phase (see Section 4.4.2).

The second type focuses on the quench initiation in an inner DP, as presented with the TFC15 quench test (red solid line) in Fig. 3.8. This time, the quench is initiated in DP2 at around $t = -0.8\,\mathrm{s}$ and has a first increase around $5.0\,\mu\Omega$ near the start of the FD. The same computation approach and single pancake quench assumption have been applied to this quench initiation case allowing to obtain the average initial quench propagation velocity of around 4.35 m/s. This type of quench behaviour only represents 16 % of the quench tests.

Finally, the third type, the quench initiation in a central DP has been presented in Fig. 3.8 as a green solid line. We can see that TFC06 has initiated the quench in the central pancake DP3 at about $t = -1.05\,\mathrm{s}$. After a slower resistance increase than the two other curves, the maximal resistance point is obtained at about $4.78\,\mu\Omega$ near the start of the FD. Again, with the same approach and same assumption, we can compute the average initial quench propagation velocity to 3.14 m/s. This last type of quench behaviour is 2 times more frequent than the second type (inner DP initiation).

Table 3.1 gives some more details about the tested coils in each type of the quench initiation phase. The previous discussions allow to conclude that the order of initial quench propagation velocity is around several meters per second and that the side DPs seem to have more frequently the coil quench initiation than the other DPs. Therefore, we may ask the following question: why the side DPs initiate the quench of the coils and govern more than half of the quench tests? This question will be discussed below in Section 3.2.2.

Table 3.1 – Three different types of the quench initiation phase

Quench initiation type	**SIDE**	**INNER**	**CENTRAL**
	TFC03	TFC01	TFC05
	TFC04	**TFC15**	**TFC06**
	TFC07	TFC18	TFC13
	TFC08		TFC14
	TFC09		TFC17
	TFC10		TFC20
	TFC10bis		
	TFC11		
	TFC12		
	TFC16		
Total Number	**10**	**3**	**6**
Percentage	**53 %**	**16 %**	**32 %**

3.2.2 Experimental analysis of the impact of different factors on the initial quench location

The above three types correspond to the three possible initial quench locations in the 19 quench tests. We recall their statistic results that: 53 % of the quench tests have the initial quench location in the side pancakes (DP1 & DP6), 16 % in the inner pancakes (DP2 & DP5) and 32 % in the central pancakes (DP3 & DP4). According to the superconductors critical surface property, the majority (or even 100 %) of quench tests should have initiated in the peak field pancakes (DP3 & DP4) due to their lowest T_{cs}. Nevertheless, the experimental results show that more than half of the quench initiation appeared in the side pancakes (DP1 & DP6) whereas only 1/3 of the quench tests have initiated in their central ones. This is thus very far away from our expectation. In order to acquire a better understanding on this "unexpected" statistic phenomenon, several factors will be taken into account to study their impact on the quench initiation dynamics including:

- the electromagnetic performance of the superconducting strands,
- the external heat load from the casing or the adjacent conductors (pancake or turn),
- the friction factor impacting the local helium cooling effect by forced flow convection

a) Strands performance

Concerning the first impact factor of the initial quench location, the superconducting strands performance is directly revealed by its current sharing temperature T_{cs} when considering the real machine applications[62]. The strands are considered to have a better performance when they have a higher T_{cs}. As already introduced in (see Section 1.2.1), the strands T_{cs} is directly driven by the magnetic field and the supplied current (or current density). We recall that the T_{cs} (or critical temperature T_c) depends on the magnetic field with an inverse relation[59], as presented in Eq. (3.13). This means that the quench can be more easily initiated at the high magnetic field location due to a lower T_{cs} (or T_c).

$$T_c = T_{c0}\,(1 - \frac{B}{B_{c20}})^{1/n} \tag{3.13}$$

with the parameters already presented in Table 1.2.

We also recall that the critical surface has been described by the Bottura's fit[62] with the critical current density as a function of the temperature and magnetic field, as presented in Eq. (3.14). Thereby, the current sharing temperature T_{cs} can be defined implicitly as the temperature at which

[62] L. Bottura. *IEEE Transactions on Applied Superconductivity* **10**. 1054–1057. 2000.
[59] M. S. Lubell. *IEEE Transactions on Magnetics* **19**. 754–757. 1983.

the operating current density in the NbTi part j_{op} is equal to the critical current density j_c (see Section 1.2.1).

$$j_c(T,B) = j_{op}(T,B) = \frac{j_{cref} * C_0}{B} \left(\frac{B}{B_{c2}(T)}\right)^{\alpha} \left(1 - \frac{B}{B_{c2}(T)}\right)^{\beta} \left(1 - \left(\frac{T}{T_{c0}}\right)^{1.7}\right)^{\gamma} \tag{3.14}$$

with $B_{c2}(T) = B_{c20}\left(1 - \left(\frac{T}{T_{c0}}\right)^{1.7}\right)$ and the parameters already presented in Table 1.2.

As discussed in Chapter 2, the closer the pancakes locate near the central position in the coil, the more the spatial field distribution is becoming curved in V-shape (see Fig. 2.6). With the Bottura's fit in Eq. (3.14) and the parameters of the JT-60SA TF coils that are determined with the average performance strands[58] (see Table 3.2), we obtain for the 3 representative pancakes (SIDE-P12, INNER-P10 and CENTRAL-P8) their spatial T_{cs} distribution in an upside-down V-shape, as presented in Fig. 3.9a. When taking a zoom view on the coil inlet in Fig. 3.9b, we can see that around 40 mK difference has been appeared between the side and central pancakes for their minimum T_{cs} (at around $x = 2.7$ m). This is actually due to the 0.1 T difference at the peak field location near the coil inlet (see Fig. 2.6). Such electromagnetic property thus makes the quench theoretically easier to initiate in the central (or inner) pancakes. Therefore, the 47 % of the quench initiations in the inner or central DPs has been explained by the effect of the strands performance in T_{cs}.

Table 3.2 – Critical parameters and values

Parameter	**Value**[1]	**Unit**
Operating current density ($\mathbf{j_{op}}$)	$4.525 * 10^8$	[A/m^2]
Maximum critical temperature at $B = 0$ T ($\mathbf{T_{c0}}$)	8.9913	[K]
Maximum upper critical field at $T = 0$ K ($\mathbf{B_{c20}}$)	14.4559	[T]
Correction coefficient ($\mathbf{j_{cref} * C_0}$)	$1.24 * 10^{11}$	[A · T/m^2]
Exponent parameters	$\boldsymbol{\alpha} = 0.8885$, $\boldsymbol{\beta} = 1.1947$ $\boldsymbol{\gamma} = 2$, $\mathbf{n} = 1.7$	[–]

[1] JT-60SA TF coils parameters determined with average performance strands

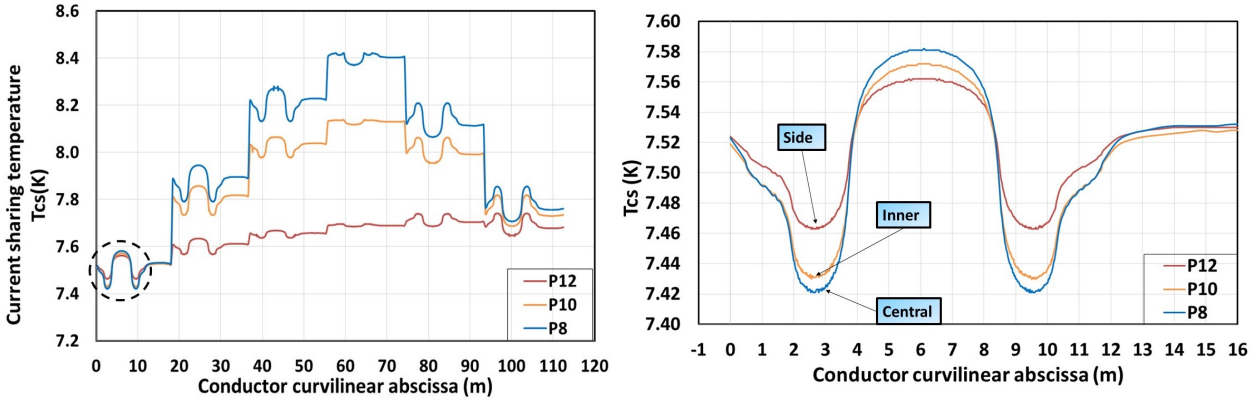

(a) General view

(b) Detailed view

Figure 3.9 – Spatial distribution of the current sharing temperature $T_{cs}(x)$

Nevertheless, the rest half of the quench tests (53 %) are still initiated in the side DPs. This could be due to another fact that the scattering of the strands performance (directly revealed with T_{cs}) would be unavoidable during the strand production. We will then compare three representative strands with their different performances, high, average and low. Here we take 3 TF coils strands that can represent the electromagnetic performance scope across the whole production: K047 (high,

[58] L. Zani, D. Ciazynski, and A. Torre. *Internal report.* 2016.

i.e. maximum exceeding specification), K102 (average, i.e. moderately over specification) and K048 (low, i.e. within specifications)[91]

With Bottura's fit in Eq. (3.14), we can compute for the three strands their T_{cs} at different positions in the coil. Table 3.3 shows that, when making the comparison for a same strand (in a same column), the peak field increases from the side pancake P12 to the central one P8, so that the T_{cs} decreases. The maximal difference of around 40 mK, as mentioned above, then makes the central pancake easier to initiate a quench than the side pancake. While making the comparison between the different strands for a same coil location (in a same row), the high performance strand (K047) has obviously a higher T_{cs} than the average and low performance strands. Their maximum T_{cs} difference can be reached to around 70 mK. This is also coherent with the strands performance definition that a high performance strand can support a higher T_{cs} thus more difficult to be quenched. The two comparisons can tell that the strands performance has a higher impact on the T_{cs} difference (70 mK) than that of the field distribution (40 mK).

Table 3.3 – Current sharing temperature of different strands

	K047 (High)	**K102 (Average)**	**K048 (Low)**
$T_{cs}(B_{max} = 3.037\,\mathrm{T})$ (central P8)	7.452 K	7.427 K	7.379 K
$T_{cs}(B_{max} = 3.015\,\mathrm{T})$ (inner P10)	7.462 K	7.437 K	7.389 K
$T_{cs}(B_{max} = 2.930\,\mathrm{T})$ (side P12)	7.495 K	7.470 K	7.422 K

In order to explain the 53 % quench initiation in the side pancakes, we will make the last but the most important comparison: when taking the lowest performance strand (K048) at the side pancake position (P12), a low T_{cs} can be computed at $B_{max} = 2.930\,\mathrm{T}$ to 7.422 K whereas the highest performance strand (K047) at the central position (P8) has a higher $T_{cs} = 7.452\,\mathrm{K}$. Such computed difference of around $\Delta T_{cs} = 30\,\mathrm{mK}$ can then switch the initial quench location from a central pancake to a side one. The same "diagonal" comparison can be applied to the inner pancakes and to have the different possible initial quench locations.

This intrinsic factor of strands performance, considered having the most important impact on the initial quench location, has also been revealed with a special quench initiation dynamics. Fig. 3.10 shows for the quench test of TFC18 a common quench initiation in almost all the DPs before the start of the FD. From inner DP2 to side DP6, their initial quench moments are within 1 s. This seemingly random phenomenon could then be a good example of the scattering strands performance appearing during the manufacture of the coil TFC18.

Thanks to the above discussions, we can conclude that different electromagnetic performance of the superconducting strands allow to cover all the possible initial quench locations during the test. Nevertheless, the side pancakes manufactured with the low performance strands statistically cannot be that frequent (53 %) to make the majority of quench tests initiate in the side pancakes. Therefore, other possible reasons impacting the statistic phenomenon of the initial quench location must be studied.

[91] L. Zani et al. *IEEE Transactions on Applied Superconductivity* **25**. 2015.

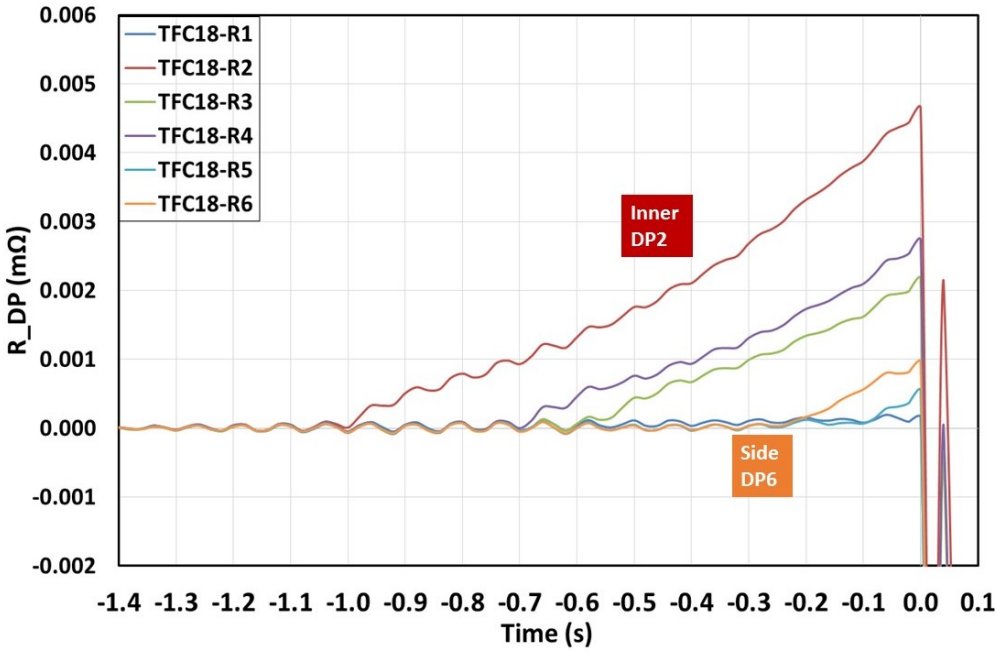

Figure 3.10 – TFC18 DPs quench resistance evolutions during the quench initiation phase

b) External heat load

The second explanation for the different initial quench location is based on the experimental observations. We always take the the representative quench test of TFC12 as an example. Fig. 3.11 shows that, during the whole test, the temperatures of the different positions in the casing generally stay at a higher or even much higher level than that of the winding pack temperature (around 5 K at nominal conditions and around 7.5 K near quench).

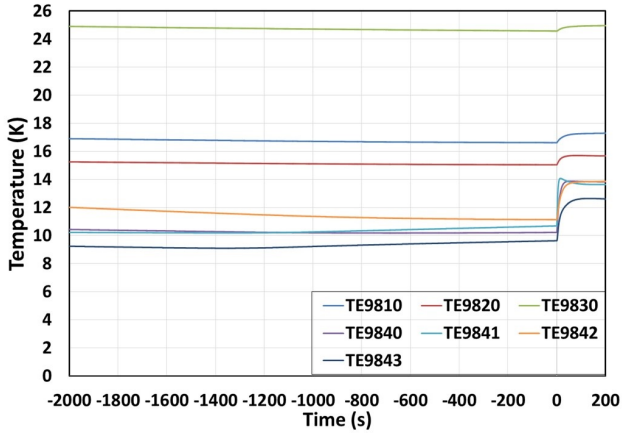

(a) Casing temperature (for TFC12)

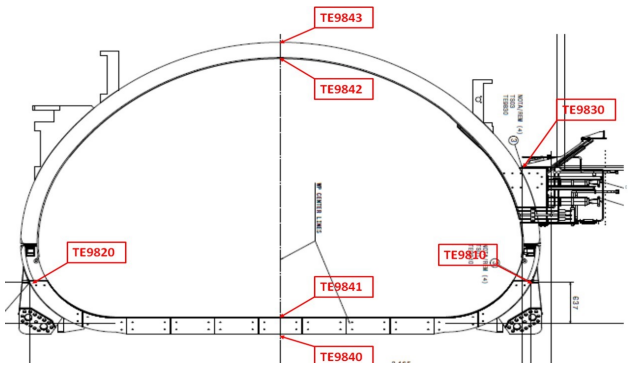

(b) Temperature transmitter position of the casing

Figure 3.11 – Measurement of the casing temperatures

We can see that the different measuring points have given a maximum difference of around 16 K between the joints position (TE9830) and the curved leg outboard (TE9843)[43] in Fig. 3.11. The majority of the temperature measurements indicate a range from 10 K to 20 K for the casing temperature, which are $2 \backsim 3$ times higher than the winding pack temperature. This is actually due to the external heat load from the test environment, including the thermal radiation from the liquid nitrogen thermal shield of the cryostat (around 80 K) and the thermal conduction from the coil supporter feet. In addition, the contact areas between the casing and its outside helium cooling

[43] W. Abdel Maksoud et al. *Fusion Engineering and Design* **124**. 14–17. 2017.

channels are limited by the welding process. The induced temperature gradient then directly leads to a non negligible heat flux from the casing to the winding pack. As the side pancakes (P12 & P1) have a higher contact area with the casing as presented in Fig. 3.12, they will then receive more heat load from the casing.

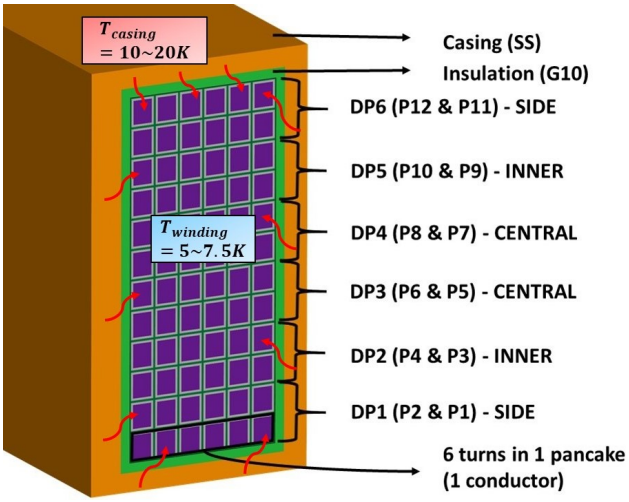

Figure 3.12 – Thermal flux induced by the temperature gradient between the casing and the winding pack

Therefore, the side pancakes, despite of their lower peak field (thus higher T_{cs}), are thermally more vulnerable. This could probably explain the most frequent quench initiation in the side pancakes of around 53 %. The external heat load factor could then be as predominant as the strands performance, for which a numerical model will be built in Chapter 4 to confirm that statement. Nevertheless, the two above factors study could never be exhaustive for such a complex TF coil to explain the different initial quench phenomena. In the following section, we will give a last assumption based on the friction coefficient of the helium flow.

c) Friction factor

As already introduced in Chapter 1, an equation system can be written with the identical pressure drop in the 6 CICCs based on their parallel helium cooling circuits in the coil, as presented in Eq. (3.15).

$$\begin{cases} \dot{m}_{tot} = \sum_{i=1}^{6} \dot{m}_i \\ \Delta P = \Delta P_i \ = f(\alpha_i,\, \beta_i,\, \gamma_i,\, \dot{m}_i) \ (i = 1, ..., 6) \end{cases} \tag{3.15}$$

We recall that the pressure drop by the Darcy-Weisbach law in Eq. (3.16) has been combined with Eq. (3.17) and Eq. (3.18) to compute the helium mass flow rate distribution in the 6 DPs. A maximal difference of 0.15 g/s has been obtained during the testing conditions between 5 K and 7.5 K.

$$\Delta P = \frac{f\,L}{D_h}\frac{\rho\,V^2}{2} = \frac{f\,L}{2\,D_h\,A_w^2}\frac{Q_m^2}{\rho} \tag{3.16}$$

$$f = \alpha + \beta \cdot Re^{\gamma} \tag{3.17}$$

$$Re = \frac{\rho V D_h}{\mu} = \frac{4 \cdot Q_m}{\mu \cdot p_w} \tag{3.18}$$

The different mass flow rate can then have an impact on the helium cooling efficiency by forced convection according to the two correlations determined in Section 1.3.2: the corrected laminar

correlation for laminar regime in the CICC (Eq. (3.19)) and the Dittus-Boelter-Giarratano correlation for turbulent regime in the CICC (Eq. (3.20)).

$$Nu = \frac{h\,D_h}{\lambda_F} = 4.36 \tag{3.19}$$

$$Nu = \frac{h\,D_h}{\lambda} = 0.0259\,Re^{0.8}Pr^{0.4}(\frac{T_{wall}}{T_{He}})^{-0.716} \tag{3.20}$$

The helium cooling effect driven by friction factor could thus be different from one pancake to another or from one coil to another, making the initial quench dynamics very random. Despite of the above difference of 0.15 g/s among the 6 DPs, we can always compute in the testing conditions (laminar regime) a same temperature difference of 8 mK between the cable and the helium. On one hand, this temperature difference could almost be neglected in front of the T_{cs} difference among the pancakes (order of 100 mK). On the other hand, the 8 mK difference also reveals the quasi-negligible impact of the helium flow friction factor on the cable temperature in the 6 DPs. It is to note that, besides the friction factor, the above mentioned heat load distribution can also have an impact on the helium flow velocity thus on the cooling effect in the different pancakes.

In parallel, the CEA Cadarache has also carried out a numerical study about the inhomogeneous friction factor impact on the initial quench dynamics during the TF coils tests[92]. The difference of friction factor due to cabling process has been numerically proven to have a very limited impact on the initial quench dynamics. A maximal difference of the normal zone length evolution has been obtained to only 2 m for the different pancakes, which is considered to be neglected impact in front of the 113.277 m total length of the conductor. Such slight difference of the normal zone length of 2 m can also be explained with the fact that a low friction factor leads to an higher helium flow as well as a better cooling effect by forced convection. Therefore, it will be more difficult to initiate and propagate a quench making the normal zone length shorter than the opposite conditions (high friction factor).

A resume can thus be made here that, due to the particular field map in the CTF on the pancakes, the slight variations in *ALL* the possible factors, including strands performance, external heat load and friction factor, together make different quench tests initiate in different quench locations. As already mentioned before, a more detailed numerical study will be carried out to verify the external heat load impact in Section 4.4.1.

3.3 Study of the physical phenomena during quench acceleration phase

3.3.1 Description of the physical phenomena during quench acceleration phase

As already introduced in Section 3.1.2, the quench acceleration dynamics can also be different from one coil to another. Here we will classify three different types presented with one representative coil each time in Fig. 3.13. The results in the following figures are all computed with the reduced signal data ($G = 10$) thanks to the complete record during the entire test (see Section 2.3.3).

We always start the explanation from the typical quench test of TFC12. Previous work has described a resistance slope change appearing relatively early near the start of the FD in DP1, as presented with the dark blue curve in Fig. 3.13. This "EARLY" quench acceleration phenomenon is actually the most common one that represents 68 % of the quench tests. Two intuitive questions could then be asked:

- Why does the "early" quench accelerates at around $t = 0$ s ?
- Why does it end at around $t = 3$ s?

[92] S. Nicollet et al. *IEEE Transactions on Applied Superconductivity.* 2018.

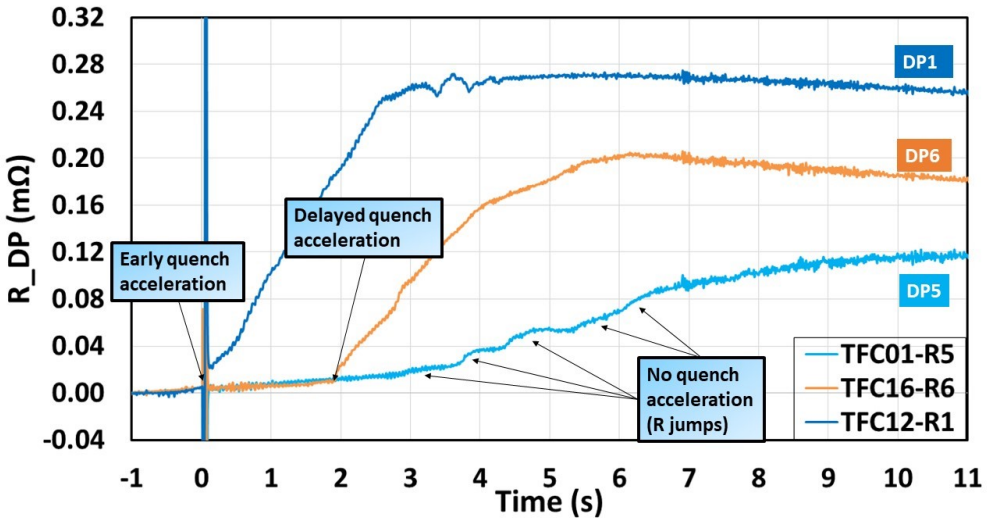

Figure 3.13 – Quench resistance evolutions during the 3 types of quench acceleration phase

A more detailed study will be carried out in the next Section 3.3.2.

Fig. 3.13 also shows another kind of quench acceleration dynamics, the "DELAYED" quench acceleration, presented with the quench test of TFC16 in DP6 (orange curve). We can see that the first sudden slope change of TFC16 occurs in the side DP6 with a delay of around 2 s after the start of the FD. Then the quench resistance evolution has a quasi-linear increase until $t = 4$ s followed by a deceleration up to the maximal resistance plateau of around 0.20 mΩ at $t = 6$ s. When comparing this quench acceleration phenomenon with the above "early" type in TFC12, we can see that TFC16 has obviously a lower quench resistance level than that of TFC12. This is actually coherent with the fact that the Joule effect energy is lower in TFC16 due to the first quench acceleration appearing approximately 2 s after the current discharge. 26 % of the quench tests belong to this "delayed" quench acceleration type. The same questions about the start and the end of this physical phenomenon will be discussed in Section 3.3.2.

Finally, we will specify a very unique observation on the quench acceleration dynamics in DP5 of TFC01 (light blue curve). This is a coil that initiates the quench in the inner DP5. However, the first slope change during the quench resistance evolution has never occurred until a series of resistance jumps appear at around $t = 3$ s. With Fig. 3.13, we can probably identify 5 consecutive resistance jumps with each jump lasting for about 1 s. As this phenomenon takes place along a same pancake, a first explanation could be the transversal quench propagation among the 6 turns of the pancake (see Section 3.3.2).

More details about the three discussed phenomena can be found in Table 3.4. It is to note that, "EARLY", "DELAYED" and "NONE" respectively represent the early quench acceleration, the delayed quench acceleration and the quench without acceleration phenomenon (or with the local resistance jumps). The coils in bold font are those that will be chosen to study in more details the different quench acceleration dynamics in Section 3.3.2.

Table 3.4 – Four different types of the quench acceleration phase

Quench acceleration type	EARLY	DELAYED	NONE
	TFC03	TFC10bis	**TFC01**
	TFC04	TFC14	
	TFC05	**TFC16**	
	TFC06	TFC17	
	TFC07	TFC18	
	TFC08		
	TFC09		
	TFC10		
	TFC11		
	TFC12		
	TFC13		
	TFC15		
	TFC20		
Total Number	**13**	**5**	**1**
Percentage	**68 %**	**26 %**	**5 %**

3.3.2 Experimental analysis of the physical phenomena during quench acceleration phase

a) Study of the predominant physical phenomenon for the early quench acceleration

Fig. 3.14 shows the details of the early quench acceleration phenomenon with the coil TFC12. An important addition to the figure is the voltage measurement of the joint JDP12 (red solid line), the outlet inter-pancake joint connecting DP1 and DP2. The same superconducting material (NbTi) has been used in this joint as in the pancakes. This means that when there is a heating front (e.g. quench) passing through the joint, an abrupt voltage increase can also be detected. Fig. 3.14 shows that at around $t = 3\,\mathrm{s}$, the joint JDP12 sees such a voltage increase. This is almost at the same moment when the DP1 quench resistance reaches the maximal value. The two observations indicates that a full quench could have propagated over the entire DP1 from the inlet (the initial quench position) to the outlet, leading to a sudden stop of the quench resistance rise. Then, an ongoing quench propagation passes through the outlet inter-pancake joint JDP12 leading to an abrupt voltage increase. Up to now, we have answered the first question about the ending phenomenon of the quench acceleration due to a full quench state established in the entire pancake.

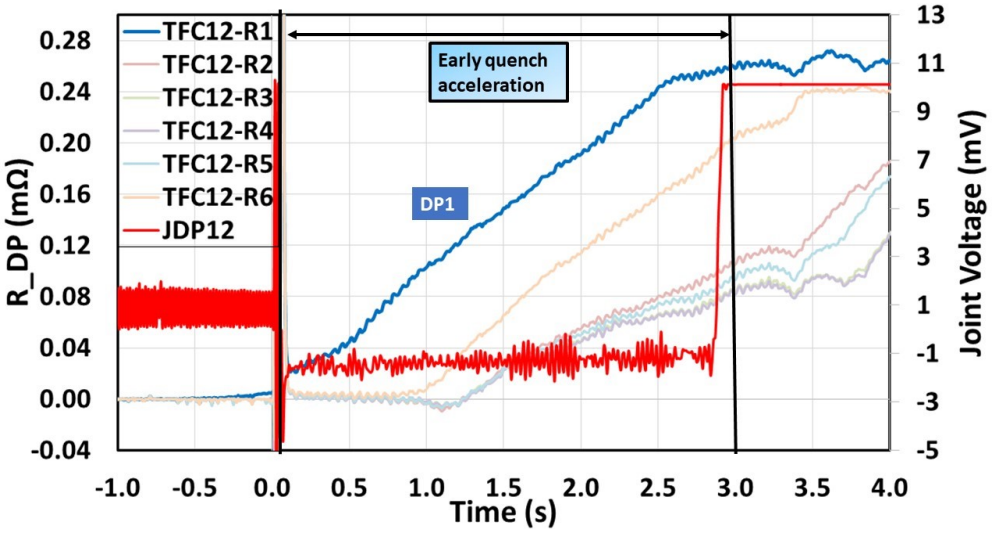

Figure 3.14 – TFC12 DPs quench resistance evolutions during the early quench acceleration phase

The above assumption of full quench state allows us to deduce an important parameter, the longitudinal propagation velocity during the quench acceleration phase. As already computed in Section 3.2.1, the normal zone length during the quench initiation phase is known to be $L_{ini} = 3.78\,\mathrm{m}$. Based on the full quench assumption, we consider that at $t = 3\,\mathrm{s}$, the normal zone length is equal to the total length of the pancake, $L_{tot} = 113.277\,\mathrm{m}$. The average quench velocity during the acceleration phase in DP1 can thus be directly computed with Eq. (3.21):

$$v_{DP1\,acc} = \frac{L_{tot} - L_{ini}}{\Delta t_{acc}} = 36.5\,\mathrm{m/s} \tag{3.21}$$

where $\Delta t_{acc} = 3\,\mathrm{s}$ is the quench propagation period during the acceleration phase assuming that the quench acceleration starts exactly at $t = 0\,\mathrm{s}$. We can see that the order of the quench acceleration velocity is about 6 times the initial quench velocity in TFC12 (36.5 m/s vs 5.82 m/s). This simple computation can, to some extent, prove that it is reasonable to classify the quench dynamics into initiation and acceleration phases at the beginning of our studies.

One may have understood that the principal difference between the early and the delayed quench acceleration phenomena is due to the time delay of appearing the slope change. Nevertheless, another difference could also be seen on the slope change itself: the "continuous" or "discontinuous" property. We will rely on a zoom view of the early quench acceleration resistance (see Fig. 3.15) to make a detailed discussion.

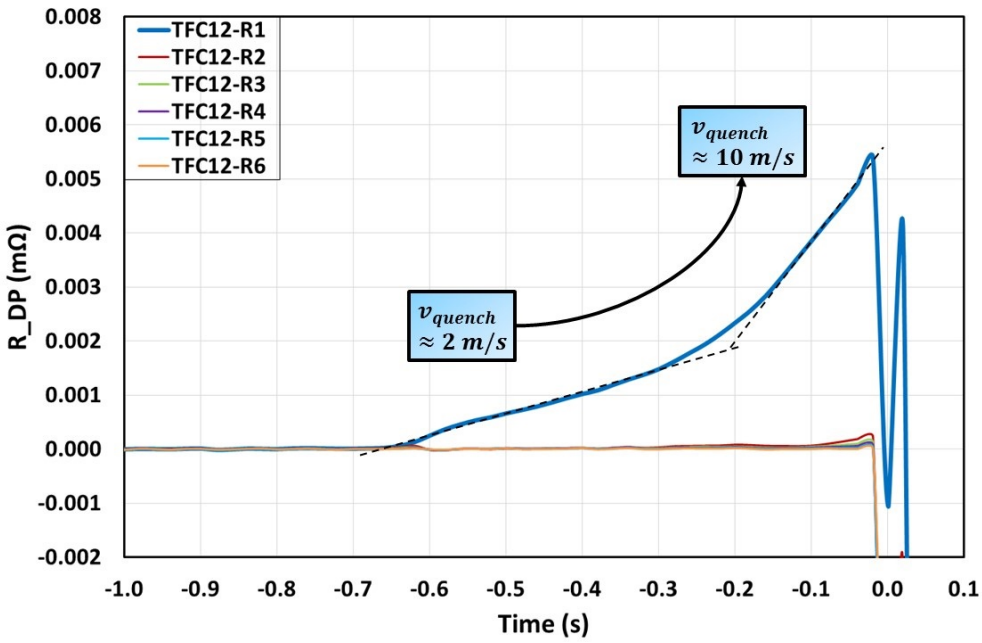

Figure 3.15 – TFC12 DP1 quench resistance evolution before the FD

Fig. 3.15 shows that the initial quench resistance evolution in TFC12 actually does not linearly increase but with a progressive slope change before the start of the FD. Two curve fittings have then been realized along the DP1 quench resistance evolution. With the same computation approach in the quench initiation analysis, we can obtain that during the 0.65 s before the FD, the progressive resistance evolution has already led to a quench velocity difference ranging from 2 m/s to 10 m/s. A factor of 5 has been appeared between the very beginning of the quench and the propagation near start of the FD. This allows us to conclude that the early quench acceleration has actually already appeared in DP1 before the FD and has a relatively continuous way in its slope change. In addition, such slope change will be very likely to keep performing in the continuous way during the entire quench acceleration including the transient moment that the precise measurements are not available (around $t = 0\,\mathrm{s}$). We can say that the early quench acceleration is accompanied by a continuous slope change, which is opposite in the "delayed" type (see the following section).

Concerning the second question, "why does the 'early' quench accelerates at around $t = 0\,\mathrm{s}$", some hypotheses have been proposed to study the quench test of TFC12 as written below:

- Effect of the global increase in helium pressure and temperature
- Effect of the heat flux by the induced eddy currents in the casing
- Competition between two possible quench acceleration mechanisms: helium expulsion driven mode by forced convection or cable quench acceleration by thermohydraulic quench-back

Global increase in helium pressure and temperature

The first hypothesis for explaining the early quench acceleration is based on the global rise of the helium temperature. Fig. 3.16 shows that, from the start of the FD ($t = 0\,\mathrm{s}$) to at least half of the quench acceleration phase at $t = 1.9\,\mathrm{s}$, the inlet and outlet pressures and temperatures all remain nearly stable. This observation reveals that the hypothesis of the global temperature rise (due to pressure rise) up to reach the T_{cs} in DP1 could not be the predominant reason to the quench acceleration dynamics. Moreover, even there appears an abrupt increase in the helium inlet temperature (blue solid line) at $t = 1.9\,\mathrm{s}$, the quench resistance still increases linearly as presented in Fig. 3.14. This again shows the quasi-negligible effect of the global rise in helium pressure and temperature.

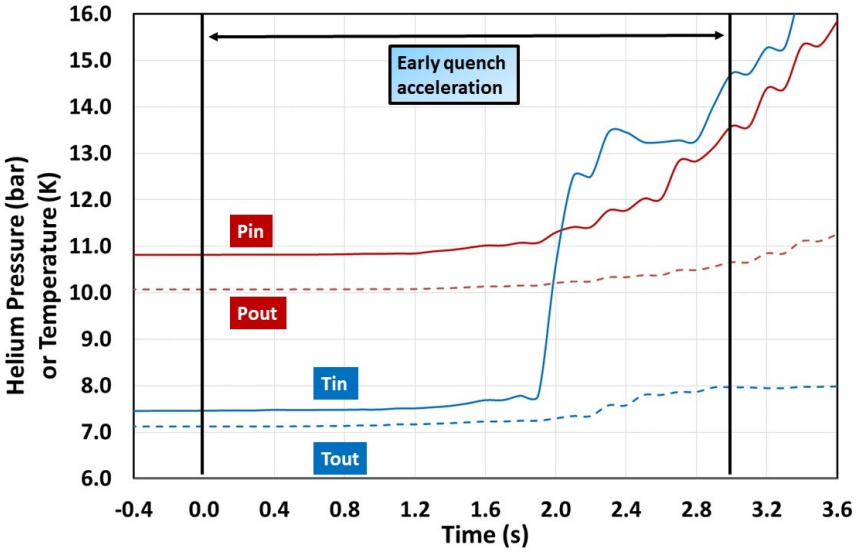

Figure 3.16 – Experimental evolution of the pressures and temperatures during the early quench acceleration phase

After reaching the maximal quench resistance plateau at $t = 3\,\mathrm{s}$, we can also see that there is an ongoing increase in pressures and temperatures. This observation allows to get rid of another hypothesis of the quench acceleration end (for question: "why the quench acceleration ends") due to the helium cooling effect by temperature decrease. This is obviously non-coherent with what we observed in Fig. 3.16.

Electromagnetic quench-back: eddy currents in the casing

As the early quench acceleration always starts near the start of the FD, the second assumption is then based on the Faraday's law of electromagnetic induction in the casing. When a varied current leads to a varied field passing through the coil, eddy currents will be induced in the casing. The heat flux will then be produced by eddy currents in the stainless-steel-made casing and then go to the Winding Pack (WP) leading to a quench acceleration. This second assumption is thus called the electromagnetic quench-back. We know that the side DPs are located at the most outside position of the WP, they will then be the first to receive the heat flux by eddy currents in the casing through a 9 mm thick G10 insulation between casing and WP. This makes the assumption a possibility to

explain the early quench acceleration often appearing at the side DPs near the start of the FD, e.g. DP1 in TFC12.

In order to verify the second assumption, we will compute the characteristic time t_c needed for heat flux to transfer through the 9 mm thick G10 insulation. We will carry out a dimensional analysis on the heat equation established for the insulation and give the characteristic time expression, as written in Eqs. (3.22) to (3.24).

$$\rho C_p \frac{\partial T(x,t)}{\partial t} = \lambda \frac{\partial^2 T(x,t)}{\partial x^2} \tag{3.22}$$

$$\rho C_p \frac{\Delta T}{\Delta t} = \lambda \frac{\Delta T}{\Delta x^2} \tag{3.23}$$

$$t_c = \frac{\rho C_p}{\lambda} l_c^2 \tag{3.24}$$

where the mass density of G10 is $\rho_{G10} = 1950\,\mathrm{kg/m^3}$. The specific heat C_{pG10} and the thermal conductivity λ_{G10} are assumed to be independent of temperature since in this computation, we only focus on the moment near the start of the FD with an average temperature measured to around 11 K. The characteristic length is equal to the insulator thickness $l_c = e_{G10} = 9\,\mathrm{mm}$.

We obtain the thermal conduction characteristic time through the insulator of around $t_c = 24.6\,\mathrm{s}$, which is much longer than the acceleration dynamics which is in the order of several hundreds of milliseconds. Therefore, the second hypothesis of electromagnetic quench-back could not be considered as predominant effect to drive an early quench acceleration.

Comparison between two quench propagation mechanisms

The third assumption focuses on the local quench propagation mechanism inside a CICC pancake. Two theories have been proposed: quench propagation driven by helium expulsion due to forced convection or by the effect of thermohydraulic quench-back.

The most common case is the so-called "standard" quench where the helium expulsion velocity v_{He} and the quench propagation velocity v_{quench} are always equal, as presented in Fig. 3.17a. This quench propagation mechanism has firstly been explained by Dresner[93] with the postulate that the helium in the conduit is the main component that governs the propagation by forced convection. The picture is that the Joule heat produced in the quench region causes the temperature of the local system to increase. This in turn increases the helium pressure leading to a flow of helium in the channel. The bubble of hot helium in the quench region then expands against the confinement by the cold helium ahead of the quench front, thereby propagating the quench. As the expanding edge of the hot helium bubble marks the edge of the normal zone, the quench propagation velocity then equals the local helium expansion velocity, $v_{He} = v_{quench}$. The direct consequence is that *the normal zone engulfs no new helium, or in other words that the heated helium comprises only the atoms originally present in the initial normal zone*[94].

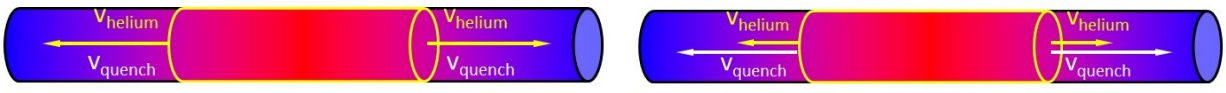

(a) Helium leading acceleration

(b) Cable quench acceleration

Figure 3.17 – Two quench acceleration physics (from L. Bottura)

In 1989, a new quench propagation mechnanism has been discovered by Luongo et al[95] during their numerical study of the CICC for the project Superconducting Magnetic Energy Storage. This

[93] Dresner, Lawrence. *Proc. 10th Symposium on Fusion Engineering*. 2040. 1983.
[94] Dresner, Lawrence. *Proc. 11th Symposium on Fusion Engineering* **2**. 1218–1222. 1986.
[95] Luongo, C. A. and Loyd, R. J. and Chen, F. K. and Peck, S. D. *IEEE Transactions on Magnetics* **25**. 1218–1222. 1989.

is known as the name, thermohdyraulic quench-back (THQB). When this THQB mechanism occurs, the quench velocity will be highly enhanced to be much greater than the helium velocity, as presented in Fig. 3.17b. The explanation is that when a quench triggered, the helium temperature in the quench region increases quickly above the T_{cs} due to the large amount of Joule heat $\dot{q}_{Joule}$ produced in the cable, as presented in Fig. 3.18. Ahead of the quench front, the helium remains essitially at its initial temperature well below the $T_{op} < T_{cs}$ and no Joule heat produced. Nevertheless, the expansion of hot helium will cause a big depletion of helium density in the quench region that leads to a compression ahead of the front ($x > x_{quench}$). This helium compression then induces a fluid motion performing work against the frictional drag force from the inner wall of conduit or the cable. Both the compressional and frictional heatings ahead of the quench front will raise the helium and the superconductor temperatures above the T_{cs} (with $T_{He} > T_{cable}$, see Fig. 3.18). Thereby, Joule heat will have a quasi-instantaneous development over the segments of the conductor. It is this sudden increase in heating power that causes the sharp increase in the quench propagation velocity known as THQB[24,96,97]. Compared to the standard quench, the THQB mechanism will engulf an increasing mass of helium within the normal zone and drive the quench acceleration[98].

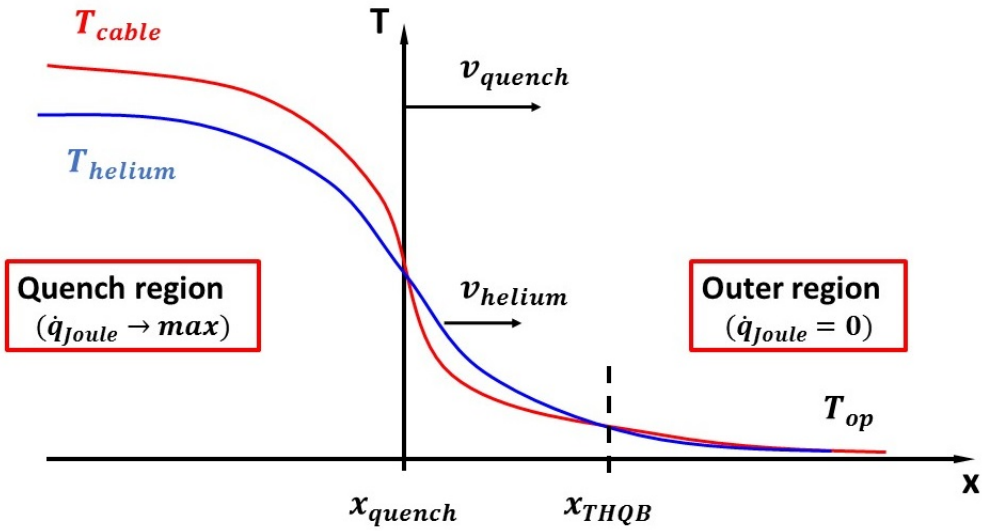

Figure 3.18 – Schematic diagram of the thermohdyraulic quench-back at the local heating front (from L. Bottura)

In addition to the THQB theory, the explosive growth of quench velocity has also been revealed with some experiments[99]. Lue et al have given a very interesting remark that when the temperature difference between the helium and the cable T_{cs} is small enough, the THQB phenomenon starts to exhibit in the CICC. This may be a good hint for us to explain the quench acceleration mechanism in the TF coils quench experiments. As already presented in Chapter 2, the TF coils quench tests are carried out with a global temperature rise from the coil inlet until reaching the quench temperature of around 7.5 K. This quench test procedure is actually very different from the classical scenario that a local heating point by energizing the electrical resistances allows to trigger a quench. The quench test in the CTF allows to establish a homogeneous temperature profile in the entire pancakes leading to a globally low temperature difference ΔT between T_{cs} and helium. Therefore, a high quench propagation velocity v_{quench} can be achieved along the entire pancake according to the inverse relation between v_{quench} and ΔT (see Eq. (1.26)). Moreover, this is also very similar to the THQB experiment by Lue et al. We thus consider that the THQB mechanism will be a plausible reason to explain the "early" quench acceleration in the TF coils.

[24] A. Shajii and J. P. Freidberg. *Journal of Applied Physics* **76**. 3149–3158. 1994.
[96] J. W. Lue and L. Dresner. *Advances in Cryogenic Engineering* **39**. 437–444. 1994.
[97] A. Shajii and J. P. Freidberg. *International Journal of Heat and Mass Transfer* **39**. 491–501. 1996.
[98] L. Bottura. *Accelerator Physics-CERN Yellow Report*. 1–9. 2013.
[99] J. W. Lue et al. *IEEE Transactions on Applied Superconductivity* **3**. 338–341. 1993.

Based on the three hypotheses discussions, we have seen that neither the global rise in temperature nor the heat flux by eddy currents can play the predominant role in the early quench acceleration. Nevertheless, the assumption of the quench acceleration by THQB mechanism is for us the best explanation. This assumption will be confirmed with a further numerical modelling by comparing the local temperature and velocity between the helium flow and the cable part in a TF coil CICC (see Section 4.4.2).

b) Some discussions about the delayed quench acceleration phenomenon

Fig. 3.19 shows the details of the delayed quench acceleration phenomena taking place in a representative coil TFC16. We can see that this time, the voltage signal JDP56 (inter-pancake joint connecting DP5 and DP6) has been added in red line, since the acceleration phase of TFC16 has occurred in the side DP6. The abrupt increase appears at around 6.6 s corresponding again to the maximal resistance value of the DP6 at around 0.2 mΩ. With the same reason, these two observations allow to make a full quench state assumption for DP6 during the test of TCF16.

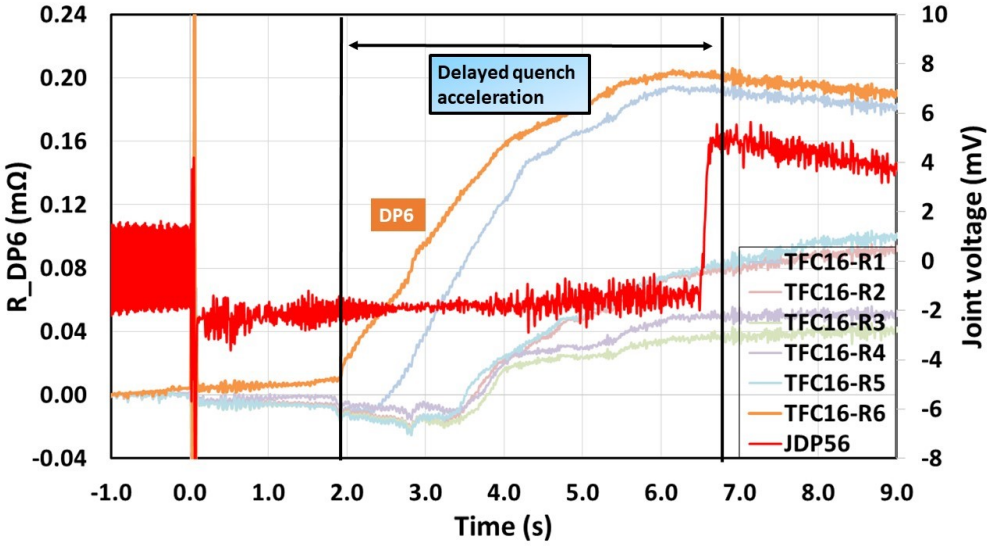

Figure 3.19 – TFC16 DPs quench resistance evolutions during the delayed quench acceleration phase

As the TFC16 has a long delayed quench acceleration dynamics with approximately 2 s after the start of the FD, the magnetic field variation as well as the pressure and temperature evolutions during this period are together making the normal zone length estimation more difficult than for TFC12 (early quench acceleration phase). Nevertheless, Fig. 3.19 tells that the DP6 quench resistance increase is almost linear during this period, which allows to make the hypothesis that the quench propagations before or after the FD are the same. Applying Eqs. (3.11) to (3.12) to the quench test of TFC16, the average quench propagation velocity can be easily computed to 2.87 m/s before the start of the FD. The normal zone length until $t = 2$ s is thus computed to 8.9 m as well as the average quench propagation velocity during the acceleration phase is around 26.1 m/s. We can see that this velocity value is about 30 % lower than the one in the side DP1 of TFC12 due to the low Joule heat produced during the delayed quench acceleration phenomenon.

Unlike the "EARLY" type, the delayed quench acceleration dynamics have a more discontinue slope change after a long initial quench propagation. The classical quench acceleration physics can no longer explain such a long delay phenomenon with slow quench propagation before accelerating. With the actual experimental approaches, we cannot really give a proper explanation. Fortunately, we find that for the first tested coil TFC10, two quench tests have been carried out and have given two different quench acceleration dynamics (early type for TFC10 and delayed type for TFC10bis). As it is happened in the same coil, the only possible reason should be the different temperature

oscillations from the cryogenic controlling system. Some attempts will be made with the numerical modelling to obtain a better understanding on this delayed quench acceleration dynamics (see Section 4.4.2).

c) Analysis of the quench dynamics for a quench test with no acceleration phenomenon

The last type describes a very special phenomenon which only took place during the quench test of TFC01: the consecutive quench resistance jumps appearing in the DP5, as presented in Fig. 3.20. It is to note that the joints voltage measurements were not available on half of the coils manufacture. This is why we cannot add the joint signal to this figure.

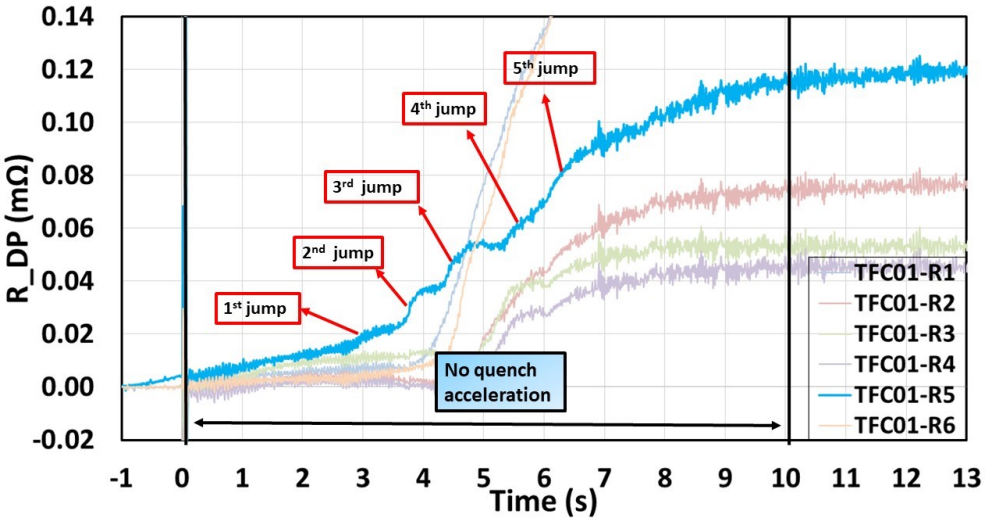

Figure 3.20 – TFC01 DPs quench resistance evolutions with no quench acceleration phenomenon

As already mentioned in Section 3.3.1, the 5 quench resistance jumps appear in succession approximately from $t = 2.8\,\mathrm{s}$ to $t = 7.0\,\mathrm{s}$ with each jump (local acceleration) lasting for about 1 s. The maximal quench resistance plateau is reached in this type at a even lower level of around $0.12\,\mathrm{m\Omega}$ and at a later moment of $t = 11\,\mathrm{s}$.

In order to explain this consecutive local acceleration phenomena, we could rely on the configuration that each pancake is wound in 6 turns in the coil. When the quench is initiated at the inlet of the pancakes, i.e. at the inner turn among the 6 turns (see Section 2.1.2), the longitudinal propagation will preheat its neighbour turn making it closer to the T_{cs}. Once this neighbour turn is quenched, the preheated part will lead to a local quench acceleration (THQB) so as to catch up with the heating front developed earlier in the inner turn. Such preheat process then acts from turn to turn until all the 6 turns are quenched. The 5 jumps of quench resistance recognized in Fig. 3.20 could then be explained with the 5 transversal quench propagations through the inter-turn G10 insulators.

With the same computations realized with Eqs. (3.22) to (3.24), we can obtain the characteristic time of thermal conduction through the 2 mm thick inter-turn G10 insulation around 1 s. This is then in a good agreement with the experimental observation of the local acceleration period, making the inter-turn transversal quench propagation assumption even more acceptable.

Finally, we can apply the same approach to compute the initial quench velocity of DP5 in TFC01 to about $3.14\,\mathrm{m/s}$. This quench test, as named with "No Acceleration", has actually a very long quench initiation phase until at least $t = 2.8\,\mathrm{s}$. If we make a simple computation with the length of one turn (about 19 m) over this initial velocity, a more than 6 s period would be needed for quench to propagate longitudinally from one turn to another. This is actually too long when comparing with the inter-turn transversal quench propagation during about 1 s. Again, the coherence of our

"transversal" assumption has been verified.

A short conclusion can be made here that such no quench acceleration dynamics could be well explained with the combination of the local THQB effect and the inter-turn transversal quench propagation assumption. The latter assumption is especially available when having a slow quench dynamics during the test, such as the case of TFC01. Nevertheless, it remains difficult to know why such dynamics appeared in TFC01.

3.4 Study of the physical phenomena during latter quench phase

3.4.1 Description of the physical phenomena during latter quench phase

As already introduced in Section 3.1.2, latter quench phase describes for the majority of the DPs their *new* quench initiation or acceleration phenomena during the test. The word "new" here is actually for distinguishing from the former quench initiation or acceleration phase. In general, there are two common phenomena taking place during the latter quench phase. The first one is the simultaneous slope change in the latter quenched DPs, e.g. DP2 $\backsim$ DP6 in TFC12. This phenomenon can be found in all the coils quench tests. The second one is that the inner and central DPs undergo two physical sub-phases after their simultaneous quench, a first quench deceleration until a resistance plateau followed by a re-acceleration up to the maximal resistance plateau. Different kinds of quench dynamics have been observed during the sub-phases phenomena. We will discuss three kinds of latter quench phase that have been identified among the 19 quench tests. With the same approach, each type will be explained by a representative quench test.

a) Full re-acceleration phenomenon

As usual, the representative quench test TFC12 is selected to present the most common phenomenon, the full re-acceleration phenomenon. This means that, during the latter quench phase, all the 4 inner and central DPs are firstly experiencing a latter quench initiation (simultaneous) followed by a deceleration to a resistance plateau at around $t = 3.4\,\mathrm{s}$ then having a re-acceleration up to maximal quench resistance plateau, as presented in Fig. 3.21. Here we only plot for the inner and central pancakes one of each, DP2 (red solid line) and DP3 (green solid line), thanks to the coils symmetric property during the quench test. The side pancake DP1 is plotted for reference.

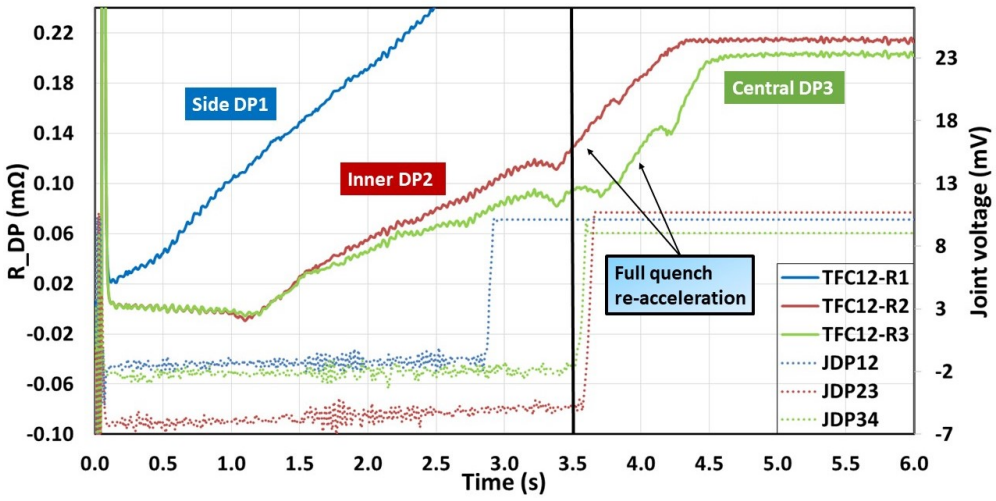

Figure 3.21 – TFC12 DPs quench resistance evolutions with full re-acceleration phenomenon during the latter quench phase

We can see that the DP2 and DP3 have a simultaneous slope change at around $t = 1.2\,\mathrm{s}$. This either indicates a new quench initiation or a quench acceleration depending on the real quench resistance. Indeed, the negative resistance value computed with the pick-up coil method for the first 1.2 s has already been discussed for its quasi-negligible impact on the quench analysis. When there appears the simultaneous slope change in the DPs, some excitation phenomena must have occurred to promote their normal zone developments. A more detailed study will be carried out to search for these possible excitation phenomena in Section 3.4.2.

After the simultaneous slope change moment, the quench resistance evolutions of DP2 and DP3 firstly show an acceleration followed by a deceleration to a resistance plateau at about $t = 3.4\,\mathrm{s}$ and then a re-acceleration up to the maximal quench resistance plateau of around $0.2\,\mathrm{m\Omega}$ at $t = 4.5\,\mathrm{s}$. In order to make a comparison with these evolutions, we have also plotted three voltage signals in thes figure: JDP12 (blue dotted line), JDP23 (red dotted line) and JDP34 (green dotted line), corresponding respectively to the inter-pancake joints connecting DP1 and DP2, DP2 and DP3, DP3 and DP4. When the DPs start the quench re-acceleration at around $t = 3.4\,\mathrm{s}$, the joints JDP23 and JDP34 also show an abrupt voltage increase indicating the quench propagation through these joints. Knowing that they all locate at the outlet of the DPs, we can thus make an assumption that a secondary quench could have been initiated at the outlet of DP2 and DP3 forming a two-direction quench propagation so that the DPs quench resistance evolutions are re-accelerating. To study this outlet secondary quench assumption (for re-acceleration phenomenon) as well as the quench deceleration phenomenon, some more detailed experimental analyses will be carried out in the following Section 3.4.2.

b) Partial re-acceleration phenomenon

The second type of quench dynamics identified during the quench sub-phases is called partial re-acceleration phenomenon. This means that only a part of the inner and central DPs have undergone the quench re-acceleration phenomenon. Fig. 3.22 shows the quench resistance evolutions and the related joints voltage measurements during the second quench test of the coil TFC10 (noted as TFC10bis).

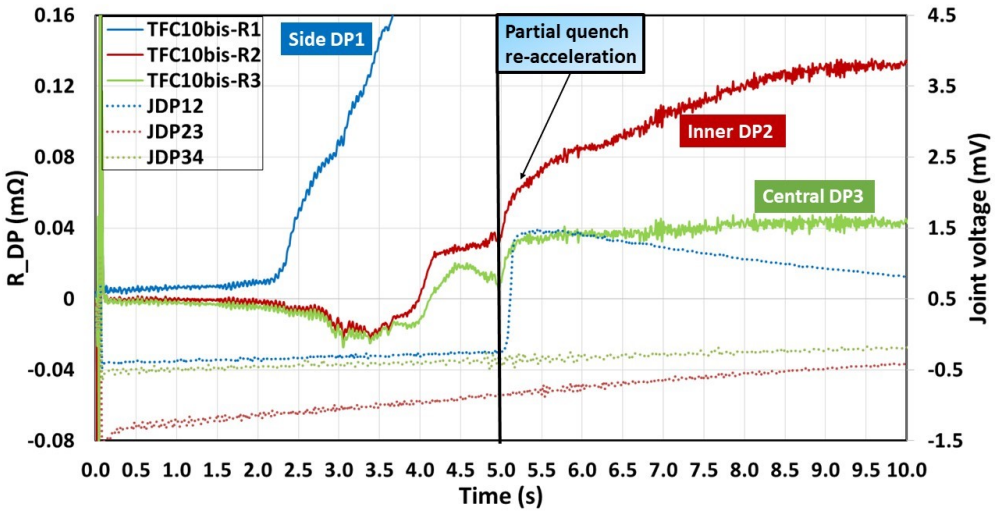

Figure 3.22 – TFC10bis DPs quench resistance evolutions with partial re-acceleration phenomenon during the latter quench phase

With the same color code, we can see that the DP2 and DP3 have simultaneous quench phenomena (slope change) at around $t = 3.5\,\mathrm{s}$ followed by a deceleration until $t = 5.0\,\mathrm{s}$. The resistance evolution of the inner DP2 then has an evident re-acceleration dynamics while the central one has a short resistance jump lasting for around 0.2 s before reaching the maximal plateau of around $0.04\,\mathrm{m\Omega}$.

Moreover, at the same time around $t = 5.0\,\mathrm{s}$, the inter-pancake joint JDP12 (blue dotted line) receives an abrupt voltage increase indicating the fact that the full quench of DP1 has arrived at the joint JDP12 and then continues to propagate into the outlet of DP2 making it quench for a second time. This actually corresponds to the re-acceleration of quench resistance evolution in DP2. Nevertheless, during the whole resistance evolution, we can also see that the joints JDP23 and JDP34 (red and green dotted lines) never show any evidence of quench. This is then coherent with our observation that the DP3 has no any re-acceleration phase.

It is clear that the quench test with a partial re-acceleration phenomenon will have a lower Joule effect energy than the full re-acceleration one when comparing the maximal resistance plateaus of DP2 and DP3.

c) No re-acceleration phenomenon

Once again, we will take the quench test of TFC16 as an example to explain the last identified latter quench dynamics, the sub-phases phenomena without any re-acceleration in the inner or central DPs. Fig. 3.23 presents the same representative DPs and joints with the same color code than before.

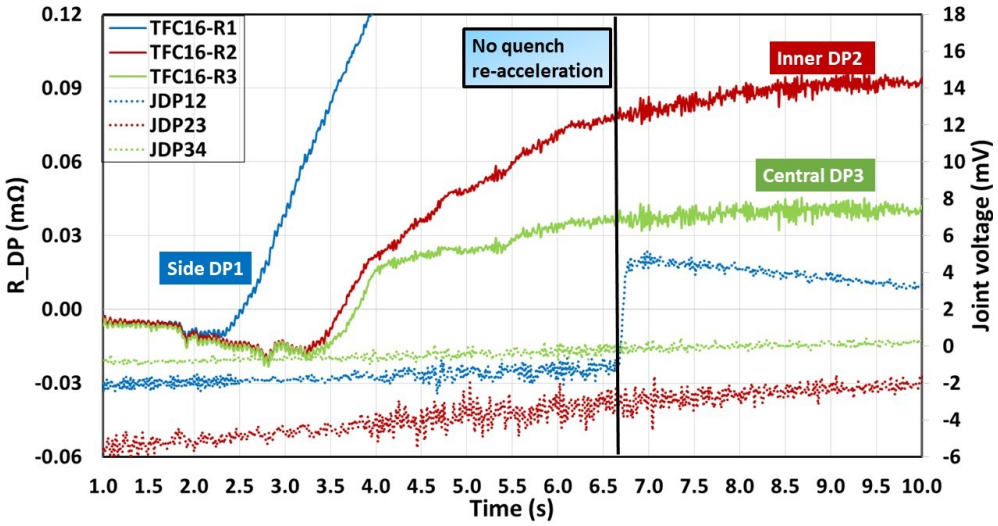

Figure 3.23 – TFC16 DPs quench resistance evolutions without any re-acceleration phenomena during the latter quench phase

We can see that simultaneous quench phenomena appear this time at around $t = 3.2\,\mathrm{s}$. The noticeable difference in quench dynamics is that after a short period of quench acceleration until $t = 4.0\,\mathrm{s}$, both DP2 and DP3 are having a decelerating resistance evolution up to their maximal plateau of respectively $0.09\,\mathrm{m\Omega}$ and $0.04\,\mathrm{m\Omega}$. These plateau levels are even lower than the partial re-acceleration quench test. One may have noted that not only the joints JDP23 and JDP34 never show any voltage jumps, but also the abrupt voltage increase in JDP12 at around $t = 6.6\,\mathrm{s}$ has no any impacts on the latter quench dynamics of the neighbour pancakes DP2. This actually indicates that even if a full quench has propagated through the entire pancakes DP1 (delayed quench acceleration), the ongoing quench propagation through the joint JDP12 could not be strong enough to initiate a quench at the outlet of DP2. This then makes it impossible to re-accelerate in the inner or central DPs. This is also the reason why the maximal resistance plateaus in DP2 and DP3 only reach such a low level, obviously leading to a low Joule effect energy.

One can find more details in Table 3.5 about the three discussed types of the latter quench dynamics. The words "FULL", "PARTIAL" and "NONE" respectively represent the latter quench phenomenon with full re-acceleration in all the inner and central DPs, with partial re-acceleration in only the

inner DPs, and without any re-accelerations in none of the inner or central DPs. We can see that the most common dynamics ("FULL") can represent nearly three quarters of the quench tests while the two others are really in a minority.

Table 3.5 – Three different types of the latter quench phase

Latter quench type (Re-Acceleration dynamics)	**FULL**	**PARTIAL**	**NONE**
	TFC03	TFC08	TFC01
	TFC04	**TFC10bis**	**TFC16**
	TFC05	TFC17	
	TFC06		
	TFC07		
	TFC09		
	TFC10		
	TFC11		
	TFC12		
	TFC13		
	TFC14		
	TFC15		
	TFC18		
	TFC20		
Total Number	**14**	**3**	**2**
Percentage	**74 %**	**16 %**	**10 %**

To summarize the above discussions, we can tell that the simultaneous quench phenomenon is very important to be studied since it is the most common phenomenon that occurs in all the quench tests. Regarding the sub-phases phenomena, the most presented type ("FULL") would be our next studying target, including the quench deceleration phenomenon and the typical re-acceleration dynamics with especially the assumption of a secondary quench at the outlet to be verified.

3.4.2 Experimental analysis of the physical phenomena during the latter quench phase

As already concluded in the last section, we propose again the two key questions when characterizing the different quench dynamics during the latter quench phase:

- Why do the inner and central DPs always have their new latter quench at nearly the same time (simultaneous phenomenon)?
- Why does the majority of the quench tests, after a simultaneous slope change, continue to perform two sub-phases in the inner and central DPs (deceleration then re-acceleration)?

Here, we still take the representative quench test of TFC12 as an example to carry out the following analyses.

a) Simultaneous quench phenomenon in the inner and central DPs

In order to answer the first question, we propose the following possible hypotheses to give some discussions:

- Impact of the inter-pancake transversal quench propagation
- AC losses effect on increasing the cable temperature up to T_{cs}
- Isochoric effect on increasing the global temperature up to T_{cs}
- Helium reverse flow effect on the simultaneous quench

Inter-pancake transversal propagation

The first hypothesis for explaining the simultaneous quench in the inner or central DPs is directly based on the transversal quench propagation through the inter-pancake insulation between these pancakes. With the same dimensional analysis with the heat equation Eqs. (3.22) to (3.24), the characteristic time of the thermal conduction through a 2 mm G10 insulator has been computed in different temperatures, as presented in Fig. 3.24.

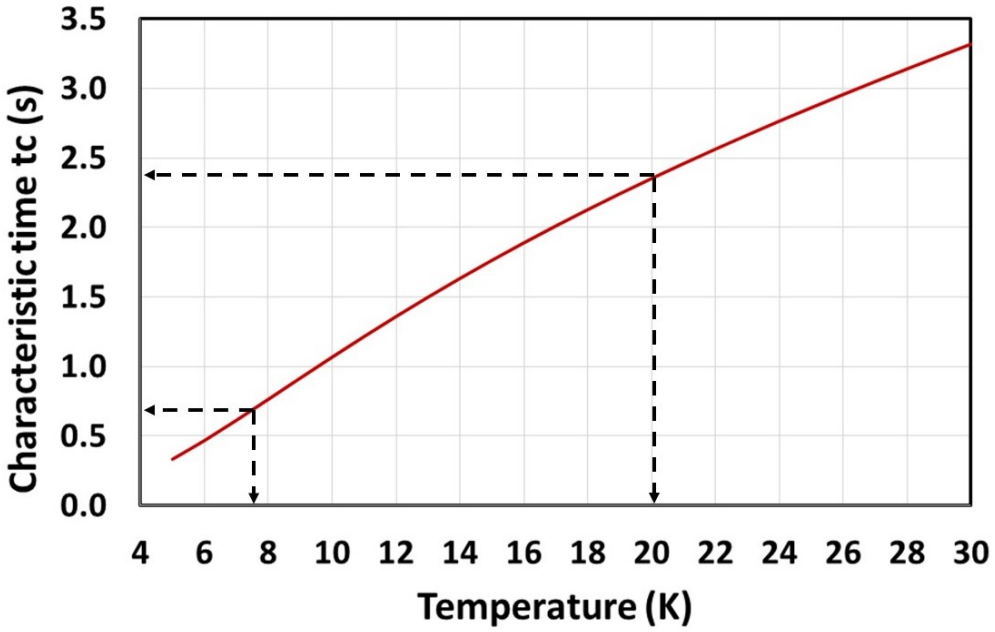

Figure 3.24 – Characteristic time of the thermal conduction through a 2 mm G10 insulation in function of the temperature

Fig. 3.24 shows that the inlet helium temperature variation during the latter quench phase in TFC12 (7.5 K $\backsim$ 20 K) leads to a characteristic time ranging from 0.7 s to 2.4 s. When the 4 inner and central DPs start their latter quench phase at around 7.5 K, we can obtain the corresponding characteristic time of 0.7 s. The real time needed for quench to propagate transversally through the inter-pancake insulation is effectively longer than the 0.7 s taking into account the additional time needed for temperature of the insulator cold side to increase up to quench. Finally, the total time for the heat flux to pass through the insulation layers and to quench the 4 inner and central DPs will be much longer than the quasi-simultaneous quench dynamics within several hundreds of milliseconds (see Fig. 3.21). Therefore, this first hypothesis cannot explain the simultaneous quench phenomenon.

AC losses effect *vs* T_{cs} increasing during the FD

The second hypothesis for explaining the simultaneous quench is the cable temperature rise induced by the AC losses effect. Generally, there are two types: coupling AC losses and hysteresis AC losses, but the coupling AC losses is predominant for TF coils[100] and will only be taken into account in the following analysis.

Fig. 3.25 shows that when a multifilamentary strand is subjected to a transverse varying field H_e, an electric field will be generated inducing eddy currents between the superconducting filaments (SC) and through the copper (Cu) as presented by the black and red circles. The coupling AC losses are only created when the currents cross the normal-conducting matrix which is the resistive part[101], as presented by the yellow circle. The thermal power by coupling AC losses can then increase the

[100] A. Louzguiti. *Thesis*. 245–247. 2017.
[101] Pascal Tixador. *ESAS summer school 2017*. 2017.

filaments temperature and even make them reach T_{cs} to initiate a quench. It is to note that the same type of AC losses can be observed (and more complex) between the strands in a cable with a higher coupling resistance.

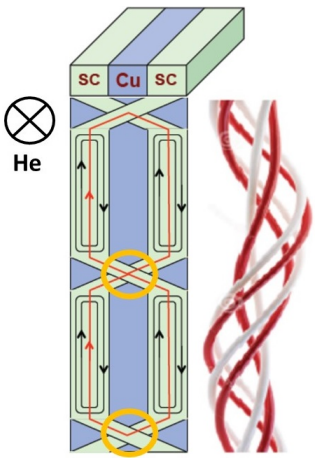

Figure 3.25 – Schematic of the coupling AC losses (from P. Tixador)

The coupling AC losses could be expressed as[102]:

$$P_{coup} = \frac{n\tau * S_{NbTi\ strands}}{\mu_0} * (\frac{dB}{dt})^2 \tag{3.25}$$

where $n\tau = 412\,\text{ms}$ corresponding to an upper estimate for the JT-60SA TF conductor[100] , $S_{NbTi\ strands} = 56.8\,\text{mm}^2$ the cross-section of superconducting strands and $\mu_0 = 4\pi * 10^{-7}\ T \cdot m/A$ the magnetic constant.

The average temperature rise due to coupling AC losses can thus be computed with the heat balance Eq. (3.26):

$$P_{coup} * \Delta t = C_{cable} * S_{cable} * \Delta T_{cable} \tag{3.26}$$

where $\Delta t = 1.2\,\text{s}$ the computation time of coupling AC losses before reaching the latter quench phase, $S_{cable} = 396\,\text{mm}^2$ the cross-section of the cable, and the volumetric thermal capacity computed with Eq. (3.27).

$$C_{cable} = \frac{S_{Cu}}{S_{cond}} * C_{Cu} + \frac{S_{NbTi}}{S_{cond}} * C_{NbTi} + \frac{S_{He}}{S_{cond}} * C_{He} = 171\,877\,\text{J/m}^3 \tag{3.27}$$

While the current decreases from nominal current 25 700 A to 22 833 A during the 1.2 s, the average temperature rise due to coupling AC losses is computed to 28.8 mK. Meanwhile, the minimal T_{cs} increase due to current decrease is computed to 184 mK, which is 6 times higher than the AC losses effect. The coupling AC losses cannot be sufficient for the inner or central DPs to reach their T_{cs} during the latter quench phase. This second hypothesis could neither be neglected nor be predominant to explain the simultaneous quench phenomenon.

Isochoric effect or Helium reverse flow effect

The third hypothesis is based on the experimental observation of a slight increase in the helium inlet temperature. Fig. 3.26 gives a zoom view of the helium inlet temperature of TFC12 (red dashed line). We can see that at the simultaneous quench moment $t = 1.2\,\text{s}$, the temperature has a very slight increase which is caused, according to us, by an isochoric effect due to helium global compression during the quench. Why asserting *isochoric* here? The reason is that when the FD begins, the inlet and outlet helium valves (noted as He Valve) close as well as the two safety valves

[102] R. Vallcorba et al. *IEEE Transactions on Applied Superconductivity* **28**. 2018.

(noted as Safety Valve) will not open until 5 s after the FD (see Fig. 3.28). This then forms an isochoric system around the coil. Therefore, a global pressure rise can lead to a global temperature increase, as detected by Tin_TFC12 in Fig. 3.26.

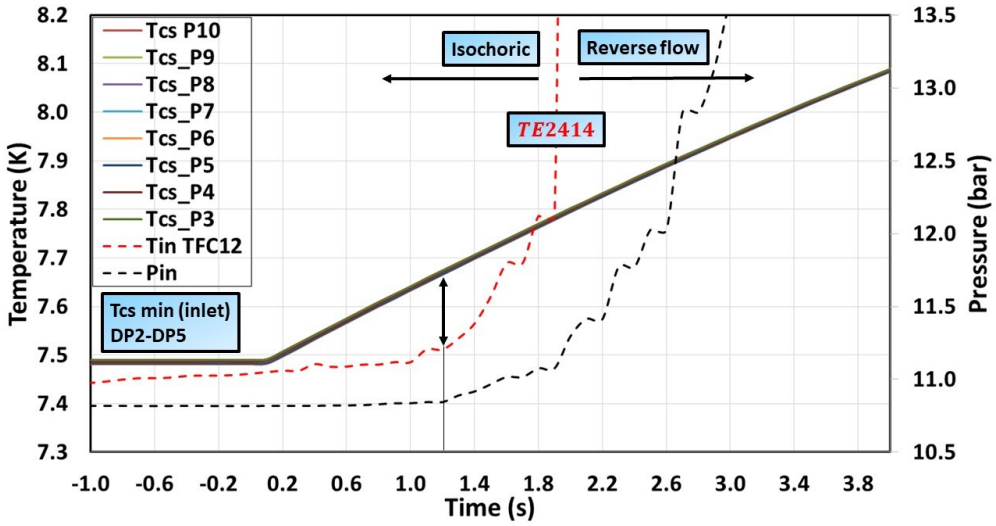

Figure 3.26 – Increase of helium temperature by the isochoric effect or the reverse flow effect

Moreover, the current sharing temperature T_{cs} at the inlet of the 4 inner and central DPs (from P3 to P10 in Fig. 3.26) can be obtained with the Bottura's fit Eq. (3.14) in fixing the critical current density:

$$j_c = j_{op} = \frac{I_{op}}{S_{NbTi}} = \frac{25\,700\,\text{A}}{5.68 * 10^{-5}\ \text{m}^2} = 4.52 * 10^8\ \text{A/m}^2 \tag{3.28}$$

and using the JT-60SA TF coil parameters already presented in Table 3.2.

Fig. 3.26 shows the evolution of the computed current sharing temperature T_{cs} in the inner or central pancakes and the helium inlet temperature measured by TE2414 during the first seconds after the FD. We can see that T_{cs} is strongly impacted by the current discharge, i.e. the magnetic field decrease. During the first 1.8 s, all pancakes T_{cs} increase faster than the measured helium inlet temperature (Tin_TFC12). At $t = 1.2$ s, the computed T_{cs} is about 150 mK higher than the helium inlet temperature slightly increased by the isochoric effect. This then indicates that the isochoric effect on temperature rise could not be sufficient for all the inner and central DPs to reach their T_{cs} during the latter quench phase. The third hypothesis could not be the predominant effect on the quench simultaneous phenomenon either.

Finally, we attempt to seek for the last possible explanation, the ***helium reverse flow effect***. It means that in the first quenched pancakes (e.g. DP1 in TFC12) the helium receives so much heat at the normal zone that it is expulsed to the outside of the pancakes. As the quench is initiated near the inlet of the coil, the heated helium could be easily expulsed from the inlet of DP1 thanks to a low pressure drop. It then enters in the other DPs via the common inlet piping of the coil to eventually quench them. This can make the inner and central DPs reach their latter quench phase in a simultaneous way. The helium reverse flow hypothesis could also explain the sudden slope change at around $t = 1.8$ s observed in the inlet temperature (Tin_TFC12) (see Fig. 3.26).

Based on the above four discussions for explaining the simultaneous quench phenomenon, the helium reverse flow effect seems to be the best assumption. In order to have a further verification, some numerical modellings will be carried out in Section 4.4.3.

b) Sub-phases phenomena during the latter quench phase

Concerning the two sub-phases phenomena taking place during the latter quench phase, the discussions will be obviously divided into two parts (always taking TFC12 as an example):

- Before $t = 3.4\,\mathrm{s}$, the inner and central DPs are firstly having a simultaneous quench initiation then decelerating to a resistance plateau near 3.4 s (see Fig. 3.21).
- After $t = 3.4\,\mathrm{s}$, the inner and central DPs are having a re-accelerating quench resistance evolution until reaching their maximal resistance plateau (see Fig. 3.21).

Quench deceleration due to the magnetic field distribution

According to the magnetic field map (see Fig. 2.6), we can know that about 35 % of the pancake length is under a low magnetic field of about 1/3 of the maximal peak field value ($B \leqslant 1\,\mathrm{T}$). This field distribution can directly lead to a higher T_{cs} for the pancakes and thus be more difficult to quench. Knowing that the quench velocity is inversely proportional to the temperature difference between the cable quench point T_{cs} and the helium T_{He}. Such higher T_{cs} can thus decelerate the quench propagation owing to the higher temperature difference as well as the better "cooling effect" with lower Joule heat. This hypothesis based on the magnetic field map will be verified with some numerical modellings in Section 4.4.3.

Quench re-acceleration due to a secondary quench initiation

Concerning the quench re-acceleration phenomenon, the most physical reason can be relied on the detection of the voltage jumps in the inter-pancake joints. It indicates a secondary quench that has been initiated at the pancakes outlet (inner or central) forming a two-direction quench propagation from the two cable ends. Therefore, a higher resistance slope has been appeared during the quench propagation. In order to explain this secondary quench assumption, two hypotheses have been proposed below:

- Normal zone propagation from the fully quenched pancakes (e.g. DP1 in TFC12) to the outlet of the latter quenched pancakes (e.g. inner or central DPs in TFC12) through the joints.
- Helium reverse flow effect performing at the outlet of the DPs.

Both of the two hypotheses are based on the observation of the DPs resistance evolutions in Fig. 3.27. We can see that at around $t = 3.5\,\mathrm{s}$, two phenomena take place at almost the same time: the fully quenched pancakes (side DP1 and DP6) reach their maximal resistance plateau and the latter quenched pancakes start the quench re-acceleration in all the inner and central pancakes (DP2 $\backsim$ DP5).

As the pancakes are connected with both electrical and hydraulic ways at the outlet, two explanations are then proposed and illustrated in Fig. 3.28. The electrical connection is made via inter-pancake joints, from JDP12 to JDP56. The normal zone propagation will not only go through the joints connection to the two connected DPs, but also transversally between the joints through the insulation as presented by the red dotted arrows in Fig. 3.28. At that point, a secondary quench can be initiated with the electrical way at the pancakes outlet and cans lead to the re-acceleration phenomenon.

Concerning the second assumption, it is actually based on the hydraulic connection at the coil outlet. When a full quench propagated over the entire DP, the helium could most probably be driven to expulse from the outlet and to enter into the outlet of the other pancakes through the principal hydraulic connections. The heated helium then initiate a secondary quench at the pancakes outlet in a quasi-simultaneous way. Therefore, a re-acceleration has been appeared in their resistance evolution. This helium reverse flow effect from the outlet has also been presented by the thick blue arrows in Fig. 3.28.

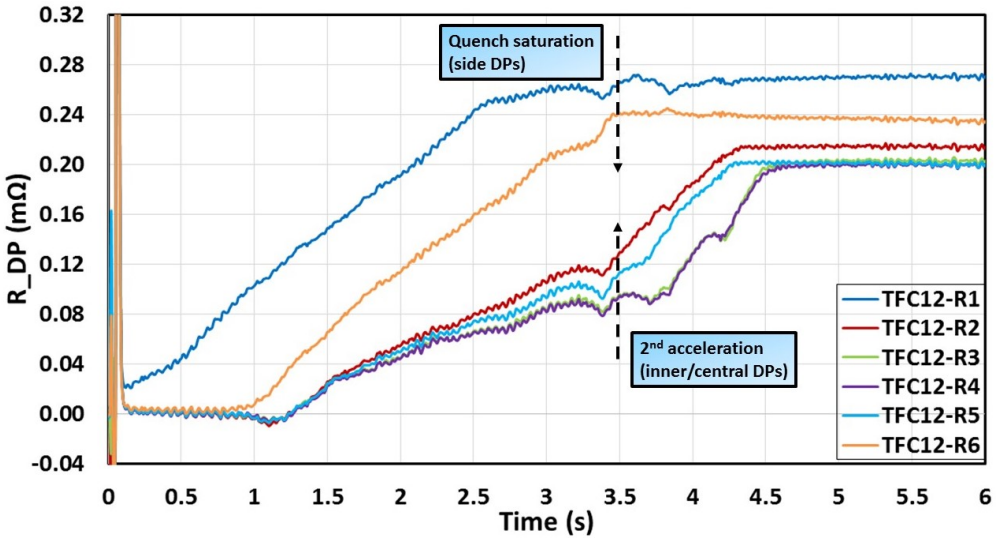

Figure 3.27 – Impact of the side DPs full quench propagation on the inner or central DPs

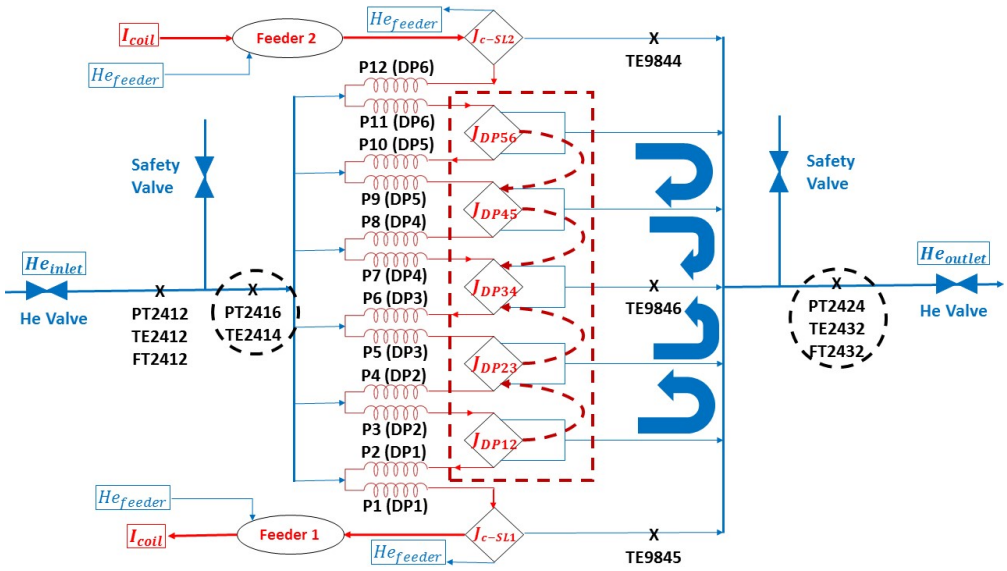

Figure 3.28 – Illustration of two hypotheses for re-acceleration phenomenon in the pancakes

Some final comments should be made here on the two hypotheses of the re-acceleration phenomenon. If tested with numerical computations, it will be necessary to build a quite complex 3D numerical model coupling at least half of the DPs (e.g. DP1 $\backsim$ DP3) for the simulations. This is not the purpose of this work as our model focuses on one single phenomenon at a time. But this could open a study direction for the future.

3.5 Study of the physical phenomena during quench saturation phase

3.5.1 Quench resistance evolution during saturation phase

As already introduced in Section 3.1.2, quench saturation phase describes the phenomena where, at the end of the quench acceleration phase or the latter quench phase, all the DPs reach a maximal resistance plateau, followed often by a global decreasing evolution along the time. Fig. 3.29 shows the quench saturation phase during the representative quench test of TFC12. According to the previous work in quench acceleration and latter quench dynamics, we know that the maximal plateau in the

side DPs of TFC12 represents the full quench propagation through the entire pancakes, while for the inner or central DPs, we still have no clear idea about their quench level (full quench over the entire pancakes or partial quench stopped somewhere inside the pancakes). To study this question, we will build a simplified physical model in the next Section 3.5.2 to give some detailed explanations.

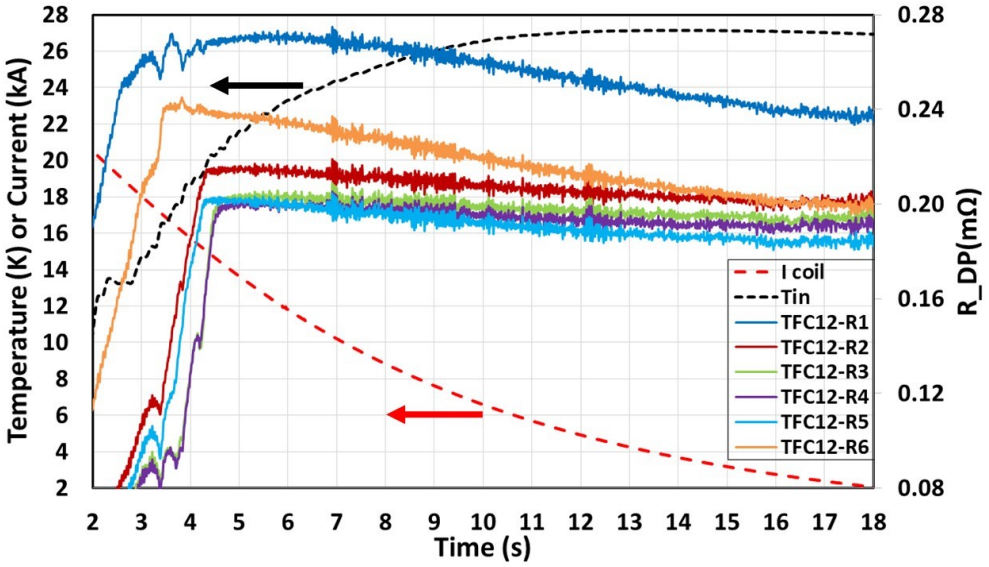

Figure 3.29 – Quench resistance evolutions with the helium temperature and current measurements for TFC12

Fig. 3.29 shows that after reaching the DPs maximal quench resistance plateaus at around $t = 3.5\,\mathrm{s}$ (for DP1 and DP6) and $t = 4.5\,\mathrm{s}$ (for DP2 $\backsim$ DP5), a progressive decrease has been appeared along the time. In order to explain this phenomenon, we plot two more curves in this figure, the coil current discharge (red dashed line) and the inlet average helium temperature (black dashed line). We can see that during the whole decrease of the maximal quench resistance plateau, the inlet helium temperature keeps increasing up to a saturated level of around 27 K while the coil current is obviously decreasing during the FD. A first indication could be that the pancakes magneto-resistance property has a predominant impact on the global decrease of the maximal resistance plateaus since the current has a very fast decrease during the FD.

Here we can take the side pancakes DP1 as an example to make some simple verifications. Fig. 3.29 presents that the quench resistance of DP1 has reduced to about 11 % from $t = 6\,\mathrm{s}$ to $t = 16\,\mathrm{s}$. Thanks to the slight increase in the average temperature of 4 K and to the electrical resistance definition equation $R = \rho(T, B)\frac{l}{S}$, we can estimate the contribution of the pure magneto-resistance property leading to a resistance decrease to around 20 %. This indicates that only with the current discharge effect (about 76 % reduction during this period), the decrease of the maximal resistance plateau will be overestimated by 9 %. This difference can then be explained with the compensation of the thermo-resistance property by Joule heat on temperature increase. The magneto-resistance property is then more predominant than the thermo-resistance property.

Meanwhile, we can also observe that the maximal resistance plateaus of the central and inner pancakes (DP2 $\backsim$ DP5) have a much lower decrease with respect to the two first quenched pancakes (DP1 and DP6). The decrease is computed to around 3 % for the inner and central pancakes if we take the same period from $t = 6\,\mathrm{s}$ to $t = 16\,\mathrm{s}$. In addition, around 17 % reduction caused by the pure magneto-resistance property can be estimated for the inner and central DPs. This means that the 14 % difference should be compensated by the Joule heat, which is even higher than the one in the side pancakes of around 9 %. Nevertheless, the thermo-resistance property is always less predominant than the magneto-resistance property.

The two above comparisons have actually proven the coherence with the thermal phenomenon that an homogenisation will take place between the warmer and the colder pancakes, i.e. between the

first quenched DPs (DP1 or DP6) and the latter quenched DPs (DP2 ∽ DP5). From this point of view, as the Joule heat releasing side, the thermo-resistance property will have a lower impact on the first quenched DPs (about 9 %) whereas the latter quenched pancakes, as the Joule heat receiving side, are more impacted by this thermo-resistance property (about 14 %).

A short conclusion can thus be made that the progressive decrease of the global quench saturation resistance is a combined result of the thermo- and magneto-resistance properties. In particular, the magneto-resistance property is more predominant than the thermal one due to a fast current discharge in the coil.

3.5.2 Study of the pancakes normal zone length with a simplified physical model

a) Description of the simplified physical model

The question about the real normal zone length has already been discussed during the previous work. It is evidently very helpful for our quench saturation study to be able to know if one DP has established a full quench state along the entire conductors or just a partial quench stopped somewhere inside the conductors. In order to realize this objective, we are trying to find a method that allows to compute the normal zone length evolution (L_{quench}) from the experimental quench resistance of each DP ($R_{exp\,DP}$), as presented below in Fig. 3.30.

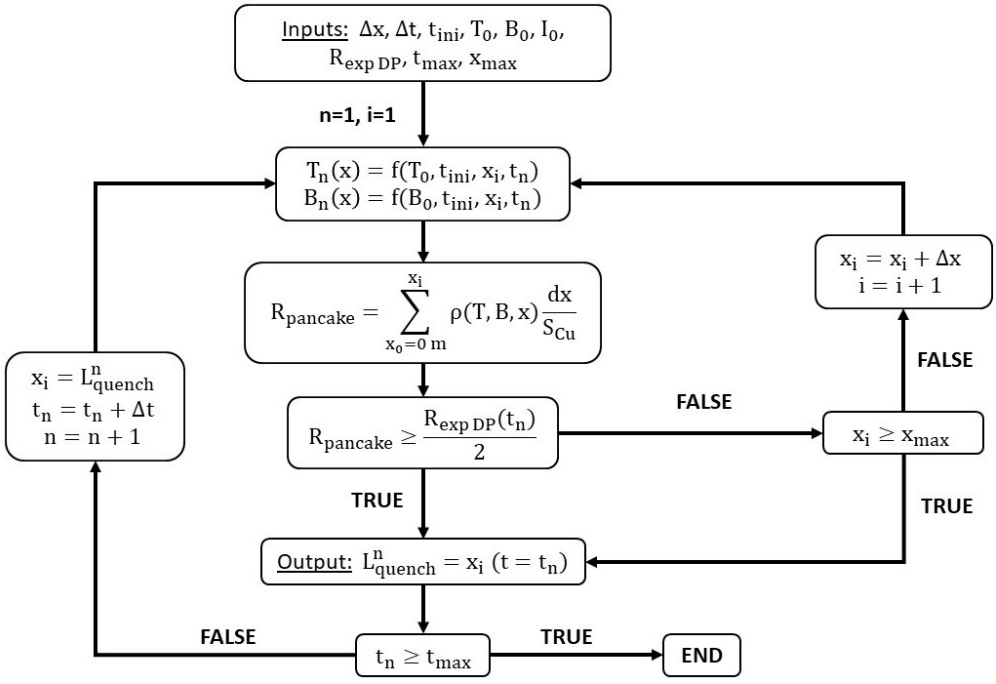

Figure 3.30 – Flow-diagram of the normal zone length computations in the simplified physical model

According to the flow-diagram, the experimental quench resistance data $R_{exp\,DP}$ is read at the beginning of the computation. The other necessary inputs are also fixed, including the element size and time step (Δx and Δt), the initial quench time (t_{ini}), the initial temperature (T_0) equal to TF coils quench temperature (around 7.5 K), the nominal values of current and magnetic field (I_0 and B_0), the maximal time of resistance evolution covering the entire quench dynamics ($t_{max} = 15$ s) as well as the maximal normal zone length which is obviously equal to the pancake total length ($x_{max} = 113.277$ m). These inputs allow to determine the temperature profile $T_n(x)$ and the magnetic field map $B_n(x)$ at each time step t_n. Based on the definition of the electrical resistance (written in discretization), the pancake normal zone length at t_n (L^n_{quench}) can then be obtained by approaching

the computed quench resistance to the experimental data. The loop logic is also a classical one that we add an element size or a time step at a time to approach the experimental value until reaching their maximum t_{max} and x_{max}. In the following, we will give a detailed description about the construction of the time- and space-varying temperature and magnetic field as well as the necessary conditions applied in this physical model.

Our simplified physical model has then been built based on the classical definition of the electrical resistance as:

$$R_{exp\,pancake} = \int_0^{L_{quench}} \rho(T, B, x) \frac{dx}{S_{Cu}} \tag{3.29}$$

The computation is realized by discretizing the cable length into small elements. Each element size is fixed to $dx = 20\,\text{mm}$ which corresponds to about one hundredth of the detectable normal zone length. Therefore, it can be considered as small enough to reproduce the quench dynamics. Moreover, this element size is satisfied with the stability criterion of finite difference method (explicit)[103] as expressed in Eq. (3.30):

$$\kappa \frac{\Delta t}{(\Delta x)^2} \leqslant \frac{1}{2} \tag{3.30}$$

where κ is the thermal diffusivity, Δt and Δx the time step and the element size in the computations. First of all, we have chosen $\Delta t = 20\,\text{ms}$ as the departure point of the model. This time step is 5 times smaller than the quench detection and action time of $\tau_{da} = 100\,\text{ms}$, thus can be taken as appropriate. We then compute a general thermal diffusivity of the entire CICC, including NbTi and Copper strands, helium flow, stainless steel jacket and G10 insulation (with experimental temperature ranging from 7.5 K to 30 K). Finally, an upper limit of the stability criterion can be obtained to $\Delta x_{min} \geqslant 11\,\text{mm}$. The 20 mm can thus be taken as a satisfied element size in this model.

The Eq. (3.29) will actually be applied at each time step ($\Delta t = 20\,\text{ms}$) in this model making the parameters both space- and time-dependent thus complex to be modelled. Here, our first hypothesis is that the quench is initiated exactly from the conductor inlet at $x = 0\,\text{m}$ for simplifying the following computations. Indeed, this assumption is somewhat close to the reality since the quench is initiated near the peak field position at $x = 2.7\,\text{m}$ (see Fig. 2.6). Such 2.7 m difference with respect to the total length of 113.277 m (around 2.4 %) can make the assumption acceptable in such a simplified model. The normal zone length L_{quench} at each time step can thus be obtained thanks to the iterative computation of the quench resistance in the pancake and the comparison with the experimental data $R_{exp\,pancake}$.

Concerning the copper electrical resistivity $\rho(T, B, x)$, it depends on the temperature and the magnetic field. As both of them are space-dependent parameters, the electrical resistivity is then also dependent on the position x in the pancake. The cross-sectional area of copper strands is always taken to $S_{Cu} = 180\,\text{mm}^2$.

One may note that, there are two unknowns in Eq. (3.29), the temperature profile $T(x, t)$ and the magnetic field map $B(x, t)$. In the following discussions, we will take the quench test conditions of TFC12 as an example to build the space- and time-varying evolution for the two parameters.

Temperature evolution

The temperature profile along the conductor will be constructed with two hypotheses:

- As the coil is always quenched near its inlet, the hot spot temperature is assumed to be appeared exactly at the inlet of the cable.
- As the longitudinal quench propagation is predominant in the cable, a linear profile of temperature is assumed to be established along the conductor.

[103] J. G. Charney, R. Fjortoft, and J. Von Neumann. *A Quarterly Journal of Geophysics-Tellus* **2**. 237–254. 1950.

First of all, we apply the following heat equation to compute the hot spot temperature, as written in Eq. (3.31).

$$(\rho C_p S)_{tot} \frac{dT}{dt} = k_{Joule}\, \rho_e\, j_{op}^2\, S_{Cu} \tag{3.31}$$

where ρ_e and j_{op} are respectively electrical resistivity and operating current density. As both of them are electromagnetic-based parameters, the magnetic field of each DP will also be determined in the next sub-section. The right-side term of Eq. (3.31) is the only heat source of the equation, the Joule heat. It is produced when the quench is initiated in the DP with the Joule coefficient $k_{Joule} = 1$. If not, $k_{Joule} = 0$. One has to know that this Joule heat term is directly related to the initial quench moment of each DP and will determine the level of the hot spot temperature at the DPs inlet. This remark could actually allow to verify the pancakes real moment of the quench initiation ("hidden" by the error of pick-up coil method). This part of analysis will be carried out in the following section. $\rho C_p S$ is the total specific heat per unit length that is expressed as the sum of the components in conductor and the helium, as written below in Eq. (3.32)).

$$(\rho C_p S)_{tot} = (\rho C_p S)_{NbTi} + (\rho C_p S)_{Cu} + (\rho C_p S)_{SS} + (\rho C_p S)_{Ins} + (\rho C_p S)_{He} \tag{3.32}$$

where each thermal part contributes a temperature-dependent specific heat ρC_p weighting with cross-sectional area. The integration of the helium part makes the heat equation a hybrid energy equation combining the conductor and the helium. This is actually based on the quasi-negligible temperature difference between the helium and the conductor (conduit wall + cables) owing to the high heat exchange efficiency by forced convection in the CICC (see Section 1.3.2). Moreover, this heat equation also relies on an optimistic assumption that the thermal homogenisation in the entire conductor (NbTi + Cu + Stainless Steel + Insulator) is fast enough to be able to take a mono temperature during the computations.

Eq. (3.31) is applied to an iterative scheme with the initial conditions equal to the quench critical temperature of TFC12 at around 7.46 K. The time evolution of the hot spot temperature in all the pancakes can then be obtained with Eq. (3.31). Fig. 3.31 shows the time evolution of the hot spot temperature of P2 at $t_{quench} = -0.65$ s (blue line), P12 at $t_{quench} = 0.9$ s (red line) and simultaneous quenched pancakes at $t_{quench} = 1.27$ s (green line). We can see that the earlier the quench moment arrived the higher the hot spot temperature can be reached. For instance, the side pancake P2 is the first to quench at $t_{quench} = -0.65$ s, its hot spot temperature is about 12 K higher than the latter quenched side pancake P12 at around $t_{quench} = 0.9$ s. This is actually coherent with the impact of the Joule heat on the hot spot temperature level.

As the last hot spot temperature evolution has been determined at the pancake inlet, the boundary conditions of the inlet temperature have thus been obtained for each time step allowing to establish a linear spacial profile along the pancake. This is expressed below in Eq. (3.33):

$$T^n(x) = \frac{(T_{hs}^n - T_0)}{L_{quench}^n} \cdot x \tag{3.33}$$

where T_{hs}^n is the hot spot temperature at the pancake inlet for each time step n, T_0 the initial temperature for TFC12 (7.46 K) and L_{quench}^n the normal zone length computed at time step n. It is to note that this simplified linear profile has been verified with our numerical model (see Chapter 4). It is actually an ongoing varied profile that can only be determined when obtaining the final normal zone length for each time step n. The time- and space-dependent temperature evolution is actually the most important part of this simplified physical model.

Magnetic field map

As mentioned in Eq. (3.29), the copper electrical resistivity $\rho(T, B, x)$ also depends on another important parameter, the magnetic field map along the condutor. Like for the temperature profile, the magnetic field map should also be determined both in time and space for all the pancakes. Fortunately, the nominal field spatial distribution has already been achieved with a preliminary

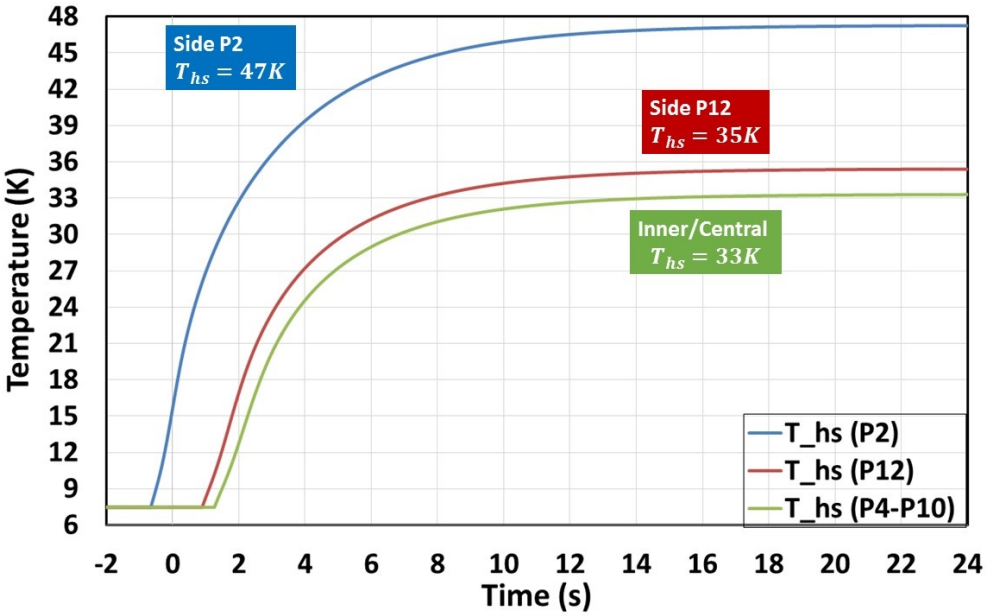

Figure 3.31 – Hot spot temperature evolutions in the different DPs

work for the JT-60SA TF coils[58] whereas the time-dependent evolution will be obtained with a simple proportional relation as written in Eq. (3.34) for magnets with no magnetic materials:

$$B(x,t) = \frac{B_n(x)}{I_n} I(t) \tag{3.34}$$

where $B_n(x)$ is the nominal field spacial distribution, I_n the nominal current imposed at 25 700 A and $I(t)$ the measured current evolution along the time. This relation is actually based on the Ampère's Law in the vacuum $curl(B) = \mu_0 \cdot j$ with the magnetic constant $\mu_0 = 4\pi * 10^{-7}$ H/m.

Thanks to the relation in Eq. (3.34), we can easily determine the time- and space-dependent profile for magnetic field. This means that, when the coil current decreases to a low level, (e.g. 1/10 of nominal current), the magnetic field will also decrease to its one tenth but stay at a same spacial profile than the nominal conditions.

Up to now, as the two key parameters, temperature and magnetic field, have been addressed, the normal zone length of each DP can then be obtained with an iterative computation comparing with the experimental quench resistances (see more code details in Chapter B).

b) Results of the simplified physical model

Fig. 3.32 shows the normal zone length evolution (solid lines) that are computed with the different DPs quench resistance (dotted lines) obtained during the quench test of TFC12. The computed normal zone dynamics are in acceptable agreement with the experimental quench resistance evolution. Here, we can see that the initial quench time of each DP is assumed to correspond to their resistance slope change, e.g. the yellow solid line of pancake P12 (noted as L12) indicates the beginning of the DP6 normal zone development at $t = 0.9$ s, as already applied in the hot spot temperature computations.

One may note that the normal zone length evolution is computed for each single pancake while the experimental quench resistance is obtained for each double-pancake. On one hand, this is due to the limit of our instrumentation to only measure the double-pancake; on the other hand, we make the assumption that the two adjacent pancakes of a same DP (e.g. P1 and P2 in DP1) should have

[58] L. Zani, D. Ciazynski, and A. Torre. *Internal report.* 2016.

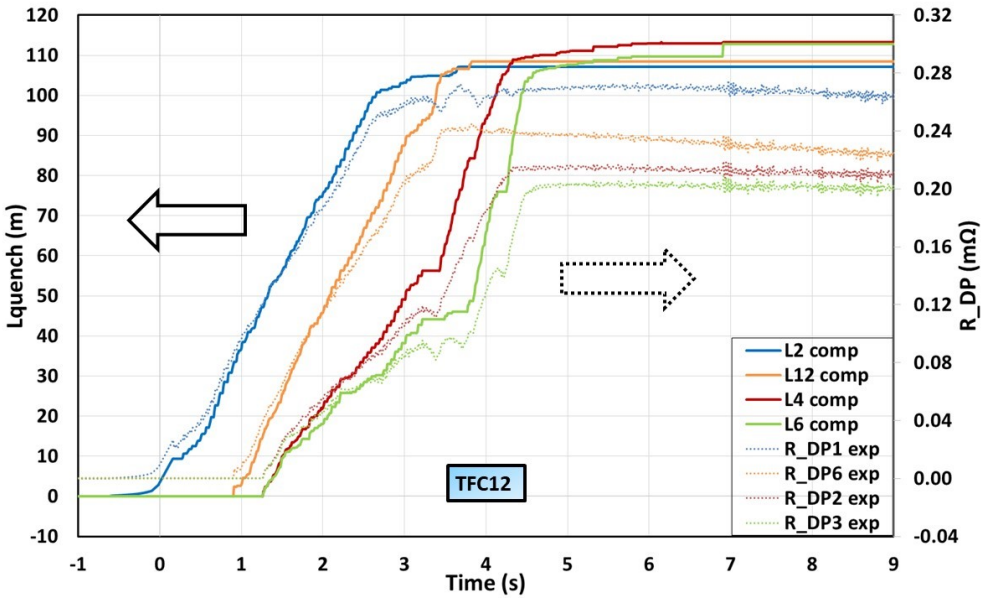

Figure 3.32 – Computed normal zone length evolution in the DPs of TFC12

almost the identical quench propagation dynamics. The experimental measurements have already showed the quasi-identical quench dynamics in the symmetric DPs of the coil (e.g. inner pancakes DP2 and DP5). Therefore, the adjacent pancakes originated from the same DP should have an even more similar quench dynamics. Moreover, the good agreement with the experimental resistance evolutions also verifies this assumption. The single pancake computation (with R_{exp} divided by factor 2) can then be considered a good representation. Meanwhile, one can note that Fig. 3.32 presents two side pancakes (DP1 and DP6) and one DP each for inner and central pancakes (DP2 and DP3). This is actually based on the above mentioned symmetric property of the coil leading to the quasi-identical quench dynamics in the corresponding pancakes.

Finally, we can say that the model computations have achieved the objective of acquiring an order of magnitude of the final normal zone length in all the DPs. Fig. 3.32 shows that the two side DPs are computed to obtain almost the same final normal zone length of around 108 m (blue and yellow solid lines) while the inner and central DPs reach a full quench state of 113 m (red and green solid lines). According to the previous study for the quench test of TFC12 (see Section 3.3.2), we know that the side DPs are definitely in a full quench state when reaching the maximal resistance plateau, i.e. final normal zone length of 113 m. This indicates an underestimation of about 4 % on the final normal zone length with our simplified physical model. When considering the simplified assumptions made in this model, the 4 % can be taken as an acceptable error. We must point out that the biggest error source is actually from the linear temperature profile assumption based on the hot spot temperature computed at the coil inlet. Indeed, the initiation of a quench will be very likely to induce a rapid temperature increase at a local position near the inlet. However, the heat transfer cannot be rapid enough to simply establish a linear profile between this hot spot point and the cold helium flow, at least not at the beginning of the normal zone development. Finally, the 4 % underestimation on the side DPs allows to take the assumption of linear temperature profile as acceptable for the physical model.

Regarding the latter quenched pancakes (L4 and L6 in Fig. 3.32), their normal zone length are both computed to reach the 113 m indicating a full quench state at the maximal resistance plateau (R_DP2 and R_DP3 in Fig. 3.32). This actually gives a surprisingly good view of the real final normal zone length in the inner and central DPs. Indeed, as the inner and central DPs have the quench resistances around 26 % lower than the side DPs, our intuitive aspect is to have a much shorter normal zone length in the inner and central DPs than that in the side DPs. At least, it could never be a full quench state in these latter quenched pancakes. Nevertheless, with the help

of this physical model, an interesting phenomenon has been discovered. In the inner and central DPs, as they are quenched later than the side ones, the hot spot temperature in these DPs (around 33 K) are much lower than that in the side ones (around 47 K), as already presented in Fig. 3.31. According to the coils thermo-resistance property $\rho(T, B)$, a lower level of temperature profile will definitely lead to a lower maximal resistance plateau, even if all these pancakes are in a full quench state. This explains the difference among the quench resistance evolutions in the pancakes even having the same final normal zone length, as what we observed in Fig. 3.32.

Here we can make a short conclusion that our model, despite of the simplified hypotheses, can be efficient enough to give the acceptable normal zone length computations. We can also tell that TFC12 has established for the entire coil a full quench state during the test.

After studying the full quench case, we take another test TFC16 that has a much shorter normal zone length in the pancakes as an example to give some discussions. Fig. 3.33 shows the three representative quench resistance evolutions of side DP6 (yellow dotted line), inner DP5 (blue dotted line) and central DP4 (purple dotted line), as well as their corresponding normal zone length computed with the physical model (solid lines). We recall that the initial quench moment of each DP has been assumed to correspond to each slope change for the TFC16 computations. This assumption considered as "correct" will be further discussed in the following section.

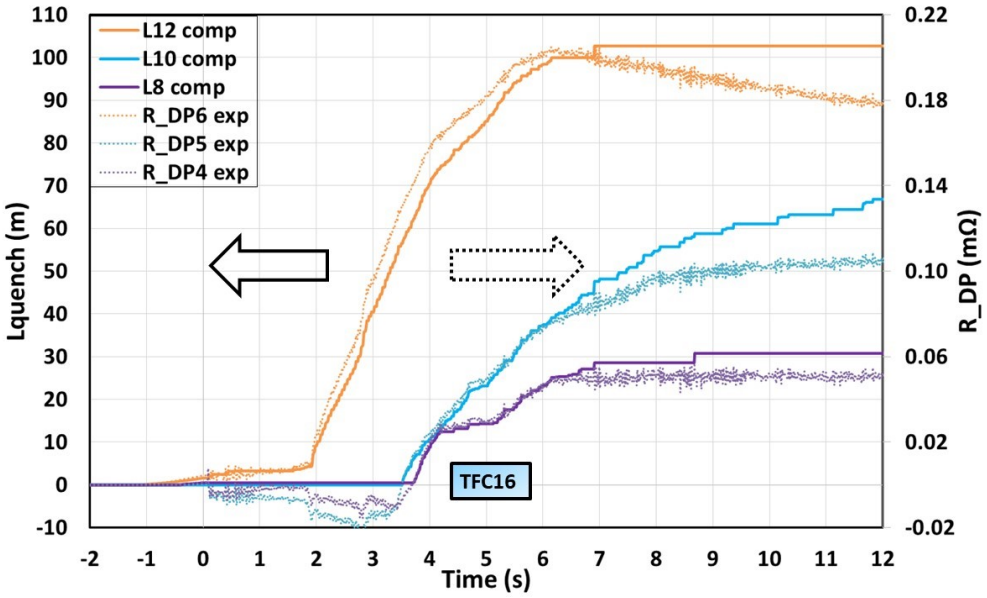

Figure 3.33 – Computation of the normal zone length in the DPs of TFC16

Again, the computed normal zone length dynamics are in good agreement with the experimental resistance evolutions. The full quench state as already identified before for the side DP6 has also been verified with this physical model, but with an underestimation of around 9 % for which we still consider it acceptable taking into account all the simplified hypotheses made in the computations. The model results show a very slow quench propagation of about 1.5 m/s during the delayed acceleration phenomenon. Fig. 3.33 shows very clearly that in the test of TFC16, the inner and central DPs are quenched respectively 60 % and 26 % of the full pancake length. This leads to a partial quench of about 62 % in the entire coil TFC16 and is somewhat coherent with the previous experimental analysis of having the slow quench dynamics in the test of TFC16.

c) Further application of the physical model

As already mentioned in our model description, the initial quench moment plays an important role in the hot spot temperature level as well as in the normal zone length computations. This section

will talk about the assumption of fixing an initial quench moment and its effect on the normal zone length computations. We still take the quench test of TFC16 with its delayed quench acceleration as an example. Fig. 3.34 shows the DP6 experimental quench resistance evolution (yellow dotted line) as well as the corresponding normal zone length computed with two assumptions, early quench initiation at $t = -1.1\,\mathrm{s}$ (red solid line) and delayed quench initiation at $t = 1.9\,\mathrm{s}$ (yellow solid line). The normal zone length in the pancake P2 (blue solid line) is also computed and presented in the same figure to make the comparisons.

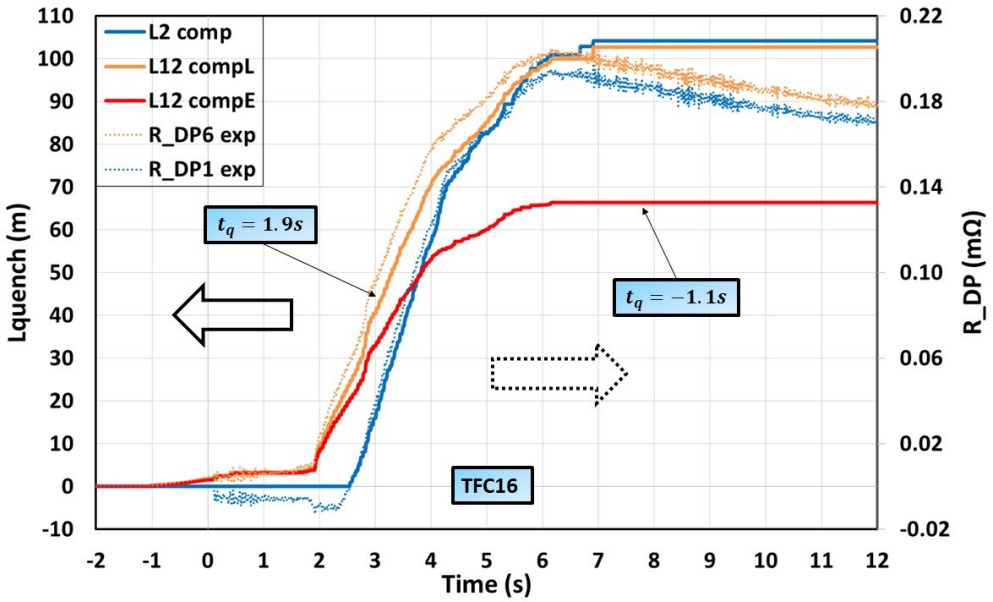

Figure 3.34 – Comparison of the P12 normal zone length evolution computed with two scenarios for TFC16

Firstly, why to choose these two assumptions. The early quench initiation time $t = -1.1\,\mathrm{s}$ corresponds to the experimental voltage increase moment during the quench test. Whereas the time of the delayed quench initiation corresponds to the normal resistance slope change at around $t = 1.9\,\mathrm{s}$. The latter one actually shows that the real quench producing the large amount of Joule effect energy is not appeared until the normal resistance slope change. Secondly, the difference between the two cases of normal zone length has been computed to around 40 m. This proves the predominant impact of the different initial quench time: the later the quench is initiated, the lower the hot spot temperature will reach, the longer the computed normal zone length can be obtained. Obviously, the assumption of delayed quench initiation (yellow solid line) agrees better with the experimental phenomenon.

In addition, when computing the normal zone length in the side pancakes DP1 (blue solid line), the same assumption of fixing the initial quench time at the normal resistance slope change has been made. Fig. 3.34 shows that a quench initiation taken at $t = 2.3\,\mathrm{s}$ gives a well coherent computation for the normal zone length. These results have presented a full quench state in DP1 and a perfectly symmetric behaviour between DP1 and the other side pancakes DP6. Again, this comparison has shown that choosing the initial quench time at the resistance slope change seems to be a better choice for the normal zone length computations.

To conclude, the underestimation part (due to the pick-up coil method uncertainty) of the quench resistance in the central or inner pancakes can be considered to remain in the superconducting state until the resistance slope change.

3.5.3 Different Joule effect energy in the tested TF coils

During the previous work, we have mentioned several times the corresponding Joule heat produced in the different type of quench dynamics. The Joule effect energy is actually another important parameter to indicate the quench state of a tested TF coil. This is why in this section, we will compute for all the 19 quench tests the Joule effect energy during the FD, as written in the classical equation Eq. (3.35):

$$E_{Joule} = \int_{t=-5\,\mathrm{s}}^{t=35\,\mathrm{s}} R_{tot}(t) \cdot I(t)^2 dt \tag{3.35}$$

Here we only focus on the time ranging from $t = -5\,\mathrm{s}$ to $t = 35\,\mathrm{s}$ since the coil current has already decreased to zero at $t = 35\,\mathrm{s}$ and the initial quench development will not start before $t = -5\,\mathrm{s}$, i.e. the quench propagation can be considered as complete during this period. According to the computed results, we have found that below or above the Joule effect energy of around 1200 kJ, the tested coils are generally having two different types of quench dynamics. One has to know that this energy threshold is a completely empirical value that depends on the quench test conditions and the coils performance itself and has not been found to have any related theories. Nevertheless, it is always interesting to study the different quench dynamics that are separated by this energy level. In order to better address this problem, we firstly present the division of the quench tests as a function of the Joule effect energy in Fig. 3.35.

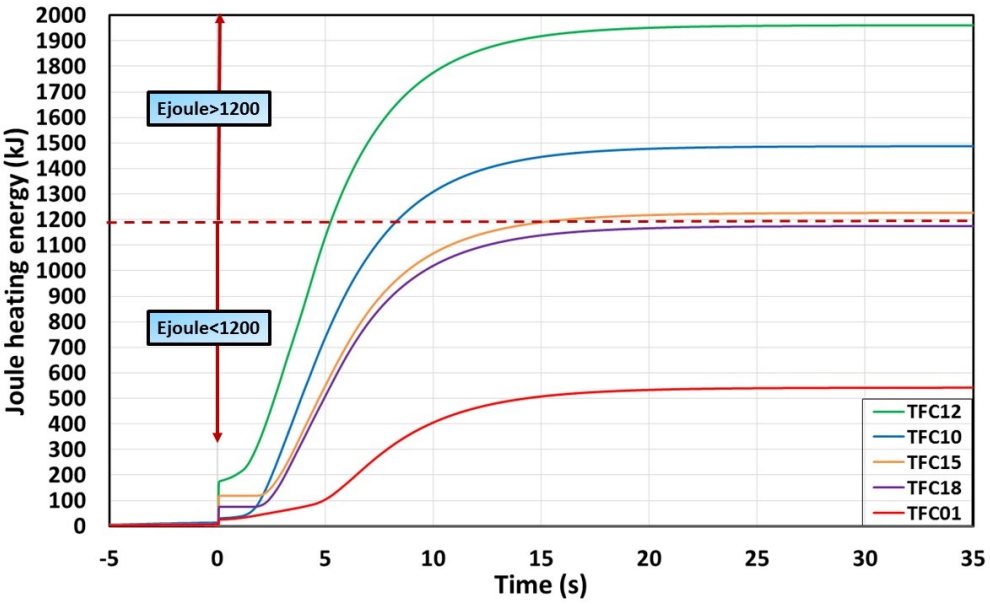

Figure 3.35 – Different level of joule effect energy during the quench tests

Fig. 3.35 shows that each type has been presented by the upper and lower limits of the maximal Joule effect energy. When $E_{Joule} < 1200\,\mathrm{kJ}$, the quench tests of TFC01 and TFC18 are respectively the lower and upper limits of around 542 kJ and 1175 kJ. When $E_{Joule} > 1200\,\mathrm{kJ}$, the quench test of TFC15 has the lower limit of around 1227 kJ while the TFC12 one reaches the highest value around 1961 kJ, including an intermediate level of 1487 kJ in the first test of TFC10. Here, we can see that among the 19 quench tests, the highest Joule effect energy value is about 4 times higher than the lowest one. This is obviously related to their different quench dynamics that will be resumed and discussed below. We can also see that the jump of the energy value very often appears near the start of the FD which corresponds to the most common phenomenon of the "early" quench acceleration dynamics. At about $t = 20\,\mathrm{s}$, all the quench tests reach a maximal energy plateau, which corresponds to around 6 % of the nominal current and to around 10 s after reaching the maximal resistance plateau. Thereby, it is in good agreement with the physics.

In the next, we will rely on an overview table of the 19 quench tests to discuss their different quench dynamics that are separated by the empirical Joule effect energy value of around 1200 kJ. Table 3.6 contains the computed Joule effect energy, the maximal helium inlet temperature and pressure measured by the sensors as well as the identified quench dynamics during the different phase for all the 19 quench tests. The abbreviation in the 7 columns are respectively:

- Quench test: name of the 19 quench tests ranged by a decreasing order of the maximal Joule effect energy.
- E_{Joule}: maximal Joule effect energy in kJ.
- $T_{in\,max}$: maximal helium inlet temperature measured by the sensor TE2414 (the closest one).
- $P_{in\,max}$: maximal helium inlet pressure measured by the sensor PT2416 (the closest one).
- INITIATION: quench initiation phase with SI, II and CI respectively the Side, Inner and Central pancakes quench Initiation phenomena.
- ACCELERATION: quench acceleration phase with EA, DA and NA respectively the Early, Delayed and No quench Acceleration phenomena.
- LATTER: latter quench phase with FR, PR and NR respectively the Full, Partial and No quench Re-acceleration phenomena.

Table 3.6 – Characterization of the 19 quench tests

Quench test	$\mathbf{E_{Joule}}$ **[kJ]**	$\mathbf{T_{in\,max}}$ **[K]**	$\mathbf{P_{in\,max}}$ **[bar]**	**INITIATION**	**ACCELERATION**	**LATTER**
TFC12	1961	27.2	20.9	SI	EA	FR
TFC05	1852	28.9	20.8	CI	EA	FR
TFC13	1634	28.8	21.1	CI	EA	FR
TFC03	1608	26.3	20.8	SI	EA	FR
TFC14	1567	26.3	21.2	CI	EA	FR
TFC09	1499	25.2	20.7	SI	EA	FR
TFC10	1487	24.8	21.0	SI	EA	FR
TFC07	1480	25.4	21.0	SI	EA	FR
TFC11	1454	23.1	21.3	SI	EA	FR
TFC06	1446	23.3	18.2	CI	EA	FR
TFC04	1275	24.2	20.8	SI	EA	FR
TFC15	1227	22.5	20.3	II	EA	FR
TFC18	1175	24.1	21.0	II	DA	FR
TFC20	1075	22.1	20.2	CI	EA	FR
TFC08	960	21.4	20.9	SI	EA	PR
TFC10bis	730	17.6	19.8	SI	DA	PR
TFC16	660	17.4	19.5	SI	DA	NR
TFC17	580	20.7	18.3	CI	DA	PR
TFC01	542	15.1	17.1	II	NA	NR

We can observe that above the value of Joule effect energy in TFC15 (including TFC15), all the 12 quench tests have always the same type of quench dynamics in the quench acceleration phase ("early acceleration" type) and in the latter quench phase ("full re-acceleration" type). When less than the 1200 kJ energy value, the quench tests start to have the different quench dynamics, e.g. delayed quench acceleration, or even no acceleration phenomenon. This is actually in good coherence with the physical phenomenon. The more quench acceleration is delayed and quench re-acceleration appearing partially in the pancakes, the lower normal zone length will be reached as well as the Joule effect energy. For instance, the lowest Joule effect energy value around 542 kJ has occurred in the quench test of TFC01 that has neither the quench acceleration nor re-acceleration phenomena.

When focusing on the 12 first quench tests with the energy level $E_{Joule} > 1200$ kJ, we can see that the initial quench location will not have a direct impact on the Joule effect energy since the quench

initiation has occurred in all the side, inner and central pancakes among these tests. Nevertheless, there is still a relatively large energy difference of around 700 kJ between the lower limit TFC15 and the higher one TFC12, even if they all have the similar quench dynamics in the two principal phases: early quench acceleration (EA) and full re-acceleration phenomenon during the latter quench phase (FR). This could be explained with the different simultaneous quench moment in the inner and central DPs. For instance, the TFC12 test has the simultaneous quench at around $t = 1$ s while the TFC15 one has this phenomenon slightly later at around $t = 2$ s. The 1 s difference in the current FD can lead to a different Joule effect energy due to the different quench resistance evolutions. Another possible phenomenon to explain the different Joule effect energy above 1200 kJ is actually the location of the early quench acceleration phase, if it is in the side DPs, in the inner DPs or in the central DPs. For instance, the test of TFC15 has its early acceleration phenomenon in the inner pancakes DP2 (lower heat load). This leads to a lower maximal resistance plateau thus a lower Joule effect energy, than the other quench tests that have an early acceleration phenomenon in the side pancakes (higher heat load).

In addition, Table 3.6 also shows that the maximal inlet helium temperature ($T_{in\,max}$) is globally increased with the Joule effect energy, varying from 15.1 K to 28.9 K, as presented in Fig. 3.36. This is well coherent with the Joule heat by quench having direct effect on the helium temperature. Nevertheless, the maximal helium inlet pressure ($P_{in\,max}$) is always keeping near the same level of around 20 bar. This can be explained by the fact that the two pneumatic safety valves are opened when reaching around 20 bar. The slight over-rise to around 21 bar is then due to the valves inertia. When the Joule effect energy is small enough, which means that the quench part of the coil is small enough, $P_{in\,max}$ then cannot overpass 20 bar leading to the safety valves always closed during the tests. For instance, the test of TFC10bis as well as those with a lower Joule effect energy are all having a pressure less than 20 bar. One may also note that, the test of TFC06 has a $P_{in\,max}$ less than 20 bar (around 18 bar) but has produced a maximal Joule effect energy of 1446 kJ. This could be explained by the fact that the quench of the TFC06 is initiated very early in the central DP3 and then initiated in the others with a long delay of about 3 s. This makes the helium pressure increase slowly thus reach a maximal value only about 18 bar. Finally, all the pancakes when reaching their quench saturation phase are almost at the same level of resistance around 0.2 mΩ leading to a relatively high Joule effect energy of 1446 kJ. It is to note that the detailed results of the TFC06 are not presented in this PhD report.

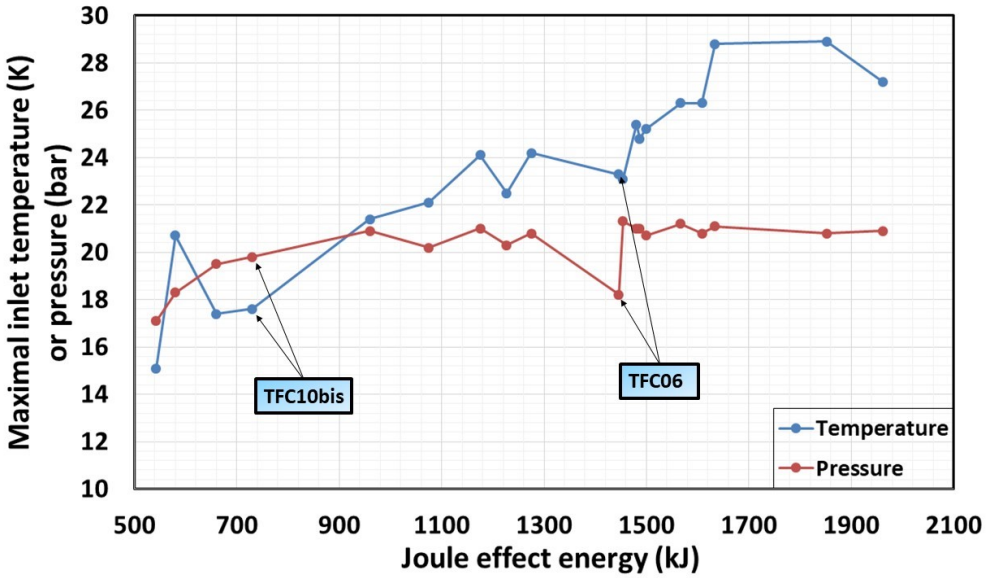

Figure 3.36 – Maximal inlet temperature and pressure values in function of different joule effect energy

Conclusions

The experimental analyses of the different physical phenomena identified during the quench dynamic phases allowed a good understanding on the superconducting TF coils quench common behaviours. The first key step of this study is to determine the most appropriate method for data processing called pick-up coil method. Thanks to this approach, we were able to compute for all the 19 quench tests their quench resistance evolutions in the 6 DPs. A general characterization of the different quench dynamics has been carried out to identify 4 common quench phases including, quench initiation phase, quench acceleration phase, latter quench phase and quench saturation phase.

The different physical phenomena have been studied during the quench dynamic phases with the necessary assumptions and experimental approaches. Concerning the quench initiation phase, the order of quench propagation velocity is computed to several meters per second (one can keep 3 m/s as referenced value). The statistic phenomena of the initial quench location has been explained with the combined effects of strands performance (high impact), external heat load (to be verified) and friction coefficient (low impact). Among the three factors, the external heat load impact remains to be studied in more details with some numerical modellings. This helps to understand why more than half of the quench tests (53 %) are initiated in the side DPs while they are theoretically more difficult to be reached the T_{cs} due to their lower peak field values.

Concerning the quench acceleration phase, the order of the quench propagation velocity has been estimated to around 30 m/s (average value). Approximately a factor 10 has been found between the quench initiation and acceleration velocities, allowing to verify the two phases classification made during the very beginning characterization study. There are in general three types of quench dynamics highlighted during the acceleration phase. The first one is the most common phenomenon called "early" quench acceleration (68 %). This type of quench dynamics has been considered to accelerate in a continuous way. The assumption of a competition between the cable quench acceleration by thermohydraulic quench-back (v_{cable}) and the helium expulsion (v_{He}) can finally explain the real quench acceleration physics in the pancakes. This assumption will be studied in more details with the numerical modellings. The second phenomenon is called the "delayed" quench acceleration (26 %). It has been discussed for its discontinuity at the acceleration moment. A more detailed numerical study will be carried out to explain the delayed and discontinuous acceleration in some quench tests. The assumption is actually based on the impact of the experimental temperature oscillations that provoke a "premature" quench initiation thus lead to a long delay before accelerating. At last, a very unique phenomenon of local resistance jumps has been analyzed for the only observed quench test TFC01. This phenomenon, without any real quench accelerations, has been explained with the transversal quench propagation through the 6 turns configuration of the pancake.

Concerning the latter quench phase, we have particularly studied two principal phenomena. The first one is the simultaneous quench phenomenon that always took place in the latter quenched pancakes. After carrying out the experimental analyses on the different possible phenomena, the most likely explanation is that, the helium reverse flow expulsed from the first quenched pancakes have re-entered into the other pancakes via the principal helium piping making them quench at the same time. A parametric study with the numerical modellings will be carried out to verify this assumption. The second major phenomenon of the latter quench phase are the quench sub-phases dynamics (about 90 % of the quench tests). After the simultaneous quench initiation, the resistance evolutions are having a deceleration to a resistance plateau then a re-acceleration up to the maximum. Such a chain phenomenon has been explained with the fact that the lower field region in the middle of the pancakes makes the conductor more difficult to quench due to a higher T_{cs} thus a lower Joule heat. The quench propagation is then decelerated. Regarding the quench re-acceleration phenomenon, it is very likely due to a secondary quench initiation at the pancakes outlet since the outlet inter-pancake joint has been observed to quench at the re-acceleration moment. A numerical study will allow to confirm the assumption for the quench deceleration phenomenon. Nevertheless, the quench re-acceleration phenomenon will not be further studied with the numerical simulations

because of the limit of our single pancake model, but will remain as a potential study direction for the future.

During the last quench saturation phase, the global decrease of the maximal resistance plateau is explained with the thermo- and magneto-resistance properties of the coil. Two important indicators of the coils "quench level" are also discussed, including the Joule effect energy and the normal zone length computed with our simplified physical model. We have acquired that the maximal energy difference is up to a factor 4 among the 19 quench tests. This is mainly linked to the different quench dynamics that, the more quench acceleration is delayed and the less quench re-acceleration is appearing among the pancakes, the lower Joule effect energy is obtained. The slight difference of the simultaneous quench time among the tests can also have a relatively important impact on the Joule effect energy values. Finally, one has to know that some key parameters during the quench saturation phase will be compared with the numerical modellings in the next chapter, e.g. the final normal zone length in the pancakes.

Based on these 19 quench tests carried out in the CTF, the JT-60SA TF coils thermohydraulic performance in case of quench as well as their mechanical and electrical reactions in nominal conditions (the same to Tokamak operating conditions) are well validated. A post-quench current fast discharge test has also been carried out for each TF coil allowing to ensure the coils performance before shipping for the Tokamak assembly. The average quench temperature is measured to be around 7.5 K in single coil configuration. This is actually in good agreement with the theoretical performance (based on the magnetic field map) estimated by the European manufacturers. Thereby, the TF system of the Tokamak JT-60SA, according to the relevant experiments and analyses, is well manufactured and in good state for the future machine operations. The acquired knowledge on the TF coils quench behaviour in the CTF condition can also be useful for the real machine operations. This part of discussion will be given in the general conclusions at the end of this PhD report.

CHAPTER 4

Numerical modelling and analysis of quench behaviours during JT-60SA TF coils quench tests

Objectives

- **To model the TF coils quench tests with the numerical code and to compare with the experimental data**
- **To carry out a further study of the physical phenomena identified during the experimental analyses thanks to the simplified numerical modellings**

4.1 Implementation of the physical model in the numerical code

After highlighting the different physical phenomena identified during the four quench dynamic phases, we are now going to apply numerical approaches to make a further study of the TF coils quench behaviours. As already mentioned in general introduction, the well-developed and validated quench study code THEA has been chosen thanks to its "open" source files that can be easily modified. Knowing that the quench experiments on real Tokamak TF coils are very complex to be fully modelled, we decided to rely on some simplified numerical modellings to try to analyze a single phenomenon at a time without building a complete coil predictive model. For this purpose, we will firstly give a description of the physical model and the boundary conditions applied in the 1D numerical quench model of THEA (in Section 4.1). Then, a convergence study will be addressed in Section 4.2 for determining the numerical parameters used for the next modellings. Due to a computation limit of the THEA 1D quench model, we are going to introduce our improvement approach in Section 4.3. Finally, the improved numerical quench model will be applied in Section 4.4 to carry out a further study of the physical phenomena identified during the experimental analyses.

4.1.1 Physical model for the quench propagation in a CICC

In order to model the quench propagation in a CICC, two major issues need to be addressed:

- Heat balance in the conductor involving the key parameters, such as thermal conduction, Joule heat, external heat load and heat exchange with the coolant flow, as presented in Fig. 4.1;
- Heat balance in the coolant flow involving the key parameters, such as heat load by friction and heat exchange with the conductor (strands + conduit), as presented in Fig. 4.1.

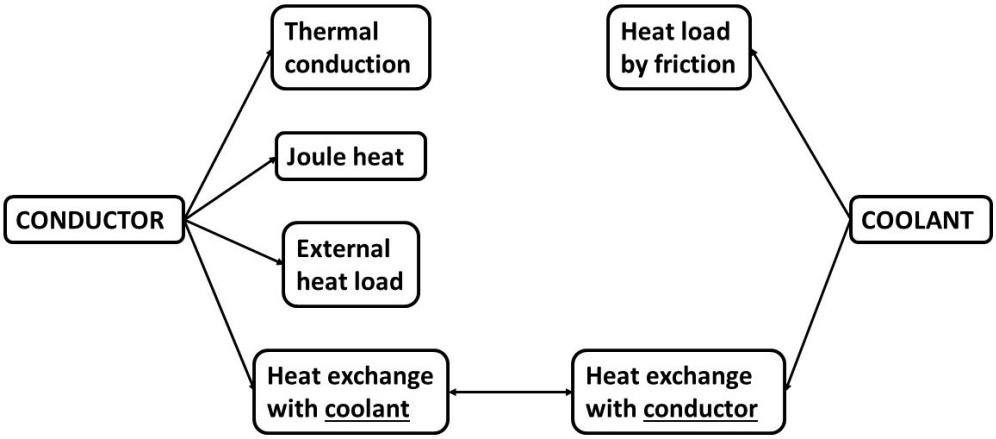

Figure 4.1 – Schematic illustration for the key parameters taken into account in the physical model of THEA

The parameters listed for the two parts of the CICC, conductor or coolant, are the key ones that will be taken into account in the following quench modellings. In particular, the heat exchange between the conductor and the coolant plays the role of coupling the thermal conduction model and the coolant flow model. More details will be explained below for these two physical models.

a) Thermal conduction model

We start from the CICC thermal conduction model implemented in THEA. The superconducting CICC can contain different thermal components, e.g. superconducting strands, electrical stabilizer like copper, structural component like Stainless Steel (SS) jacket, and electrical insulators. Each of them can transport heat by conduction and exchange heat at their mutual interfaces. Some components like strands and SS jacket can exchange heat at the interface with a cooling medium (e.g. helium). And the majority of the Joule heat is generated in the copper matrix. A fundamental assumption has been made in this thermal conduction model where the ratio of conductor length to cross-sectional dimension in the CICC is often large enough (more than 3 orders of magnitude) to allow the equations to be written in 1D[29]. This means that the transversal dimension along the cable cross-section is neglected. Nevertheless, the temperature difference as well as the heat flux among different materials in the CICC will still be considered in this model. Eq. (4.1) shows the general 1D heat transport equation for each component i:

$$A_i\rho_i C_i\frac{\partial T_i}{\partial t} - \frac{\partial}{\partial x}(A_i\lambda_i\frac{\partial T_i}{\partial x}) = \dot{q}'_i + \dot{q}'_{Joule,i} + \sum_{j=1,\ j\neq i}^{N}\frac{(T_j - T_i)}{R_{th,ij}} + \sum_{h=1}^{H} p_{ih}h_{ih}(T_h - T_i) \qquad (4.1)$$

where A_i is the total cross-section of the component i obtained as sum of the partial cross-section of the constituents. For instance, the cable cross-section of JT-60SA CICC contains approximately 30 % of NbTi material and 70 % of copper matrix stabilizer. T_i is the temperature of the component i, which is assumed to be constant within the cross-section in the 1D numerical model. ρ_i, C_i and λ_i are respectively the mass density, the mass specific heat and the thermal conductivity of the component i which are all assumed to be homogeneous within the cross-section. ρ_i and λ_i are obtained with the area weighting while C_i is using the mass weighting of the constituents.

$\dot{q}'_i$ represents an external heat source expressed as the power per unit length. $\dot{q}'_{Joule,i}$ represents the Joule heat per unit length if the component is carrying a current, as written in Eq. (4.2).

$$\dot{q}'_{Joule,i} = I_i E_i \qquad (4.2)$$

[29] L. Bottura, C. Rosso, and M. Breschi. *Cyogenics* **40**. 617–626. 2000.

where E_i is the electric field and I_i the current. For a component like the superconducting cable of JT-60SA (including NbTi strands and copper matrix stabilizer), the electric field is obtained experimentally and is usually fitted using a power law as below:

$$E_i = E_0(\frac{I_i}{I_c})^n \tag{4.3}$$

where the constant E_0 is the electric field set as the criterion to define the critical current I_c. The typical range for E_0 is $10^{-4} - 10^{-5}\, V/m$. The n value defines the electric field dependence on current close to the I_c transition. This value is of the order of 10 or even higher when the cable properties are uniform. For instance, a relatively high value of $n = 30$ has been applied in our model relying on the production control measurements of the NbTi cables in JT-60SA TF coils[50]. This is coherent with the uniform properties of the classical Low Temperature Superconducting (LTS) material like NbTi.

The two last summations in Eq. (4.1) represent the heat exchange among thermal components by introducing the thermal resistance per unit length $R_{th,ij}$ between components i and j (with temperatures respectively T_i and T_j), and the heat exchange between component i and H different coolant channels (with T_h the coolant temperature in channel h) depending on the wetted perimeter p_{ih} and the heat convection coefficient h_{ih}. Indeed, the thermal resistance between a jacket and strands is a very problematic parameter, not only because the respective contact perimeter cannot be accurately determined, but also because the value of the contact heat transfer coefficient may span quite a wide range from about $250\,\mathrm{W/m^2 \cdot K}$ to more than $2500\,\mathrm{W/m^2 \cdot K}$, depending on the surface pressure[104]. Here, we just take the THEA default value of $1\,\mathrm{W/m \cdot K}$ for the jacket-strands contact thermal resistance[105] for our first computations. It is to note that the second summation of coolant convection is actually the coupling term between the thermal conduction model and the coolant flow model.

b) Coolant flow model

The coolant flow model is written for H parallel, 1D channels that can exchange mass, momentum and energy among them. The coupling of the channels can happen either through convection heat transfer at the mutual interface, or through direct mass transfer from one channel flow to the other. Three conservation equations will be written in the non-conservative form for the coolant flow, including the mass conservation expressed in volumetric flow $V_h = A_h v_h$ in Eq. (4.4a), the momentum conservation expressed in pressure p_h in Eq. (4.4b) and the energy conservation expressed in temperature T_h in Eq. (4.4c). Comparing to the conservative form, these non-conservative form equations can have three advantages: more easily to be treated thanks to the pressure term explicitly appearing, more stable in terms of the numerical solution and more accurate since it can be valid for any coolant fluid[29].

$$\rho_h \frac{\partial V_h}{\partial t} + \frac{\rho_h V_h}{A_h}\frac{\partial V_h}{\partial x} + A_h \frac{\partial p_h}{\partial x} - \frac{\rho_h V_h^2}{A_h^2}\frac{\partial A_h}{\partial x} = -A_h F_h - \sum_{k=1,\ k\neq h}^{H} (\Gamma_{hk}^v - v_h \Gamma_{hk}^\rho) \tag{4.4a}$$

$$A_h \frac{\partial p_h}{\partial t} + V_h \frac{\partial p_h}{\partial x} + \rho_h c_h^2 \frac{\partial V_h}{\partial x} = -\sum_{k=1,\ k\neq h}^{H} \left\{ c_h^2 \Gamma_{hk}^\rho + \phi_h \left[\Gamma_{hk}^e - v_h \Gamma_{hk}^v - (h_h - \frac{v_h^2}{2})\Gamma_{hk}^\rho \right] \right\} + \phi_h V_h F_h + \phi_h \dot{q}_h' + \phi_h \dot{q}_{cf,h}' \tag{4.4b}$$

[50] L. Zani, P. Barabaschi, and E. Di Pietro. *Fusion Engineering and Design* **88**. 555–558. 2013.
[104] K. Takahata, H. Tamura, and T. Mito. *IEEE Transactions on Applied Superconductivity* **14**. 1477–1480. 2004.
[105] CryoSoft. *CryoSoft*. 2016.

$$A_h\rho_h C_h\frac{\partial T_h}{\partial t}+\rho_h V_h C_h\frac{\partial T_h}{\partial x}+\rho_h\phi_h C_h T_h\frac{\partial V_h}{\partial x}=-\sum_{k=1,\ k\neq h}^{H}\left[\Gamma^e_{hk}+v_h\Gamma^v_{hk}-(h_h-\frac{v_h^2}{2}-\phi_h C_h T_h)\Gamma^\rho_{hk}\right] + V_h F_h+\dot{q}'_h+\dot{q}'_{cf,h} \quad (4.4c)$$

where ρ_h is the density of the coolant in the channel h, A_h the cross-section of the channel h, v_h the coolant velocity, c_h the isentropic sound speed, h_h the specific enthalpy, C_h the specific heat at constant volume, ϕ_h the Gruneisen parameter describing the evolution direction of the fluid pressure as a function of the temperature variation (or internal energy variation) in an isochoric system, defined as $\phi_h=\frac{1}{\rho}(\frac{\partial p}{\partial u})_V$[80], and finally F_h the friction force which is defined using the friction factor f_h and the hydraulic diameter D_h as written in Eq. (4.5):

$$F_h=2\,\rho_h\frac{f_h}{D_h}v_h|v_h| \quad (4.5)$$

The quantities Γ^ρ_{hk}, Γ^v_{hk} and Γ^e_{hk} are the distributed sources of mass, momentum and stagnation enthalpy per unit length of channel, coming from the mass transfer and the heat exchange between the channels h and k. These terms will not be taken into account (so *zero*) in our following simulations since the JT-60SA TF coils are manufactured with single channel CICC.

Two heat sources have been considered in the coolant model in Eq. (4.4c). The first one $\dot{q}'_{cf,h}$ represents the heat flux due to the counterflow mechanism in superfluid conditions. This will be *zero* as well in the following simulations since the helium circulated in the JT-60SA TF coils has a temperature much higher ($4.7\,\mathrm{K}\backsim 7.5\,\mathrm{K}$) than the superfluid transition temperature of 2.17 K at saturated vapour pressure[63].

However, the second one noted as $\dot{q}'_h$ will play an important role in coupling the coolant flow model and the thermal conduction model. It represents the heat exchange between the wetted perimeter of the conductor and the coolant flow, e.g. helium forced flow convection in the CICC of JT-60SA. We can see that the last summation of the thermal conduction model in Eq. (4.1) is equal to this $\dot{q}'_h$ expressed in Eq. (4.6):

$$\dot{q}'_h=\sum_{h=1}^{H}p_{ih}h_{ih}(T_i-T_h) \quad (4.6)$$

4.1.2 Boundary conditions in THEA

a) Cable boundary conditions

Two types of standard boundary conditions are proposed by THEA in the thermal conduction model:

- Dirichlet conditions imposing the temperature at the boundary
- Neumann conditions imposing the heat flux at the boundary

Regarding the numerical quench modellings of the JT-60SA CICC, the Neumann conditions will be imposed, as expressed in Eq. (4.7):

$$-A_i\lambda_i\frac{\partial T_i}{\partial x}=\dot{q}_{boundary}=0 \quad (4.7)$$

where $\dot{q}_{boundary}$ is the heat flux at the boundary.

[80] Walid Abdel Maksoud. *Thesis.* 2010.
[63] Steven Van Sciver. *International Cryogenics Monograph Series.* 2012.

Here $\dot{q}_{boundary} = 0$ indicates that the cable ends (excluding the helium coolant) are assumed to be adiabatic. This is based on the fact that during the JT-60SA TF coils quench tests, the thermal conduction flux between the cable ends and the inter-pancake joints are nearly negligible when comparing to the heat exchange by helium forced flow convection. From physical aspect, this assumption is also coherent with the coil design objective that the heat flux through the connecting joints (or current leads) at the cable ends must be kept as small as possible to decrease the external heat load[27].

b) Helium flow boundary conditions

When imposing the coolant boundary conditions, there are also two standard types offered by THEA to be chosen:

- A closed pipe condition without any volumetric flow $V_h = 0$, e.g. helium bath cooling system
- The condition where the in- and out-flow are into a volume at given pressure and temperature

According to our testing conditions of the JT-60SA TF coils, the second case will be applied in the quench model, since the TF coils CICC is cooled with forced helium flow passing from the inlet to the outlet. In addition, it will be necessary for the helium flow to prescribe two Riemann variables at inflow and one at outflow sections[106] in this coolant flow model. Based on the non-conservative equations in Eq. (4.4), the preferred choice for an explicit application in THEA is then to impose at inlet cross-sections pressure and temperature (2 variables at inflow), and at outlet cross-sections only pressure (1 variable at outflow)[27]. Indeed, temperature and pressure are the two parameters that can be directly obtained by the experimental measurements, thus will be used for the boundary conditions.

As already explained in Chapter 2, the quench tests of JT-60SA TF coils are carried out by increasing the inlet helium temperature and maintaining a quasi-isobaric condition, all controlled by the CTF automatism, up to reach the coil quench temperature. The experimental measurements of the three variables (inlet temperature and pressure and outlet pressure) for TFC12 are shown in Fig. 4.2. It is to note that the time range ($0 - 2600$ s) presented here is only available for this part of discussion.

Fig. 4.2 shows that, the inlet helium temperature (red line) generally keeps a smooth increasing evolution thanks to the CTF controlling automatism. Nevertheless, there always remains some temperature oscillations during the experiment due to the hydraulic inertia of the helium flow and the precision limit of the hydraulic controlling system. In order to obtain the stable numerical computations in THEA, the helium inlet temperature conditions are determined by fitting these experimental curves, with a steady state temperature at 4.83 K followed by a higher slope increase of 0.41 K/min during 227 s and a lower slope one of 0.045 K/min up to quench. Concerning the pressure evolutions, Fig. 4.2 shows the inlet and outlet pressures respectively averaging around 10.75 bar and 10.08 bar. As the pressure oscillations due to the rapid temperature increase between $t = 1000$ s and $t = 1500$ s will lead to a divergent numerical computations, the two average pressure values will thus be used as the boundary conditions of the numerical quench model (for quench test of TFC12).

As one of the possible factors that could impact the initial quench location, the friction coefficient (f) also need to be applied in the numerical model. According to the previous study in Section 3.2.2, different friction coefficient can lead to different helium flow velocity so as to the different heat exchange by forced helium flow convection. Nevertheless, the effect has been proved to be slight. The friction coefficient has been measured for each CICC of the JT-60SA TF coils and has been

[27] L. Bottura. *Journal of Computational Physics* **125**. 26–41. 1996.
[106] W. J. Usab. *Adv. Comput. Transonics*. 1985.

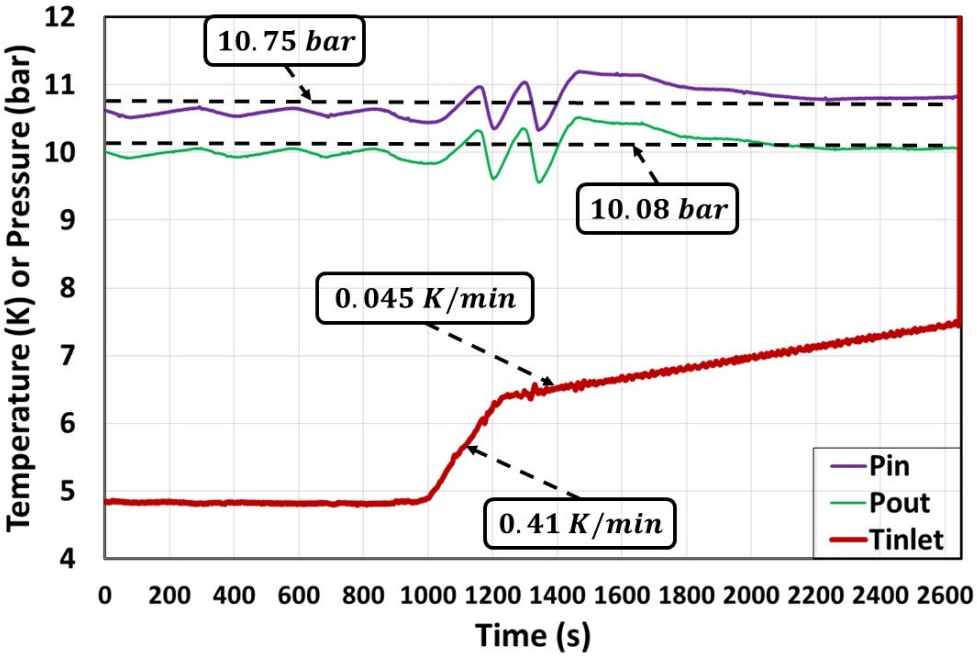

Figure 4.2 – Experimental boundary conditions in the quench test of TFC12

fitted with the following correlation (already introduced in Chapter 1) as written in Eq. (4.8):

$$f = \alpha + \beta \cdot Re^{\gamma} \tag{4.8}$$

where Re is the Reynolds number of the helium flow and α, β and γ are the 3 constant parameters which have been determined with the CICC hydraulic experiments performed in the OTHELLO of CEA Cadarache[49]. Their values of the 6 DPs (CICCs) in TFC12 can be found in Table 1.4[107]. These values will also be imposed in the numerical model for the corresponding pancakes simulations.

The last important parameter of the helium flow model in CICC is the heat transfer coefficient by forced convection. In our numerical quench model, we will choose Dittus-Boelter-Giarratano (DBG) correlation[79] (see Eq. (1.16)) to model the heat exchange between expelled helium and the normal zone propagation during the fast transient state. The DBG correlation has been proved to be adapted to the forced convection of supercritical helium in a CICC (like JT-60SA TF coils) and to be valid with Reynolds number ranged from 10^4 to 3.8×10^5, pressures from 3 bar to 20 bar and fluid temperatures from 4.4 K to 30 K (as in our quench test conditions).

Nevertheless, one may recall that Chapter 1 has already talked about a corrected laminar correlation (see Eq. (1.15)) which is applied during the helium temperature-increasing phase before quench from 5 K to 7.5 K. Indeed, the Reynolds number in TF coils CICC has been computed to be around $1600 \backsim 2080$ during this temperature-increasing phase. The laminar correlation then computed for the forced convection coefficient a value around $378\,\mathrm{W/m^2 \cdot K}$ leading to a temperature difference less than 10 mK between conductor and helium. Such temperature difference is nearly neglected when comparing to the 300 mK difference between helium inlet and outlet or to the T_{cs} difference among the different positions in the CICC (more than 100 mK), which proved the high cooling efficiency in a forced flow-cooled CICC.

If we apply the turbulent regime DBG correlation to the same temperature-increasing conditions, a forced convection coefficient has been computed to around $445\,\mathrm{W/m^2 \cdot K}$ thus an even more negligible temperature difference can be obtained to 6.7 mK. Such computations (applying turbulent regime correlation to a laminar flow condition) seeming like incoherent has actually allowed us

[49] P. Decool et al. *IEEE Transactions on Applied Superconductivity* **26**. 2016.
[107] P. Decool et al. *Internal report*. 2016.
[79] P. Giarratano, V. Arp, and R. Smith. *Cryogenics*. 385–393. 1971.

to confirm one fact that conductor and helium in the CICC are always having a quasi-identical temperature during the laminar regime no matter what correlation to be applied.

Therefore, our next numerical simulations will only take into account the DBG correlation for a model simplification. Two reasons can be summarized. The first one is that DBG correlation is a largely valid turbulent correlation that allows to correctly model the forced convection coefficient during the fast transient quench phase, which is actually the most important part of our study. The second one is that conductor and helium have been proved to always have the quasi-identical temperature during laminar regime thanks to the CICC high cooling efficiency. The different correlations applied during this temperature-increasing phase will not have an impact on the physical study.

c) Electric circuit boundary conditions

Finally, we recall the necessary boundary conditions of the electric circuit during a quench test. As introduced in Chapter 2, when a voltage increase overpasses the threshold value of 100 mV and lasts for 100 ms, the Magnet Safety System (MSS) will open the main breaker and lead to a current discharge with a time constant experimentally estimated to 8.2 s. The magnetic energy stored in the coil will then be released on a dump resistor of 6.2 mΩ. These values will be taken into account in the following CICC quench modellings.

4.2 System solution and numerical parameters in THEA

4.2.1 Description

Both the thermal conduction model and the coolant flow model can be expressed by a parabolic-hyperbolic system of Partial Differential Equations (PDEs) as in Eq. (4.9):

$$\mathbf{m}\frac{\partial \mathbf{u}}{\partial t} + \mathbf{a}\frac{\partial \mathbf{u}}{\partial x} - \frac{\partial}{\partial x}(\mathbf{g}\frac{\partial \mathbf{u}}{\partial x}) + \mathbf{su} = \mathbf{q} \tag{4.9}$$

where the vector of unknowns $\mathbf{u}$(x,t) is defined assembling the unknowns of each PDE, e.g. the thermal component temperature T_i, the hydraulic temperature T_h and pressure p_h, etc. The other vectorial parameters ($\mathbf{m}$, $\mathbf{a}$, $\mathbf{g}$, $\mathbf{s}$ and $\mathbf{q}$) will be explicitly or implicitly dependent on the system variables[27], e.g. thermal conductivity, mass density or even current density, etc.

THEA then solves for each component a set of PDEs, and obtains at any time the distribution in space (along the conductor length) for the system variables. The solution satisfies the initial and boundary conditions explained above. To solve the system of PDEs, THEA uses independent space and time discretization. The space discretization is based on the finite element method[108], and uses 1-D lagrangian elements with at most fifth order shape functions. The time discretization is based on a multi-step finite difference algorithm of the Beam and Warming family[109] with at most third order accuracy. The time step defined between maximum and minimum values can be adapted automatically to achieve a user-defined error during the computations[105]. The combination of an independent space and time discretizations can provide a flexible and accurate way to solve large parabolic-hyperbolic systems[27]. High accuracy for both space and time integration is also necessary to avoid growing errors such as numerical quench-back[110].

[27] L. Bottura. *Journal of Computational Physics* **125**. 26–41. 1996.
[108] O. C. Zienkiewicz, R. L. Taylor, and J. Z. Zhu. *Butterworth-Heinemann.* 2005.
[109] R. M. Beam and R. F. Warming. *Siam Journam on Scientific and Statistical Computing* **1**. 131–159. 1980.
[105] CryoSoft. *CryoSoft.* 2016.
[110] L. Bottura and A. Shajii. *International Journal for Numerical Methods in Engineering* **43**. 1275–1293. 1998.

In order to correctly start the quench numerical modelling with THEA, a convergence study must be carried out to determine the most appropriate values of the numerical parameters, such as mesh size.

4.2.2 Convergence study

As introduced above, the time step is defined between maximum and minimum values and can be adapted automatically by the code to achieve a user-defined error. In the following computations, we will take for the numerical model two time step limits: $\Delta t_{min} = 10^{-6}\,s$ and $\Delta t_{max} = 0.01\,\text{s}$. Indeed, the latter one has been determined with a factor 10 lower than the quench detection and action time of $\tau_{da} = 0.1\,\text{s}$. $\Delta t_{max} = 0.01\,\text{s}$ can thus be considered as precise enough for producing the quench physics in the numerical computations. In the following studies, we will focus on the mesh size effect on the quench numerical computations. The side pancake P1 of the "typical" quench test TFC12 will be computed in this case.

Mesh size effect on the quench numerical computations

Fixing the above values for time step, the quench numerical computations will be carried out with different mesh size (MS). Fig. 4.3 shows that different mesh size has nearly no impact on the global numerical quench dynamics within a mesh size scope ranging from 1 m to 0.01 m. Only 1 % difference has been revealed at the maximal resistance plateaus. Nevertheless, the biggest difference that can be observed is actually during the quench initiation phase before the start of the FD, as presented in the red dashed circle. Fig. 4.4 shows a zoom view of the red dashed circle. We can see that at

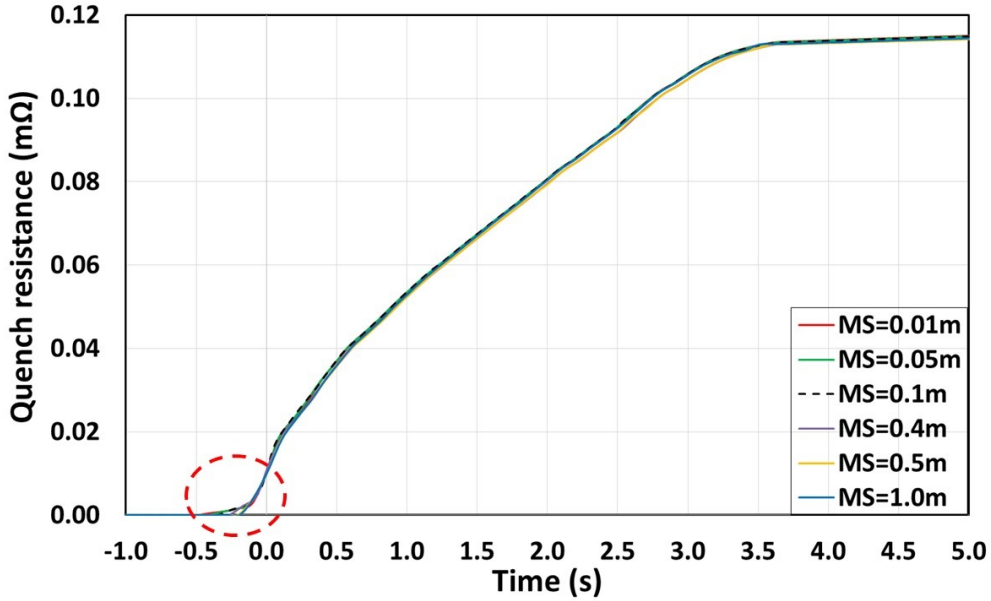

Figure 4.3 – Convergence study of the mesh size impact on the numerical quench resistance evolution (side pancake P1): general view

$t = -0.1\,\text{s}$, the quench resistances are nearly reaching the same level of around $4\,\mu\Omega$ which actually corresponds to the quench detection voltage of 100 mV. The quench detection time τ_{da} has also accurately appeared 100 ms before the start of the FD ($t = 0\,\text{s}$). This gives a first demonstration of having correctly implemented the electric circuit boundary conditions in the THEA model. Between the two limit mesh sizes, 0.01 m in red solid line and 1.0 m in blue solid line, a 0.25 s difference of the initial quench time can be noticed. The more the mesh size is refined, the more the initial quench propagation can be accurate (also slower in dynamics). The nearly superposed curves between 0.05 m and 0.01 m then indicate a convergence in the numerical computations. In the following study, we will take 0.1 m as the most appropriate mesh size for our model (black dashed line). This is actually a compromise between computation time and computation convergence. In addition, one need to know that the detected normal zone length is computed to 2.67 m which is much longer

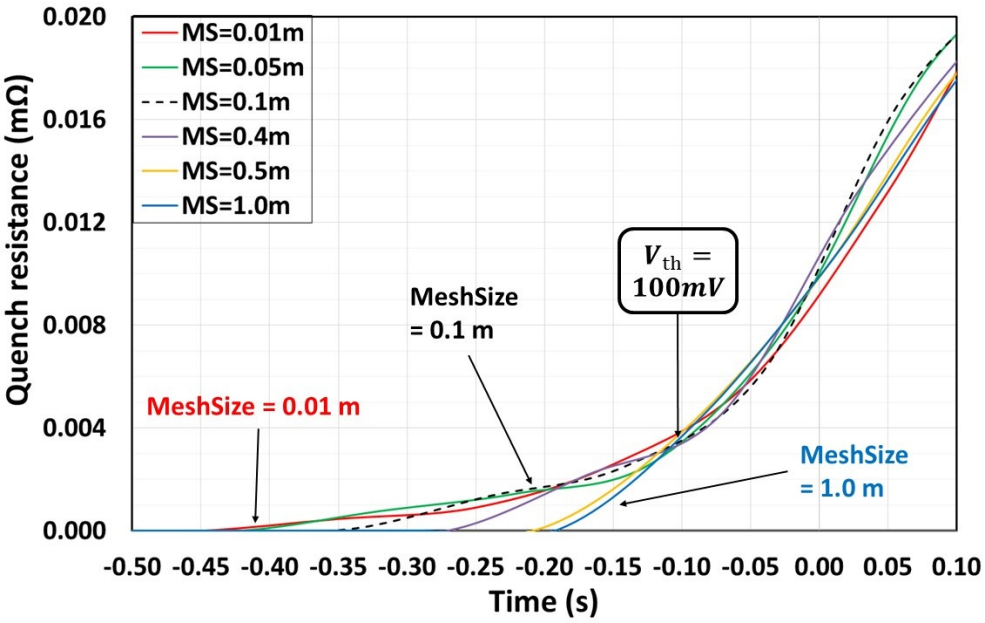

Figure 4.4 – Convergence study of the mesh size impact on the numerical quench resistance evolution (side pancake P1): detailed view

than the above chosen value of 0.1 m. Thereby, this mesh size can be considered as both precise and accurate for the following quench computations.

A short conclusion can be made here that the most appropriate values have been determined for the two numerical parameters, with mesh size of 0.1 m and maximum time step of 0.01 s. The following simulations will all be based on these two values.

4.3 Inter-turn thermal coupling model

4.3.1 Introduction of the inter-turn thermal coupling model

Before carrying out the numerical study of the quench behaviour in the superconducting coils, it is necessary to verify the computation accuracy of the above presented 1D numerical model of THEA. We then make a first numerical computation in a pure thermohydraulic case with no quench (temperature-increasing phase) for the side pancake P1 of TFC12, as presented in Fig. 4.5. It is to note that the time range from 0 s to 2000 s is only available for this part of discussion.

One can see that the increasing evolution of the numerical outlet temperature (blue dash-dotted line) is completely different from the experimental one (blue solid line). Actually, this numerical outlet temperature has the same slope than the inlet temperature fit (red dashed line), but with an approximate delay of 900 s. This phenomenon corresponds to a pure motion of the warm helium front flowing through the 113.28 m pancake. The average flow velocity in the numerical simulations can then be calculated to 0.12 m/s. This is in good agreement with the measured value of around 0.11 m/s in the quench test of TFC12 (at inlet boundary conditions: 10.08 bar, 4.83 K and 2 g/s). This coherence reminds that the long delay around 900 s may be due to the limit of our 1D single pancake model that only takes into account helium flow longitudinal heat transfer.

In addition, the characteristic time of transversal thermal conduction through the six turns can be analytically estimated to about 8 s, with the same approach already presented in Section 3.3.2. It is more than 100 times shorter than the pure longitudinal heat transfer time by helium flow (around 900 s). This could then explain the "quasi-immediate" evolution of the experimental T_{out} in

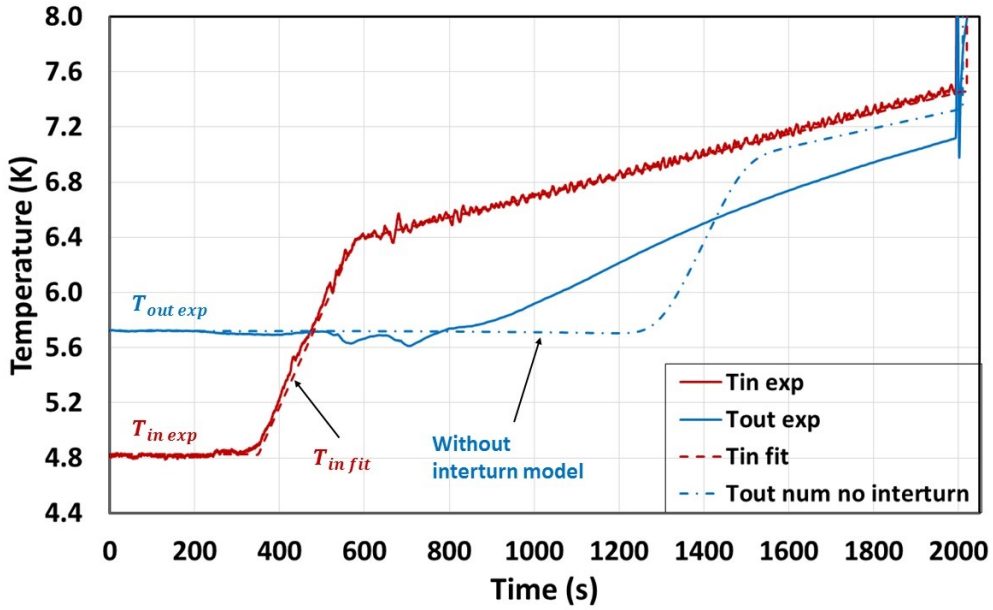

Figure 4.5 – Comparison of the temperature evolution between TFC12 experimental measurements and the 1D numerical model results

Fig. 4.5 (blue solid line) just after the increase of the inlet temperature. Therefore, we make the assumption that the real temperature evolutions in the inlet and outlet are due to the inter-turn transversal heat exchange phenomenon. Actually, it will be more feasible to verify this transversal heat exchange effect with the actual 1D numerical model than to directly construct a complex 3D model for the entire TF coil and to combine all the possible thermal effects[111]. Because the potential modifications could be achieved within the single pancake model via the user-defined thermal coupling functions in THEA.

Based on the above discussions, we will firstly present a proper way of implementing the transversal heat exchange in the existing 1D numerical model in THEA inspired from a DEMO TF coil study[112]. We will call this new model the *inter-turn thermal coupling model*. Then a further verification will be carried out by comparing our new model results to the experimental data, as presented in Section 4.3.3.

4.3.2 Implementation of the inter-turn thermal coupling model in THEA

The inter-turn thermal coupling model takes into account a very important parameter for the heat transfer in pancakes, the transversal heat flux between the adjacent turns. Fig. 4.6 shows the cross-section of one pancake which is wound in 6 turns. Each rectangle represents the cross-section of one turn including three thermal components: NbTi/Cu strands, Stainless Steel jacket (SS) and impregnated G10 insulation (see Chapter 2). Fig. 4.6 also gives the main heat sources involved in the 1D heat transport equation solved by THEA for each thermal component. Section 4.1.2 has already discussed the details of this heat transport equation. Here, we will only take one mesh, e.g. $x_{1,i}$ (lower right), to address an illustrative review about the heat sources.

First of all, the index couple represents the i-th mesh in the first turn 1 noted as $x_{1,i}$. Then the next mesh in the same turn 1 is noted as $x_{1,i+1}$ as well as the corresponding mesh in the adjacent turn 2 noted as $x_{2,i}$. Focusing on the mesh $x_{1,i}$, there is the longitudinal thermal conduction flux q_{long}, the joule heat q_{joule} during the quench and the heat exchange between conductor and helium by forced flow convection q_{conv}. Another important term of the model is the external heat load q_{lin} which is

[111] V. Tomarchio and M. Wanner. *IEEE Transactions on Applied Superconductivity* **28**. 2018.
[112] Q. Le Coz et al. *IEEE Transactions on Applied Superconductivity* **28**. 1–5. 2018.

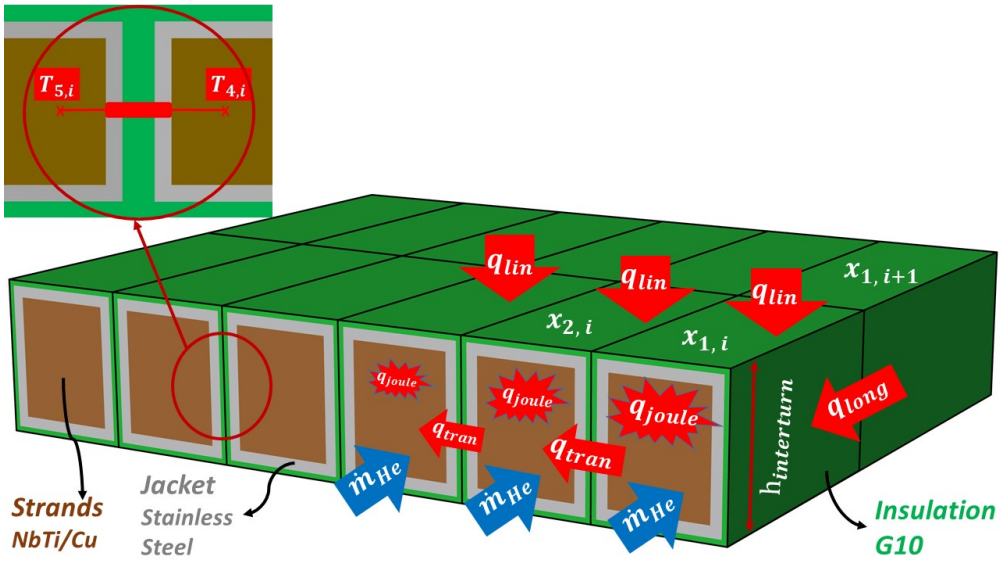

Figure 4.6 – Heat sources involved in the inter-turn thermal coupling model

applied on the insulation component. This term models the heat coming from the casing or the adjacent conductor. The last term, transversal heat flux noted as q_{tran}, is thus the key parameter of the inter-turn thermal coupling model. A simplified energy balance equation including all the mentioned heat sources and the energy variation in the pure cable part (without helium) can be written for the unit length of CICC in Eq. (4.10):

$$\rho C_p \frac{dT}{dt} S_{cable} = q_{joule} + q_{lin} + q_{long} + q_{conv} + q_{tran} \tag{4.10}$$

q_{tran} here is modelled as a multi-component thermal conduction between two turns cable part. This is given by the ratio between the inter-turn temperature difference and the thermal resistance (R_{th}) between the two adjacent turns. It is to note that, the way of taking into account the inter-jacket thermal resistance has already be attempted and proven to give nearly the same results to the "inter-turn" way. The R_{th} between two adjacent turns is finally taken as the modelling way for the practical assumption of a homogeneous temperature in the strands part, as written in Eq. (4.11):

$$\begin{aligned} R_{th} &= R_{th\,SS} + R_{th\,G10} \\ \text{with } R_{th\,SS} &= (\frac{e}{\lambda(T)})_{SS} \\ R_{th\,G10} &= (\frac{e}{\lambda(T)})_{G10} \end{aligned} \tag{4.11}$$

where $R_{th\,SS}$ and $R_{th\,G10}$ are respectively the thermal resistance of SS jacket and G10 insulation, e_{SS} and e_{G10} respectively the thickness of SS jacket (4 mm) and G10 insulator (2 mm), λ the thermal conductivity of each material depending on temperature.

An example has been given in Fig. 4.6 (see upper left) to explain the way of calculating the inter-turn thermal resistance. We can see that the inter-turn thermal resistance is generated between the turns 4 and 5 with their cable part temperatures respectively $T_{4,i}$ and $T_{5,i}$. Here the transversal temperature profile between the adjacent turns has been simplified to be linear so that the inter-turn thermal resistance can be computed by an average temperature as written in Eq. (4.12):

$$R_{th}(\frac{T_{4,i}+T_{5,i}}{2}) = (\frac{e}{\lambda(\frac{T_{4,i}+T_{5,i}}{2})})_{SS} + (\frac{e}{\lambda(\frac{T_{4,i}+T_{5,i}}{2})})_{G10} \tag{4.12}$$

One has to know that the transversal heat flux can come from two directions for a conductor. For example, Fig. 4.6 shows for the turn 2 an inflow of heat flux from turn 1 (supposed to be the first

quenched location) as well as an outflow one towards the turn 3 under a temperature gradient. In order to address the transversal heat flux on each mesh, two cases will be considered:

– When it is in the two side turns, i.e. turn 1 and turn 6, there is only one direction transversal heat flux between the meshes, q_{tran} can be written as Eq. (4.13):

$$\begin{aligned} q_{tran\ 1,i} &= h_{interturn}\frac{T_{2,i}-T_{1,i}}{R_{th\ 2,i}(\frac{T_{2,i}+T_{1,i}}{2})} \\ q_{tran\ 6,i} &= h_{interturn}\frac{T_{5,i}-T_{6,i}}{R_{th\ 5,i}(\frac{T_{5,i}+T_{6,i}}{2})} \end{aligned} \tag{4.13}$$

where i is the mesh number and $h_{interturn}$ the height of the inter-turn adjacent side (see Fig. 4.6).

– When it is not the case, i.e. from turn 2 to turn 5, the transversal heat flux will necessarily exchange from two directions, the upstream turn and downstream turn, as written in Eq. (4.14):

$$q_{tran\ t,i} = h_{interturn}[\frac{T_{t-1,i}-T_{t,i}}{R_{th\ t-1,i}(\frac{T_{t-1,i}+T_{t,i}}{2})} - \frac{T_{t+1,i}-T_{t,i}}{R_{th\ t+1,i}(\frac{T_{t+1,i}+T_{t,i}}{2})}] \tag{4.14}$$

with $t = 2, ..., 5$.

In order to implement the transversal heat flux term in the 1D THEA model, the key matter is to transform the longitudinal coordinate along the conductor to a curvilinear one. We firstly make space discretization for the 6 turns from the inlet (turn 1) to the outlet (turn 6) by dividing the 113.277 m length into 6 isometric segments, e.g. turn 1 ranges from 0 m to 18.88 m, as presented in the left of Fig. 4.7. The right zoom view (presented in red circle) allows to get a clearer overview of the mesh distribution on the 6 turns. As previously mentioned, the index couple (t,i) always represents the i-th mesh in the t-th turn ($t = 1, .., 6$). When THEA realizes the computations on the position X in the longitudinal coordinate, we will put it into the curvilinear coordinate system. For instance, the red X in Fig. 4.7 has been located at the turn 3 of the system, with $37.76\,\mathrm{m}(l_{turn2}) \leqslant X < 56.64\,\mathrm{m}(l_{turn3})$. Then we standardize this position X into the curvilinear system with Eq. (4.15):

$$x_{stand} = \frac{X - l_{turn2}}{l_{turn3} - l_{turn2}} \tag{4.15}$$

where x_{stand} represents the standardized coordinate of the position X, l_{turn2} and l_{turn3} the longitudinal coordinate of the end of turns 2 and 3.

This step actually indicates the relative position of X in the turn 3 so as to give the upstream or downstream position in the adjacent turns. For instance, the upstream position X_{+1} in Fig. 4.7 can be determined by:

$$X_{+1} = l_{turn3} + (l_{turn4} - l_{turn3}) * x_{stand} \tag{4.16}$$

We then rely on a predefined function "BSearchArrayR" in THEA to find the node number of the position X_{+1} as well as the strands temperature $T_{X_{+1}}$ at this point by interpolation. The same computation can be applied to the downstream position X_{-1} and to the strands temperature $T_{X_{-1}}$. Finally, we can compute the inter-turn transversal heat flux by applying the above determined temperatures to Eq. (4.14) and obtain Eq. (4.17) as written below:

$$q_{tran\,X} = h_{interturn}[\frac{T_{X_{-1}}-T_X}{R_{th\ X_{-1}}(\frac{T_{X_{-1}}+T_X}{2})} - \frac{T_{X_{+1}}-T_X}{R_{th\ X_{+1}}(\frac{T_{X_{+1}}+T_X}{2})}] \tag{4.17}$$

To summarize, the inter-turn thermal coupling model has built a curvilinear coordinate system in the pancake based on the original rectilinear one in THEA. This allows to take into account the transversal heat exchange between the adjacent turns for each computation position X. With this new model, we will again carry out the numerical computations in the pure thermohydraulic case with no quench (temperature-increasing phase) in order to verify its efficiency.

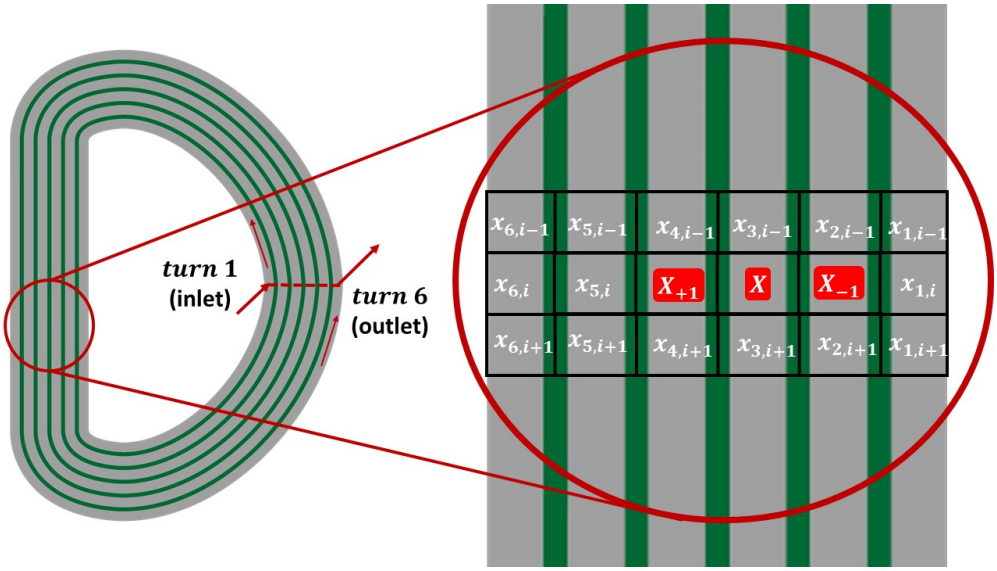

Figure 4.7 – Scheme of the inter-turn thermal coupling model implementation in THEA

4.3.3 First results with the inter-turn thermal coupling model

Based on the same experimental measurements of TFC12, Fig. 4.8 shows a comparison between the two numerical outlet temperatures during the temperature-increasing phase. The result of the inter-turn thermal coupling model (blue dashed line) is much closer to the experimental curve (blue solid line) than the one with the original 1D model (blue dash-dotted line). We can see that the numerical T_{out} of our new model has a "quasi-immediate" evolution after the increase of the inlet temperature. This proves our assumption of the predominant effect of the inter-turn transversal heat exchange in the pancake (analytically estimated to be about 8 s through the six turns). In addition, one may also note a little difference (about 2 %) between the result of the inter-turn thermal coupling model and the experimental one. This overheat phenomenon produced in our new model can be explained by the fact that the temperature is computed at the outlet of the side pancake P1 whereas the experimental one corresponds to the whole coil outlet temperature. Knowing that the side pancake sees more heat loads than the other pancakes, the computed outlet temperature is thus higher than the average experimental one. In conclusion, this inter-turn thermal coupling model presents good improvement in the computation of the pancake temperature map during the temperature-increasing phase. Moreover, this improved temperature map will also be a key input of the following quench propagation computations which takes place at around $t = 2000$ s in Fig. 4.8.

In addition, Fig. 4.8 also shows that when the inlet temperature increases at around $t = 500$ s, the experimental outlet temperature starts to oscillate. This could be due to the fact that the regulation system is taking action to keep the pressure constant during the temperature rise, as already presented in the experimental boundary conditions (see Fig. 4.2).

Finally, one can note that this inter-turn thermal coupling model is a quasi-steady state model well adapted to the temperature-increasing phase just before quench. Nevertheless, the fast transient phase during quench propagation still remains to be verified with this model. Indeed, the experimental analysis in Chapter 3 allows to deduce that during the quench phase, the time needed for the quench to propagate longitudinally from a turn to the next one is about 0.5 s (e.g. $v_{acc} = 36.5$ m/s for TFC12) while the time needed to quench the adjacent turn due to the inter-turn heat exchange is of the order of several seconds (see Section 1.4.3). Therefore, we can consider that this inter-turn thermal coupling model will improve the temperature map as an input for the quench initiation without inducing high limitations on the predominant phenomenon driving the "further" quench propagation. Regarding the quench predominant longitudinal propagation phenomenon, it

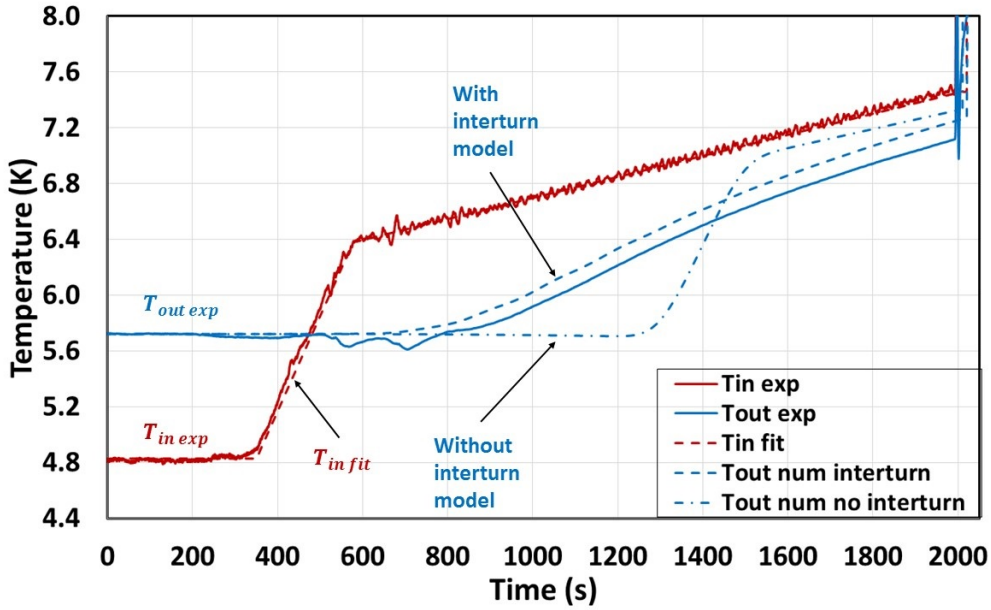

Figure 4.8 – Comparison of the temperature evolution between experimental measurements and numerical modelling results

is modelled in a fully transient way with THEA, as already presented in general introduction.

4.4 Numerical analysis for the physical phenomena identified during the quench tests of JT-60SA TF coils

After obtaining the improved numerical model for quench simulations, we will address the second issue of this chapter: carrying out a further numerical study of the physical phenomena identified during the quench test experimental analysis in Chapter 3. As usual, we still take the "typical" quench test of TFC12 as an example to carry out our following studies. In order to cover all the phenomena that will be analyzed with our single pancake quench model, two representative DPs have been chosen to be modelled, DP1 for its most exposed heat load from casing and DP3 for the peak field location in the coil. We recall that:

- During the quench initiation phase, the external heat load effect on the initial quench location remains to be verified with the numerical modelling. In order to achieve this goal, we will compare the numerical quench initiation time between the two representative DPs by varying the external heat load.
- During the quench acceleration phase, we still need to give further verifications for the effect of the quenched pancakes number on the normal zone acceleration dynamics, for the assumption of the thermohydraulic quench-back during the normal zone acceleration and for the effect of the testing temperature oscillations on the delayed quench acceleration phenomenon. A comparison of the normal zone length evolution will be followed to verify the computation accuracy of the simplified physical model (see Section 3.5.2) with respect to the numerical results.
- During the simultaneous quench phase, the helium reverse flow effect will be modelled and compared with the experimental data in the central pancakes DP3. The numerical approach is simply to vary the injection time of the warm helium at the inlet boundary conditions of DP3 to acquire the different quench dynamics.

4.4.1 Study of the external heat load effect on the initial quench location

According to the experimental analysis of the initial quench location in Section 3.2.2, the external heat load effect still remains to be verified with a further numerical modelling. This section will address the external heat load effect in two steps. Firstly, an analytical estimation will be attempted to obtain the order of magnitude of the external heat load deposited on each pancake. As we only focus on two representative DPs, a heat load distribution will be given to the side pancake P1 (DP1) and the central pancake P6 (DP3), noted as ($q_{ex\,P1}$, $q_{ex\,P6}$). Secondly, a parametric study will be initiated with this determined analytical results ($q_{ex\,P1}$, $q_{ex\,P6}$) and then be carried out by varying the heat load distribution values to obtain the effect on the two pancakes initial quench time.

a) Analytical computation for the external heat load on each pancake

In order to estimate the external heat load for each pancake, we make a first hypothesis that the thermal balance system in the first half of the winding pack is identical to the second half due to the coil symmetry property. Moreover, the gravitational effect is also assumed to be negligible since the tested coils are horizontally oriented in the cryostat of the CTF. These two hypotheses allow to focus our following estimation on the half 6 pancakes (P1 $\backsim$ P6). Therefore, a first global thermal balance equation can be written on one half of the winding pack as in Eq. (4.18):

$$\dot{m}_{tot} \cdot C_p(\frac{T_{out} + T_{in}}{2}) \cdot (T_{out} - T_{in}) = \dot{Q}_{tot} = \dot{Q}_{feeder} + \sum_{p=1}^{6} \dot{Q}_p \tag{4.18}$$

where $\dot{m}_{tot} = 12\,\mathrm{g/s}$ is the total helium mass flow rate in the half 6 pancakes of 2 g/s each, C_p the average specific heat in the half 6 pancakes estimated at the average temperature between the coil inlet ($T_{in} = 4.83\,\mathrm{K}$) and outlet ($T_{out} = 5.75\,\mathrm{K}$) and with an average pressure around 10 bar (idem for the following C_p). An overall experimental heat load deposited on the 6 studied pancakes can thus be computed to $\dot{Q}_{tot} = 48.7\,\mathrm{W}$. This total value actually consists of two parts, the feeder heat load contribution $\dot{Q}_{feeder}$ due to the resistive joint connecting the P1 outlet and the superconducting feeder as well as the heat flux from casing to the 6 pancakes $\sum_{p=1}^{6} \dot{Q}_p$. Indeed, the latter one is the part of external heat load that is really deposited on the pancakes and that will be taken into account in the following computations.

Based on the experimental conditions, the feeder heat load contribution can be estimated to $\dot{Q}_{feeder} = 6.3\,\mathrm{W}$ so that the casing heat load on the 6 pancakes can be deduced to $\sum_{p=1}^{6} \dot{Q}_p = 42.4\,\mathrm{W}$ with the same thermal balance equation in Eq. (4.18). As the casing heat load on each pancake is proportional to the contact area between them (through G10 insulation), we can compute for the 6 pancakes the external heat load from the casing contribution, as presented in Table 4.1. In particular, with the highest contact area of $3.47\,\mathrm{m}^2$, the side pancake P1 receives the highest heat load from casing of 17.6 W.

Table 4.1 – Casing heat load distribution on the pancakes

Pancake	Contact area (m^2)	Casing heat load (W)
P1	3.47	17.6
P2	0.98	5.0
P3	0.98	5.0
P4	0.98	5.0
P5	0.98	5.0
P6	0.98	5.0
Total	**8.36**	**42.4**

In addition to the casing heat load deposited on each pancake, the heat exchange between these pancakes also needs to be taken into account to obtain the final external heat load for each pancake.

A system of heat equations have been established for the 6 pancakes from P1 to P6, as written in the equation system Eq. (4.19):

$$\begin{cases} \dot{m}_1 \cdot C_{p\,1}(T) \cdot (T_{out\,1} - T_{in}) = \dot{Q}_1 - \lambda_{iso}(T) \displaystyle\int_{x=0}^{x=L} \frac{T_1(x) - T_2(x)}{e_{iso}}\, l_{interpan} dx \\ \dot{m}_i \cdot C_{p\,i}(T) \cdot (T_{out\,i} - T_{in}) = \dot{Q}_i + \lambda_{iso}(T) \displaystyle\int_{x=0}^{x=L} \frac{T_{i-1}(x) - T_i(x)}{e_{iso}}\, l_{interpan} dx \\ \qquad\qquad - \lambda_{iso}(T) \displaystyle\int_{x=0}^{x=L} \frac{T_i(x) - T_{i+1}(x)}{e_{iso}}\, l_{interpan} dx \quad (i = 2, ..., 5) \\ \dot{m}_6 \cdot C_{p\,6}(T) \cdot (T_{out\,6} - T_{in}) = \dot{Q}_6 + \lambda_{iso}(T) \displaystyle\int_{x=0}^{x=L} \frac{T_5(x) - T_6(x)}{e_{iso}}\, l_{interpan} dx \end{cases} \tag{4.19}$$

where $\dot{m}_i$ is the helium mass flow rate in each pancake of around 2 g/s, T_{in} the measured helium inlet temperature assuming to be the same for all the pancakes (close to the testing conditions), $\dot{Q}_i$ the casing heat load on each pancake i ($i = 1, ..., 6$) presented in Table 4.1, λ_{iso} the thermal conductivity of the G10 insulation computed with the average temperature between the inlet and outlet for simplification, e_{iso} the thickness of the inter-pancake G10 insulation of 2 mm, $l_{interpan}$ the width of the inter-pancake side of 22 mm and $T_i(x)$ the temperature profile in each pancake i assumed to be linear for a simplification in the computations. For instance, the linear temperature profile in the two pancakes P1 and P2 can be expressed as below in Eq. (4.20):

$$\begin{cases} T_1(x) = \dfrac{T_{out\,1} - T_{in}}{L} \cdot x + T_{in} \\ T_2(x) = \dfrac{T_{out\,2} - T_{in}}{L} \cdot x + T_{in} \end{cases} \tag{4.20}$$

where L is the total length of the pancake equal to 113.277 m.

Applying the couple Eq. (4.20) in the first equation of Eq. (4.19), we can rewrite the integral form of the inter-pancake heat exchange in an explicit way, as written in Eq. (4.21):

$$\lambda_{iso}(T) \int_{x=0}^{x=L} \frac{T_1(x) - T_2(x)}{e_{iso}}\, l_{interpan} dx = \lambda_{iso}(\frac{T_{out\,1} + T_{out\,2}}{2}) \cdot \frac{l_{interpan}\, L}{2\, e_{iso}} \cdot (T_{out\,1} - T_{out\,2}) \tag{4.21}$$

With the same approach, the whole system equations Eq. (4.19) can be rewritten in an explicit way leading to the only unknown for each equation, the outlet helium temperature $T_{out\,i}$ ($i = 1, ..., 6$). Therefore, we have developed for all the pancakes a closed system with 6 equations for resolving 6 unknowns (the 6 outlet helium temperatures $T_{out\,i}$). The real external heat load deposited on each pancake can then be obtained with the classical thermal balance equation in Eq. (4.22):

$$\dot{Q}_{hl\,i} = \dot{m}_i \cdot C_{p\,i}(T) \cdot (T_{out\,i} - T_{in}) \quad (i = 1, ..., 6) \tag{4.22}$$

where $\dot{Q}_{hl\,i}$ is the real external heat load on each pancake.

Table 4.2 presents for the 6 pancakes the outlet helium temperature, external heat load and external heat load per unit length.

Finally, the theoretical external heat load per unit length (q_{lin}) for the two representative pancakes, P1 and P6 of TFC12, can be written as $(0.0807; 0.0528)$. We will call it "ideal distribution" in the following analyses since these values are obtained from a theoretical model as described above. After acquiring the order of magnitude of the external heat load, we still need to take into account the diverse factors that can lead to the distribution uncertainty from one coil to another, including:

- the material property such as the inter-pancake insulation that can affect the heat exchange between the pancakes,
- the electrical resistance in the inter-pancake joints that can induce different Joule heat for each pancake during the quench test,

Table 4.2 – Total heat load for each pancake

Pancake	Outlet temperature (K) T_{out}	Heat load (W) $\dot{Q}_{hl}$	Linear heat load (W/m) q_{lin}
P1	5.95	9.1	0.0807
P2	5.79	7.8	0.0693
P3	5.69	7.0	0.0618
P4	5.62	6.4	0.0569
P5	5.58	6.1	0.0541
P6	5.56	6.0	0.0528
Total		**42.4**	

– the Lorentz force when energized at nominal current that can deform the coil so as to modify the contact area between the casing and winding pack.

The possibility of having different heat load distributions in different coils is actually the departure point of our following parametric study. The ideal distribution will then be applied for launching the first numerical computations.

b) Parametric study of the external heat load effect on the initial quench time

According to the experimental analysis, quench can be initiated at different locations: 53 % of the quench tests are initiated on side pancakes whereas 32 % are initiated on central pancakes and 16 % on inner ones. Such a seemingly random behaviour could actually be explained with one parameter, the external heat load deposited on the pancakes (q_{lin}).

As estimated before, the theoretical heat load distribution or the so-called "ideal distribution" is $(0.0807; 0.0528)$ for the pancakes (P1, P6) in TFC12. Since the developed model is dedicated to a single pancake configuration, we begin by taking each one of these q_{lin} values and launch two separate simulations for P1 and P6. And then we compare the initial quench time between the two modellings. Here we fix the initial quench time of the central pancake P6 as a reference. This means that when the initial quench time computed in P1 is later than that in P6, the difference will be positive, otherwise it will be negative. Fig. 4.9 shows that, with the first "ideal distribution" values, P1 (first point of the blue line) quenches in the computations around 28 s later than P6 (first point of the green line). This is completely opposed to the experimental fact that the quench of TFC12 was initiated on the side pancakes DP1 (P1). Nevertheless, this is to some extent, in agreement with the fact that 32 % of the quenches are initiated on the central pancakes (like P6) owing to their peak field value of the coil (i.e. the lowest T_{cs}) thus be "magnetically" more vulnerable for quench.

One can see that a big initial quench time difference has been produced with this "ideal distribution" computation. Indeed, a theoretical distribution could be very far away from the reality, especially the real thermal resistance between pancakes could be very different from a coil to another due to different assembly process, insulation impregnation process or to the mechanical compression of its insulation when energizing the coil (which could increase the thermal link between pancakes). In order to continue this study, we fix the total external heat load deposited on the pancakes to $\sum_{p=1}^{6} \dot{Q}_p = 42.4\,\mathrm{W}$ and we increase slightly the thermal conductivity of the inter-pancake insulation in Eq. (4.19) to compute other possible q_{lin} distributions.

Fig. 4.9 shows all the computed initial quench time as a function of the relative increase of q_{lin} against the ideal value computed for P1 (0.0807 W/m). We can see that when increasing the external heat load deposited on the side pancake P1 (i.e reducing that of the central pancake P6), the initial quench time of P1 can be computed to a much earlier value, until the existence of a "critical distribution" of $(0.0866; 0.0504)$ for which the two pancakes could quench at the same time. Being

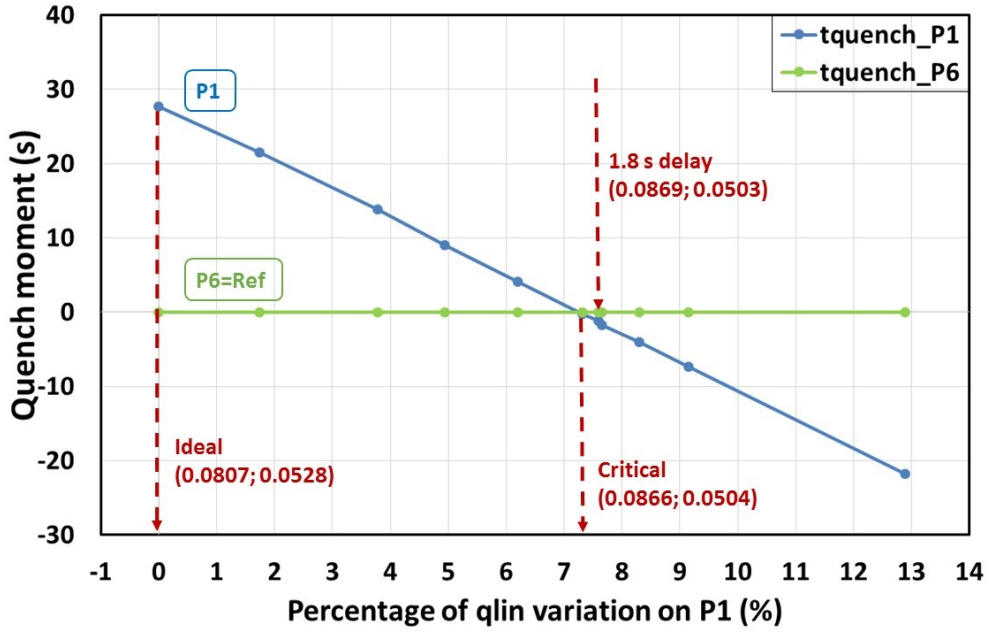

Figure 4.9 – Effect of the external heat load on the initial quench time

lower or higher than this "critical distribution" makes P1 quench before or after P6. Actually, the difference between the "ideal distribution" and the "critical distribution" corresponds to about 7 % more power on P1 and less on P6 (see Fig. 4.9), but can already make an important variation on the pancakes initial quench time. This margin can be taken as a reasonable value when considering the assumptions made for the different external heat load computations, including the uncertainties like the different resistive joint heat as well as the different thermal contacts due to material properties or mechanical deformation by Lorentz forces.

We recall that in the quench test of TFC18, a common quench initiation has appeared in most of the pancakes, from inner pancakes DP2 to side pancakes DP6 within 1 s (see Fig. 4.10). This has been explained with the scattering strands performance appearing during the manufacture of the coil TFC18 in Section 3.2.2. Nevertheless, as the external heat load effect is proved to be as predominant as the strands performance impact on the different initial quench location, the common quench initiation among the DPs could now be more probably explained with the competition between the external heat load and the strands performance.

Finally, one may also note that, in Fig. 4.9, there is a third distribution of $(0.0869; 0.0503)$, named "1.8 s delay". The computations based on this distribution have actually obtained for P1 and P6 an initial quench time difference of about 1.8 s which is coherent with the experimental data of the quench test in TFC12. In the following studies, this determined "1.8 s delay" distribution will be applied to carry out the numerical simulations for TFC12.

4.4.2 Study of the different quench acceleration mechanisms

a) Evaluation of the number of quenched pancakes in a double-pancake

After addressing the quench initiation issues, we are now going to achieve a better understanding on the quench acceleration mechanism. The question about the number of quenched pancakes in the same DP has already been asked when estimating the normal zone propagation velocity before the start of the FD (see Section 3.2.1). As we only have the access to the voltage measurements of a double-pancake, the possibility of having one or two pancakes quenched in a DP could then lead to an acceleration in the quench resistance evolution. We will rely on the numerical approach to

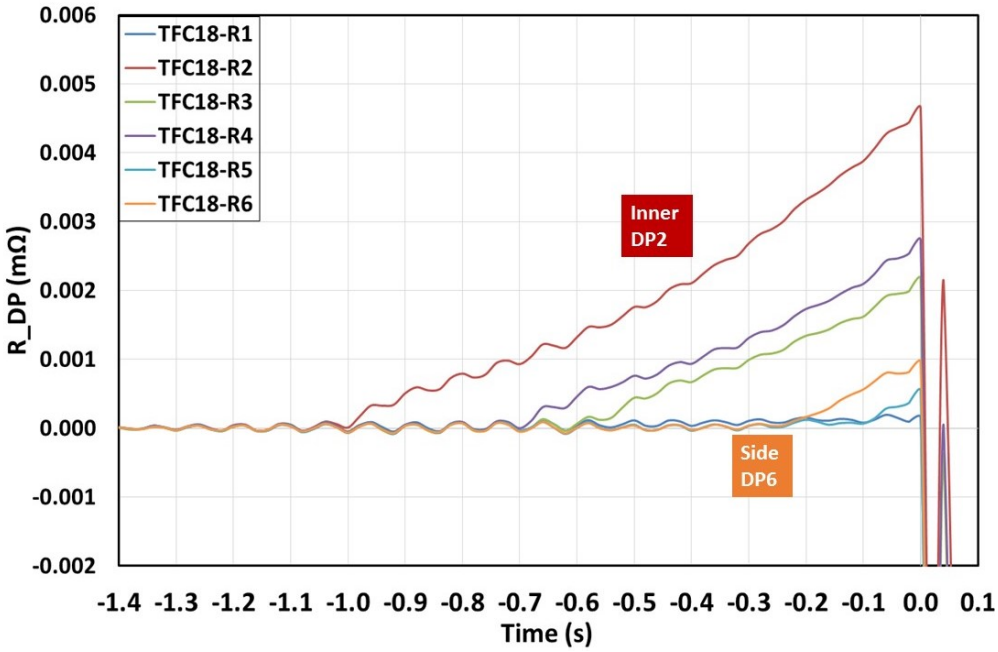

Figure 4.10 – TFC18 DPs quench resistance evolutions during the quench initiation phase

give a verification of this quenched pancake number problem.

We always take the two representative DPs, side pancakes DP1 (P1 & P2) and central pancakes DP3 (P5 & P6), to carry out the numerical computations. It is to note that these computations are always made in a single pancake model and that the double-pancake resistance is deduced from the single pancake numerical resistance, e.g. $R_{DP1\,num} = R_{P1\,num} + R_{P2\,num}$. The external heat load distribution between P1 and P6 will use the "1.8 s delay" distribution of $(0.0869; 0.0503)$, matching the experimental conditions. Fig. 4.11 then shows the comparison between the numerical results of the quench resistance time evolutions and the experimental data. The time $t = 0\,\mathrm{s}$ always indicates the start of the FD.

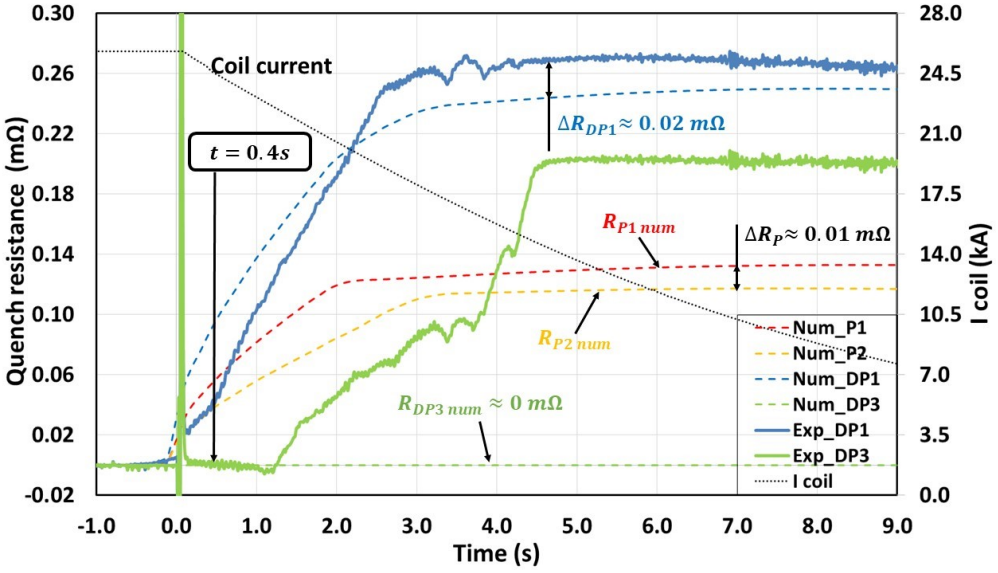

Figure 4.11 – General quench resistance evolution during the FD

First of all, we focus on the analysis of the side pancakes DP1 (P1 & P2). The numerical quench resistances of the two adjacent pancakes P1 and P2 are respectively plotted in red dashed line and yellow dashed line. The outer side pancake P1 has effectively a faster quench resistance evolution

than the inner one P2. This could be explained by the slight difference in the field distribution and the different external heat loads (refer to Table 4.2). Different quench dynamics also lead to the different maximal quench resistance plateau with P1 having around 0.01 mΩ higher than P2 and with a different arriving time of about 1 s delay. One should note that these single pancake quench resistances are both in an order of half of the experimental resistance in DP1 (blue solid line). This allows to verify the first assumption that both of the two adjacent pancakes in the DP1 have been quenched and have probably reached a full quench state to achieve such a maximal resistance of around 0.27 mΩ.

When adding the above two computed quench resistances of P1 and P2, a numerical result of DP1 can be obtained (see blue dashed line). We can see that the DP1 numerical resistance evolution has almost the same period of quench acceleration from 0 s to 3 s than the experimental evolution (blue solid line). This allows to give the correct order of the average quench propagation velocity around 35 m/s in TFC12 (comparing to the experimental value of 36.5 m/s). However, we can also see that the numerical quench resistance evolution is faster than the experimental one before $t = 0.4$ s (a zoom view will be given below) and then has a lower quench resistance plateau than the experimental one with around 0.02 mΩ difference. The first time delay could be explained by the lack of cooling effect from the adjacent pancakes within such a single pancake numerical model. An over heated pancake could then lead to a faster quench dynamics in the computations. Concerning the maximal quench resistance difference, this could be due to the constraint of our single pancake model which does not take into account the heat exchange from other pancakes or from the casing (Joule heat by eddy currents). In addition, the potential uncertainties from the correlations implemented in the numerical model could also lead to the quench resistance discrepancy, such as the correlation of the copper electrical resistivity or the computations of the cable temperature. In conclusion, the DP1 numerical results obtained with this single pancake quench model are in agreement with the experimental data with only 7.7 % uncertainty with respect to the experimental data (corresponding to the 0.02 mΩ difference).

Fig. 4.11 also shows that the computations predict no quench in the central pancakes DP3, i.e. $R_{DP3} \approx 0$ mΩ as plotted in green dashed line. One has to know that when carrying out these computations, the beginning of the FD has been fixed by the early quenched pancake P1. This means that the central pancake P6 with an initiation delay of 1.8 s (when applying the distribution of $(0.0869; 0.0503)$) will have an earlier FD than the real quench initiation. Based on these modelling conditions, the no quench phenomenon in P6 can then be explained. When current is fast decreasing, T_{cs} is increasing. So if P6 is not already quenched before the FD beginning, it cannot quench in this model later during the FD because the temperature in P6 will never reach the continuously increased T_{cs}. Such no quench phenomenon appeared during the numerical computations is completely incoherent with the experiment, which also leads us to search for the possible explanations of the simultaneous quench phenomenon in the central pancakes (see the following Section 4.4.3).

One may note that in Fig. 4.11, the time near $t = 0.4$ s seems to show a slope change of the DP1 experimental resistance evolution. Indeed, before $t = 0.4$ s, the numerical quench resistance evolution of DP1 is faster than the experimental one. This could give a possible verification for the quenched pancakes number in a double-pancake. Thereby, we will take a zoom view of the quench resistance evolution in the two single pancakes (P1 and P2) with the same color code in Fig. 4.12.

One can see that before $t = 0.4$ s, the single pancake resistance of P2 (yellow dashed line) is in good agreement with the experimental data (blue solid line), despite of the incoherence during the ± 0.1 s near the start of the FD (probably due to the overheat effect in our single pancake model). After this moment, the slope of the DP1 experimental resistance becomes much closer to that of the numerical resistance of double-pancake. This direct comparison allows to tell that a single pancake P2 quenches first alone at $t = -0.65$ s (see Fig. 3.8) due to its peak field location closer to the coil inlet. And then at $t = 0.4$ s, the adjacent side pancake P1 quenches as well due to the highest external heat load coming from the casing. The two quenches with around 1 s delay can be due to the time needed for reaching the quench temperature in the two different field maps (thus

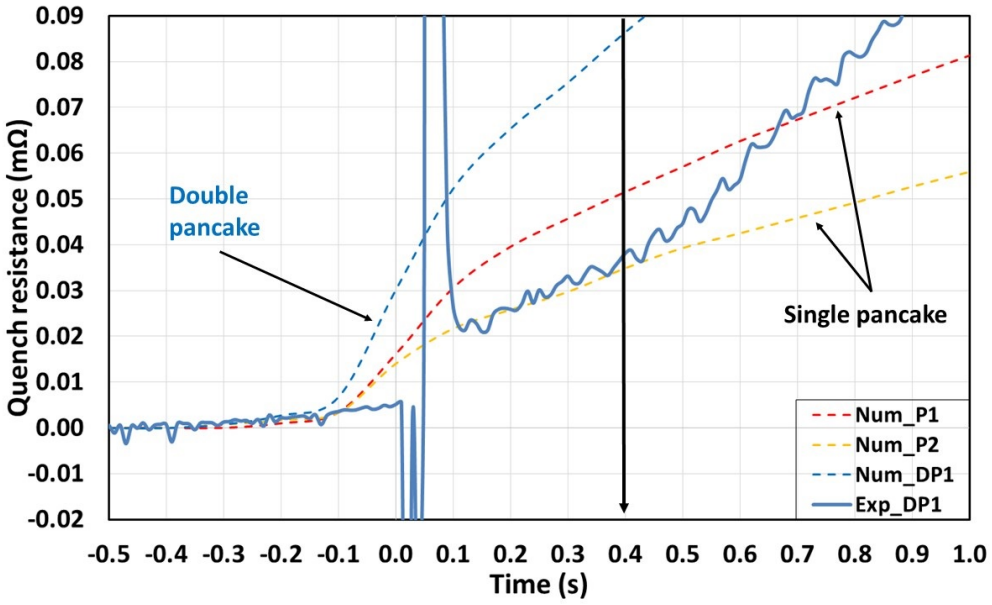

Figure 4.12 – Effect of the quenched pancakes number on the normal zone acceleration dynamics

different T_{cs}), due to the helium reverse flow from the early quenched pancake to the later one, or due to the thermal conduction through the 2 mm inter-pancake insulation. A further complex model coupling two or more pancakes need to be built to carry out a more accurate verification of the the consecutive quench propagation phenomena in a double-pancake.

In conclusion, we can say that the number of quenched pancakes in the same DP can have an effect on the quench resistance evolution. In addition, the single pancake assumption for calculating the normal zone propagation velocity before the FD has also been verified.

b) Comparison between two quench acceleration mechanisms

In order to address the thermohydraulic quench-back (THQB) assumption on the quench acceleration mechanism, two types of parameter should be considered here (refer to Section 3.3.2):

- Temperature: comparison between the cable temperature T_{cable} and the helium temperature T_{He} ahead of the quench front
- Velocity: comparison between the cable quench propagation velocity v_{cable} and the helium flow expulsion velocity v_{He}

Fig. 4.13 shows the spacial temperature profiles at the beginning of the quench acceleration in TFC12 around $t = -0.2$ s (see Fig. 3.15). We can see that behind the quench front ($x < 10.3$ m), i.e. within the quench region, the cable temperature T_{cable} (red solid line) is higher than the helium one T_{He} (blue dashed line). This is coherent with a "standard" quench mechanism[94] saying that the Joule heat produced in the cable firstly increases the temperature of the cable itself then will be transferred to the helium by forced convection to make T_{He} increase. This in turn increases the helium pressure inducing a flow of helium in the channel. The warm helium in the quench region then expands against the cold helium in the outer region, thereby propagating the quench front (at $x = 10.3$ m in Fig. 4.13). Nevertheless, when looking at the region just ahead of the quench front, denoted as the outer region and characterized with zero Joule heat, there is a slight increase in the helium temperature leading to $T_{He} > T_{cable}$. This is actually due to the preheating of the helium compression (caused by Joule heat in quench region) which is against the frictional drag force by

[94] Dresner, Lawrence. *Proc. 11th Symposium on Fusion Engineering* **2**. 1218–1222. 1986.

the inner wall of conduit and the cable. According to the already mentioned effect of THQB[51,97] in Section 3.3.2, when this preheating effect raises the helium temperature in the outer region above T_{cs}, the Joule heat develops almost instantaneously over the segments of the conductor in the outer region. This sudden increase in heating power then strongly enhances the quench propagation in the CICC, known as THQB. The observation of $T_{He} > T_{cable}$ between 10.3 m and 10.41 m is thus in good agreement with the THQB effect. The front at $x = 10.41$ m can also be taken as a THQB front that drives the quench acceleration in the cable.

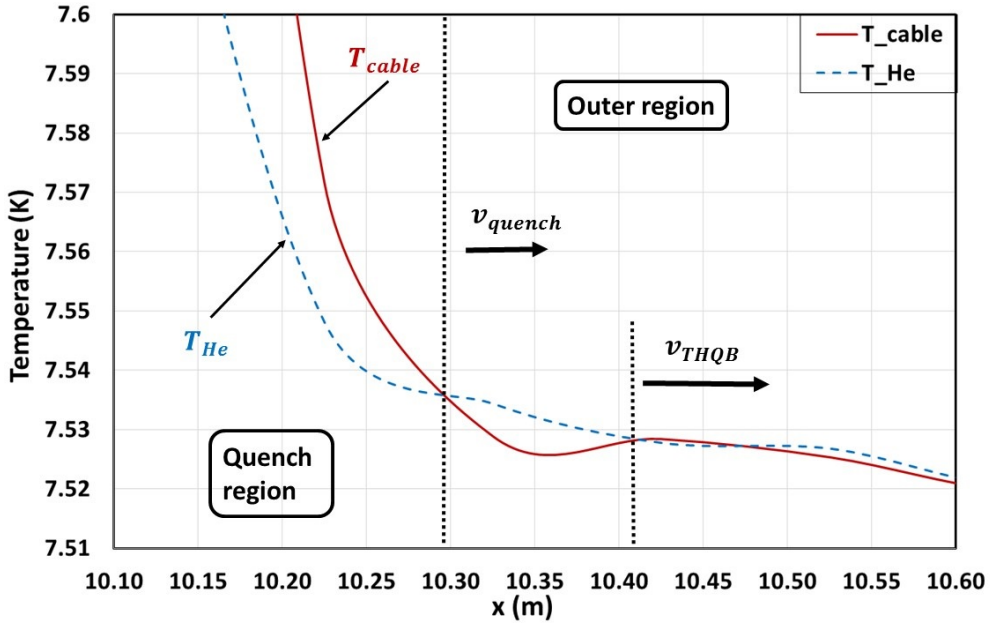

Figure 4.13 – Temperature comparison between the cable and the helium at the quench front

The above discussion gives us an important verification for the THQB effect on the quench acceleration. Meanwhile, we have also talked about a consequence of the THQB effect, the competition between the helium expulsion velocity v_{He} and the cable quench propagation velocity v_{cable}. Here, we choose the two ends positions of the side pancake P1 in TFC12 to plot the time evolution of the helium velocity, v_{in} and v_{out}, as presented in Fig. 4.14. Indeed, the pressure drop is decreasing when the helium is approaching to the cable ends. With the helium expulsion fully developed in the entire pancake, the two ends can then see the highest helium velocity. Therefore, we focus on the numerical results at the two ends position of the pancake. The time at $t = 0$ s always indicates the start of the FD.

Fig. 4.14 shows that the inlet helium velocity (red solid line) reaches a maximum value of 16.5 m/s at about 4 s whereas the outlet one (blue solid line) reaches around 13 m/s at 5.5 s. As the initial quench location is near the inlet, the heated helium will then be more easily expelled from the inlet than the outlet thanks to less pressure drop from the inlet side. Therefore, an early increase of the helium velocity has appeared at the inlet and has reached a maximal value of about 3.5 m/s higher than the outlet one. These helium velocity computations can thus be considered as qualitatively verified.

When we focus on the value of the helium velocity, the maximum helium expulsion velocity is around $v_{He} = 16.5$ m/s which is less than half of the quench propagation velocity through the cable estimated to $v_{cable} = 36.5$ m/s in Section 3.3.2. Such big difference indicates that the helium expulsion is slower than the quench propagation in the cable and that the assumption of the helium driven mode by forced convection could not be the explanation of the quench acceleration mechanism. This again verifies the only possibility of the THQB effect in the TFC12.

[51] A. Shajii and J. P. Freidberg. *Journal of Applied Physics* **76**. 3159–3171. 1994.
[97] A. Shajii and J. P. Freidberg. *International Journal of Heat and Mass Transfer* **39**. 491–501. 1996.

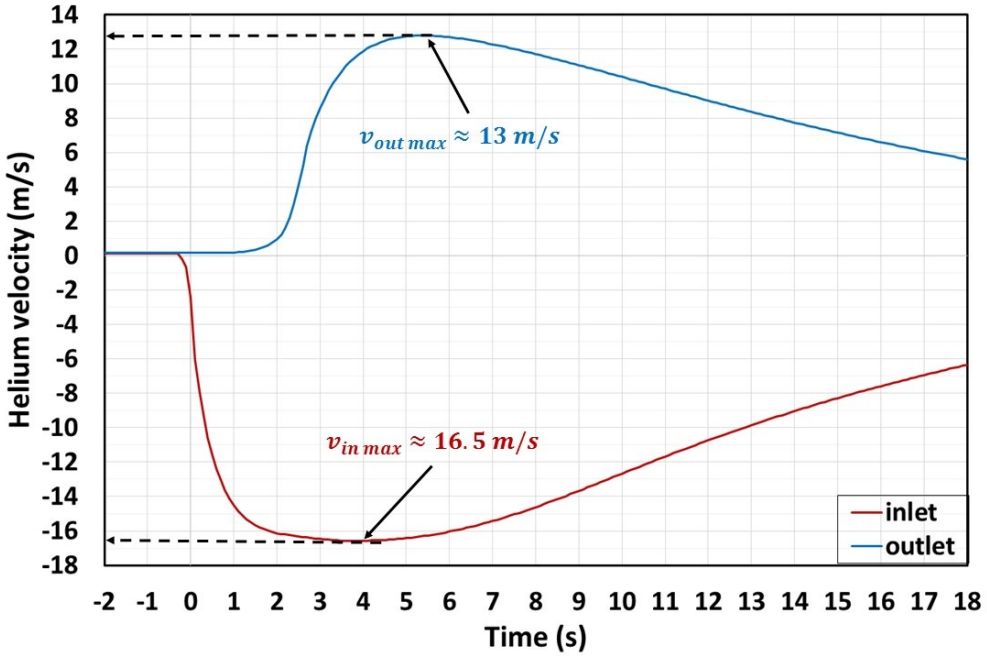

Figure 4.14 – Helium expulsion velocity during the quench propagation

Nevertheless, one could be somewhat surprised by observing such a "non-standard" quench in the JT-60SA TF coils, since in the most common case, the quench process in CICC is always governed by the helium in the conduit due to the forced convection. Such a "surprise" can actually be explained by our special quench test protocol in the CTF (see Section 2.3). We recall that the quench has been triggered with a globally increased temperature in the entire coil with T_{in} about 0.3 K higher than the T_{out}. This then leads to a generally low temperature difference between T_{cs} and conductor through the entire coil. According to the inverse relation presented in Eq. (1.26), this low temperature difference can then lead to a higher quench propagation velocity in the globally heated pancake than the helium flow expulsion velocity ($v_{cable} > v_{He}$). Such temperature difference impact leading to the appearance of the THQB effect has also been observed in some previous experiments[99].

To conclude, the two types of parameter (temperature and velocity) both confirm the quench acceleration mechanisms due to thermohydraulic quench-back (THQB) effect. The cable quench propagation advances faster than the helium expulsion flow in the case of CTF quench test protocol for the JT-60SA TF coils. Nevertheless, the application of this THQB effect in the Tokamak conditions should still be discussed, depending on the quench conditions (local initial transition or global initial transition) and on the TF coils configurations in the Tokamak (vertical position and assembly together). More discussions will be given in the general conclusions at the end of this PhD report.

c) Impact of the testing temperature oscillations on the quench acceleration dynamics

In order to find an appropriate explanation for the delayed quench acceleration phenomenon (see Fig. 3.19), we are once again making all the possible observations on the available experimental data. When comparing the two quench tests carried out on the same coil TFC10, we find that the two quench acceleration dynamics are very different from each other. The first one (noted as TFC10) has a common "early" acceleration like that of TFC12 whereas the second one (noted as TFC10bis) has the quench acceleration in a "delayed" type that will be discussed here. As the two different behaviours result from the same coil TFC10, we will then have to focus on the testing

[99] J. W. Lue et al. *IEEE Transactions on Applied Superconductivity* **3**. 338–341. 1993.

conditions before quench to find the possible explanations.

Fig. 4.15 shows the inlet temperature conditions during the temperature-increasing phase (measurements on TE2412). The time $t = 0\,\mathrm{s}$ always indicates the start of the FD when detecting a quench. We can see that the temperature oscillation in the first test TFC10 (red line) is small enough (an order of amplitude around 10 mK) leading to an "early" type of quench acceleration like the one in TFC12. Whereas the second test TFC10bis (blue line) has undergone an oscillation of around 100 mK amplitude and has seen a "delayed" quench acceleration phenomenon (like the one in TFC16). These observations allow us to make the assumption that the quench acceleration delay should be related to the different oscillations of the testing temperatures (caused by the temperature regulation of the cryogenic control system).

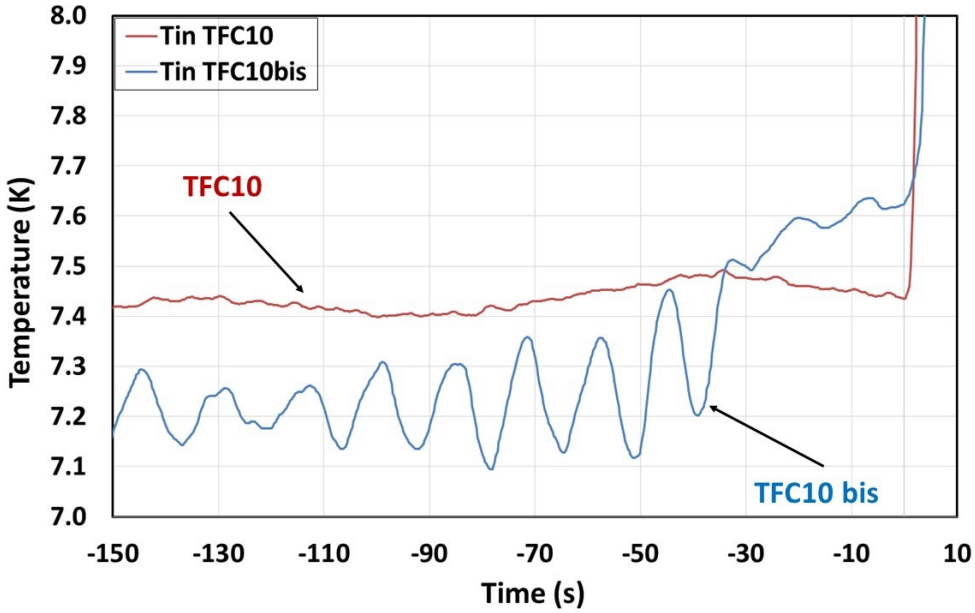

Figure 4.15 – Comparison of the inlet temperature oscillations (TE2412) between the two quench tests of TFC10 during the temperature-increasing phase before quench

Indeed, the oscillations during the temperature-increasing phase could probably lead to a short heat peak that initiates a "premature" quench when the general helium environment still remains "colder", i.e. generally below the T_{cs}. This assumption could then explain the phenomenon that the quench propagation velocity keeps at a low level for a certain time before achieving the acceleration (representing about 25 % of the quench tests). In order to verify this assumption with a numerical approach, we will build for the inlet testing temperatures T_{in} a time dependent function combining the principal temperature fits T_{fit} (see Fig. 4.2) and the temperature oscillations in a sinusoidal function T_{oscill}, as written in Eq. (4.23):

$$T_{in}(t) = T_{fit}(t) + T_{oscill}(t) = T_{fit}(t) + A\,sin(\frac{2\pi}{T_{per}}\,t - \varphi) \tag{4.23}$$

where A is the temperature oscillation amplitude, T_{per} the oscillation period and φ the phase shift.

The impact of these oscillation parameters (A, T_{per} and φ) on the quench acceleration dynamics will then be studied. Here we take two extreme cases with their oscillation amplitude covering the entire scope of the 5 delayed quench acceleration tests: the minimum of 35 mK in TFC16 and the maximum of 125 mK in TFC10bis (see Fig. 4.16). We can see that the highest amplitude of 125 mK in TFC10bis is more than 3 times higher than the lowest one of 35 mK in TFC16. This leads to 5 different dynamics of the delayed quench acceleration. Indeed, the oscillation amplitude can have a direct impact on the spacial temperature profile that brings the different slope of temperature increase (or decrease) thus the different heating (or cooling) effect when reaching the quench at T_{cs}. The oscillation amplitude should then play an important role in the quench acceleration dynamics.

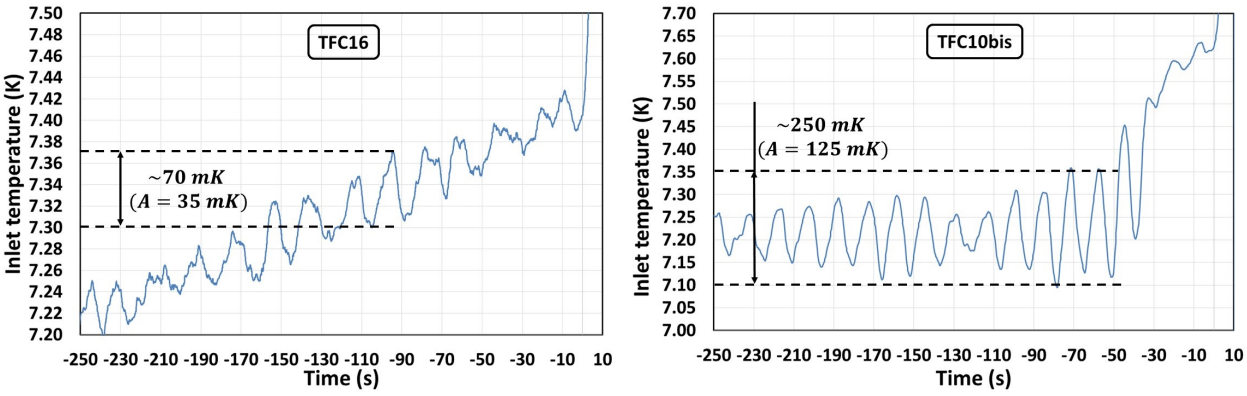

(a) Quench test TFC16 (b) Quench test TFC10bis

Figure 4.16 – Inlet temperature oscillations during the quasi-steady state

When talking about the impact of the slope change, the oscillation period should also be taken into account. With the same oscillation amplitude, shorter period leads to higher slope thus higher impact on the quench propagation. Concerning the oscillation phase shift φ, it could also play an important role in the quench dynamics. When varying the phase shift φ, the T_{cs} could be reached at different positions of the sinusoidal oscillation wave. If it is reached at the wave crest, the quench propagation should probably be decelerated by cooling effect since the temperature will decrease during the next moment. If it is the opposite case (wave trough), an acceleration effect would play during the quench propagation. These are only two simple extreme cases. The other possible quench positions could also be appeared with the different phase shift φ and thus have different effects on the quench propagation. This is to be studied.

One can note that the experimental period of the temperature oscillation is nearly constant to around 20 s. In the following study, we will fix $T_{per} = 20\,\text{s}$ to verify the impact of the oscillation amplitude A and phase shift φ on the quench acceleration dynamics.

Temperature oscillation amplitude

The first parametric study will be carried out on the temperature oscillation amplitude. In order to implement this parameter in our numerical model, the new sinusoidal temperature fit in Eq. (4.23) will be applied in the helium inlet boundary conditions during the temperature-increasing phase. The different computations will then be made by varying the oscillation amplitude from 35 mK to 125 mK and by taking the representative "delayed" quench test TFC16 as the model input.

Fig. 4.17 shows the time evolution of the quench resistance computed with different amplitude values. The oscillation period has been fixed to 20 s. The modelling results with the amplitude from 0 mk (no oscillation) to 125 mK have been plotted in solid lines. The experimental quench resistance of DP6 in TFC16 has also been plotted in the same figure for comparisons (black dotted line). The time at $t = 0\,\text{s}$ always indicates the start of the FD.

We can see that from the no oscillation computation at $A = 0\,\text{mK}$ to the maximal amplitude one at $A = 125\,\text{mK}$, the beginning moment of the quench acceleration (or the resistance slope change moment) is more and more delayed. This is generally coherent with our assumption that a larger oscillation amplitude can trigger an earlier "premature" quench due to the sharp temperature peak. The earlier the quench initiates during the temperature-increasing phase, the longer the quench acceleration will be delayed due to a slow quench propagation under high temperature difference (ΔT) between T_{cs} and conductor temperature.

Fig. 4.17 shows three types of numerical quench dynamics. The first one actually corresponds to the most common phenomenon, an "early" quench acceleration near the start of the FD. It is produced when there is no temperature oscillations, or when the oscillation amplitude is not high enough,

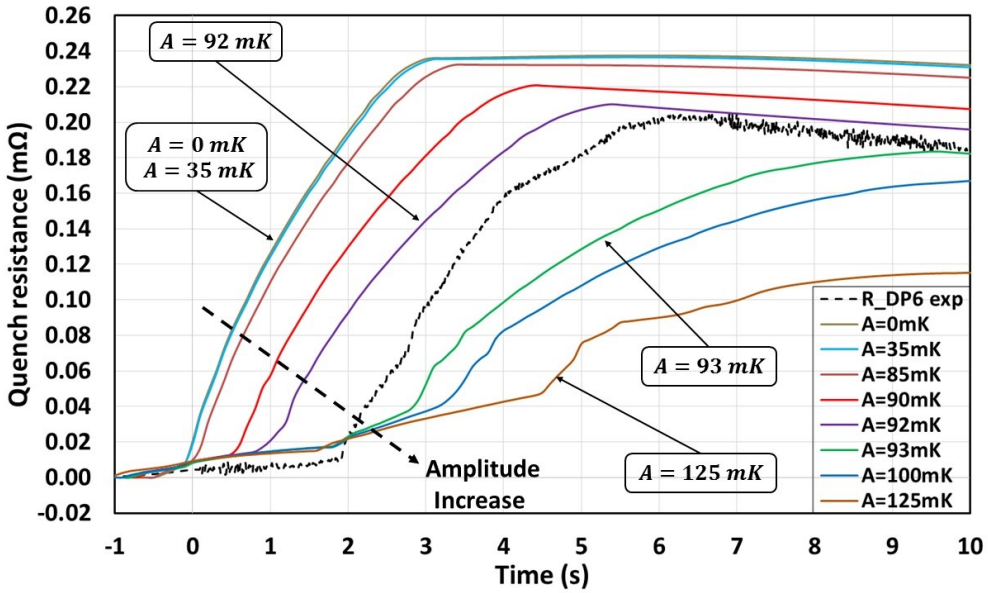

Figure 4.17 – Impact of the temperature oscillation amplitude on the quench acceleration beginning delay, with $T_{per} = 20\,\text{s}$ and $\varphi = 0\,\text{s}$

e.g. $A = 35\,\text{mK}$ or $A = 85\,\text{mK}$. The second type is the long delayed quench acceleration produced when the amplitude is large enough, e.g. $A = 93\,\text{mK}$, $A = 100\,\text{mK}$ or $A = 125\,\text{mK}$. In this case, the slow quench propagation has lasted for about 2 s followed by a series of resistance jumps which are very similar to the phenomenon observed in the TFC01. The testing temperature oscillations could then be an explanation for the very unique phenomenon of the resistance jumps in the DP5 of TFC01. Due to the time constraint, this phenomenon, however, will not be studied numerically in this document. The last type is the short delayed quench acceleration (between 0.5 s and 1 s delay) produced with the intermediate amplitude, e.g. $A = 90\,\text{mK}$ and $A = 92\,\text{mK}$. This type of numerical quench dynamics is the closest to the experimental one but always leaves a certain difference maybe due to the limit of our single pancake model that cannot take into account the adjacent pancakes effect.

In order to explain these different quench dynamics produced with the different amplitudes, the spacial temperature profiles at different moments are plotted for two extreme cases, $A = 35\,\text{mK}$ and $A = 125\,\text{mK}$. Fig. 4.18 shows that, with small oscillation amplitude ($A = 35\,\text{mK}$), the cable temperature firstly reaches T_{cs} near the peak field position around $x = 2.2\,\text{m}$ at $t = -5\,\text{s}$ (blue dashed line). This indicates that the current starts to pass through the resistive copper strands and to produce the Joule heat from this moment. According to these numerical computations, we can know that the normal zone has already a certain propagation before the current discharge at $t = 0\,\text{s}$ since the second peak field position (near $x = 9.5\,\text{m}$) is seen quenched at around $t = -0.2\,\text{s}$ that will produce an even higher Joule heat. This allows to explain the early quench acceleration appearing before the current discharge. Indeed, the small oscillation amplitude has been rapidly smoothed after 3 m owing to the inter-turn or inter-pancake heat exchange and cannot have much impact on the temperature profile so that the general ΔT keeps at a low level (e.g. $\Delta T < 70\,\text{mK}$ at $x = 9.5\,\text{m}$ at the quench initiation time) allowing to achieve an "early" quench acceleration.

When plotting the spacial temperature profiles for $A = 125\,\text{mK}$ (long delayed quench acceleration), one can find an evident difference in Fig. 4.19 that the cable temperature, this time, firstly reaches T_{cs} at the conductor inlet (which is not the peak field position) with an earlier moment around $t = -8\,\text{s}$ (red dashed line). In addition, the peak field position near $x = 3\,\text{m}$ has only been quenched after 7.7 s at $t = -0.3\,\text{s}$ (yellow dashed line). According to the numerical computations, such "slow" quench initiation mode has never triggered a quench at the second peak field position (around $x = 9.5\,\text{m}$) before the current discharge at $t = 0\,\text{s}$ (dark blue solid line). This is very probably due to the large average ΔT between T_{cs} and conductor temperature produced with the large helium

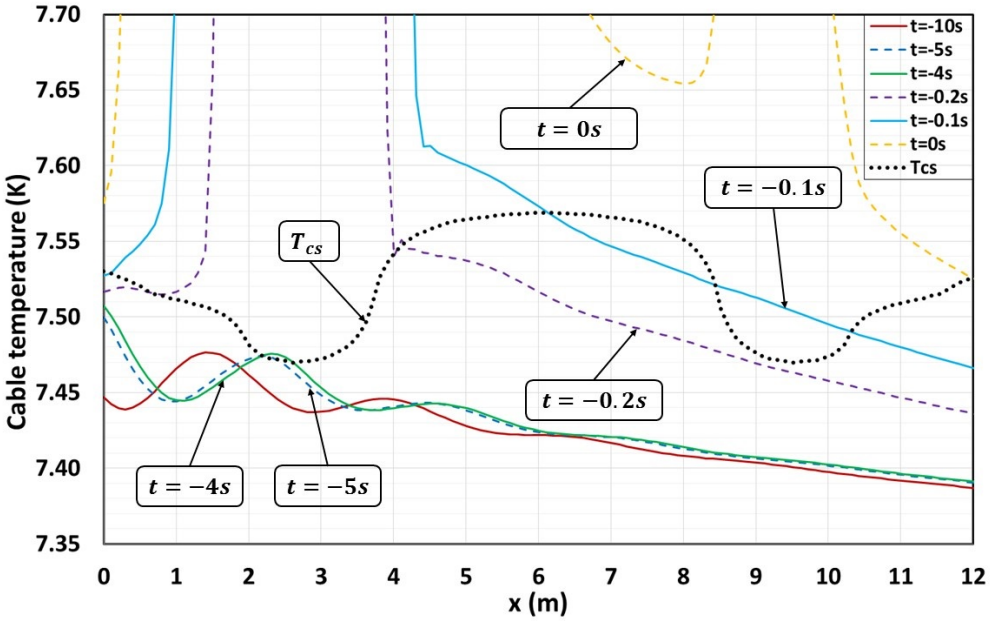

Figure 4.18 – Spacial temperature profiles for the early quench acceleration case ($A = 35$ mK, $T_{per} = 20$ s and $\varphi = 0$ s) compared with the nominal conditions T_{cs} at 25.7 kA

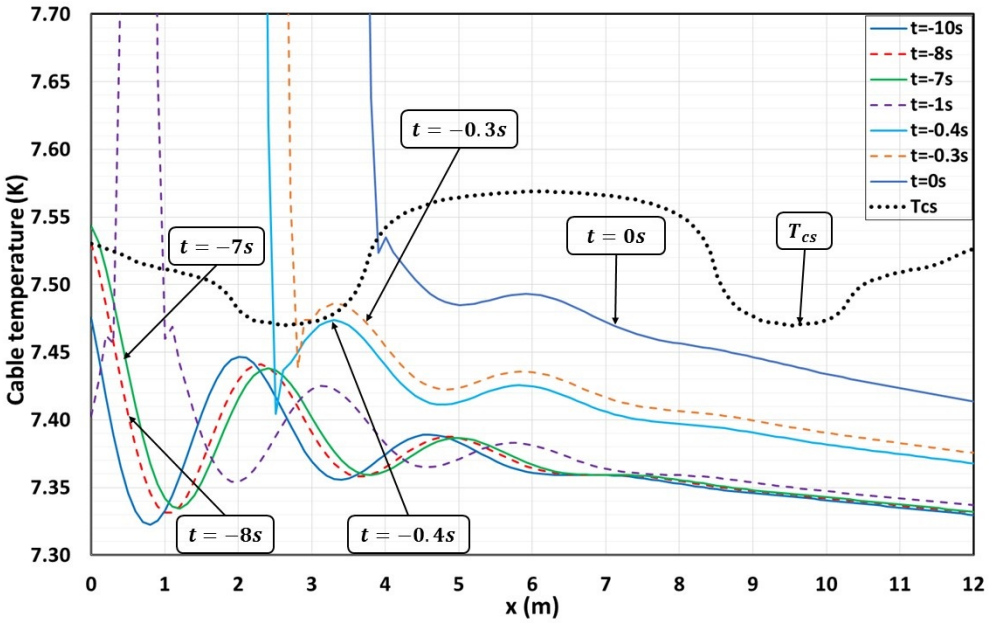

Figure 4.19 – Spacial temperature profiles for the delayed quench acceleration case ($A = 125$ mK, $T_{per} = 20$ s and $\varphi = 0$ s) compared with the nominal conditions T_{cs} at 25.7 kA

temperature oscillation amplitude. In particular, a $\Delta T > 100$ mK at $x = 9.5$ m can be observed at the transition moment of $t = -8$ s. This then allows to explain the long period of low quench propagation velocity since T_{cs} becomes even higher and the quench will be even more difficult to be reached after the current discharge.

A brief conclusion can be made here that, when a quench initiates near the peak field position, it will be easier for quench to accelerate since the normal zone can propagate along two directions and the temperature profile is also more uniform (due to a small oscillation amplitude in this case) leading to a lower ΔT between helium and conductor temperature. Thus an "early" quench acceleration can be achieved. Whereas the opposite case (large oscillation amplitude) will more probably delay the start of a quench acceleration due to the single direction propagation from the the coil inlet and

due to the higher ΔT leading to a lower normal zone propagation velocity thus a longer time to trigger the THQB effect.

One may also note that, in Fig. 4.17 the oscillation amplitude of $A = 92\,\text{mK}$ seems to be a special value that separates two kinds of numerical quench dynamics. Below or equal to this amplitude, the quench resistance evolution will have a short delay within 1 s before acceleration or even an "early" acceleration. Whereas 1 mK higher in the oscillation amplitude ($A = 93\,\text{mK}$) will completely change the quench dynamics to a TFC01-like acceleration. Such huge sensibility of oscillation amplitude then leads us to study the other possible impact on the quench dynamics: the oscillation phase shift φ. This is a parameter that can affect the quench initiation position at the temperature oscillation wave, as studied below.

Temperature oscillation phase shift

In order to study the oscillation phase shift effect on the quench dynamics, the following simulations will be carried out by varying φ from 0 to 2π. As the oscillation period is always fixed to 20 s, the corresponding phase shift values will then be from 0 s to 20 s. The special value of $A = 92\,\text{mK}$ will be precisely studied with our numerical model as well as the $A = 93\,\text{mK}$ amplitude case will be given some discussions.

Fig. 4.20 shows the time evolution of the quench resistances computed with the same amplitude $A = 92\,\text{mK}$ but with the different oscillation phase shifts plotted in solid lines. The DP6 experimental resistance evolution (black dotted line) is also plotted in the same figure for comparisons. The time at $t = 0\,\text{s}$ always indicates the start of the FD. One can see that, even with same oscillation period (20 s) and amplitude (92 mK), different phase shift can lead to completely different quench acceleration dynamics. For instance, $\varphi = 1\,\text{s}$ or 5 s gives a long delayed quench acceleration whereas $\varphi = 10\,\text{s}$ or 15 s leads to an early quench acceleration. The phase shift of $\varphi = 0\,\text{s}$ (dark blue dashed line) actually corresponds to the same curve of $A = 92\,\text{mK}$ in Fig. 4.17. This gives a first verification that different quench positions in the temperature oscillation wave will provoke different thermal effects on the quench acceleration itself.

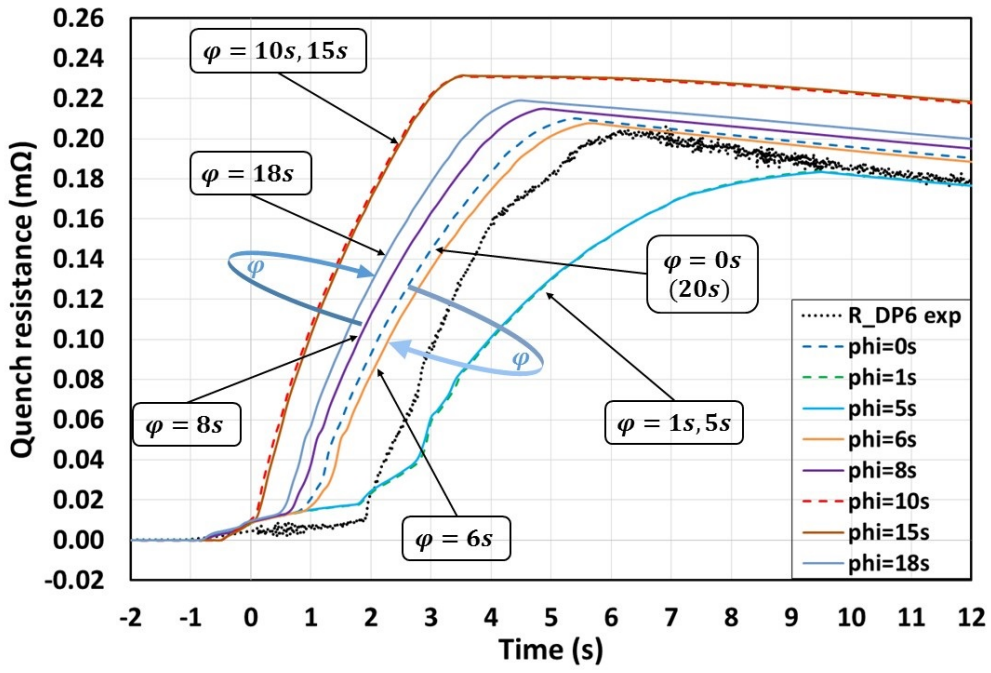

Figure 4.20 – Impact of the oscillation phase shift on the quench acceleration beginning delay, with $A = 92\,\text{mK}$, $T_{per} = 20\,\text{s}$ and $\varphi = 0\,\text{s} \backsim 20\,\text{s}$

According to Fig. 4.20, we can find that from $\varphi = 0\,\text{s}$ to $\varphi = 5\,\text{s}$, the phase shift has a higher

and higher "cooling" effect on the quench propagation probably due to the ΔT between T_{cs} and conductor temperature getting higher and higher, so that the quench acceleration is more and more delayed. After then, the phase shift effect starts to accelerate the quench propagation until $\varphi = 15\,\mathrm{s}$. Finally, the quench propagation is re-delayed between $\varphi = 15\,\mathrm{s}$ and $\varphi = 20\,\mathrm{s}$ ($\varphi = 0\,\mathrm{s}$) due to the periodical property of the oscillation wave. In order to verify the "cooling" effect assumption, the spacial temperature profiles are once again plotted for both the "delayed" case ($\varphi = 1\,\mathrm{s}$) and the "early" case ($\varphi = 10\,\mathrm{s}$).

Fig. 4.21 shows the spacial temperature profiles in the delayed quench acceleration. A phase shift of 1 s has made the quench initiation appear firstly at the conductor inlet around $t = -6\,\mathrm{s}$ (dark blue dashed line) and has made the first peak field position (near $x = 3\,\mathrm{m}$) only reach T_{cs} after about 5.5 s (violet solid line). Moreover, due to such "slow" quench initiation mode (at the inlet), the temperature at the second peak field position (near $x = 9.5\,\mathrm{m}$) is never reached to T_{cs} before the current discharge at $t = 0\,\mathrm{s}$ (dark blue solid line). This actually shows the impact of the phase shift that leads to an initial quench position relatively far away from the peak field and a local ΔT relatively high thus a "cooling" effect on the quench propagation. Therefore, a long delayed quench acceleration has been produced with this phase shift of $\varphi = 1\,\mathrm{s}$ even for an intermediate amplitude of $A = 92\,\mathrm{mK}$.

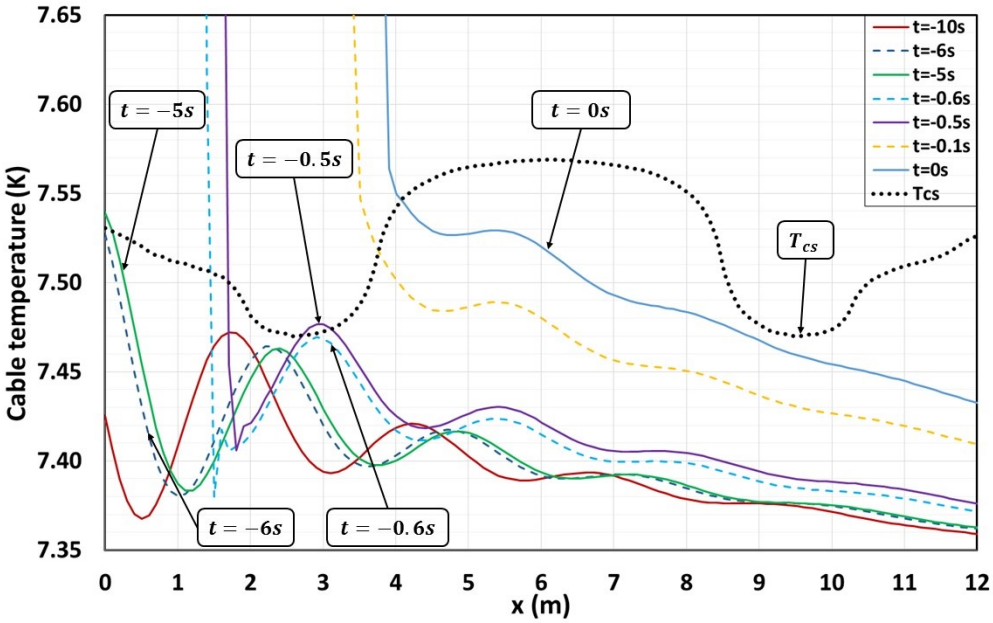

Figure 4.21 – Spacial temperature profiles for delayed quench acceleration at different moments compared with the nominal conditions T_{cs} at 25.7 kA, with $A = 92\,\mathrm{mK}$, $T_{per} = 20\,\mathrm{s}$ and $\varphi = 1\,\mathrm{s}$

When focusing on the spacial temperature profiles obtained with a phase shift of $\varphi = 10\,\mathrm{s}$, one can see in Fig. 4.22 that a first quench has been initiated this time near the peak field position at around $t = -5\,\mathrm{s}$ (dark green solid line). In this case, the conductor inlet is quenched about 2 s after. As a "fast" quench initiation mode (near the peak field) is triggered, the normal zone is able to propagate to the second peak field before the current discharge at $t = 0\,\mathrm{s}$ (light green solid line) and to produce even higher Joule heat to accelerate the normal zone propagation itself. Thereby, an "early" quench acceleration has been produced near the start of the FD.

Both of the above two cases are based on the same oscillation amplitude of $A = 92\,\mathrm{mK}$. The phase shift actually only changes the quench initiation position with respect to the peak field. When a quench is initiated near the peak field, the normal zone propagation will be reinforced and accelerated more easily than elsewhere since the local ΔT is lower near the peak field position. This is again in good agreement with our last conclusion that the small oscillation amplitude can lead to a lower average ΔT allowing to achieve an "early" quench acceleration.

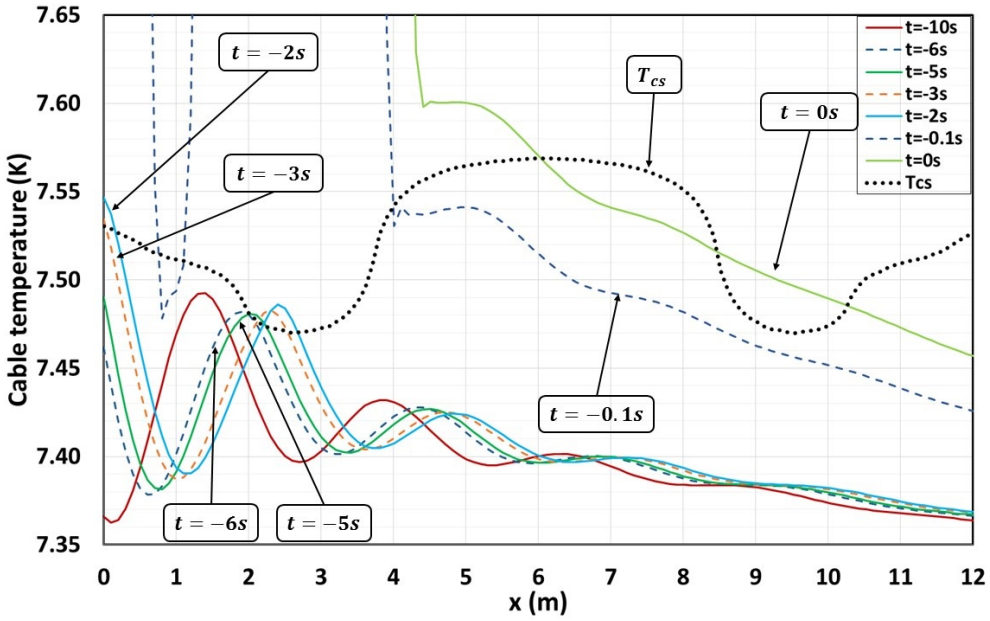

Figure 4.22 – Spacial temperature profiles for early quench acceleration at different moments compared with the nominal conditions T_{cs} at 25.7 kA, with $A = 92$ mK, $T_{per} = 20$ s and $\varphi = 10$ s

The second verification for the amplitude impact sensibility on quench acceleration dynamics can be carried out with the computations of $A = 93$ mK. We recall that 1 mK higher in the oscillation amplitude has completely changed the quench dynamics (see Fig. 4.17). This could not only be explained by the average ΔT produced with different oscillation amplitudes but also be related to the quench initiation position or the local ΔT due to the oscillation phase shift. Fig. 4.23 again confirms the predominant effect of the phase shift parameter. From $\varphi = 0$ s to $\varphi = 15$ s, the quench acceleration dynamics have totally changed, from a "long delayed" type (blue dashed line) to an "intermediate delayed" one (green solid line) as in the results of $A = 92$ mK and even to an "early" quench acceleration (red solid line). As already studied before, these different quench dynamics are always related to the quench initiation position and to the ΔT between T_{cs} and conductor temperature. This means that the special value of 92 mK is, to some extent, a random value determined with all the possible uncertainties of the oscillation including amplitude, phase shift and even period (fixed to 20 s in this study).

To conclude, we can say that, even if our single pancake model cannot give a quantitatively coherent result to the delayed quench acceleration, the effects of oscillation amplitude and phase shift have still been qualitatively verified. Both the oscillation amplitude and the phase shift can have a direct effect on the quench initiation position and on the ΔT between T_{cs} and conductor temperature. These will lead to the accelerating or decelerating effect on the quench propagation dynamics. A delayed quench acceleration like observed in the TFC16 must be due to all the studied effects resulting from the testing temperature oscillations. One also need to note that due to the time constraint, the DP5 resistance jumps phenomenon in the TFC01 has not been analyzed numerically. But the above discussions can more or less give a further study direction. A more global model coupling two or more pancakes will be necessary to carry out these studies.

d) Verification of the normal zone length evolution

When the quench arrived at the end of the acceleration phase, the normal zone length becomes an important parameter to be verified. Because this parameter allows to give a direct indication of the pancakes quench level, if it is a full quench or not, as already discussed Chapter 3. We will then compare the numerical results with the previous computations of the simplified physical model to carry out some analyses.

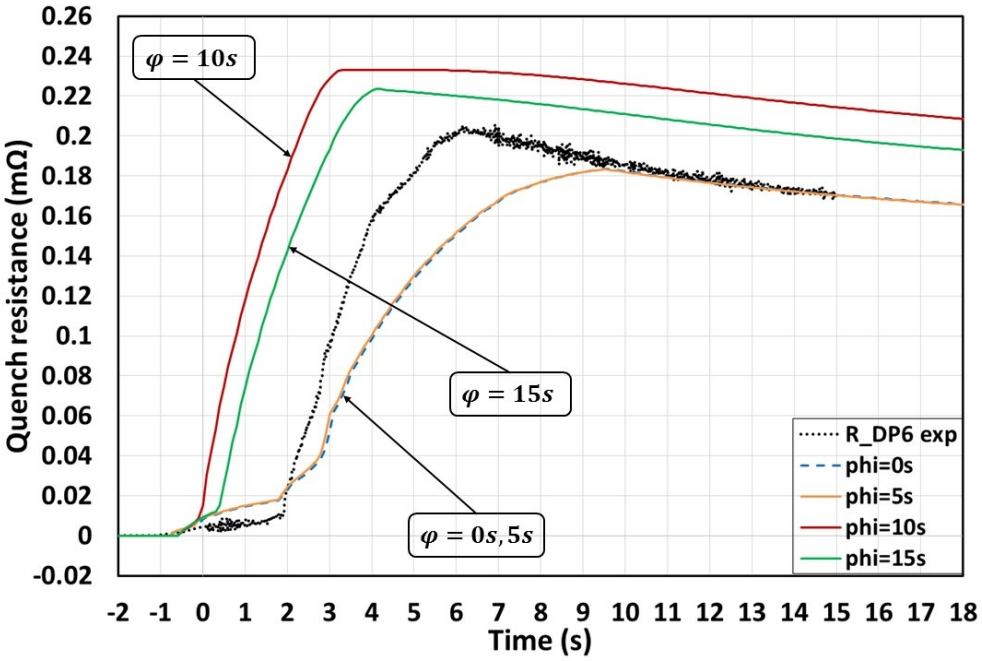

Figure 4.23 – Impact of the temperature oscillation phase on the quench acceleration beginning delay, with $A = 93\,\text{mK}$ and $T_{per} = 20\,\text{s}$

As usual, we take the first quenched pancake P2(DP1) of TFC12 as an example to present the results. Fig. 4.24 shows that the two curves computed with the simplified physical model (red line) and the numerical model (blue line). Generally, the two normal zone length evolutions are in good agreement during the quench acceleration phase lasting for the first 3.5 s. Thereby, a good agreement can be revealed in their curve slope. This allows to calculate the average quench propagation velocity to be around 35 m/s for numerical model and 37 m/s for physical model. When comparing to the experimental value of 36.5 m/s, both of them are having a good coherence within a certain acceptable discrepancy (4.1 % for numerical model and 1.4 % for physical model). In addition, we can see that, the maximal normal zone length has been computed to around 108 m with the simplified physical model, whereas a full quench state of 113.28 m has been achieved by the numerical model. The 4 % difference with respect to the full quench length can again confirm the accuracy of our simplified physical model. Regarding this slight difference, it could be due to the limit of our simplified physical model that only takes into account the longitudinal heat exchange in the pancake. Indeed, the inter-turn transversal heat exchange can have a cooling effect on the cable leading to a lower temperature level ($T_{max} = 37\,\text{K}$ in the numerical model), i.e. a lower copper electrical resistivity (ρ_{Cu}), thus a higher normal zone length, as observed in the numerical results.

Nevertheless, we can also find that during the entire quench propagation, from $t = -0.5\,\text{s}$ to $t = 3.5\,\text{s}$, the numerical normal zone length evolution is always slightly ahead of the one obtained with physical model. A maximal difference can be observed to around $\Delta t = 0.5\,\text{s}$. This could be explained by two facts. The first one is always the cooling effect from adjacent turns in the numerical model. So that a lower temperature (i.e. lower ρ_{Cu}) can allow to develop a longer normal zone length when reaching the same resistive voltage for quench detection ($V_{th} = 100\,\text{mV}$). For instance, at $t = -0.1\,\text{s}$ in Fig. 4.24, the numerical normal zone length is more than 10 m longer than the one obtained with physical model. The second reason could be due to the temperature oscillation effects causing a certain delay in the experimental quench acceleration dynamics (as studied in the last subsection). Indeed, the temperature oscillation has not been taken into account in the numerical model of TFC12 quench test since the TFC12 has been identified to have an "early" quench acceleration dynamics. Thus a slight delay of Δt can be observed between the numerical and physical model results.

To conclude, our inter-turn thermal coupling model has generally an acceptable accuracy on the

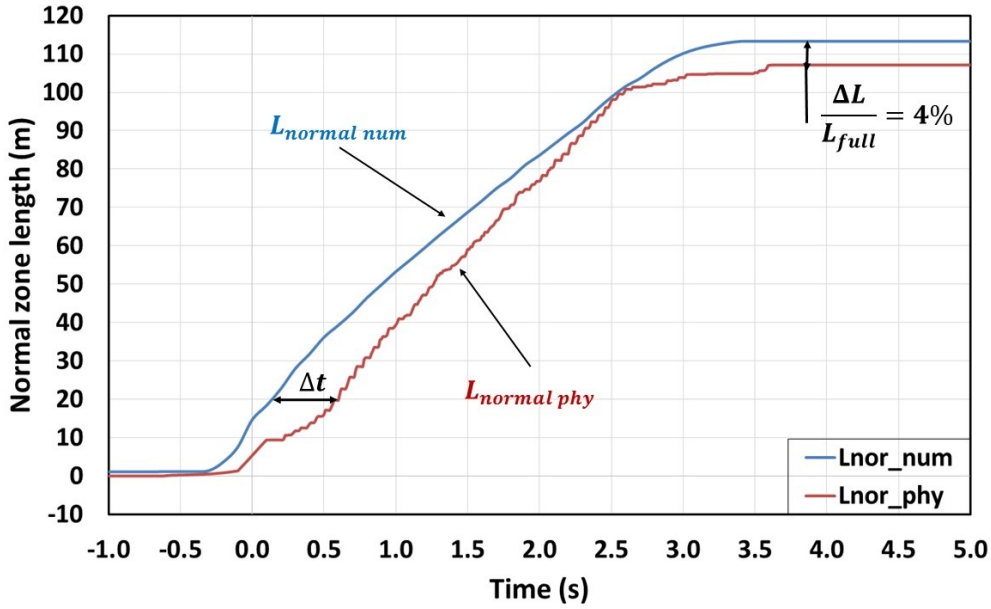

Figure 4.24 – Comparison between the analytical and the numerical results of the normal length evolution in the case of P2 in TFC12

computations of the quench propagation dynamics. In addition, the previously constructed physical model is also an efficient model to verify the normal zone length level as well as the the full quench phenomenon that we observed in the majority of the quench tests.

4.4.3 Helium reverse flow effect on the simultaneous quench phenomenon

We recall that in the above studies, the numerical computations predict no quench in the central pancakes DP3 while the experimental data shows a latter quench initiation at about $t = 1.2\,\mathrm{s}$, as presented in Fig. 4.25. This allows to tell that without the extra excitations like a warm helium flow injection, the latter quenched pancakes (including DP3) could not reach T_{cs} by themselves after an earlier current discharge in the coil. The simultaneous quench in these pancakes will then be even impossible to take place. These previous numerical computations can thus give a first verification of the helium reverse flow assumption identified during the experimental analysis (see Section 3.4.2). We recall this assumption that the helium in the first quenched DP1 is heated and expelled from the cable ends (especially from the inlet) and then will be re-injected into all the other pancakes including DP3 through the coil principal inlet making them quench simultaneously.

One has to know that a rapid temperature increase (up to about 30 K, see Table 3.6) has been measured at the principal inlet temperature sensor (TE2414) with a delay of 0.6 s after the simultaneous quench moment due to the 5 m distance away from the coil. This gives an indirect experimental observation of the helium reverse flow effect on the simultaneous quench phenomenon. In order to achieve a further verification of the helium reverse flow assumption, a parametric study will be carried out with our numerical model:

- applying the same external heat load for the central pancake P6 as in the "1.8 s delay" distribution, with $q_{lin} = 0.0503\,\mathrm{W/m}$
- fixing the same start time of the FD as in the computations of Fig. 4.25 which numerically predicts no quench in P6 (DP3)
- imposing a warm helium flow of 30 K in the P6 inlet boundary conditions
- varying the injection time of this warm helium flow from $t = 0\,\mathrm{s}$ to $t = 0.5\,\mathrm{s}$

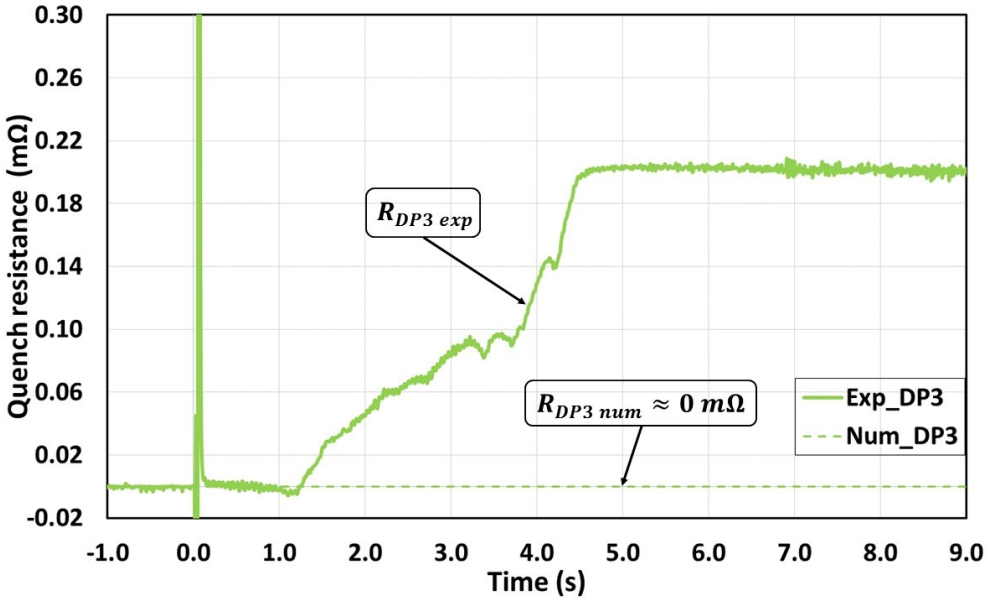

Figure 4.25 – Numerical and experimental evolution of the quench resistance in the central pancakes DP3

Fig. 4.26 shows that the more we increase the injection time of the warm helium flow at the P6 inlet (t_{in}), the longer the quench initiation phase will last for. Among the tested cases, the computation with an injection time of 0.28 s is in good agreement with the experimental curve until $t = 3.7$ s. This confirms the predominant effect of the warm helium reverse flow on the quench initiation in the central pancakes. This also indicates that the external heat load distribution previously determined to have a delay of 1.8 s has actually no effect on the quench initiation of the central pancake P6, since the delay is more likely driven by the helium reverse flow effect.

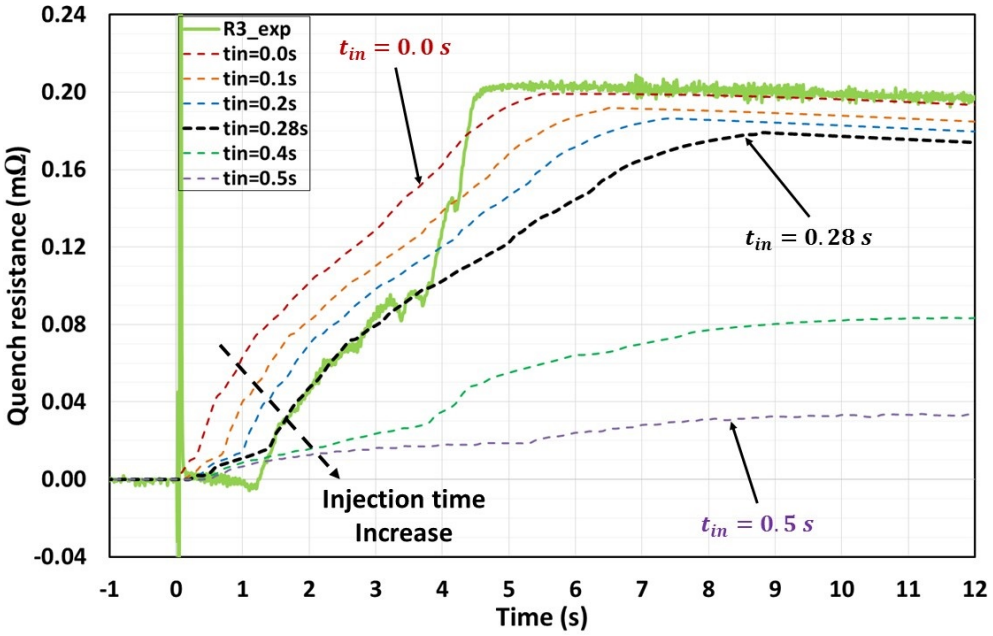

Figure 4.26 – Effect of the helium reverse flow on the simultaneous quench phenomena, with warm helium injection time ranging from $t = 0$ s to $t = 0.5$ s

One may note that before $t = 1.2$ s, a slight difference appears between the experimental quench resistance (green solid line) and the numerical result at $t_{in} = 0.28$ s (black dashed line). The latter one shows that the central pancake DP3 has already quenched at $t = 0.5$ s followed by a quench

initiation phase lasting for about 0.7 s then accelerated. Nevertheless, this initial quench resistance evolution has not been revealed in the experimental curve due to the underestimation of the pick-up coil method. Such comparison allows to indicate the error of the pick-up coil method as well as the real state of the pancakes (low level of normal zone length) before the resistance slope change at $t = 1.2\,\text{s}$. Moreover, this seems to be incoherent with our previous study with the physical model that a "real" quench initiation time should have arrived at the resistance slope change moment at $t = 1.2\,\text{s}$. Indeed, this "choice" has only been applied for estimating an appropriate Joule effect energy in order to obtain a reasonable hot spot temperature and normal zone length computation for the physical model. Therefore, the numerical results indicating an already quenched state before this slope change (at around $t = 0.5\,\text{s}$) should be taken as the "real" quench initiation dynamics in the latter quenched pancakes.

After $t = 1.2\,\text{s}$, the good coherence between the experimental and numerical results has lasted to $t = 3.7\,\text{s}$. This also allows to explain the DP3 quench deceleration phenomenon after the simultaneous quench. We recall that the assumption of the deceleration in DP3 has been explained in Section 3.4.2. It is due to the lower field region in DP3 ("V-shaped" field map) having higher T_{cs} thus higher temperature difference between T_{cs} and conductor that makes the quench propagate at a lower velocity and obviously a lower Joule heat leading to an even further "cooling" effect. Therefore, the good agreement between experimental and numerical results until $t = 3.7\,\text{s}$ allows to verify the assumption of the magnetic field map effect. Indeed, the central pancake field map has been correctly imposed at the boundary conditions in THEA.

Fig. 4.26 also shows that the actual model cannot reproduce the quench re-acceleration phenomenon from $t = 3.7\,\text{s}$ up to reach the maximal resistance plateau at around $t = 4.5\,\text{s}$. Indeed, the quench re-acceleration phenomenon has been explained with the assumption that a secondary quench is initiated at the outlet of DP3 due to the full quench propagation from the first quenched pancakes DP1 (see Section 3.4.2). These numerical computations are then, to some extent, coherent with the fact that the secondary quench phenomenon has not been integrated to our numerical model. A future work could be attempted to integrate this assumption to the actual model.

To conclude, the helium reverse flow effect has been proven to play a major role in the simultaneous quench of the central and inner pancakes. The "V-shaped" field map has also been revealed to have a predominant impact on the quench propagation dynamics (deceleration) of the central and inner pancakes. The final re-acceleration phenomenon remains to be verified with a more global model taking into account the adjacent pancakes quench propagation and the joint connection.

Conclusions

In this chapter, we have firstly developed an inter-turn thermal coupling model that allows to improve the computation accuracy of the original 1D quench model in THEA. The key parameter that has been added to this new model is, as said by the name, the traversal heat flux between the turns. This new model accuracy has been verified with a pure thermohydraulic case with no quench, i.e. the temperature-increasing phase before quench. Despite of its partial validity only for this quasi-steady state, we still consider that this new model can be applied for the whole quench test covering both the temperature-increasing phase and the fast transient quench phase. Indeed, the objective of the inter-turn thermal coupling model is to improve the temperature boundary conditions just at the quench initiation without inducing high limitations on the predominant phenomenon that drives the "further" quench propagation. Regarding the predominant phenomenon of the quench longitudinal propagation, it is modelled in a fully transient way with THEA. Therefore, such improved model can allow us to make a further study of the physical phenomena identified during the quench experimental analysis.

During the quench initiation phase, the experimental analysis has identified for the statistic

phenomenon of the initial quench location a predominant factor to be verified numerically, the external heat load. An analytical estimation has been realized to give the order of the external heat load deposited on the pancakes ($0.05\,\mathrm{W/m} \backsim 0.08\,\mathrm{W/m}$). The uncertainties and hypotheses applied in the analytical computations lead to a parametric study of the external heat load impact on the initial quench location. We have obtained that 7 % of the external heat load variation is enough to obtain a completely different consequence in the quench location, from side pancake to central one. This verifies the predominant effect of the external heat load during the initial quench dynamics. Moreover, the 7 % difference is also in a reasonable margin when considering the different Joule heat from the joints, the different thermal contact due to the insulation manufacturing process or due to the mechanical deformation by Lorentz forces.

Concerning the study of the quench acceleration dynamics, we have firstly verified that the two single pancakes in a same DP can have different quench initiation time (less than 1 s difference). In addition, the number of quenched pancakes in a DP are proven to have a certain accelerating effect on the quench resistance evolutions, especially during the beginning of the quench acceleration phase. Further work needs to be continued to verify more precisely the phenomenon of having consecutive quench propagations in the two adjacent pancakes of a double-pancake. Secondly, the quench acceleration mechanism has been identified to be related to the thermohydraulic quench-back (THQB) effect. The observation of a slight helium temperature increase ahead of the quench front allowed to verify this phenomenon as well as the maximal helium expulsion velocity computed to around half of the experimentally estimated quench propagation velocity. This THQB effect must be related to our quench test mode leading to a generally low temperature difference between T_{cs} and conductor in the entire pancake ($\Delta T_{max} = 0.3\,\mathrm{K}$) and thus a quench propagation faster than the helium expulsion. Finally, the delayed quench acceleration phenomenon has been explained with the testing temperature oscillations. Both the oscillation amplitude and the phase shift are verified to have a predominant effect on the quench acceleration dynamics. Finally, the normal zone length evolution has been compared between numerical and physical models which allows to verify the results accuracy of the physical model built in Section 3.5.2.

During the latter quench phase, the most common phenomenon, the simultaneous quench in the inner or central pancakes, has been principally analyzed with a numerical approach. A parametric study has been carried out to show the impact of the inlet helium injection time on the central pancakes quench dynamics. A delay of 0.28 s has proved to be the most coherent moment for obtaining the experimental quench dynamics. This has, to some extent, verified our assumption of the helium reverse flow (from the first quenched pancakes) triggering the simultaneous quench phenomenon (in the latter quenched pancakes). In addition, the quench deceleration dynamics up to a resistance plateau has also been reproduced with the numerical simulations. This allows to verify our assumption of the magnetic field map impact on the quench deceleration phenomenon. Nevertheless, there always remains the last but not the least phenomenon to be studied, the quench re-acceleration phenomenon. As our model is limited to a single pancake configuration, a further multi-pancakes model (coupled with FLOWER[113] or Cast3M[114]) or a more complex 3D model could give a more accurate study on the quench re-acceleration phenomenon.

[113] L. Bottura and C. Rosso. *Cyogenics* **43**. 215–223. 2003.
[114] Cea team. *Site de Cast3M.*. 2018.

General conclusions and perspectives

This PhD report has focused on the thermohydraulic phenomena taking place during the quench of a superconducting magnet cooled with supercritical helium. The entire study has been based on the driving physical phenomena identified during four principal quench dynamic phases of the JT-60SA TF coils, including quench initiation phase, quench acceleration phase, latter quench phase and quench saturation phase. This last chapter presents first a short review of the magnet safety issues in case of quench then highlights the main achievements of this PhD study based on the above quench dynamic phases. To finish, some eventual directions to be investigated will be proposed for the continuation of the present work.

The quench transition of a CICC-based magnet from its superconducting state to its normal state induces a large deposition of the Joule effect energy leading to an abrupt temperature increase in the conductor as well as a large pressure rise in the helium. Any excess of these two parameters can cause an irreversible damage either to the magnet or to the cryogenic system. A good understanding of the magnet performance in case of quench (as well as a verification of the fabrication risks) is then necessary for ensuring the operations of a superconducting Tokamak. As a result, the JT-60SA TF coils have been cold tested to the full operating conditions (5 K and 25.7 kA) before integrating in the Tokamak machine. A progressive temperature increase has been applied to the helium inlet up to the quench temperature, followed by a current fast discharge as soon as the quench is detected to protect the coil. Such quench experiments have been performed on all the 18 superconducting TF coils and their experimental data have also been acquired for the following quench study.

The first work during this PhD study has been to determine an appropriate data processing method, called the pick-up coil method, allowing to deduce the experimental quench resistance evolutions thanks to the pick-up coil inductive voltage measurements. Based on these quench resistance evolutions, four different quench dynamic phases have been identified in the 6 DPs during each quench test, from the first phase of quench initiation to the last one at quench saturation. The driving physical phenomena have been highlighted and analyzed in both experimental and numerical approaches within the four quench dynamic phases.

During the ***quench initiation phase***, a statistic phenomenon has been observed with 53 % of the quench tests initiated in the side DPs and the rest in the inner or central DPs. These different quench locations have been explained with the combined effects of strands magnetic performance (related to field map and T_{cs}), external heat load (from casing or resistive joints) and CICC friction factor (related to cooling efficiency). Among them, the external heat load effect on the initial quench location was proven to be as predominant as the strands magnetic performance, whereas the friction factor effect is almost negligible. It is to note that the casing temperature in the CTF conditions is much higher than the one in the Tokamak conditions due to the thermal shield radiation (liquid nitrogen) of the CTF cryostat and due to the limited capacity of the helium cooling channels on the casing. Thereby, the external heat load effect will be much reduced during the Tokamak operations leading to the possible quench location mainly linked to the strands magnetic performance. This means that it will be more likely to initiate a quench in the central DPs of the Tokamak TF system. Nevertheless, two major differences should also be noted here. The first one is that the TF coils have been tested horizontally in the CTF whereas in the Tokamak, they are installed vertically with a height of around 7.5 m. The gravitational effect then plays an important role in the helium

pressure thus in the helium flow velocity when considering the same mass flow rate. So that, the top position of the vertical coil should be more easily quenched due to the lower cooling effect of the helium (due to a smaller flow velocity). This assumption has been more or less verified by the CTF quench experiments where 80 % of the side DPs quench has been observed in DP6 (20 % in DP1), i.e. in the upper side DP. Concerning the second difference, we remind that the statistic phenomenon of quench location is observed in the case of CTF temperature-increasing protocol for initiating a quench at the coils inlet. The local quench initiation in the middle of the pancakes (e.g. due to the dysfunctions in the Tokamak) can then not be predicted or well detected according to this statistic phenomenon. Technically, a more detailed protection system will be needed to detect the unexpected local quench in the Tokamak.

Concerning the external heat load effect, 7 % of variation was proven, by our inter-turn thermal coupling model, to have a sufficient effect to change the initial quench location, from the side pancake to the central one. Such 7 % difference is also reasonable when considering the different Joule heat from the joints and the different thermal contact due to the insulation manufacturing process or due to the mechanical deformation by Lorentz forces. The inter-turn thermal coupling model is actually a single pancake numerical model developed in THEA code. It takes into account both longitudinal and transversal heat transfers in a pancake and allows to model the quench state in a fully transient way. It has been validated on the quench experiments data and has been successfully applied to study the driving physical phenomena identified during the different quench dynamic phases.

During the ***quench acceleration phase***, the quench propagation velocity varied from about 3 m/s to about 30 m/s. Approximately a factor 10 has been seen between the quench initiation and acceleration velocities. This also verifies the acceptance of the two phases classification made in the study. There are in general three types of quench dynamics highlighted during the acceleration phase.

The first one is the most common phenomenon called "early" quench acceleration (68 %). This type is characterized with a continuous quench resistance slope change near the start of the FD. Two driving phenomena have been identified, the effect of the number of quenched pancakes in the same DP on the quench resistance slope change as well as the quench acceleration mechanism by thermohydraulic quench-back (THQB) effect. Both of them have been verified with the inter-turn thermal coupling model. The THQB effect identified here must be related to the TF coils quench experimental protocol leading to a generally low temperature difference between T_{cs} and conductor in the entire pancake ($\Delta T_{max} \approx 0.3\,\mathrm{K}$).

The second type of quench acceleration dynamics is a "delayed" one (26 %). It has been characterized with a discontinuous quench resistance slope change taking place with a certain delay (0.5 s $\backsim$ 2 s) after the start of the FD. This phenomenon has been explained with the experimental temperature oscillations that can provoke a "premature" quench initiation thus lead to a long delay before accelerating. The principal oscillation parameters (period, amplitude and phase shift) have been verified numerically to have a predominant effect on the beginning delay of the quench acceleration dynamics. It is to note that the temperature oscillations can never be completely avoided due to the hydraulic controlling system, no matter in which test facility, CTF in Saclay or JT-60SA in Naka. This part of analysis could then be useful for understanding the potential quench behaviour during the future Tokamak operations.

When talking about the last type of quench acceleration dynamics, only TFC01 has been observed to have undergone a series of local resistance jumps without any evident quench acceleration. This phenomenon has been explained with the transversal quench propagation through the 6 turns within the same pancake and also with the local THQB preheat effect. However, this phenomenon has not yet been integrated in this numerical model due to the time constraint.

During the ***latter quench phase***, two driving physical phenomena have been studied. The first one is the simultaneous quench phenomenon that always took place in the latter quenched pancakes (usually the inner and central pancakes). The experimental analyses allow to give the most likely

explanation: the helium reverse flow repulsed from the first quenched pancakes have re-entered into the other pancakes via the principal helium piping making them quench in a simultaneous way. In order to make a further verification, a parametric study has been carried out in the numerical model by varying the injection time of the warm helium flow at the inlet of the central pancakes. A delay of 0.28 s has been proved to be the most coherent condition for reproducing the experimental evolution. This then, to some extent, verified the assumption of the simultaneous quench phenomenon induced by the helium reverse flow effect.

The second major phenomenon of the latter quench phase is the quench sub-phases dynamics. Indeed, after the simultaneous quench initiation, the resistance evolutions are having a deceleration to a resistance plateau followed by a re-acceleration up to the maximum. Such a chain phenomenon has been firstly explained with the fact that the lower field region in the middle of the pancakes makes the conductor more difficult to be quenched due to a higher T_{cs}. A lower Joule heat will then decelerate the quench propagation. Regarding the quench re-acceleration phenomenon, it is very likely due to a secondary quench initiation at the pancakes outlet since the outlet inter-pancake joints have been observed to quench at the re-acceleration moment. With the numerical model, the quench deceleration dynamics up to a resistance plateau has been reproduced with the above condition of 0.28 s delay. As the magnetic field map has been precisely imposed at the boundary conditions, the impact of the low field region can then be considered as predominant in the quench deceleration phenomenon. Due to the time constraint, the quench re-acceleration phenomenon has not yet been integrated in this numerical model.

Anyway, the coils structure involving inter-pancake joints and common helium piping will not be modified when assembling in the Tokamak. This makes the analysis of the latter quench phase still available when the similar physics, such as simultaneous quench or re-acceleration dynamics, takes place during the quench of the Tokamak operations.

During the last ***quench saturation phase***, the global decrease phenomenon of the saturation resistance plateau has been explained with the competing effect between thermo-resistance increase (temperature rise) and the magneto-resistance decrease (current discharge). Moreover, two important parameters are also discussed to indicate the coils "quench level", including the Joule effect energy and the normal zone length. Concerning the Joule effect energy, a maximal difference up to a factor 4 has been acquired among the 19 quench tests. This is mainly linked to the different quench dynamics identified before. The more the quench acceleration is delayed and the more the quench re-acceleration has been reduced among the pancakes, the lower the Joule effect energy will be obtained. In addition, the slight difference of the simultaneous quench moment among the different quench tests can also have a relatively important impact on the Joule effect energy level. Concerning the normal zone length, a simplified physical model has been built by taking the experimental quench resistance as model input. The results of this model has also been verified with the numerical computations of the normal zone length. Both of them allow to give a further verification of the coils "quench level" (if it is a full quench state or a partial one). This part of analyses have also been combined to the final categorisation of the whole quench tests.

To finish, we are going to give some eventual directions on which a continuation of this PhD work can be focused. As we have already studied for the quench acceleration phase, the number of quenched pancakes in the same DP can have a certain effect on the quench resistance slope change. Nevertheless, a more global numerical model coupling two pancakes will be more accurate to verify the combined quench phenomena taking place in the two adjacent pancakes of the same DP. Regarding the unique phenomenon observed in the TFC01, the similar consecutive resistance jumps have actually also been revealed when modelling the temperature oscillation effects on the delayed quench acceleration. This could give a study direction of focusing on the experimental temperature conditions of TFC01. Nevertheless, due to the quantitatively incoherent results obtained during the delayed quench acceleration study, a more global model coupling two or more pancakes may be a good departure point to carry out a more accurate study of the consecutive resistance jumps phenomenon in the TFC01. Finally, when studying the quench re-acceleration phenomenon (latter

quench phase), we have only proposed an assumption of a secondary quench launched at the pancakes outlet relying on a quench observation on the outlet inter-pancake joint. Indeed, this secondary quench could be either triggered by the helium reverse flow from the outlet piping or by the thermal diffusion through the inter-pancake joint itself. Nevertheless, these physical phenomena can only be integrated in a numerical model where the 12 pancakes (or 6 pancakes by coil symmetry property) are coupled both thermally and hydraulically. For instance, a global 3D model could be built coupling the actual single pancake model in THEA code and the codes FLOWER and Cast3M for realizing the thermohydraulic coupling in the entire TF coil. In addition to these quench propagation phenomena, the helium pressure rise detected in the TF coils quench tests could also be an interesting direction of future work. Indeed, the helium pressure measurements have only been used directly as boundary conditions when carrying out the quench computations. The physical phenomena related to pressure rise have never been successfully reproduced or well analyzed. In order to carry out this study, one can take the simplified physical model (constructed in this PhD report) as a first step to determine the normal zone length evolution. Then, a pressure rise model could be completed relying on the warm and cold volumes of helium (determined with the normal zone evolution) as well as the related computations of mass density and enthalpy (as model inputs).

APPENDIX A

Résumé en Français: Étude et modélisation des phénomènes thermohydrauliques résultant du quench d'un aimant supraconducteur refroidi en hélium supercritique

A.1 Introduction

Inspiré par le processus de fusion naturelle du Soleil, un travail considérable a été réalisé pour tenter d'utiliser l'énergie de fusion contrôlée pour produire de l'électricité sur Terre. Les principaux avantages[1] de l'énergie de fusion ont été identifiés comme sûr (combustibles de fusion non radioactifs), respectueux de l'environnement (substance inerte hélium comme produit de fusion) et, dans une certaine mesure, source d'énergie illimitée (production de combustible à base de lithium et d'eau). Depuis le milieu du siècle dernier, plusieurs tentatives de fusion artificielle ont été tentées, par exemple, la fusion muonique[2], la fusion par confinement inertiel[3] et la fusion par confinement magnétique[1]. Parmi eux, la dernière a été démontrée comme étant le moyen le plus faisable de réaliser une centrale électrique de fusion. Deux machines à confinements toroïdaux ont ainsi été inventées, Stellarator[3] et Tokamak[4]. L'idée est d'appliquer des forts champs magnétiques sur les particules chargées à haute température, appellées plasmas (environ $1,5 \times 10^8$ °C), afin de les maintenir suffisamment loin de la paroi du récipient de sorte que la surface de la paroi ne fondra pas ou ne s'évaporera pas pour refroidir le matériau de fusion. Enfin, la configuration Tokamak a été choisie comme le processus essentiel de réalisation d'une centrale de fusion grâce à sa stabilité optimisée du confinement de plasma chaud et aussi en raison de la complexité de la construction pendant les premières réalisations de Stellarator[1].

Afin de vérifier la faisabilité scientifique d'un Tokamak et de résoudre les problèmes potentiels liés aux techniques de fabrication, plusieurs machines Tokamak ont été construites au cours des dernières décennies. De la première machine de petite taille T-3[4] aux grands Tokamaks, Joint European Torus (JET)[5] à Culham (Royaume-Uni), Tokamak Fusion Test Reactor (TFTR)[6] à Princeton (États-Unis) et JT-60U Tokamak[7] à Naka (Japon), les scientifiques de la fusion ont réussi à atteindre la puissance de fusion à grande échelle de 2 MW à 16 MW, avec l'amplification de puissance la plus élevée jusqu'à $Q = 0,65$ (=puissance de fusion produite/puissance totale d'entrée)

[1] J. Ongena et al. *Nature Physics* **12**. 398–410. 2016.
[2] L. W. Alvarez et al. *Physical Review* **105**. 1127–1128. 1957.
[3] G. McCracken and P. Stott. *Academic Press*. 2012.
[4] L. A. Artsimovich. *Nuclear Fusion* **12**. 215–252. 1972.
[5] P. H. Rebut. *Plasma Physics and Controlled Fusion* **34**. 1749–1758. 1992.
[6] K. M. McGuire et al. *Physics of Plasmas* **2**. 2176–2188. 1995.
[7] T. Fujita et al. *Nuclear Fusion* **39**. 1627–1636. 1999.

dans JET[8]. Toutes ces expériences de Tokamak démontrent ensemble la faisabilité scientifique de la fusion par confinement magnétique. Néanmoins, ces Tokamaks sont tous fabriqués avec des aimants en cuivre résistifs refroidis par de l'eau. Les grandes quantités d'énergie électrique consommées par ces aimants en cuivre sont en fait la plus grande limite pour atteindre une puissance de sortie nette du Tokamak ($Q > 1$). Donc, la meilleure solution est d'utiliser des aimants supraconducteurs. Ils sont fabriqués avec des matériaux supraconducteurs qui, lorsque la température diminue à une valeur critique (T_c), n'auront aucune résistance contre un courant électrique, tels que NbTi et Nb_3Sn. De plus, ces aimants supraconducteurs sont basés sur une configuration de conducteur à haute efficacité de refroidissement, appelée conducteur par câble en conduit (CICC)[9], dans laquelle l'hélium supercritique circule par écoulement forcé. La propriété supraconductrice et l'efficacité de refroidissement du CICC ont permis aux aimants de fusion d'obtenir des énergies magnétiques plus puissante et des conditions cryogéniques plus stables. Cependant, la complexité de tels aimants supraconducteurs amène également une multitude de problèmes de conception qui doivent être résolus pendant tout le programme de R&D. L'un de ces problèmes s'appelle ***quench***. En effet, le mot "quench" est pour décrire une transition rapide de l'aimant de son état supraconducteur à son état résistif normal. Quand un quench a lieu dans un aimant supraconducteur, de grandes quantités d'énergie par effet Joule seront produites dans la *zone normale* des conducteurs et augmenteront rapidement la température des conducteurs. Si cette température atteint une valeur suffisamment élevée, une détérioration irréversible sera alors apportée à l'aimant supraconducteur due à la dilatation thermique excessive dans les matériaux. De plus, la grande chaleur par effet Joule devra être également transférée par convection forcée au réfrigérant à l'hélium supercritique. L'hélium est alors rapidement chauffé et pressurisé jusqu'à atteindre un seuil au-dessus duquel l'ensemble du système cryogénique sera endommagé. Du point de vue de la sécurité de l'aimant, tels phénomènes thermohydrauliques résultant du quench ont ainsi attiré beaucoup d'attention dans le domaine de recherche sur les Tokamaks.

Afin de résoudre les problèmes physiques ci-dessus ainsi que les caractéristiques techniques potentielles nécessaires pour réaliser une centrale électrique de fusion en supraconducteur, le plus grand projet de fusion au monde, International Thermonuclear Experimental Reactor (ITER) a ainsi été lancé en 2006 à côté du CEA Cadarache en France. L'objectif principal de l'ITER est d'atteindre une puissance de fusion de 500 MW qui correspond à une amplification de puissance de $Q = 10$[11]. En parallèle, certains Tokamaks supraconducteurs de plus petite taille ont également été construits et exploités pour fournir des expériences directes à l'ITER, telles que l'EAST en Chine[12], le KSTAR en Corée[13], le SST-1 en Inde[14], le WEST (mis à niveau de Tore Supra) en France[15,16] et la JT-60SA (mise à niveau de JT-60U) au Japon[17]. Ces Tokamaks supraconducteurs sont des équipements récents et sont toujours très difficiles à fabriquer des points de vue économique et technique, donc sont rares à trouver dans le monde. Comme le plus grand Tokamak supraconducteur devant être construit avant ITER, JT-60SA est entièrement fabriqué avec des aimants supraconducteurs. En particulier, son système de champ toroïdal (TF) composé de 18 aimants supraconducteurs permet de fournir un fort champ toroïdal pour stabiliser le plasma. Par conséquent, le Tokamak JT-60SA aura l'énergie de plasma la plus élevée (courant de plasma autour de 5.5 MA) ainsi que la plus haute énergie magnétique stockée (champ de crête dans le TF système autour de 5.65 T) jamais obtenue auparavant. Une multitude de nouveautés concernant à la fois les recherches scientifiques et les caractéristiques techniques seront certainement fournis par ce projet à la communauté internationale de fusion. Leur problème de sécurité des TF bobines (aimants) en cas de quench sera également nécessaire à étudier pour une meilleure exécution des opérations Tokamak dans l'avenir.

[8] M. Keilhacker et al. *Nuclear Fusion* **39**. 209–234. 1999.
[9] M. O. Hoenig and D. B. Montgomery. *IEEE Transactions on Magnetics* **11**. 569–572. 1975.
[11] IAEA Vienna. *ITER Engineering Design Activities Documentation*. 2001.
[12] B. Wan. *Nuclear Fusion* **49**. 2009.
[13] G. S. Lee et al. *Nuclear Fusion* **40**. 575–582. 2000.
[14] S. Pradhan et al. *Nuclear Fusion* **55**. 2015.
[15] C. Bourdelle et al. *Nuclear Fusion* **55**. 2015.
[16] Editor. *World nuclear news*. 2016.
[17] K. Yoshida et al. *The Journal of Japan Society of Plasma Science and Nuclear Fusion Research* **9**. 214–219. 2010.

Le phénomène de quench dans un CICC a été largement étudié avec la réalisation du test de quench classique dans un CICC de petite taille[18–20] jusqu'à une échelle d'aimant[21] en imposant une puissance de chauffage locale ou un courant critique pour quencher les supraconducteurs. Plusieurs modèles analytiques[22–24] ont été précisément proposées pour analyser les phénomènes thermohydrauliques résultant du quench dans un CICC, combinant la propagation du quench, l'augmentation de la pression d'hélium et l'expulsion de l'écoulement d'hélium. Néanmoins, très peu d'études ont été menées avec précision pour analyser les expériences de quench dans un aimant réel du Tokamak. Le Tore Supra, avec la configuration similaire à JT-60SA, a en fait subi plusieurs expériences de quench sur deux des 18 TF bobines supraconductrices ainsi que quelques analyses sur les phénomènes de quench[10]. Cependant, les TF bobines de Tore Supra sont refroidies dans un bain d'hélium superfluide à 1.8 K, ce qui est différent des TF bobines de JT-60SA refroidies avec un écoulement forcé de l'hélium supercritique dans le CICC. De plus, le protocole expérimental de quench provoqué dans les TF bobines de JT-60SA sont également différentes des expériences classiques de quench sur un CICC. En effet, ces bobines supraconductrices ont été testées en augmentant la température globale de l'hélium avec une injection de l'écoulement chaud à l'entrée pour déclencher un quench. Ceci a pour but d'éviter toute modification de la disposition à l'intérieur de la bobine. En conséquence, une étude précise des expériences de quench réalisées sur l'ensemble des 18 TF bobines supraconductrices comme dans le JT-60SA n'a presque jamais été faite auparavant.

Afin d'obtenir une meilleure compréhension des phénomènes thermohydrauliques résultant du quench d'un aimant supraconducteur fabriqué en CICC, plusieurs codes numériques ont également été développé au cours des dernières décennies, à partir du code au niveau de conducteur, comme Gandalf[27], Mithrandir[28] ou THEA[29], au code à l'échelle d'aimant, comme Vincenta[30] ou 4C[31]. Ils sont basés sur des caractéristiques analytiques similaires et ont été largement validés avec des expériences de quench effectuées sur des CICCs[32–35] ou sur une couche insérée[36,37]. Néanmoins, il est très rare de trouver une étude numérique des expériences de quench réalisées sur un aimant réel de Tokamak qui est en fait beaucoup plus compliqué à modéliser. Ainsi, cette thèse appliquera l'approche de la modélisation et de l'identification d'un seul phénomène physique à la fois lors de l'analyse numérique des tests de quench sur les TF bobines de JT-60SA sans construire un modèle prédictif d'un aimant entier. Afin d'atteindre cet objectif, le code 1D THEA à l'état-de-l'art sera choisi grâce à sa capacité de modéliser le quench de manière entièrement transitoire et à sa possibilité d'être facilement modifié dans les fichiers "open source" pour des études physiques.

Les trois déclarations ci-dessus justifient le grand intérêt d'étudier et de modéliser les phénomènes thermohydrauliques résultant du quench d'un aimant supraconducteur refroidi en hélium supercritique.

[18] C. A. Luongo et al. *Cryogenics* **34**. 611 –614. 1994.
[19] A. Martinez et al. *Cryogenics* **34**. 591 –594. 1994.
[20] P. Bruzzone et al. *IEEE Transactions on Applied Superconductivity* **12**. 516–519. 2002.
[21] A. Anghel. *Cryogenics* **38**. 459–466. 1998.
[22] L. Dresner. *IEEE Transactions on Magnetics* **25**. 1710–1712. 1989.
[23] L. Bottura and O. C. Zienkiewicz. *Cryogenics* **32**. 659–667. 1992.
[24] A. Shajii and J. P. Freidberg. *Journal of Applied Physics* **76**. 3149–3158. 1994.
[10] D. Ciazynski et al. *IEEE Transactions on Magnetics* **24**. 1567–1570. 1988.
[27] L. Bottura. *Journal of Computational Physics* **125**. 26–41. 1996.
[28] R. Zanino, S. DePalo, and L. Bottura. *Journal of Fusion Energy* **14**. 25–40. 1995.
[29] L. Bottura, C. Rosso, and M. Breschi. *Cyogenics* **40**. 617–626. 2000.
[30] V. Amoskov et al. *Plasma Devices and Operations* **14**. 47–59. 2006.
[31] R. Zanino et al. *Fusion Engineering and Design* **85**. 752–760. 2010.
[32] S. DePalo, L. Bottura, and R. Zanino. *Journal of Fusion Energy* **14**. 49–58. 1995.
[33] R. Zanino, L. Bottura, and C. Marinucci. *Advances in Cyogenics Engineering* **43**. 181–188. 1998.
[34] L. Bottura, C. Marinucci, and P. Bruzzone. *IEEE Transactions on Applied Superconductivity* **12**. 1528–1532. 2002.
[35] K. Sedlak and P. Bruzzone. *Cryogenics* **72**. 9 –13. 2015.
[36] R. Zanino, R. Bonifetto, and L. S. Richard. *IEEE Transactions on Applied Superconductivity* **20**. 491–494. 2010.
[37] R. Bonifetto et al. *IEEE Transactions on Applied Superconductivity* **27**. 1–8. 2017.

A.2 Description expérimentale

Afin de vérifier la performance des aimants et donc d'atténuer leurs risques de fabrication, toutes les 18 TF bobines supraconductrices de JT-60SA ont été testées dans une configuration à une seule bobine dans leurs conditions de fonctionnement nominales (25.7 kA et 5 K). Pour faire cela, un ensemble de systèmes électriques et cryogéniques ont été installés dans la station d'essai (CTF) au CEA Saclay permettant de protéger l'aimant en cas de quench et d'obtenir les données expérimentales nécessaires pour les futures analyses. En général, CTF contient le réfrigérateur d'hélium de 500 W à 5 K, l'alimentation d'énergie de 25.7 kA, le système de vide du cryostat et de la boîte à vanne ainsi que le système de sûreté d'aimant indispensable pour protéger la bobine. Chaque TF bobine de JT-60SA a été fabriquée par 6 CICCs entourés dans les sens horaire ou antihoraire sous forme "D". Ce qui rend la bobine une configuration de 6 double-galettes (DGs) qui peuvent être classifiée en double-galettes latérales, intérieures et centrales en fonction de leur position relative dans le bobine. Chaque galette seule est de 113.277 m de long avec une fraction de vide de 32 % dans le CICC. Le champ de crête en condition nominale dans la configuration de test à une seule bobine dans CTF peut atteindre 3.04 T. Afin d'obtenir tous les paramètres nécessaires à l'étude du comportement de quench des TF bobines, un ensemble des instruments cryogéniques ont également été installés dans le CTF. Il contient le système d'acquisition de données (AS-Net) à 1 kHz (jusqu'à 10 kHz) pour la mesure du courant ainsi que pour toute les tensions nécessaires dans chaque section électrique de la bobine, par exemple, la DG, les joints, les fils d'alimentation, etc. Les températures d'entrée et de sortie de l'hélium ont été mesurées avec le capteur Cernox avec une précision de 20 mK sous conditions nominales (5 K). Les pressions d'entrée et de sortie de l'hélium ont été mesurées avec un capteur de mode membrane. Le débit massique d'hélium a été mesuré avec le venturi classique.

Pour mettre en place un test de quench pour la TF bobine, le protocole expérimental du CTF est composé de trois étapes principales. La première étape consiste à alimenter la bobine au courant nominal de 25.7 kA à 5 K. En raison du réchauffement aux joints par effet Joule, une stabilité thermohydraulique doit être ré-obtenue dans la bobine avec la température de sortie environ 1 K supérieure à celle d'entrée. Ensuite, une augmentation progressive de la température a été appliquée à l'entrée de l'hélium pour d'abord dépasser la température de sortie puis atteindre jusqu'à la température de quench. Cette étape de protocole permet d'initier un quench proche de l'entrée de la bobine. En effet, comme le champ de crête de 3.04 T se situe à l'entrée de la bobine, la température de quench est donc plus facile à atteindre à cet endroit. De plus, toute la phase d'augmentation de la température dure environ 30 minutes d'une manière très progressive. Il s'agit donc d'un état transitoire thermique lent, pour lequel une étude numérique a été réalisée dessus. La dernière étape consiste à détecter le quench puis déclencher une décharge rapide (DR) du courant afin de protéger la bobine. La phase DR est en effet un état transitoire thermique rapide pendant lequel tous les phénomènes liés à la propagation de quench apparaissent. La majorité de l'étude se concentrera alors sur cette phase de phénomène. Dans le but de vérifier l'ensemble du système d'instrumentation dans le CTF, deux expériences de quench ont été réalisés sur la première TF bobine testée. Au total, 19 tests de quench ont finalement été réalisés sur les 18 TF bobines supraconductrices.

A.3 Analyses expérimentales et numériques de quench

Le premier travail au cours de cette étude a été de déterminer une méthode appropriée de traitement des données, appelée méthode de la bobine de détection, permettant de déduire les évolutions expérimentales de la résistance de quench grâce aux mesures de tension inductive de la bobine de détection. Basé sur cette évolution de résistance, quatre phases dynamiques de quench ont été identifiées dans les 6 DGs lors de chaque test de quench[38]. Elles sont respectivement la phase d'initiation de quench, la phase d'accélération de quench, la phase de quench simultané ainsi que la

[38] Y. Huang et al. *Fusion Engineering and Design* **124**. 147 –152. 2017.

phase de saturation de quench. Les phénomènes physiques prépondérants dans chaque phase ont été mis en évidence et analysés avec des approches à la fois expérimentale et numérique.

Pendant la phase d'initiation, un phénomène statistique a été observé avec 53 % des tests de quench initiés dans les DGs latérales ainsi que le reste dans les DGs internes ou centrales. Ces différents emplacements de quench ont été expliqués avec les effets combinés de la performance magnétique des brins (lié à la carte de champ et aux T_{cs}), de la charge thermique externe (venant de la boîte à bobine ou des joints résistifs) et du facteur de frottement dans le CICC (lié à l'efficacité de refroidissement). Parmi eux, l'effet de charge thermique externe a été prouvé être aussi prédominante que la performance magnétique des brins, alors que le facteur de frottement a un effet quasi négligeable sur l'emplacement de quench initial. En particulier, environ 7 % de variation de la charge thermique, révélée par notre modèle numérique de couplage thermique inter-tour, a été montrée comme être suffisante pour changer les emplacements de quench initial, de la galette latérale à la galette centrale. Une telle différence est également dans une marge raisonnable en considérant les différentes chaleurs par effet Joule dans les joints et les différents contacts thermiques qui dépendent du processus de fabrication d'isolation ou de la déformation mécanique par les forces de Lorentz. Le modèle de couplage thermique inter-tour est en fait un modèle numérique d'une seule galette développé dans le code THEA. Il prend en compte les transferts de chaleur à la fois longitudinal et transversal dans une galette et permet de modéliser l'état de quench d'une façon entièrement transitoire[39]. Il a été validé sur les données d'expériences de quench et a été appliqué avec succès à étudier les phénomènes physiques prépondérants identifiés au cours des différentes phases dynamiques de quench. Un ordre de la vitesse de propagation de quench a été obtenu à environ 3 m/s pour la phase d'initiation de quench.

Pendant la phase d'accélération de quench, l'ordre de la vitesse de propagation de quench a été estimé à environ 30 m/s. Un facteur 10 a été vu entre la vitesse de quench pendant la phase d'initiation et celle de la phase d'accélération. Cela vérifie également l'acceptation de la classification de ces deux phases faite au début de l'analyse. Trois types de dynamiques de quench ont été mis en évidence lors de la phase d'accélération. Le premier est le phénomène le plus commun appelé accélération de quench immédiate (68 %). Ce type est caractérisé par un changement continu de pente de résistance de quench près du début de la DR. Deux phénomènes de conduite ont été identifiés, l'effet du nombre de galettes quenchées dans la même DG sur le changement de pente de résistance de quench ainsi que le mécanisme d'accélération de quench par effet de quench-back thermohydraulique (THQB). Les deux ont été vérifiés avec le modèle de couplage thermique inter-tour. En ce qui concerne le premier, deux galettes adjacentes (dans la même DG) ont été calculées pour avoir une différence de temps de quench inférieure à 1 s. Ce qui donc permet d'introduire un certain effet d'accélération sur les évolutions de résistance de quench près du début de la DR. Le second effet THQB a été démontré avec une légère augmentation de la température de l'hélium à l'avant du front de quench ainsi qu'une vitesse maximale de l'expulsion d'hélium calculée à environ la moitié de celle de la propagation de quench expérimentale. L'apparition de l'effet THQB dans les TF bobines doit être liée à leur protocole expérimental de quench avec lequel une faible différence de température (ΔT) entre T_{cs} et conducteur a été obtenue dans l'ensemble de la galette ($\Delta T_{max} \approx 0.3\,\mathrm{K}$). Le deuxième type de dynamique d'accélération de quench est caractérisé comme "retardé" (26 %). Il a été mis en évidence par un changement de pente discontinue de la résistance de quench se produisant avec un certain retard ($0.5\,\mathrm{s} \backsim 2\,\mathrm{s}$) après le début de la DR. Ce phénomène a été expliqué avec les oscillations expérimentales observées pendant la phase de l'augmentation de la température d'hélium à l'entrée. Ces oscillations peuvent en effet provoquer un quench "prématuré" entraînant une grande ΔT donc une longue durée de faible vitesse de la propagation de quench (i.e. un long délai avant que le quench accélère). Les principaux paramètres d'oscillation (période, amplitude et déphasage) ont été vérifiés numériquement d'avoir tous un effet prédominant sur le retard de début de l'accélération de quench. Le dernier type de dynamique d'accélération de quench n'a été observé que dans le test de quench du TFC01 où une série de sauts de résistance locaux ont apparu sans une réelle accélération de quench. Ce phénomène a été expliqué avec la propagation de quench transversale à travers les 6

[39] Y. Huang et al. *IEEE Transactions on Applied Superconductivity* **28**. 1–5. 2018.

tours dans la même galette. Cependant, ce phénomène n'a pas encore été intégré dans le modèle de couplage thermique inter-tour en raison de la contrainte de temps.

Au cours de la phase de quench simultané, deux phénomènes physiques prépondérants ont été étudiés. Le premier est le phénomène de quench simultané qui a toujours eu lieu dans les galettes quenchées ultérieurement (souvent dans les galettes intérieure et centrale). Les analyses expérimentales permettent de donner la plus probable explication: l'écoulement inverse de l'hélium repoussé des galettes quenchées au premier sont rentrés dans les autres galettes via la canalisation principale d'hélium les faisant transiter de manière simultanée. Afin de procéder à une vérification supplémentaire, une étude paramétrique a été réalisée dans le modèle de couplage thermique inter-tour en faisant varier le temps d'injection de l'écoulement d'hélium chaud à l'entrée des galettes centrales. Un retard de 0.28 s s'est avéré être la condition la plus cohérente pour reproduire l'évolution expérimentale. Cela a ensuite, dans une certaine mesure, vérifié l'hypothèse du phénomène de quench simultané induit par l'effet de l'écoulement inverse de l'hélium. Le deuxième phénomène prédominant est la dynamique des sous-phases de quench. En effet, après l'initiation simultanée de quench dans les galettes interne ou centrale, les évolutions de la résistance ont d'abord une décélération vers un plateau puis une ré-accélération jusqu'à la résistance maximale. Un tel phénomène de chaîne a d'abord été expliqué par le fait que la région du faible champ magnétique au milieu des galettes rend le conducteur plus difficile à être quenché en raison d'une T_{cs} plus élevée. Une faible chaleur par effet Joule ralentira alors la propagation de quench. En ce qui concerne le phénomène de ré-accélération de quench, il est très probable qu'une initiation de quench secondaire a eu lieu à la sortie des galettes déclenchée par un quench qui traverse les joints inter-galette en sortie. Ces joints en sortie ont été observés quenché quasiment au même moment de la ré-accélération de quench. Avec le modèle de couplage thermique inter-tour, la dynamique de décélération de quench jusqu'à un plateau de résistance a pu être reproduit avec la condition ci-dessus de 0.28 s de retard. En effet, la carte de champ magnétique a été précisément imposée comme conditions aux limites, l'impact de la région de faible champ peut alors être considéré comme prédominant dans le phénomène de décélération de quench. Par contre, le phénomène de ré-accélération de quench n'a pas encore été intégré dans ce modèle numérique en raison de la contrainte de temps.

Au cours de la dernière phase de saturation de quench, le phénomène de décroissance globale du plateau de résistance saturé a été expliqué avec la compétition entre l'augmentation de la thermo-résistance (augmentation de température) et la diminution de la magnéto-résistance (décharge de courant). De plus, deux autres paramètres importants sont également discutés pour indiquer le "niveau de quench" des bobines, y compris l'énergie par effet Joule et la longueur de la zone normale. Concernant l'énergie par effet Joule, une différence maximale allant jusqu'à un facteur 4 a été acquis parmi les 19 tests de quench. Ceci est principalement lié aux différentes dynamiques de quench qui sont identifiée avant. Plus l'accélération de quench est retardée et plus la ré-accélération de quench a été réduite parmi les galettes, plus l'énergie par effet Joule sera faible. En outre, la légère différence du moment de quench simultané parmi les différents tests peuvent également avoir un certain impact sur le niveau d'énergie par effet Joule. Concernant le deuxième indicateur, la longueur de la zone normale, un modèle physique simplifié a été construit en prenant la résistance de quench expérimentale comme entrée de modèle. Les résultats de ce modèle ont également été vérifiés avec les calculs numériques. Tous les deux calculs permettent de donner une double vérification du "niveau de quench" des bobines pour voir s'il s'agit d'un état de quench complet ou partiel.

A.4 Perspectives

Pour finir, nous allons donner quelques directions éventuelles sur lesquelles une poursuite de travail de ce doctorat peut être ciblé. Comme nous avons déjà étudié pour la phase d'accélération de quench, le nombre de galettes quenchées dans la même DG peut avoir un certain effet sur le changement de pente de la résistance de quench. Néanmoins, un modèle numérique plus global couplant deux galettes sera plus précis pour vérifier les phénomènes de quench combinés ayant lieu dans les deux

galettes adjacentes de la même DG. En ce qui concerne le phénomène unique observé dans le TFC01, les sauts de résistance consécutifs ont également été révélés de façon similaire lors de la modélisation des effets d'oscillation de la température sur l'accélération retardé. Cela pourrait donner une direction d'étude de se concentrer sur les conditions expérimentales de TFC01. Néanmoins, en raison des incohérences quantitative obtenue lors de l'étude de l'accélération de quench retardée, un modèle plus global couplant deux ou plusieurs galettes peut être un bon point de départ pour effectuer une étude plus précise du phénomène des sauts de résistance consécutifs dans le TFC01. Enfin, lors de l'étude du phénomène de ré-accélération de quench (dernière phase de quench), nous avons proposé une hypothèse d'un quench secondaire déclenché à la sortie des galettes basant sur une observation de quench sur les joints inter-galette. En effet, le quench secondaire pourrait être déclenché soit par l'écoulement inverse d'hélium de la tuyauterie de sortie soit par la diffusion thermique à travers les joints inter-galette eux-même. Néanmoins, ces phénomènes physiques ne peut être intégré que dans un modèle numérique où les 12 galettes (ou 6 galettes par la symétrie de bobine) sont couplés à la fois thermiquement et hydrauliquement. Par exemple, un modèle 3D global pourrait être construit en couplant le modèle numérique actuel d'une seule galette en THEA avec les codes FLOWER[113] et Cast3M[114] pour réaliser le couplage thermohydraulique dans toute la bobine TF. En plus de ces phénomènes de propagation de quench, l'augmentation de la pression d'hélium détectée dans les essais de quench est aussi une direction intéressante pour le futur travail. En effet, les mesures de pression d'hélium ont été utilisées directement comme conditions aux limites lors de la simulation de quench. Les phénomènes physiques liés à l'élévation de pression n'ont jamais été reproduits avec succès ou bien analysés. Pour mener à bien cette étude, on peut prendre le modèle physique simplifié (construit dans cette thèse) comme première étape pour déterminer l'évolution de la longueur normale de la zone. Ensuite, un modèle d'augmentation de pression pourrait être complété en s'appuyant sur les volumes chauds et froids de l'hélium (déterminé avec l'évolution de la zone normale) ainsi que les calculs correspondants de densité massique et d'enthalpie comme entrées du modèle.

[113] L. Bottura and C. Rosso. *Cyogenics* **43**. 215–223. 2003.
[114] Cea team. *Site de Cast3M.*. 2018.

APPENDIX B

Code description of the simplified physical model for normal zone length computation

In order to give a more detailed explanation about the simplified physical model, the normal zone length computation in DP2 has been taken as an example to present some code details. It is to note that the model is implemented in *VBA*. Some parameters and numbers used in the code are specifically related to the Excel file of the computations.

The first part of the code is dedicated to the inputs of the model. We start with the sheet activation command *Sheets*("*Ltr_DP2*").*Activate* in order to ensure the computation in the objective sheet, e.g. the sheet for DP2. The basic inputs contain the mesh size `dx` in [m], the copper cross-sectional area `S_Cu` in [m^2], the minimal quench resistance considered in this model `Rmin` in [mΩ] and the copper RRR. Then, the key parameters are also input in the model, including the magnetic field map of P4 (DP2) `Tab_B4`, the hot spot temperature `Tab_Tpc`, the coil current `Tab_Iexp` as well as the experimental quench resistance `Tab_R4`. The last three inputs are all time dependent. The predefined field map of P4 has been read and standardized according to the mesh size personalized in the model. More explanations can be found in the code with the separation in `'---'`.

```
Sheets("Ltr_DP2").Activate
'-------------
' Basic inputs
'-------------
dx = 0.02
S_Cu = 0.00018
Rmin = 0.0001
RRR = 130

'-----------------------------------------------------
' Input of the magnetic field map and standardization
' The number in the table corresponds to the position
' of the data predefined in the sheet.
'-----------------------------------------------------
For i = 0 To 1775                    'space dimension of the input field map (P4)
  Tab_B4(i, 0) = Cells(i + 3, 12)    'abscissa
  Tab_B4(i, 1) = Cells(i + 3, 13)    'field map
Next

'-------------------------------------------------------------------------------
' To create a new table of the standardized field map depending on the
' personalized mesh size.
```

```
' kk = space dimension of the standardized field map table
' Number of meshes = kk + 1
' The standardized field map is defined with the space distribution of the input
' field map.
'-------------------------------------------------------------------------
Tab_B4x(0, 0) = dx
kk = 0
For i = 0 To 6000                    'real space dimension is limited to i = 5663
  If Tab_B4x(i, 0) < 113.277 Then
    Tab_B4x(i + 1, 0) = Tab_B4x(i, 0) + dx
    kk = kk + 1
  Else
    GoTo 10
  End If
Next
10

For i = 0 To kk
  For j = 0 To 1774
    If Tab_B4x(i, 0) >= Tab_B4(j, 0) And Tab_B4x(i, 0) < Tab_B4(j + 1, 0) Then
      Tab_B4x(i, 1) = Tab_B4(j, 1)
      GoTo 11
    Else
      If Tab_B4x(i, 0) >= Tab_B4(1775, 0) Then
        Tab_B4x(i, 1) = Tab_B4(1775, 1)
      End If
    End If
  Next
11
Next


'-------------------------------------------------------------------------
' Input of quench resistance, hot spot temperature and coil current for P4
' Tab_R4   = table of the P4 experimental resistance
' Tab_Tpc  = table of the hot spot temperature
' Tab_Iexp = table of the coil current
'-------------------------------------------------------------------------

For i = 0 To 1601                    'time dimension of the input data
  Tab_R4(i, 0) = Cells(i + 3, 5)     'time
  Tab_R4(i, 1) = Cells(i + 3, 6) / 2 'resistance [mOhm]
Next

Sheets("Tpc_DP").Activate
For i = 0 To 1700                    'time dimension of the input data
  Tab_Tpc(i, 0) = Cells(i + 803, 8)  'time
  Tab_Tpc(i, 1) = Cells(i + 803, 18) 'hot spot temperature
  Tab_Iexp(i, 0) = Cells(i + 803, 8) 'time
  Tab_Iexp(i, 1) = Cells(i + 803, 9) 'coil current
Next
```

After the input data preparation, the normal zone length `Li` has been computed by discretization.

The computations are initiated with the experimental conditions obtained at $t = -2\,\mathrm{s}$. At this moment, the normal zone length has not yet been detected in any of the DPs. As the temperature space profile is also time dependent, it will take much computation time to find the coherent normal zone length by comparing the computed quench resistance `Ri` with the experimental data `Tab_R4`. Indeed, each time the normal zone length varying will change the temperature space profile so that the quench resistance will need to be recomputed from the first mesh. A key step in this code is to assume that the normal zone length, when starts to propagate, will always increase along the time. This will allow to obtain the coherent normal zone length directly from the previous time step as well as the temperature profile that can be built relying on the previous normal zone length. This largely improves the computation speed of the normal zone length at each time step. More explanations can be found in the code with the separation in `'---'`.

```
'-------------------------------------------------------
' Computation of the normal zone length by discretization
'-------------------------------------------------------
Sheets("Ltr_DP2").Activate

'-----------------------------------
' Initiate the iterative computation
'-----------------------------------
T0 = 7.46
Iexp = 25795
nTpc = 0
nRi = 1
nLi = dx
Ri = 0

For i = 0 To 1601                    '1601 =  time dimension of Tab_R4
  If (Tab_R4(i, 1) < Rmin) Then
    Lquench(i) = 0
  Else
    For j = nTpc To 1700             '1700 = time dimension of Tab_Tpc
                                     'nTpc allows to start the computation
                                     'directly from the previous time step.
      If ((Tab_Tpc(j, 0) >= Tab_R4(i, 0))
      And (Tab_Tpc(j, 0) < Tab_R4(i + 1, 0))) Then
        Tpc = Tab_Tpc(j, 1)
        Ii = Tab_Iexp(j, 1)
        nTpc = j
        GoTo 12
      End If
    Next
12

'----------------------------------------
'To find the coherent quench resistance Ri
'by adding the mesh size at each iteration.
'----------------------------------------
    Li = nLi                         'nLi and nRi also allow to start the
                                     'computation directly from the previous
                                     'time step.
    For k = nRi To kk                'kk = 5663 : space dimension of Tab_B4x
```

```
      If (k >= kk) Then             'If reach the maximal length of the conductor,
                                    'directly output Lcond=113.277 (at 14).
        isat = i
        GoTo 14
      Else                          'Field in the 1st mesh size;
                                    'Ri in the 1st mesh size;
                                    'Tpc: temperature of the 1st mesh size
        If (Ri < Tab_R4(i, 1)) Then
          Bi = Tab_B4x(0, 1) * Ii / Iexp
          Ri = rho_Cu(RRR, Tpc, Bi) * dx / S_Cu * 1000
          For l = 1 To k            'Change of temperature profile with k:
                                    'the more the mesh number, the longer the
                                    'normal zone length.
            Bi = Tab_B4x(l, 1) * Ii / Iexp
            Ti = (T0 - Tpc) * l / (k + 1) + Tpc
            Ri = Ri + rho_Cu(RRR, Ti, Bi) * dx / S_Cu * 1000
          Next
          Li = Li + dx
        Else                        'nLi et nRi here play the same role
          If (Ri >= Tab_R4(i, 1)) Then
            Lquench(i) = Li
            nLi = Li
            nRi = k
            GoTo 13                 'To output Li
          End If
        End If
      End If
    Next                            'To go to the next mesh at k+1

  End If
13
Cells(i + 3, 7) = Lquench(i)
Next

14
'-------------------------------------------------
'When reaching the maximal length of the conductor,
'it only remains to output Lcond=113.277 .
'-------------------------------------------------
For i = isat To 1601
Cells(i + 3, 7) = Tab_B4x(kk, 0)
Next
```

Bibliography

[1] J. Ongena, R. Koch, R. Wolf, and H. Zohm. "Magnetic-confinement fusion". *Nature Physics* **12**, 398–410, May. 2016.
DOI: {10.1038/NPHYS3745} (see pp. ix, 137)

[2] L. W. Alvarez, H. Bradner, F. S. Crawford, J. A. Crawford, P. Falk-Variant, M. L. Good, J. D. Gow, A. H. Rosenfeld, F. Solmitz, M. L. Stevenson, H. K. Ticho, and R. D. Tripp. "Catalysis of Nuclear Reactions by mu Mesons". *Physical Review* **105**, 1127–1128, Feb. 1957.
DOI: {10.1103/PhysRev.105.1127} (see pp. ix, 137)

[3] G. McCracken and P. Stott. "Fusion: The Energy of the Universe". *Academic Press*, June. 2012.
URL: {https://www.elsevier.com/books/fusion/mccracken/978-0-12-384656-3} (see pp. ix, 137)

[4] L. A. Artsimovich. "Tokamak devices". *Nuclear Fusion* **12**, 215–252. 1972.
URL: {http://stacks.iop.org/0029-5515/12/i=2/a=012} (see pp. ix, 137)

[5] P. H. Rebut. "The JET preliminary tritium experiment". *Plasma Physics and Controlled Fusion* **34**, 1749–1758. 1992.
URL: {http://stacks.iop.org/0741-3335/34/i=13/a=002} (see pp. ix, 137)

[6] K. M. McGuire, H. Adler, P. Alling, C. Ancher, H. Anderson, J. L. Anderson, J. W. Anderson, V. Arunasalam, G. Ascione, D. Ashcroft, and TFTR team. "Review of deuterium–tritium results from the Tokamak Fusion Test Reactor". *Physics of Plasmas* **2**, 2176–2188. 1995.
DOI: {10.1063/1.871303} (see pp. ix, 137)

[7] T. Fujita, Y. Kamada, S. Ishida, Y. Neyatani, T. Oikawa, S. Ide, S. Takeji, Y. Koide, A. Isayama, T. Fukuda, T. Hatae, Y. Ishii, T. Ozeki, H. Shirai, and JT-60 Team. "High performance experiments in JT-60U reversed shear discharges". *Nuclear Fusion* **39**, 1627–1636. 1999.
URL: {http://stacks.iop.org/0029-5515/39/i=11Y/a=302} (see pp. ix, 137)

[8] M. Keilhacker, A. Gibson, C. Gormezano, P. J. Lomas, P. R. Thomas, M. L. Watkins, P. Andrew, and JET Team. "High fusion performance from deuterium-tritium plasmas in JET". *Nuclear Fusion* **39**, 209–234. 1999.
URL: {http://stacks.iop.org/0029-5515/39/i=2/a=306} (see pp. ix, 138)

[9] M. O. Hoenig and D. B. Montgomery. "Dense supercritical-helium cooled superconductors for large high field stabilized magnets". *IEEE Transactions on Magnetics* **11**, 569–572, Mar. 1975.
DOI: {10.1109/TMAG.1975.1058601} (see pp. ix, 3, 138)

[10] D. Ciazynski, C. Cure, J. L. Duchateau, J. Parain, P. Riband, and B. Turck. "Quench and safety tests on a toroidal field coil of TORE SUPRA". *IEEE Transactions on Magnetics* **24**, 1567–1570, Mar. 1988.
DOI: {10.1109/20.11546} (see pp. ix, xi, 139)

[11] IAEA Vienna. "Summary of the ITER Final Design Report". *ITER Engineering Design Activities Documentation*, July. 2001.
URL: {https://www-pub.iaea.org/books/iaeabooks/6442/Summary-of-the-ITER-Final-Design-Report} (see pp. x, 3, 138)

[12] B. Wan. "Recent experiments in the EAST and HT-7 superconducting tokamaks". *Nuclear Fusion* **49**, 2009.
URL: {http://stacks.iop.org/0029-5515/49/i=10/a=104011} (see pp. x, 138)

[13] G. S. Lee, J. Kim, S. M. Hwang, C. S. Chang, H. Y. Chang, M. H. Cho, B. H. Choi, K. Kim, K. W. Cho, and KSTAR team. "The KSTAR project: An advanced steady state superconducting tokamak experiment". *Nuclear Fusion* **40**, 575–582. 2000.
URL: {http://stacks.iop.org/0029-5515/40/i=3Y/a=319} (see pp. x, 138)

[14] S. Pradhan, Z. Khan, V. L. Tanna, A. N. Sharma, K. J. Doshi, U. Prasad, H. Masand, K. B. Patel, M. K. Bhandarkar, and SST-1 Team. "The first experiments in SST-1". *Nuclear Fusion* **55**, 2015.
URL: {http://stacks.iop.org/0029-5515/55/i=10/a=104009} (see pp. x, 138)

[15] C. Bourdelle, J. F. Artaud, V. Basiuk, M. Bécoulet, S. Brémond, J. Bucalossi, H. Bufferand, G. Ciraolo, and the WEST team. "WEST Physics Basis". *Nuclear Fusion* **55**. 2015.
URL: {http://stacks.iop.org/0029-5515/55/i=6/a=063017} (see pp. x, 138)

[16] Editor. "First plasma for WEST fusion reactor". *World nuclear news*, Dec. 2016.
URL: {http://www.world-nuclear-news.org/NN-First-plasma-for-WEST-fusion-reactor-1912161.html} (see pp. x, 138)

[17] K. Yoshida, K. Tsuchiya, K. Kizu, H. Murakami, K. Kamiya, M. Peyrot, and P. Barabaschi. "Design and Construction of JT-60SA Superconducting Magnet System". *The Journal of Japan Society of Plasma Science and Nuclear Fusion Research* **9**, 214–219, Feb. 2010.
URL: {https://pdfs.semanticscholar.org/1bb9/3bb8866894e4376201e9f2e73bce0cd4cad0.pdf} (see pp. x, 138)

[18] C. A. Luongo, K. D. Partain, J. R. Miller, G. E. Miller, M. Heiberger, and A. Langhorn. "Quench initiation and propagation study (QUIPS) for the SMES-CICC". *Cryogenics* **34**, 611 –614. 1994.
DOI: {10.1016/S0011-2275(05)80143-2} (see pp. x, 139)

[19] A. Martinez, J. Duchateau, G. Bon Mardion, A. Gauthier, and B. Rousset. "Supercritical helium cooling of a cable in conduit conductor with an inner tube". *Cryogenics* **34**, 591 –594. 1994.
DOI: {10.1016/S0011-2275(05)80138-9} (see pp. x, 139)

[20] P. Bruzzone, A. M. Fuchs, B. Stepanov, and G. Vecsey. "Performance evolution of Nb3Sn cable-in-conduit conductors under cyclic load [for Tokamaks]". *IEEE Transactions on Applied Superconductivity* **12**, 516–519, Mar. 2002.
DOI: {10.1109/TASC.2002.1018456} (see pp. x, 139)

[21] A. Anghel. "QUELL experiment: analysis and interpretation of the quench propagation results". *Cryogenics* **38**, 459–466, May. 1998.
DOI: {10.1016/S0011-2275(98)00016-2} (see pp. x, 139)

[22] L. Dresner. "Quench pressure, thermal expulsion, and normal zone propagation in internally cooled superconductors". *IEEE Transactions on Magnetics* **25**, 1710–1712, Mar. 1989.
DOI: {10.1109/20.92630} (see pp. x, 4, 139)

[23] L. Bottura and O. C. Zienkiewicz. "Quench analysis of large superconducting magnets. Part I: model description". *Cryogenics* **32**, 659–667. 1992.
DOI: {10.1016/0011-2275(92)90299-P} (see pp. x, 4, 139)

[24] A. Shajii and J. P. Freidberg. "Quench in superconducting magnets .1. Model and numerical implementation". *Journal of Applied Physics* **76**, 3149–3158, Sept. 1994.
DOI: {10.1063/1.357498} (see pp. x, 4, 71, 139)

[25] A. Ulbricht, J.L. Duchateau, W.H. Fietz, D. Ciazynski, H. Fillunger, S. Fink, R. Heller R.and Maix, S. Nicollet, S. Raff, and et al. "The ITER toroidal field model coil project". *Fusion Engineering and Design* **73**, 189–327. 2005.
DOI: {10.1016/j.fusengdes.2005.07.002} (see p. xi)

[26] T. Kato, H. Tsuji, T. Ando, Y. Takahashi, H. Nakajima, M. Sugimoto, T. Isono, and et al. "First test results for the ITER central solenoid model coil". *Fusion Engineering and Design* **56-57**, 59 –70. 2001.
DOI: {10.1016/S0920-3796(01)00235-6} (see p. xi)

[27] L. Bottura. "A numerical model for the simulation of quench in the ITER magnets". *Journal of Computational Physics* **125**, 26–41, Apr. 1996.
DOI: {10.1006/jcph.1996.0077} (see pp. xi, 4, 101, 103, 139)

[28] R. Zanino, S. DePalo, and L. Bottura. "A two-fluid code for the thermohydraulic transient analysis of CICC superconducting magnets". *Journal of Fusion Energy* **14**, 25–40, Mar. 1995.
DOI: {10.1007/BF02214031} (see pp. xi, 4, 139)

[29] L. Bottura, C. Rosso, and M. Breschi. "A general model for thermal, hydraulic and electric analysis of superconducting cables". *Cyogenics* **40**, 617–626, Oct. 2000.
DOI: {10.1016/S0011-2275(01)00019-4} (see pp. xi, 4, 98, 99, 139)

[30] V. Amoskov, A. Belov, V. Belyakov, O. Filatov, O. Ilyasov, V. Kalinin, M. Kaparkova, V. Kukhtin, N. Shatil, S. Sytchevsky, and V. Vasiliev. "Validation of VINCENTA modelling based on an experiment with the central solenoid model coil of the international thermonuclear experimental reactor". *Plasma Devices and Operations* **14**, 47–59, Mar. 2006.
DOI: {10.1080/10519990500518001} (see pp. xi, 4, 139)

[31] R. Zanino, D. Bessette, L. Richard, and L. Savoldi. "Quench analysis of an ITER TF coil". *Fusion Engineering and Design* **85**, 752–760, Aug. 2010.
DOI: {10.1016/j.fusengdes.2010.04.056} (see pp. xi, 139)

[32] S. DePalo, L. Bottura, and R. Zanino. "Computer analysis of the thermohydraulic measurements on CEA dummy cables performed at CEN-Grenoble". *Journal of Fusion Energy* **14**, 49–58, Mar. 1995.
DOI: {10.1007/BF02214033} (see pp. xi, 139)

[33] R. Zanino, L. Bottura, and C. Marinucci. "Computer simulation of Quench propagation in QUELL". *Advances in Cyogenics Engineering* **43**, 181–188, Feb. 1998.
DOI: {10.1007/978-1-4757-9047-4} (see pp. xi, 139)

[34] L. Bottura, C. Marinucci, and P. Bruzzone. "Application of the code THEA to the CONDOPT experiment in SULTAN". *IEEE Transactions on Applied Superconductivity* **12**, 1528–1532, Mar. 2002.
DOI: {10.1109/TASC.2002.1018693} (see pp. xi, 139)

[35] K. Sedlak and P. Bruzzone. "Results and analysis of the hot-spot temperature experiment for a cable-in-conduit conductor with thick conduit". *Cryogenics* **72**, 9 –13. 2015.
DOI: {10.1016/j.cryogenics.2015.07.003} (see pp. xi, 139)

[36] R. Zanino, R. Bonifetto, and L. S. Richard. "Analysis of Quench Propagation in the ITER Poloidal Field Conductor Insert (PFCI)". *IEEE Transactions on Applied Superconductivity* **20**, 491–494, June. 2010.
DOI: {10.1109/TASC.2010.2041547} (see pp. xi, 139)

[37] R. Bonifetto, T. Isono, N. Martovetsky, L. Savoldi, and R. Zanino. "Analysis of Quench Propagation in the ITER Central Solenoid Insert (CSI) Coil". *IEEE Transactions on Applied Superconductivity* **27**, 1–8, June. 2017.
DOI: {10.1109/TASC.2016.2634598} (see pp. xi, 139)

[38] Y. Huang, W. Abdel Maksoud, L. Genini, D. Ciazynski, P. Decool, and A. Torre. "Quench tests analysis of the first JT-60SA Toroidal Field coils". *Fusion Engineering and Design* **124**, 147 –152. 2017.
DOI: {10.1016/j.fusengdes.2017.02.055} (see pp. xii, 140)

[39] Y. Huang, W. Abdel Maksoud, B. Baudouy, D. Ciazynski, P. Decool, L. Genini, B. Lacroix, Q. Le Coz, S. Nicollet, F. Nunio, A. Torre, R. Vallcorba, and L. Zani. "Numerical Modeling of the Quench Propagation Phase in the JT-60SA TF Coils". *IEEE Transactions on Applied Superconductivity* **28**, 1–5, Apr. 2018.
DOI: {10.1109/TASC.2018.2799176} (see pp. xii, 141)

[40] P. Decool, R. Gonde, G. Gros, G. Jiolat, J. L. Marechal, A. Torre, J. C. Vallet, M. Nusbaum, G. Billotte, B. Crepel, A. Bourquard, S. Davis, and E. Di Pietro. "Manufacturing and acceptance by CEA of the first JT-60SA TF coils". *Fusion Engineering and Design* **124**, 24 –28. 2017.
DOI: {10.1016/j.fusengdes.2017.06.019} (see p. 1)

[41] P. Decool, G. Gros, G. Jiolat, J.L. Marechal, A. Torre, J.C. Vallet, M. Nusbaum, G. Billotte, B. Crepel, A. Bourquard, S. Davis, and E. Di Pietro. "Completion of the French Contribution to the JT-60SA Toroidal Field Magnet". *IEEE Transactions on Applied Superconductivity* **28**, 4200604, Apr. 2018.
DOI: {10.1109/TASC.2017.2768182} (see p. 1)

[42] Gian Mario Polli, Antonio Cucchiaro, Valter Cocilovo, Valentina Corato, Paolo Rossi, Giovanni Drago, Paolo Pesenti, Franco Terzi, Enrico Di Pietro, and Valerio Tomarchio. "JT-60SA TF coils procured by ENEA: An intermediate assessment". *Fusion Engineering and Design* **124**, 123 –126. 2017.
DOI: {10.1016/j.fusengdes.2017.03.033} (see p. 1)

[43] W. Abdel Maksoud, L. Genini, D. Ciazynski, P. Decool, Y. Huang, S. Nicollet, and A. Torre. "Results of the first JT-60 SA toroidal field coils tests in the cold testfacility". *Fusion Engineering and Design* **124**, 14–17, Nov. 2017.
DOI: {10.1016/j.fusengdes.2017.02.009} (see pp. 2, 43, 63)

[44] W. Abdel Maksoud, L. Genini, D. Ciazynski, Y. Huang, and L. Vieillard. "Progress of the JT-60 SA Toroidal Field Coils Tests in the Cold Test Facility". *IEEE Transactions on Applied Superconductivity* **28**, 1–4, Apr. 2018.
DOI: {10.1109/TASC.2017.2786687} (see p. 2)

[45] A. Torre. "JT60-SA TF coil field map calculation at Cold Test Facility". *Internal report*, Dec. 2015.
(See pp. 2, 33)

[46] L. Dresner, W. A. Fietz, S. Gauss, P. N. Haubenreich, B. Jakob, T. Kato, P. Komarek, M. S. Lubell, J. W. Lue, J. N. Luton, W. Maurer, K. Okuno, S. W. Schwenterly, S. Shimamoto, Y. Takahashi, A. Ulbricht, G. Vecsey, F. Wuchner, and J. A. Zichyt. "Results of the international Large Coil Task: a milestone for superconducting magnets in fusion power". *Cryogenics* **29**, 875–882, Sept. 1989.
DOI: {10.1016/0011-2275(89)90199-9} (see p. 3)

[47] K. Takahata, T. Mito, N. Yanagi, M. Sakamoto, A. Nishimura, S. Yamada, J. Yamamoto, S. Mizumaki, K. Nakamoto, K. Yamamoto, T. Yoshida, H. Itoh, M. Shimada, Y. Wachi, and H. Shinohara. "Experimental results of the R&D forced-flow poloidal coil (TOKI-PF)". *Fusion Engineering and Design* **20**, 161–166, Jan. 1993.
DOI: {10.1016/0920-3796(93)90038-J} (see p. 3)

[48] P. Bruzzone. "Superconductors for fusion: Achievements, open issues, roadmap to future". *Physica C - Superconductivity and Its Applications* **470**, 1734–1739, Nov. 2010.
DOI: {10.1016/j.physc.2010.05.196} (see p. 3)

[49] P. Decool, H. Cloez, G. Jiolat, M. Tena, L. Zani, C. Hoa, W. Abdel Maksoud, and M. Verrechia. "JT-60SA TF Coils: Experimental Check of Hydraulic Operating Conditions". *IEEE Transactions on Applied Superconductivity* **26**, June. 2016.
DOI: {10.1109/TASC.2016.2520585} (see pp. 3, 16, 17, 32, 102)

[50] L. Zani, P. Barabaschi, and E. Di Pietro. "Status of European manufacture of Toroidal Field conductor and strand for JT-60SA project". *Fusion Engineering and Design* **88**, 555–558, Oct. 2013.
DOI: {10.1016/j.fusengdes.2012.12.032} (see pp. 4, 99)

[51] A. Shajii and J. P. Freidberg. "Quench in superconducting magnets .2. Analytic solution". *Journal of Applied Physics* **76**, 3159–3171, Sept. 1994.
DOI: {10.1063/1.357499} (see pp. 4, 118)

[52] L. Muzzi, G. De Marzi1, A. Di Zenobio, and A. della Corte. "Cable-in-conduit conductors: lessons from the recent past for future developments with low and high temperature superconductors". *Superconductor Science and Technology* **28**, 1–2, Mar. 2015.
DOI: {10.1088/0953-2048/28/5/053001} (see p. 5)

[53] H. Kamerlingh Onnes. "The disappearance of the resistance of mercury". *Proceedings of Huygens Institute* **14 I**, 113–115. 1911.
DOI: {10.1007/978-1-4757} (see p. 5)

[54] W. Meissner and R. Ochsenfeld. "Ein neuer Effekt bei Eintritt der Supraleitfahigkeit". *Naturwissenschaften* **21**, 787–788. 1933.
(See p. 5)

[55] N. Haleeda, M. Awang Kechik, and R. Abd-Shukor. "PJSRR (2016) 2(1): Effect of Yb2O3 Nanoparticle Addition on Superconducting Properties of BSCCO (2223)/Ag Tapes by Acetate Precipitation Method". *Pertanika Journal of Science and Technology* **2**, Jan. 2016.
(See p. 5)

[56] A. Abrikosov. "Nobel Lecture: Type-II superconductors and the vortex lattice". *Reviews of Modern Physics* **76**, 975 –979, July. 2004.
URL: {https://journals.aps.org/rmp/pdf/10.1103/RevModPhys.76.975} (see p. 6)

[57] Y. Iwasa. "Case Studies in Superconducting Magnets - Design and Operational Issues (Second Edition)". *Springer*, Jan. 2009.
DOI: {10.1063/1.2808214} (see p. 6)

[58] L. Zani, D. Ciazynski, and A. Torre. "Considerations on TF strand TCS in JT-60SA TF coil cold test configuration". *Internal report*, Jan. 2016.
(See pp. 7, 8, 61, 87)

[59] M. S. Lubell. "Empirical scaling formulas of critical current and critical field for commercial NbTi". *IEEE Transactions on Magnetics* **19**, 754–757, May. 1983.
DOI: {10.1109/TMAG.1983.1062311} (see pp. 7, 60)

[60] Charles Bean. "Magnetization of High-Field Superconductors". *Reviews of Modern Physics* **36**, 31 –39, Jan. 1964.
DOI: {10.1103/RevModPhys.36.31} (see p. 7)

[61] D. G. Hawksworth and D. C. Larbalestier. "The high field Jc and scaling behavior in Nb-Ti and alloyed Nb-Ti superconductors". *Proceedings of the 8th Symposium on Engineering Problems of Fusion Research* **1**, 249–254, Nov. 1979.
URL: {http://adsabs.harvard.edu/abs/1979epfr.conf..249H} (see p. 7)

[62] L. Bottura. "A practical fit for the critical surface of NbTi". *IEEE Transactions on Applied Superconductivity* **10**, 1054–1057, Mar. 2000.
DOI: {10.1109/77.828413} (see pp. 8, 60)

[63] Steven Van Sciver. "Helium Cryogenics". *International Cryogenics Monograph Series*. 2012.
DOI: {10.1007/978-1-4419-9979-5} (see pp. 9, 13, 14, 100)

[64] F. C. Schwerer, J. W. Conroy, and Sigurds Arajs. "Matthiessen's rule and the electrical resistivity of iron-silicon solid solutions". *Journal of Physics and Chemistry of Solids* **30**, 1513 –1525, June. 1969.
DOI: {10.1016/0022-3697(69)90213-3} (see p. 10)

[65] E. Floch. “Specific heat, thermal conductivity and resistivity of Cu and NbTi - A bibliographical study”. *Cern*, Aug. 2003.
(See pp. 10, 12)

[66] V. Arp. “Metalpak program”. *Nist*. 2003.
URL: {http://www.htess.com/metalpak.htm#METALPAK} (see p. 10)

[67] P. Eckels, R. Stewart, and V. Arp. “CryoComp program”. *Eckels Engineering Inc.* 1993.
URL: {http://www.eckelsengineering.com/} (see pp. 10, 11)

[68] R. Radebaugh, P. Bradley, M. Lewis, and G. Hardin. “NIST - Material Properties”. *Material Measurement Laboratory / Applied Chemicals and Materials Division*. 2018.
URL: {https://trc.nist.gov/cryogenics/materials/materialproperties.htm} (see p. 11)

[69] V. Arp, B. McCarty, and J. Fox. “Hepak program”. *Nist*. 1993.
URL: {http://www.htess.com/hepak.htm} (see p. 13)

[70] J. Weisbach. “Lehrbuch der Ingenieur- und Maschinen-Mechanik”. *Theoretische Mechanik, Vieweg und Sohn, Braunschweig* **1**, 535. 1845.
(See p. 16)

[71] H. Darcy. “Recherches expérimentales relatives au mouvement de l’eau dans les tuyaux”. *Mallet-Bachelier, Paris*, 268. 1857.
(See p. 16)

[72] B. Baudouy, G. Defresne, P. Duthil, and J. Thermeau. “Transfert de chaleur à basse température”. *Techniques de l’Ingénieur*, 12–16, Jan. 2015.
URL: {https://www.techniques-ingenieur.fr/base-documentaire/energies-th4/froid-cryogenie-applications-industrielles-et-peripheriques-42596210/transfert-de-chaleur-a-basse-temperature-be9812/} (see p. 19)

[73] O. Reynolds. “On the Extent and Action of the Heating Surface for Steam Boilers”. *Proc. Manchester Lit. Philos. Soc.* **14**, 7–12. 1874.
DOI: {10.1016/0017-9310(61)90087-4} (see p. 19)

[74] A. P. Colburn. “A Method of Correlating Forced Convection Heat Transfer Data and a Comparison with Fluid Friction”. *Trans. Am. Inst. Chem. Eng.* **29**, 174–210. 1933.
DOI: {10.1016/0017-9310(64)90125-5} (see p. 19)

[75] F. Dittus and L. Boelter. “Heat transfer in automobile radiators of the tubular type”. *University of California Publications in Engineering* **2**, 443–461, Oct. 1930.
DOI: {10.1016/0735-1933(85)90003-X} (see p. 19)

[76] X. Cheng. “Transversal heat transfer in the cable-in-conduit conductor for the Wendelstein 7-X magnet system”. *Cryogenics* **34**, 659–666. 1994.
DOI: {10.1016/0011-2275(94)90144-9} (see p. 19)

[77] Y. Wachi, M. Ono, and T. Hamajima. “Heat Transfer Characteristics of the Supercritical Helium in a Cable-in-conduit Conductor”. *IEEE Transactions on Applied Superconductivity* **5**, 568–571, June. 1995.
DOI: {10.1109/77.402614} (see p. 19)

[78] F. Juster. “Boucle de tests JT60 - Estimation des charges cryogeniques”. *Internal report*, Dec. 2011.
(See p. 20)

[79] P. Giarratano, V. Arp, and R. Smith. “Forced convection heat transfer to supercritical helium”. *Cryogenics*, 385–393, Oct. 1971.
DOI: {10.1016/0011-2275(71)90038-5} (see pp. 20, 102)

[80] Walid Abdel Maksoud. “Modélisation des phénomènes thermohydrauliques résultant du quench d’un aimant supraconducteur refroidi à l’hélium superfluide”. *Thesis*, Dec. 2010.
URL: {http://www.theses.fr/2010PA112254} (see pp. 24, 100)

[81] W. H. Cherry and J. I. Gittleman. “Thermal and electrodynamic aspects of the superconductive transition process”. *Solid State Electronics* **1**, 287–305, Sept. 1960.
DOI: {10.1016/0038-1101(60)90071-X} (see p. 24)

[82] R. Wesche. “Results of the test of industrially manufactured HTS currentleads with novel design features”. *IEEE Transactions on Applied Superconductivity* **24**, June. 2014.
DOI: {10.1109/TASC.2013.2281121} (see p. 30)

[83] Walid Abdel Maksoud, Patrick Bargueden, Andre Bouty, Gilles Dispau, Andre Donati, Dominique Eppelle, Laurent Genini, Patrice Guiho, Quentin Guihard, Jean-Michel Joubert, Olivier Kuster, Damien Medioni, Frederic Molinie, Armand Sinanna, Nicolas Solenne, Sebastien Somson, and Laurence Vieillard. “Status of the cold test facility for the JT-60SA tokamak toroidal field coils”. *Fusion Engineering and Design* **96-97**, 208–211, Oct. 2015.
DOI: {10.1016/j.fusengdes.2015.06.146} (see pp. 30, 45)

[84] M. Chantant, L. Genini, P. Bayetti, F. Millet, M. Wanner, V. Massaut, A. Della Corte, F. Ardelier-Desage, V. Catherine-Dumont, A. Dael, P. Decool, A. Donati, J. L. Duchateau, P. Garibaldi, S. Girard, J. C. Hatchressian, P. Fejoz, P. Jamotton, L. Jourdheuil, F. P. Juster, O. Kuster, P. Lebourg, F. Leroux, F. Molinie, B. Renard, P. Reynaud, T. Schild, P. Spuig, S. Turtu, L. Vieillard, and C. Walter. “A coil test facility for the cryogenic tests of the JT-60SA TF coils”. *Fusion Engineering and Design* **86**, 561–564, Oct. 2011.
DOI: {10.1016/j.fusengdes.2011.03.050} (see p. 30)

[85] D. Ciazynski, A. Torre, L. Zani, P. Decool, S. Nicollet, F. Peytavy, W. Abdel Maksoud, and L. Genini. “Performance of JT-60SA toroidal field coils in light of strand and conductor test results”. *Fusion Engineering and Design* **124**, 169–172, Nov. 2017.
DOI: {10.1016/j.fusengdes.2016.12.028} (see p. 33)

[86] LakeShore Cryotronics. “Specifications: Cernox temperature sensors”. *Website*, 2018.
URL: {https://www.lakeshore.com/products/Cryogenic-Temperature-Sensors/Cernox/Models/pages/Specifications.aspx} (see pp. 35, 38)

[87] Yokogawa Electric Corp. “Pressure transmitters: absolute pressure and differential pressure”. *Website*, 2018.
URL: {https://www.yokogawa.com/solutions/products-platforms/field-instruments/pressure-transmitters/} (see p. 39)

[88] A. Serrand, W. Abdel Maksoud, and L. Genini. “Etalonnage des tubes de Venturi de JT-60SA CTF à température ambiante”. *Internal report*, June. 2013.
(See p. 41)

[89] Michael J. Reader-Harris. “Venturi Meters”. *Thermopedia*, Feb. 2011.
DOI: {10.1615/AtoZ.v.venturi_meters} (see p. 41)

[90] AspenCore. “LR Series Circuit”. *Electronics Tutorials*, 2018.
URL: {https://www.electronics-tutorials.ws/inductor/lr-circuits.html} (see p. 46)

[91] L. Zani, P. Barabaschi, E. Di Pietro, and M. Verrecchia. “Extended Quality Control Process Applied on TF Strand and TF Conductor Production for JT-60SA Project”. *IEEE Transactions on Applied Superconductivity* **25**, June. 2015.
DOI: {10.1109/TASC.2014.2375291} (see p. 62)

[92] S. Nicollet, W. Abdel Maksoud, J. Cazabonne, D. Ciazynski, P. Decool, Y. Huang, B. Lacroix, A. Torre, and L. Zani. “Parametric Analyses of JT-60SA TF Coils in the Cold Test Facility with SuperMagnet Code”. *IEEE Transactions on Applied Superconductivity*, Jan. 2018.
DOI: {10.1109/TASC.2018.2799162} (see p. 65)

[93] Dresner, Lawrence. “The growth of normal zones in cable-in-conduit superconductors”. *Proc. 10th Symposium on Fusion Engineering*, 2040. 1983.
URL: {https://inis.iaea.org/search/search.aspx?orig_q=RN:16059562} (see p. 70)

[94] Dresner, Lawrence. “Protection considerations for force-cooled superconductors”. *Proc. 11th Symposium on Fusion Engineering* **2**, 1218–1222. 1986.
URL: {https://www.osti.gov/biblio/6485425} (see pp. 70, 117)

[95] Luongo, C. A. and Loyd, R. J. and Chen, F. K. and Peck, S. D. “Thermal-hydraulic simulation of helium expulsion from a cable-in-conduit conductor”. *IEEE Transactions on Magnetics* **25**, 1218–1222, Mar. 1989.
DOI: {10.1109/20.92602} (see p. 70)

[96] J. W. Lue and L. Dresner. “Normal zone propagation and thermal-hydraulic quenchback in a cable-in-conduit superconductor”. *Advances in Cryogenic Engineering* **39**, 437–444. 1994. (See p. 71)

[97] A. Shajii and J. P. Freidberg. “Theory of thermal hydraulic quenchback”. *International Journal of Heat and Mass Transfer* **39**, 491–501, Feb. 1996.
DOI: {10.1016/0017-9310(95)00147-2} (see pp. 71, 118)

[98] L. Bottura. “Magnet Quench 101”. *Accelerator Physics-CERN Yellow Report*, 1–9, Jan. 2013.
DOI: {10.5170/CERN-2013-006.1} (see p. 71)

[99] J. W. Lue, L. Dresner, S. W. Schwenterly, C. T. Wilson, and M. S. Lubell. “Investigating thermal hydraulic quenchback in cable-in-conduit superconductor”. *IEEE Transactions on Applied Superconductivity* **3**, 338–341, Mar. 1993.
DOI: {10.1109/77.233474} (see pp. 71, 119)

[100] A. Louzguiti. “Magnetic screening currents and coupling losses induced in superconducting magnets for thermonuclear fusion”. *Thesis*, 245–247, Dec. 2017.
URL: {https://ecole-doctorale-353.univ-amu.fr/fr/soutenance/2104} (see pp. 78, 79)

[101] Pascal Tixador. “Models & AC losses”. *ESAS summer school 2017*, June. 2017. (See p. 78)

[102] R. Vallcorba, B. Lacroix, D. Ciazynski, Q. Le Coz, S. Nicollet, F. Nunio, A. Torre, L. Zani, V. Corato, and M. Coleman. “Thermohydraulic Analyses on CEA Concept of TF and CS Coils for EU-DEMO”. *IEEE Transactions on Applied Superconductivity* **28**, Apr. 2018.
DOI: {10.1109/TASC.2017.2787654} (see p. 79)

[103] J. G. Charney, R. Fjortoft, and J. Von Neumann. “Numerical Integration of the Barotropic Vorticity Equation”. *A Quarterly Journal of Geophysics-Tellus* **2**, 237–254, Nov. 1950.
DOI: {10.1111/j.2153-3490.1950.tb00336.x} (see p. 85)

[104] K. Takahata, H. Tamura, and T. Mito. “Thermal contact conductance between the bundle and the conduit in cable-in-conduit conductors”. *IEEE Transactions on Applied Superconductivity* **14**, 1477–1480, June. 2004.
DOI: {10.1109/TASC.2004.830658} (see p. 99)

[105] CryoSoft. “User’s Guide - THEA Thermal, Hydraulic and Electric Analysis of Superconducting Cables”. *CryoSoft*, Sept. 2016.
URL: {https://supermagnet.sourceforge.io/thea.html} (see pp. 99, 103)

[106] W. J. Usab. “Embedded mesh solutions of the Euler equation using a multiple-grid method”. *Adv. Comput. Transonics*. 1985.
DOI: {http://hdl.handle.net/1721.1/70615} (see p. 101)

[107] P. Decool, H. Cloez, G. Jiolat, and M. Tena. “Contract F4E-OPE-0580: Expertise support on JT-60SA TF conductor hydraulic tests-Extended tests final report”. *Internal report*, July. 2016. (See p. 102)

[108] O. C. Zienkiewicz, R. L. Taylor, and J. Z. Zhu. “The Finite Element Method: Its Basis and Fundamentals, Sixth Edition”. *Butterworth-Heinemann*, May. 2005.
URL: {https://www.elsevier.com/books/the-finite-element-method-its-basis-and-fundamentals/zienkiewicz/978-0-08-047277-5} (see p. 103)

[109] R. M. Beam and R. F. Warming. "Alternating direction implicit methods for parabolic equations with a mixed derivation". *Siam Journam on Scientific and Statistical Computing* **1**, 131–159. 1980.
DOI: {10.1137/0901007} (see p. 103)

[110] L. Bottura and A. Shajii. "Numerical quenchback in thermofluid simulations of superconducting magnets". *International Journal for Numerical Methods in Engineering* **43**, 1275–1293, Dec. 1998.
URL: {https://doi.org/10.1002/(SICI)1097-0207(19981215)43:7<1275::AID-NME469>3.0.CO;2-0} (see p. 103)

[111] V. Tomarchio and M. Wanner. "On a Full Three-Dimensional Thermal Structural and Hydraulic Finite Element Model of the JT-60SA Toroidal Field Coils". *IEEE Transactions on Applied Superconductivity* **28**, Apr. 2018.
DOI: {10.1109/TASC.2018.2806392} (see p. 106)

[112] Q. Le Coz, D. Ciazynski, M. Coleman, V. Corato, B. Lacroix, S. Nicollet, F. Nunio, R. Vallcorba, and L. Zani. "Quench Simulation of a DEMO TF Coil Using a Quasi-3D Coupling Tool". *IEEE Transactions on Applied Superconductivity* **28**, 1–5, Apr. 2018.
DOI: {10.1109/TASC.2017.2786717} (see p. 106)

[113] L. Bottura and C. Rosso. "Flower a model for the Analysis of Hydraulic Networks and Processes". *Cyogenics* **43**, 215–223, Mar. 2003.
DOI: {10.1016/S0011-2275(03)00038-9} (see pp. 131, 143)

[114] Cea team. "Numerical code: Cast3M". *Site de Cast3M*. 2018.
URL: {http://www-cast3m.cea.fr} (see pp. 131, 143)

université PARIS-SACLAY | ÉCOLE DOCTORALE PHENIICS

Titre : Etude et modélisation des phénomènes thermohydrauliques résultant du quench d'un aimant supraconducteur refroidi en hélium supercritique

Mots clés : thermohydraulique, quench, aimant supraconducteur, hélium supercritique

Résumé : Au cours des dernières décennies, le phénomène de quench a été une des problématiques les plus importantes abordées dans les conceptions d'aimants supraconducteurs. En effet, la transition de quench d'un aimant de son état supraconducteur à son état normal induit une grande quantité de l'énergie par effet Joule. Cet apport de chaleur va ensuite augmenter rapidement la température du conducteur ainsi que la pression du liquide de refroidissement à l'hélium. Le dépassement d'un certain seuil sur ces deux paramètres peut engendrer une détérioration irréversible à l'aimant et au système de refroidissement cryogénique. Afin de mettre en évidence les comportements de quench des bobines supraconductrices à champ toroïdal (TF) du Tokamak JT-60SA, nous avons réalisé des études expérimentales et numériques sur les phénomènes thermohydrauliques résultant du quench d'un aimant supraconducteur fabriqué en câble-en-conduit conducteur (CICC) et refroidi par l'écoulement forcé à l'hélium supercritique.

Dans ce cadre, toutes les 18 TF bobines de JT-60SA ont été testées dans une configuration à une seule bobine dans leurs conditions de fonctionnement nominales de courant et de température (25,7 kA et 5 K). Une augmentation progressive de la température a été appliquée à l'entrée de l'hélium jusqu'à la température de quench, suivie d'une décharge rapide du courant dès que le quench est détecté pour protéger l'aimant. Les analyses expérimentales de ces tests ont d'abord permis d'identifier plusieurs phases dynamiques très différentes pendant toute la propagation de quench. Ensuite, les phénomènes physiques parcourant chacune de ces phases ont été étudiés et les plus prédominants ont été mis en évidence tels que les charges thermiques externes, les performances magnétiques des brins, les transferts thermiques conducto-convectifs entre conducteurs et hélium ou encore l'expulsion d'hélium et le reverse flow. Sur la base de ces analyses expérimentales, un modèle numérique d'une seule galette a été développé dans le code THEA afin d'analyser un phénomène physique à la fois sans construire un modèle global trop complexe de l'ensemble de l'aimant. Ce modèle d'une seule galette a été validé sur les données d'expériences de quench et a été appliqué avec succès pour faire d'autres analyses plus détaillées des phénomènes physiques ainsi que des phases dynamiques identifiées pendant la propagation de quench des TF bobines. Ce modèle numérique a même permis d'identifier certains phénomènes prépondérants qui n'ont pas pu être étudiés dans l'analyse expérimentale, tels que l'impact des instabilités des conditions de test sur la dynamique de quench. Les très bons résultats de ce modèle et sa cohérence avec les analyses physiques expérimentales en font une étape très intéressante vers la modélisation complète de toute la TF bobine de JT-60SA et l'étude de son comportement de quench dans une vraie machine Tokamak et non en conditions d'essais.

Université Paris-Saclay
Espace Technologique / Immeuble Discovery
Route de l'Orme aux Merisiers RD 128 / 91190 Saint-Aubin, France

université PARIS-SACLAY | ÉCOLE DOCTORALE PHENIICS

Title : Study and modelling of the thermohydraulic phenomena taking place during the quench of a superconducting magnet cooled with supercritical helium

Keywords : thermohydraulic, quench, superconducting magnet, supercritical helium

Abstract : During the last decades, the quench phenomenon has been one of the most important issues addressed in the superconducting magnets designs. Indeed, the quench transition of a magnet from its superconducting state to its normal state induces a large deposition of the Joule effect energy leading to an abrupt temperature increase in the conductor as well as a large pressure rise in the helium coolant. Any excess of these two parameters can cause an irreversible damage either to the magnet or to the cryogenic system. In order to achieve a better understanding of the quench behavior of the TF coils in the superconducting Tokamak JT-60SA, we carried out both experimental and numerical studies of the thermohydraulic phenomena taking place during the quench of a superconducting magnet manufactured with Cable-In-Conduit Conductor and cooled in forced flow with supercritical helium.

In this framework, all the 18 JT-60SA TF coils were tested in a single coil configuration at their nominal operating conditions of current and temperature (25.7 kA and 5 K). A progressive temperature increase has been applied to the helium inlet up to the quench temperature, followed by a current fast discharge as soon as the quench is detected to protect the magnet. The experimental analyses of these tests allowed first to identify several very different dynamic phases in the overall quench propagation time. Then, the physical phenomena driving each one of these phases have been studied and the most predominant ones have been highlighted such as the external heat loads, the strands magnetic performances, the conductive and convective heat transfers between conductors and helium or even the helium expulsion and reverse flow. Based on these experimental analyses, a single pancake numerical model has been developed in the THEA code in order to analyze one physical phenomenon at a time without building a too complex global model of the entire magnet. This single pancake model has been validated on the quench experiments data and has been successfully applied to make further more detailed analyses of the physical phenomena as well as the dynamic phases identified during the TF coils quench propagation. This numerical model even allowed identifying some driving physical phenomena that could not be studied in the experimental analysis, such as the impact of the testing conditions instabilities on the quench dynamics. The very good results of this model and its coherence with physical experimental analyses makes it a very interesting step towards the full modelling of the entire JT-60SA TF coil and the study of its quench behavior in real Tokamak and not test facility conditions.

Université Paris-Saclay
Espace Technologique / Immeuble Discovery
Route de l'Orme aux Merisiers RD 128 / 91190 Saint-Aubin, France